CONSEQUENCES OF ANCIENT NEAR-EARTH SUPERNOVAE ON THE HELIOSPHERE AND THROUGHOUT THE SOLAR SYSTEM

BY

JESSE ALAN MILLER

DISSERTATION

Submitted in partial fulfillment of the requirements
for the degree of Doctor of Philosophy in Astronomy
in the Graduate College of the
University of Illinois Urbana-Champaign, 2022

Urbana, Illinois

Doctoral Committee:

Professor Brian D. Fields, Chair, Director of Research
Professor Paul M. Ricker
Professor Leslie W. Looney
Associate Professor Yue Shen

Abstract

An abundance of data now shows evidence for recent supernova activity within 100 pc of our solar system in the last 10 Myr. Two supernovae, one 3 Myr ago and the other 7 Myr ago, have been identified by careful measurements of ^{60}Fe in the geological record. This dissertation explores some effects nearby supernovae have had throughout the solar system.

First, we examine how cosmic rays impinging on the surface of asteroids introduces a background ^{60}Fe flux. This background is found to be approximately two orders of magnitude smaller than the amount delivered by the supernova.

Next, we propose that a mass extinction in the late Devonian 360 Myr ago was triggered by a nearby supernova 20 pc away. Current evidence is consistent with this idea, and we show how measurements of long-lived radioisotopes can test this hypothesis.

After that, we run a suite of simulations showing how the onset of the supernova blast impacts and compresses the heliosphere. Using 2D axisymmetry and idealized hydrodynamics, we show that ram pressure balance gives the penetration distance into the solar system. The Earth is protected from the blast by the solar wind, but much of the outer solar system is left exposed. As a result, the ^{60}Fe observed on Earth must have arrived in the form of dust. The heliosphere rebounds over the following ~ 300 kyr as the supernova remnant continues to evolve and fade.

Based on the recent detection of ^{244}Pu, we then suggest that the local interstellar medium was enriched by a kilonova explosion. The supernova, then, was unlikely to have made ^{244}Pu, but instead pushed the pre-existing isotope onto Earth. Given that the r-process occurred, the isotope ^{129}I should be have a particularly high abundance.

Lastly, we present a model for how the supernova blast dynamically pushes bodies in the Oort cloud. Small particles like dust grains are completely ejected, but objects larger than ~ 10 m are unaffected.

While this dissertation explores many aspects of how supernovae interact with Earth and the solar system, the scope is necessarily incomplete. This field is ripe for further activity from a variety of scientists, including astronomers, nuclear physicists, geologists, biologists, planetary scientists, and more.

This dissertation is dedicated to

the first member of Australopithecus

to glance up at that bright star

that suddenly appeared in the sky

and think,

"Interesting. . . "

Acknowledgments

This dissertation would not be possible without the support of many people I am grateful for.

First, I am delighted to thank my advisor, Brian Fields, who's infectious enthusiasm and boundless energy inspire so much joy in the process of science. Our many hours-long conversations about supernovae, astroparticle physics, and more have been an inspiration to me.

Thank you to the excellent collaborators I have worked with on papers presented in this dissertation: John Ellis, Brian Fry, Xilu Wang, Adam Clark, Bruce Lieberman, Adrian Melott, Rebecca Surman, and Brian Thomas. Thank you also to those in the heliophysics community for helpful conversations that greatly improved my work, including Merav Opher, Elena Provornikova, and Pontus Brandt. I also acknowledge some exceptional undergraduate students who have been a part of our group: Zhenghai, Phil, and Leeanne.

I gratefully thank the many friends that have stood by me in graduate school, especially Sam and Ada (the hivemind!). You have all made the department a warm, welcoming environment.

Finally, thank you to my family, especially my parents and sister, for their unwavering support throughout not just graduate school, but my entire life. Your constant encouragement has made all the difference, and I would not be here without it.

Table of contents

Chapter 1

Introduction

Our place in the solar system and the Milky Way Galaxy influences our lives on Earth. We often think of the sky as unchanging, but sometimes the Universe intervenes dramatically.

1.1 Supernovae

A massive star ($> 8M_{\odot}$) ends its life as a core-collapse supernova (SN), a dramatic explosion that shreds the star apart from the inside. The event releases an intense surge of light visible across some ∼10 billion light-years, an enormous 10^{51} ergs of kinetic energy, and a gargantuan 10^{53} ergs of neutrinos. Similarly, a thermonuclear supernova marks the end of a white dwarf with a similar energy (though much fewer neutrinos). This cosmic blast scatters the nucleosynthetic ash of the dying star into the galaxy. Astronomers find supernovae valuable to probe a wide variety of questions, including the creation of elements (Burbidge et al., 1957) and the cosmological effects of dark energy (Riess et al., 1998; Perlmutter et al., 1999).

Over the life of a massive star, progressively heavier elements are fused together in the core. The majority of its lifetime is spent fusing hydrogen into helium via the proton-proton chain or CNO cycle. Once core hydrogen is depleted, the next stage of stellar evolution begins fusing helium into carbon in the triple alpha process. As the star evolves, it makes successively heavier elements until it reaches iron. At this point, energy can no longer be extracted from fusion, and the star runs out of its nuclear energy source. The core cannot support itself against gravity and collapses. Outer layers rebound off the core, causing the titanic explosion that is a supernova. (For excellent review of this process, see Burrows, 2013 and Woosley et al., 2002.)

After the explosion, the blast wave races outwards into the interstellar medium (ISM), eventually encompassing a significant volume. The supernova remnant (SNR) goes through multiple phases before fading away and dissolving into the ISM. Draine (2011) has an excellent overview of this process, which is summarized here. First comes free expansion, where the blast travels outwards at a near-constant speed. Once the mass of the swept-up ISM is approximately equal to the mass within the remnant, momentum conservation becomes important and the Sedov-Taylor phase begins (Sedov, 1946; Taylor, 1950). Remarkably, simple dimensional analysis using ISM density, explosion energy, radius, and time yields approximately the correct result for the evolution of this phase. After enough time, however, radiation at the leading edge of the blast becomes significant, and the SNR enters the "snowplow" phase. Finally, the speed of the blast wave reaches the typical ISM velocity dispersion, and the SNR fades, mixing into the surrounding medium.

Historical supernovae in our Galaxy have been recorded by Chinese, Korean, Japanese, Arab, and European astronomers for at least one thousand years. Surviving records tell the exact year (and sometimes date) when a supernova was first observed, making these records a valuable chronometer for astronomers. Supernovae were seen in the years 1604, 1572, 1181, 1054, and 1006, and potentially even earlier (Green & Stephenson, 2003), the remnants of which can be observed today. Interestingly, most of these supernovae occurred away from the center of the Galaxy, which should house the majority of supernovae (Murphey et al., 2021). Another supernova, G1.9+0.3, exploded in the late 1800s, but due to its location close to the Galactic center, it was completely obscured by dust clouds and not visible to the astronomers of that day. A similar argument can be made for the non-observation of Cas A. In modern times, nearly 300 Galactic supernova remnants have been catalogued (Green, 2019), making our Galaxy no stranger to these explosions.

Supernovae also affect the Galactic Habitable Zone (GHZ), the region of the Galaxy capable of hosting planets with complex life (Gonzalez et al., 2001; Lineweaver et al., 2004; Morrison & Gowanlock, 2015; Spinelli et al., 2021). Life (especially intelligent life) may find existence difficult if too many nearby stars explode.[1] The inner region of the Galaxy is often excluded from the GHZ due to the frequent occurrence of supernovae delivering cosmic rays, γ-rays, and X-rays to nearby stellar systems (Lineweaver et al., 2004).

[1] Another cosmic explosion to worry about is a gamma-ray burst (GRB) (Scalo & Wheeler, 2002). Their highly-beamed γ-rays make them deadly out to 2 kpc and have been hypothesized to be responsible for the Late Ordovician mass extinction (Thomas et al., 2005, 2020).

1.2 Near-Earth supernovae

Should our solar system happen to be close to the supernova, we could be engulfed in the blast wave. In order for a near-Earth core-collapse supernova to occur, a star must meet three requirements:

1. it must have a mass $\gtrsim 8\ M_\odot$,
2. it must be highly evolved (approaching the end of its life), and
3. it must be within ~ 150 pc of our solar system.

Any two of these requirements are easily met, but satisfying all three makes it rare (on the 100 yr timescale of human lives, at least).

Based on a statistical argument, it is likely that the solar system has encountered several near-Earth supernovae throughout its 4.5 Gyr voyage (Ellis et al., 1996). As near as I can find, the first calculation of the near-Earth supernova rate in the literature is from Krassovskij & Šklovskij (1958), who estimates a nearby supernova less than 8 pc every 200 Myr.[2] Another early calculation was done by Shklovskii & Sagan (1966) in their book *Intelligent Life in the Universe*, who calculate a rate of 1 SN per 750 Myr within 10 pc, a result that holds up well even today. A similar but updated calculation by Fields (2004) estimates the nearby supernova rate λ within a distance r as

$$\lambda(<r) \sim \begin{cases} (10\ \text{Myr})^{-1} \left(\frac{r}{30\ \text{pc}}\right)^3, & r < h \\ (0.3\ \text{Myr})^{-1} \left(\frac{r}{100\ \text{pc}}\right)^2, & r > h \end{cases} \tag{1.1}$$

where $h \sim 100$ pc is the scale height of the Galactic plane.[3] A near-Earth supernova is therefore a common event throughout the history of the solar system. The near-Earth supernova rate depends highly on the average Galactic supernova rate. There are many methods to extract this value, though an average between them yields 1.63 ± 0.46 core-collapse supernovae per century (Rozwadowska et al., 2021). A more detailed calculation of the nearby supernova rate can be performed by including a radial Galactic distribution for the stars, for example. More complexities can be added up to the point of doing a full hydrodynamic simulation, such as in Fujimoto et al. (2020).

[2] Coincidentally, the 8 pc they chose is today known as the "kill distance", the distance at which a supernova will sterilize the Earth.

[3] Within a distance $r < h$, the rate scales with volume, r^3. Once the scale height of the Galactic plane is reached, the rate scales with the area of the disc, r^2.

Firestone (2014) tabulated six near-Earth supernova candidates today (both core-collapse and thermonuclear), but none are likely to explode soon. The closest, Betelgeuse, at ~ 170 pc, is in the early stages of helium burning (Joyce et al., 2020) and will likely take ∼100,000 years before it explodes. Even the nearest known supernova remnant (aside from the Local Bubble), the Antlia SNR (McCullough et al., 2002), lies at a distance of $200 - 300$ pc (Fesen et al., 2021). This remnant will dissipate before the blast wave reaches our solar system. Based on presolar abundances of radioactivities, (Looney et al., 2006) showed that the solar system must have been within $\lesssim 1.6$ pc of a supernova during its formation – in other words, our Sun was born in a cluster that produced massive stars. Further evidence of an early nearby supernova may come from the misalignment between the Sun's spin axis and the planetary disk or the location of the Kuiper belt (Zwart et al., 2018). These days, Earth is in no danger of a near-Earth supernova. This is fortunate, as protecting our planet from such an event would require extraordinary feats of astroengineering (Ćirković & Vukotić, 2016).

1.3 Evidence and implications

The main evidence for near-Earth supernovae comes from radioisotopes found in terrestrial deposits. The evidence layed out here is also summarized in Fields et al. (2019). Radioisotopes with half-lives of ∼Myr are excellent for probing supernova activity because they must have been made recently, yet still have a long enough lifetime to trace back over several million years (Ellis et al., 1996; Korschinek et al., 1996). The expected surface density of a radioisotope is (Fields & Ellis, 1999):

$$N_i(t) = \frac{M_i/A_i m_p}{16\pi r^2}\ \mathrm{e}^{-t/\tau_i} \tag{1.2}$$

$$= 4.6 \times 10^8\ \mathrm{e}^{-t/\tau_i}\ \text{at cm}^{-2}\ \left(\frac{A_i}{60}\right)^{-1} \left(\frac{M_i}{10^{-5} M_\odot}\right) \left(\frac{r}{30\ \text{pc}}\right)^{-2} \tag{1.3}$$

where M_i is the supernova-ejected mass of isotope i (assumed here to be ^{60}Fe for scaling), A_i is the mass number of the i, m_p is the proton mass, r is the distance to the supernova, t is the time since explosion, and τ_i is the mean lifetime of i. Note that this measurement is $\mathcal{O}(10^8)$ atoms cm^{-2} – a minuscule amount! Measurements of this surface density require extraordinarily high precision.

Supernovae make ^{60}Fe through successive neutron captures onto ^{58}Fe. In order to release ^{60}Fe

into the ISM, it cannot be part of the core material that is accreted onto the proto-neutron star. Instead, it is mainly made at the base of the helium-burning layer and the carbon-burning layer during explosive nucleosynthesis (Jones et al., 2019) and is highly sensitive to the ^{59}Fe$(n,\gamma)^{60}$Fe reaction rate. The overall production of ^{60}Fe in a supernova varies across both simulation codes and physical parameters like stellar mass (Limongi & Chieffi, 2006, 2018; Wanajo et al., 2013; Sukhbold et al., 2016; Curtis et al., 2019). A good estimate appears to be in the range of $10^{-5} - 10^{-4}$M$_\odot$ of ^{60}Fe per supernova.

There is now abundant data of supernova-produced, undecayed ^{60}Fe ($t_{1/2} = 2.6$ Myr, Rugel et al., 2009; Wallner et al., 2015a; Ostdiek et al., 2017) in deep-sea samples. Knie et al. (1999a) presented the first detection of ^{60}Fe in a deep ocean ferromanganese (FeMn) crust.[4] These crusts grow at the slow rate of ~ 1 mm/Myr, absorbing mostly iron and manganese from the surrounding seawater. Knie et al. (2004) built on this discovery with a time-resolved study, finding a sharp peak of ^{60}Fe 2.8 Myr ago. Fitoussi et al. (2008) analyzed a sediment with a growth rate of 3 mm/kyr to get better time-resolution. They found a significantly more extended signal width of ~ 0.5 Myr. These initial ^{60}Fe detections were proposed to be from micrometeorites (Basu et al., 2007; Stuart & Lee, 2012), however, such claims have dwindled in the face of abundant additional evidence. Ludwig et al. (2016) further confirmed this signal by analyzing the iron content in magnetotactic bacteria buried within ocean sediment. Wallner et al. (2016) used FeMn crusts, sediment, and nodules to clarify that the signal was a global deposition that was not limited to one region of the Earth. Their search out to longer times revealed hints of a second, older supernova around 7 Myr. Recently, Wallner et al. (2021) provided confirmation of the 7 Myr supernova.

Supernova-produced ^{60}Fe has also been found in lunar samples (Fimiani et al., 2016) brought back by Apollo astronauts.[5] This detection confirms that no terrestrial process is responsible for the observed ^{60}Fe and therefore the signal must be astrophysical. There still exists a current influx of ^{60}Fe today, as shown in Koll et al. (2019) by finding ^{60}Fe in a surface layer of Antarctic snow. Finally, Binns et al. (2016) found an ^{60}Fe component in cosmic rays. This detection is consistent with that of a nearby supernova, but could also be from nearby massive star clusters.

[4] The ^{60}Fe/Fe ratio has been measured to an astounding $\sim 10^{-15}$ or better! Such precise techniques are achieved with accelerator mass spectrometry.

[5] ^{60}Fe is also made by cosmic rays on the lunar surface; Fimiani et al. (2016) measured an excess of ^{60}Fe above this amount.

The supernovae 3 and 7 Myr ago each had their own individual ^{60}Fe abundance. This value is difficult to measure for both astrophysical and geophysical reasons. Further complicating the picture, the amount of ^{60}Fe we receive varies by distance in accordance with the inverse-square law (Ellis et al., 1996; Fields & Ellis, 1999). Estimates of the distance to the 3 Myr old supernova place it around 60-130 pc (Fry et al., 2015). Admittedly, this "radioactivity distance" has a wide range. In order to calculate a more precise distance, many parameters need to be more tightly constrained, including the supernova ^{60}Fe generation, amount of ^{60}Fe incorporated into dust, the uptake fraction into sediment and ferromanganese crusts, and the total abundance of ^{60}Fe in terrestrial samples.

^{60}Fe is not the only isotope that has been associated with nearby supernovae. Several studies have hinted at detections of ^{244}Pu (Wallner et al., 2004, 2015b; Paul et al., 2001; Raisbeck et al., 2007), but have yielded at most one atom. More recently, Wallner et al. (2021) showed strong evidence of astrophysical ^{244}Pu in the same ferromanganese crusts as ^{60}Fe. This finding suggests a nearby source for the r-process,[6] either as a supernova or a previous neutron star merger that enriched the local interstellar medium. Korschinek et al. (2020) claim to detect ^{53}Mn, though further data is needed to calculate the abundance and flux over time. Feige et al. (2018) searched for ^{26}Al coincident with the ^{60}Fe signal, but did not find any due to the high terrestrial background. They placed constraints on the ^{60}Fe/^{26}Al ratio that is similar to the expected Galactic average.

Several groups have looked for ^{244}Pu alongside the ^{60}Fe supernova signal, but found little evidence for it (one atom at most). Recently, however, Wallner et al. (2021) presented substantial evidence of ^{244}Pu in a ferromanganese crust coincident with ^{60}Fe for both the 3 Myr and 7 Myr events. Pu is an r-process element that requires a very neutron-rich environment in order to form. The most likely astrophysical environments for this appear to be in binary neutron star mergers (kilonova) and some rare types of supernovae (see, e.g., Cowan et al., 2021, and references therein). It would be exceedingly improbable for both known near-Earth supernova to have produced ^{244}Pu.

In the ISM, ^{60}Fe and ^{26}Al are also notable in that their decay emits specific gamma ray lines that can be detected by gamma ray telescopes (see, e.g., Harris et al., 2005; Diehl, 2006; Kretschmer et al., 2013).[7] The abundance of these isotopes helps constrain the average Galactic supernova rate

[6] The r-process is the sequence of rapid neutron captures that synthesizes many heavy elements above iron and nickel.

[7] In more detail, it follows the decay chain $^{26}\mathrm{Al} \xrightarrow{t_{1/2}=7.17\ \mathrm{Myr}} {}^{26m}\mathrm{Mg} \xrightarrow{t_{1/2}\sim 100\ \mathrm{fs}} {}^{26}\mathrm{Mg} + \gamma$, but the ^{26m}Mg halflife is negligible. Similarly, the ^{60}Fe decay chain is $^{60}\mathrm{Fe} \xrightarrow{t_{1/2}=2.6\ \mathrm{Myr}} {}^{60m}\mathrm{Co} \xrightarrow{t_{1/2}=10\ \mathrm{min}} {}^{60}\mathrm{Co} + \gamma \xrightarrow{t_{1/2}=5.3\ \mathrm{yr}} {}^{60}\mathrm{Ni}$.

(Diehl et al., 2006). Fujimoto et al. (2020) showed that the unexpectedly large scale height of ^{26}Al is consistent with that of a nearby, local supernova. In that sense, the ^{26}Al distribution maps may not represent a true Galactic distribution, but are contaminated by the near-Earth supernova.

While radioisotopes are an excellent way to probe local supernova activity, several additional methods have contributed to our understanding. The solar system currently resides in the Local Bubble, a region of low-density that was carved out by multiple supernovae several Myr ago (see e.g., Smith & Cox, 2001; Frisch et al., 2011; Frisch & Dwarkadas, 2017; Breitschwerdt et al., 2016; Schulreich et al., 2017; Zucker et al., 2022). The stellar clusters that first shaped the Local Bubble still contain massive stars today. The locations for near-Earth supernovae are likely from these clusters, such as the Scorpius-Centaurus OB association (Maíz-Apellániz, 2001; Benítez et al., 2002) or the Tucana-Horologium cluster (Mamajek, 2015; Hyde & Pecaut, 2018). By tracing the locations of nearby clusters back in time, Sørensen et al. (2017) estimated which ones were likely responsible for nearby supernovae over the past 35 Myr. And by back-tracing the locations of pulsars and runaway stars over time, Neuhäuser et al. (2020) suggest a specific pair (the pulsar PSR B1706-16 and the runaway star ζ Oph) that were in a similar location $\sim$1.8 Myr ago. These two stars could have been the progenitor system for a supernova at that time. Similarly, Tetzlaff et al. (2013) suggested a progenitor for the Antlia supernova remnant (McCullough et al., 2002). Finally, additional evidence comes from the cosmic ray spectrum. Cosmic ray anisotropy was shown to be consistent with a nearby supernova (Savchenko et al., 2015), as were several features in both the proton and anti-proton cosmic ray spectra (Kachelrieß et al., 2015, 2018).

Potential biological effects of nearby supernovae have also been explored for decades. If the supernova occurs too close to our solar system, it could cause significant damage to the ozone layer around Earth (Ruderman, 1974; Gehrels et al., 2003). This could result in a mass extinction (Terry & Tucker, 1968; Ellis & Schramm, 1995; Crutzen & Brühl, 1996). Indeed, Alvarez et al. (1980) even considered the possibility that a supernova caused the K-Pg event that extincted all the non-avian dinosaurs. (They ruled out this scenario due to the close distance the amount of iridium implied and the lack of ^{244}Pu in the geological boundary layer.) Typically, 8 pc is taken as the canonical "kill distance" for a supernova (Gehrels et al., 2003), though this distance depends on the gamma ray flux and varies among supernovae. The fact that you and I are alive today is strong indication that an event this close has not occurred in the past few million years.

More distant supernovae that do not trigger a mass extinction may still have an effect on the biosphere. Even supernova from 50-100 pc may increase cosmic ray exposure and cause minor extinctions of marine megafauna (Melott et al., 2018) or additional effects (Thomas et al., 2016; Thomas, 2017; Melott et al., 2017; Melott & Thomas, 2017). Excitingly, it has been proposed that the 3 Myr old supernova may even have contributed to human evolution (Melott & Thomas, 2019), though such links are still very tenuous. Karam (2002) estimate that without an atmosphere, supernovae may be deadly out to 1 kpc, which has implications for interstellar and interplanetary panspermia.

Many other interesting ideas to probe nearby supernova activity have been presented, though not all have been as successful as oceanic ^{60}Fe. Rood et al. (1979) claimed to detect spikes in nitrates (NO_3^-) made by supernova γ- and X-rays that became incorporated into Antarctic ice within the past $\sim$1000 years, and Burgess & Zuber (2000) make a similar claim relating nitrates to the Vela supernova remnant. Iyudin (2002) later showed that supernova-produced nitrates are difficult to disentangle from solar activity. Later, Motizuki et al. (2009) showed evidence of nitrates in an Antarctic ice core dated to SN 1006 and SN 1054 above the solar background. Sonett et al. (1987) made a similar claim about ^{10}Be in an ice core 33 and 60 kyr ago. A recent study reports dating Antarctic ice cores out to 2 Myr (Yan et al., 2019), a promising way to probe the late dust fallout from the 3 Myr supernova.

Damon et al. (1995) attributed an increase in ^{14}C in tree rings to SN 1006. Another ^{14}C increase was found in tree rings around 774-775, but a supernova cause has been ruled out (Miyake et al., 2012). Later, Cole et al. (2006) searched for supernova dust grains in an ice core over the past 72 kyr, but could not positively identify any.[8] Another interesting proposal is that SN neutrinos could convert a small amount of molybdenum (Mo) ore to technetium (Tc) via inverse beta decay (Haxton & Johnson, 1988). Solar neutrinos also induce this reaction, but about $\sim 10-20\%$ of ^{97}Tc in Mo ore should be due to supernovae (Lazauskas et al., 2009).

Taken together, this abundance of data presents compelling evidence for nearby supernova activity in the past $\sim$10 Myr. Two supernovae have been well-characterized, one at 3 Myr and the other at 7 Myr. The geological epoch these supernova occurred in are the Pliocene ($5.3-2.6$

[8]The recent detection of ^{60}Fe in Antarctic ice (Koll et al., 2019) still suggests an influx of interstellar dust even today, so it is interesting that this search found none.

Myr ago) and the Miocene ($23 - 5.3$ Myr ago); hence we (informally) call them the Pliocene and Miocene supernovae.

1.4 Delivering ^{60}Fe from a supernova to Earth

Considerable theoretical work has gone into understanding the transport of ^{60}Fe from the supernova explosion to deep-sea ocean samples on Earth, and great strides forward have been achieved in recent years. Fry et al. (2015) showed that the ^{60}Fe must have originated in a core-collapse or electron-capture supernova, and estimated distances to the explosion based on the total ^{60}Fe deposition. Thermonuclear supernovae and neutron star mergers produce very little ^{60}Fe, so in order to produce the measured abundance, they would have been well within the 8 pc "kill distance".

Asymptotic giant branch (AGB) and super-AGB stars also produce ^{60}Fe that their stellar winds blow into the Galaxy (Doherty et al., 2014). However, their winds are slow, typically only $5 - 15$ km s^{-1} (Höfner & Olofsson, 2018). The dust would have spent considerable time diffusing through the ISM, decaying as it travelled. A single AGB star passing very close to our solar system could then deliver ^{60}Fe to Earth. This argument is admittedly unsatisfying, as AGB stars cannot be conclusively ruled out as the source of ^{60}Fe. However, the abundance of additional data beyond ^{60}Fe collectively support the supernova hypothesis.

No terrestrial processes make ^{60}Fe, and given the halflife of 2.62 Myr, none has survived from the formation of the Earth. Extinct ^{60}Fe has been a valuable chronometer for early solar system processes (Tachibana & Huss, 2003).

The other known source of ^{60}Fe comes from cosmic ray (CR) nucleosynthesis on the surface of rocky solar system bodies. A proton or secondary neutron striking nickel (Ni) in these rocky bodies produces a small amount of ^{60}Fe. In the detection of supernova ^{60}Fe in lunar samples (Fimiani et al., 2016), this effect had to be taken into account, such that an excess of ^{60}Fe over cosmic ray production was observed. A steady influx of meteors burn up in the atmosphere and spread their material across the globe. If a large enough influx of asteroids strike the Earth, they may imitate the ^{60}Fe signal. Even if this large influx did not occur, it is worth calculating the background due to this process. This calculation can help clarify what portion of the total ^{60}Fe abundance is due to CR nucleosynthesis and therefore how much comes from the supernova. This possibility was

initially investigated by Wallner et al. (2016), who conclude that the total amount of ^{60}Fe from meteoroids is insignificant. In order to determine the purity of supernova ^{60}Fe in terrestrial samples, the abundance of ^{60}Fe from cosmic rays impinging on impactors must be more tightly constrained. Barring this as-yet unmeasured source, all other ^{60}Fe appears to be from a supernova.

Initially, ^{60}Fe-bearing dust was assumed to travel with the gas in the SNR. The profile of ^{60}Fe would have been a proxy for supernova remnant evolution (likely in the Sedov-Taylor phase) and have a duration of $\lesssim 0.1$ Myr. While the initial measurement with a time profile (Knie et al., 2004) seemed to support this idea, following measurements have shown a much longer duration of ^{60}Fe of ~ 1 Myr (Ertel et al., 2022). Breitschwerdt et al. (2016) and Schulreich et al. (2017) suggest that the profile is not from one supernova, but instead the sum of several more distant supernovae that carved out the Local Bubble. Future ^{60}Fe measurements with more precise time resolution may corroborate or rule out this scenario. Slavin et al. (2020) track dust grain dynamics in an evolving SNR, though they focus on grain composition. Fry et al. (2020) examined the kinetics of dust in an expanding supernova remnant. Dust reaching the forward shock encounters a magnetic field that reflects the grain back into the remnant. This "pinball" model suggests that the dust decouples from the gas and leads to a 1 Myr fallout time, matching the width of the ^{60}Fe signal for a single supernova. This also implies that directional information is partially scrambled by the remnant itself, even before reaching our solar system. Fry et al. (2016) follows supernova-produced dust through the heliosphere, Earth's atmosphere, and to the ocean floor.

The composition of the grains that brought ^{60}Fe is unclear. Given that ^{60}Fe does not form in the same location as typical iron in the supernova explosion, ^{60}Fe that arrives at Earth may not be part of iron grains. The composition of some supernova dust grains can be directly measured from presolar grains (for a review, see Zinner, 1998, and references therein). These grains are formed from AGB stars or supernova ejecta out of refractory elements. The forming solar system incorporates them into comets and asteroids, which preserve them for billions of years. By locating and analyzing these grains in meteorites, a more complete understanding of supernova nucleosynthesis and dust formation can be achieved. Searches for individual silicon carbide (SiC) dust grains from the supernova 3 Myr ago in the same sediment as ^{60}Fe has thus far not proven fruitful (Ogliore et al., 2020), but it is possible that all dust was vaporized upon impact with the atmosphere.

Ertel et al. (2022) analyzed the ^{60}Fe profile extensively from a statistics perspective. While

various line shapes fit to the data agree that the data has a width of $\gtrsim 1.6$ Myr, the specific shape of the profile is not well-constrained. This extended width strongly suggests that the dust decoupled from the gas as the SNR evolved. Chaikin et al. (2021) explored how the trajectory of the solar system interacts with a supernova remnant. Even assuming the dust is entrained in the gas, various trajectories naturally give rise to a 1 Myr duration of ^{60}Fe. The signal profile depends in large part on how the SNR mixes into the ISM.

After travelling through interstellar space, the dust arrives at the heliosphere. The present-day heliosphere filters dust from the ISM (see e.g., Wallis, 1987; Frisch et al., 1999; Belyaev & Rafikov, 2010; Mann, 2010; Slavin et al., 2010; Alexashov et al., 2016; Strub et al., 2018). However, dust in the local ISM today follows the gas dynamics (up to the heliospheric boundary). It has a velocity similar to the speed of the Sun through the local ISM, 26 km s^{-1} (Lallement & Bertaux, 2014; Strub et al., 2015; Möbius et al., 2012, see also Table 1 in Linsky et al., 2019). The dust from the supernova had a velocity great enough that very little deflection occurred ($< 1°$, Athanassiadou & Fields, 2011; Fry et al., 2016). The blast wave from the supernova greatly compressed the heliosphere during its initial arrival (Fields et al., 2008; Miller & Fields, 2022), but the ^{60}Fe timescale shows that dust continued flowing into the solar system long after the heliosphere would have rebounded. Therefore, the heliosphere likely has little effect on the abundance and direction of ^{60}Fe dust grains on their journey to Earth.

As the ^{60}Fe-bearing dust grains travel through the solar system, they eventually reach Earth. The dust grains, presumably moving at very high velocity, would be completely vaporized in the atmosphere. Fry et al. (2016) finds that Earth's atmosphere scrambles the ^{60}Fe signal across the globe, erasing any directional information. The dust reforms and falls through the atmosphere, eventually accumulating at the bottom of the ocean. The Moon, with a lack of substantial atmosphere, may still preserve directional information. Current data taken from multiple Apollo sites (Fimiani et al., 2016), is not precise enough to make any definitive statements about the direction of ^{60}Fe dust. Future samples, such as those from NASA's upcoming Artemis mission[9] to the lunar South Pole (Smith et al., 2020), may assist in constraining the direction, though the pinball model of dust dynamics (Fry et al., 2020) complicates the situation.

[9] https://www.nasa.gov/artemisprogram

1.5 Other effects throughout the solar system

A supernova may affect the solar system in multiple ways via the initial photon blast, forward shock, and cosmic ray exposure. Stern & Shull (1988) examined how the photon blast flash-heats the outer surfaces of comets in the Oort cloud. Compared to passing stars, supernovae heat these surfaces to a higher temperature, but their fleeting nature means the high temperature does not penetrate deeply into the comet. Stern (1990), again looking at the Oort cloud, estimated that the hot environment of a supernova remnant will erode comets by only 10^{-2} g cm^{-2}. Over the lifetime of the solar system, this amount is comparable to the erosion from the warm ISM but only 1% that of passage through molecular clouds.

A supernova blast is among the most dramatic environments the heliosphere encounters, and represents an interesting bridge between heliophysics and astrophysics. The heliosphere prevents all ISM plasma from reaching the inner solar system (Parker, 1958, 1965; Baranov et al., 1991), though some dust and neutral particles can infiltrate the inner solar system. Given that the size of the heliosphere changes over time in response to the local Galactic environment (Müller et al., 2006, 2009), the forward shock of the SNR must compress the solar wind. Simulations have shown that the blast wave exposes much of the outer solar system, but even a close supernova blast does not reach all the way to Earth (Fields et al., 2008; Miller & Fields, 2022). Therefore, the ^{60}Fe observed on Earth must not have arrived as a plasma, but as dust grains that punched through the heliosphere.

The blast still swept across much of the outer solar system, and any additional effects it may have had remain to be seen. The shocks that form the heliosphere (such as the termination shock and the bow shock) accelerate cosmic rays through Fermi acceleration (Zank et al., 1996; Lazarian & Opher, 2009). A detailed model of how these cosmic rays propagate over time as the heliosphere rebounds could assist with a more accurate calculation of biological damage and space weathering. Finally, knowing how far the supernova blast penetrated into the solar system, we can question what other effects the blast wave could have had and whether those effects are still observable 3 Myr later.

1.6 Structure of this dissertation

The structure of this dissertation is as follows:

- In Chapter 2, we present calculations showing how primary and secondary cosmic rays can generate ^{60}Fe on the surfaces of asteroids. Our conclusions agree that meteoritic ^{60}Fe is extremely unlikely to have an appreciable contribution to the supernova signal, though experimental methods are quickly approaching the point where this background signal may be detected.

- In Chapter 3, we hypothesize that a supernova caused ozone depletion and a subsequent mass extinction at the Devonian-Carboniferous boundary 360 Myr ago. A recent paper (Marshall et al., 2020) showed evidence for ozone depletion at this time. We note that this relation does not constitute evidence for a supernova-triggered extinction; we also show how our hypothesis could be further tested with long-lived radioisotopes.

- In Chapter 4, we show hydrodynamic simulations of the heliosphere being compressed by a supernova blast wave. This is a follow-up to a previous study (Fields et al., 2008) that used very close distances to the supernova (30 pc at most). We take advantage of axisymmetry and assume a steady solar wind. Our model shows ram pressure balance as the primary factor in the size of the heliosphere. The results are highly dependent on distance to the supernova, as the strength of the shock decreases over distance. We use ram pressure scaling to determine how the heliosphere rebounds over 300 kyr as the SNR evolves.

- In Chapter 5, we present calculations of the r-process in binary neutron star mergers and supernovae that could account for the ^{244}Pu detection. Rather than be produced by both supernovae, we suggest that an older binary neutron star merger enriched the giant molecular cloud that gave rise to the Local Bubble. The observed ^{244}Pu was therefore not made by these supernovae, but was still incorporated into the ^{60}Fe-containing medium. We show how relative isotope abundances can help distinguish between the supernova and kilonova scenarios.

- In Chapter 6, we describe a simple model of how outer bodies in the Oort cloud may have received enough kinetic energy from a supernova blast to modify their orbits. As part of the

Undergraduate Research Apprenticeship Program, the undergraduate Leeanne Smith assisted with this work. We find that while objects larger than ~ 100 m are stationary in their orbits, small dust grains are completely ejected.

- In Chapter 7, I conclude the work presented in this dissertation and give my thoughts about upcoming work and the future of the field.

Chapter 2

Bounds on Earth-impactor production of ^{60}Fe: terrestrial detections require extrasolar sources

2.1 Introduction

When a massive star undergoes core-collapse and explodes as a supernova, it scatters enriched material into the surrounding interstellar medium. Should our solar system be near the supernova ($\lesssim 100$ pc), supernova debris may engulf the solar system and supernova dust literally rains upon the Earth (Fields et al., 2008; Fry et al., 2016). The deposition of live (not decayed) radioisotopes provides the geological smoking gun for such events (Ellis et al., 1996), as long as there is no appreciable background from terrestrial or solar system processes. A simple statistical calculation of an average supernova rate in the Galaxy suggests that such a near-Earth supernova occurs every few million years (Fields, 2004; Shklovskij, 1969).

Remarkably, several studies now have indeed found live ^{60}Fe ($t_{1/2} = 2.62$ Myr) in layers of ocean sediments and crusts from around the world (Knie et al., 1999a, 2004; Fitoussi et al., 2008; Wallner et al., 2016; Ludwig et al., 2016; Wallner et al., 2021) and even lunar samples returned by Apollo astronauts (Fimiani et al., 2016) and in Antarctic snow (Koll et al., 2019). Since no terrestrial processes make ^{60}Fe (e.g., antropogenic fissile sources are negigible Koll et al., 2019), the discovery of ^{60}Fe indicates that an astrophysical source is responsible. The common interpretation is that

dust (Benítez et al., 2002; Athanassiadou & Fields, 2011) from a near-Earth supernova reached Earth and was deposited 2-3 Myr ago, and points to one or more events within a "radioactivity distance" $\sim$ 100 pc of Earth (Fry et al., 2015; Fields et al., 2005).

Supernovae are not the only extraterrestrial producers of ^{60}Fe. Fry et al. (2015, FFE15 hereafter) systematically examined all astrophysical sources of ^{60}Fe to investigate the source of this radioisotope. Core-collapse supernovae are major ^{60}Fe producers. In contrast, Type Ia (thermonuclear) supernova ^{60}Fe yields are so small that in order to account for the observed signal, the supernova would need to be about 0.6 pc away. This is not only improbably but is excluded because it is deeply within the $\sim$ 8 pc "kill distance" at which supernova ozone destruction is catasrophic (Gehrels et al., 2003). FFE15 similarly rule out a neutron star merger. Another possibility is from the winds of super-AGB stars. While FFE15 does not explicitly rule this out, the winds of these stars are small compared to supernovae: dust containing ^{60}Fe would take a long time to diffuse through space to Earth, and it is not clear what transport mechanisms would be responsible a timely arrival. FFE15 thus find that core-collapse explosions are the only plausible astrophysical (i.e., extrasolar) sites for the deep-ocean ^{60}Fe.

One final process to generate ^{60}Fe that FFE15 did not consider is not extrasolar, but rather the result of cosmic-ray (CR) nucleosynthesis on rocky interplantary bodies. CRs impinging on nickel-bearing bodies generate ^{60}Fe through a set of nuclear reactions. Should these objects enhanced with CR-enriched material then fall to Earth, they may imitate the supernova signal.

This possibility was investigated by Wallner et al. (2016), who studied the effects of both meterotic dust and a single giant impactor. They find that, given the total amount of ^{60}Fe observed, the background micrometeorite contribution to the ^{60}Fe total is insignificant ($\sim$400 times lower than observed). Backgrounds for other potential radioisotopes are analyzed in Fields et al. (2005). Wallner et al. (2016) further note that not nearly enough Ni in a single large impactor could be exposed to CRs to make the required amount of ^{60}Fe. Their measured [Ni]/[^{60}Fe] ratio shows that $\sim$4500 times more Ni would need to be exposed to cosmic rays than was in the outer 3 m of the K-Pg impactor (the dinosaur-killer, about 10 km across). Finally, they examine the ratio of Ni to Fe and conclude that even if all of the observed Ni were extraterrestrial, only half the observed abundance of ^{60}Fe is expected.

While Wallner et al. (2016) considered only one impactor (and rightfully ruled it out), multiple

smaller impactors would have a greater surface/volume ratio, thereby producing more ^{60}Fe per gram of Ni. To this end, we reproduce calculations of CR-generated ^{60}Fe in impactors across a wide range of sizes. This allows us to both fully address the impactor hypothesis for the ^{60}Fe signal 2–3 Myr ago, but also to estimate the ^{60}Fe flux today given the observed distribution of present-day impactors.

This chapter is structured as follows: in section 2.2 we describe the model used for cosmic ray propagation and nuclear reactions, and how energy and depth are separated; in section 2.3 we show how to constrain the problem with Ni; in section 2.4 we show the results of our models and Ni fitting; in section 2.5 we extend this model to the long-lived isotope ^{92}Nb; and in section 2.6 we give our discussion and concluding marks.

2.2 Radioisotope production formalism

2.2.1 Equations used

In order to examine how multiple impactors can deliver ^{60}Fe, production rates must first be calculated. These calculations involve a large set of nuclear reactions and their products as a shower of secondary particles travels through the surface of an asteroid. Michel et al. (1991) has already investigated these reactions, so we will follow their approach and use their results where appropriate.

For the reactions of the form $i + k \rightarrow j$ (where i is the target, k is the incoming cosmic ray and j is the product), Michel et al. (1991) gives the production rate of the isotope j as

$$q_j(z) = \rho \sum_{i=1}^{N} \frac{X_i}{A_i u} \sum_{k=1}^{3} \int_0^\infty \sigma_{j,i,k}(E) J_k(E, z)\, dE\,. \tag{2.1}$$

where q_j is the production rate per volume, z is depth, ρ is the density of the impactor, N is the number of reaction pathways by target, X_i is the mass fraction of the target k, A_i is the mass number of the target, u is the atomic mass unit, σ is the cross-section (excitation function) of the reaction as a function of energy, E is the energy of the incoming particle, and J_k is differential flux density of the incoming particle k (in units of particles cm^{-2} s^{-1} MeV^{-1}). Strictly speaking, the sum over k goes from 1 to 3 for protons, neutrons, and α particles, and k should even be larger to include all components of CRs. However, it is common practice (e.g., Ammon et al., 2009; Leya

& Masarik, 2009; Leya et al., 2000; Michel et al., 1991) to examine only protons and neutrons, claiming that α particles are shattered into two protons and two neutrons on their first inelastic reaction. The result of this shattering is to simply multiply the proton and neutron flux by 1.55, thereby ignoring direct α-induced reactions. While there are no unbound neutrons in the cosmic ray spectrum, many proton reactions generate secondary neutrons. Michel et al. (1991) have done extensive simulations of these reactions, and we will use their data for the remainder of this study. Since CR fluxes are measured experimentally, α shattering and secondary reactions are already taken into account and we do not need to worry about recreating these processes.

Equation 2.1 is valid for the production of any isotope. For a radioisotope that maintains both a production and decay rate, the abundance is driven towards an equilibrium state. This state takes a few half-lives to equalize, assuming the CR flux that does not change over time – solar modulation (a result of the solar cycle) will cause galactic rays to lose energy at different rates over its 11 year cycle, but that will average out over millions of years. Thus we ignore any effects of the solar cycle on ^{60}Fe production. In equilibrium, the production and decay rates balance, so the amount of the radioisotope is

$$\dot{n}_j = q_j - \frac{n_j}{\tau_j} \overset{\text{eq}}{=} 0 \tag{2.2}$$

$$n_j \overset{\text{eq}}{=} \tau_j q_j \tag{2.3}$$

where τ_j is the mean lifetime of the radioisotope. By combining Eqn. 2.2 with Eqn. 2.1 and integrating over depth, the surface density of the radioisotope is

$$N_j = \rho \tau_j \sum_{i=1}^{N} \frac{X_i}{A_i u} \sum_{k=1}^{3} \int_0^{z_{\max}} \int_0^{\infty} \sigma_{j,i,k}(E) J_k(E,z)\, dE\, dz\,. \tag{2.4}$$

We are left with a two-dimensional integral in which we must integrate the cross-section over energy and the flux over both energy and height. However, this equation can be made simpler with the assumption that the two quantities of the flux (energy and height) are independent of one another, allowing us to apply separation of variables. According to work by Michel et al. (1991) and Gaisser et al. (2016), the energy and the height can indeed be treated as separable in the energy range we are concerned with. We note that above ∼1000 MeV, separability begins to break

down. Instead of solving one two-dimensional integral, we solve two one-dimensional integrals. The separation takes the form

$$J_k(E, z) = \varphi_k(E) Z_k(z) \tag{2.5}$$

which allows us to rewrite the surface density as

$$N_j = \rho \tau_j \sum_{i=1}^{N} \frac{X_i}{A_i u} \sum_{k=1}^{3} \int_0^{z_{\max}} Z_k(z)\, dz \int_0^{\infty} \sigma_{j,i,k}(E) \varphi_k(E)\, dE\,. \tag{2.6}$$

Given this separation of energy and depth, the next step is to calculate the energy dependence and cross-sections separately before combining them.

2.2.2 Energy fitting

The functions $Z_k(z)$ and $\varphi_k(E)$ in Eqn. 2.6 are measured and shown in Michel et al. (1991). We estimate a fit for these functions, thus getting a depth profile for the cosmic rays. They are integrated to yield the height-dependence of the radioisotopes. Doing the same for flux, we calculate the radioisotope production of the given reactions.

The approximations of our fitting is shown in Fig. 2.1. The neutron fitting seems to accurately reflect the measured data up to the >1000 MeV bin. At higher energies, our model underestimates J_k by a small margin. However, this difference becomes negligible compared to the peak flux at a depth of $\sim$50 g cm^{-2}.

On the other hand, the proton spectra have a different shape at the highest energy bin. The two bins within $1 - 100$ MeV are well-fit, but the $100 - 1000$ MeV bin begins to deviate, both at small and large depth. The result is that protons, unlike neutrons, are not well-approximated when separating energy and depth, especially at high energies. As we will show, nuclear cross-sections peak in the range of $10 - 100$ MeV. An improved model should take this lack of separability into account. In addition, we will discuss how neutron reactions generate far more ^{60}Fe than proton ones, so this inexact treatment of protons will not have an enormous effect on the outcome of these calculations.

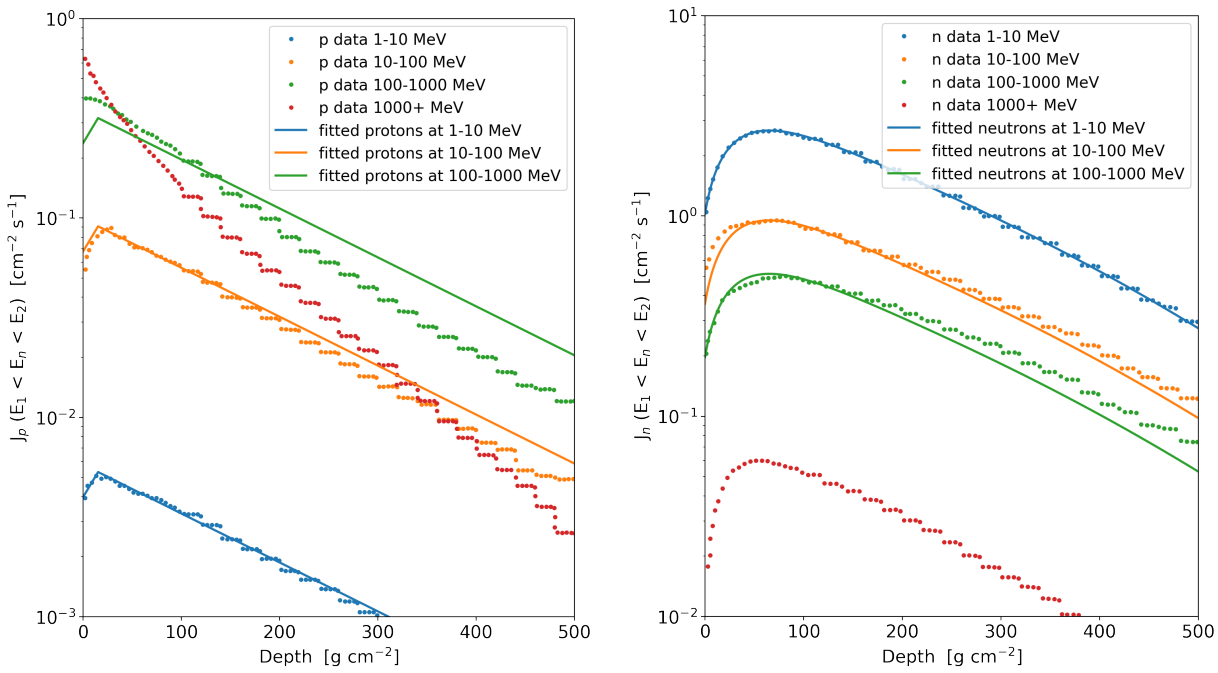

(a) (b)

Figure 2.1: Approximations of fluxes for protons (left) and neutrons (right) as a function of depth in an asteroid. Data points come from Michel et al. (1991), Figs. 2a and 2b. Our approximations are shown as solid lines.

2.2.3 Cross-section calculations

The TALYS program calculates cross-sections and products of nuclear reactions at energies in the range from 1 keV – 200 MeV (Koning et al., 2007). TALYS was chosen in large part due to its previous use in the field (e.g., Fimiani et al., 2016; Ammon et al., 2009; Leya & Masarik, 2009), which was in turn based on both accuracy and user-friendliness. Ideally, the cross-sections of these reactions will have been experimentally measured in a lab, but this is only sometimes the case. One study by Merchel et al. (2000) gives the cross-sections that produce ^{60}Fe in the energy range of 30 MeV – 2.6 GeV. Several channels produce ^{60}Fe, though their cross-sections have mostly not been measured experimentally. Therefore, we turn to nuclear simulations to calculate cross-sections in more detail.

Figure 2.2 shows a few TALYS-calculated cross-sections for a set of nuclear reactions resulting in the production of ^{60}Fe. The dominant reaction by far is that of a neutron onto natural nickel, particularly in the region below 200 MeV. The data for the proton reaction match the data calculated

by TALYS in two of the three points, but the cross sections over 200 MeV appear to be a factor of ~ 5 greater. Unfortunately, the neutron reaction has not been measured experimentally and therefore has no data to compare to.

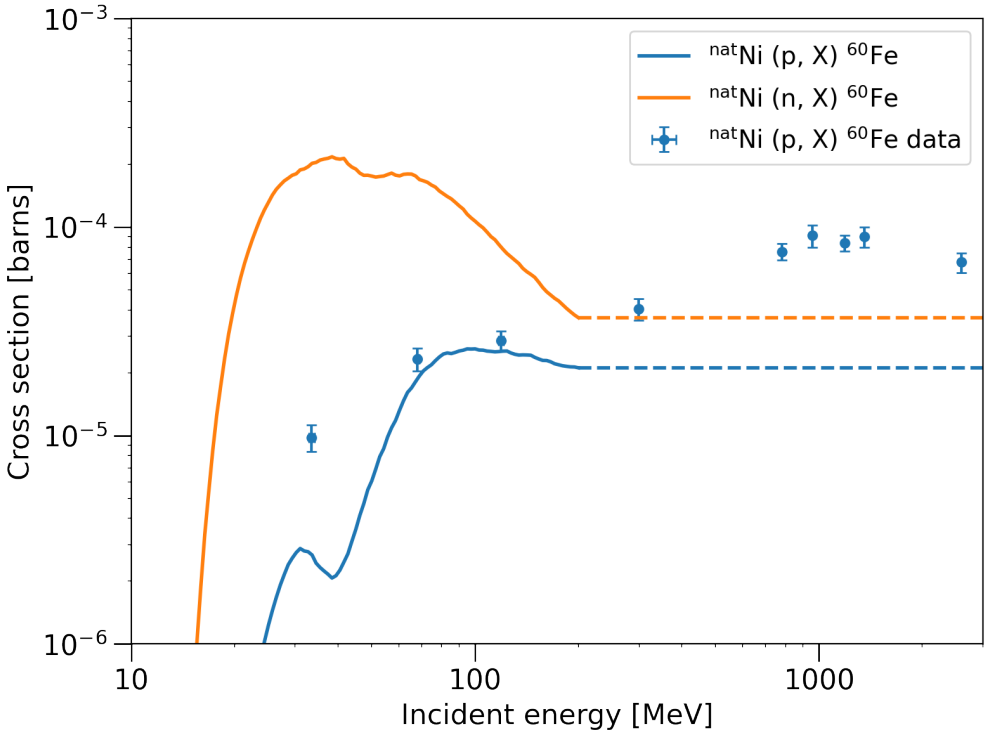

Figure 2.2: Cross-sections for proton and neutron reactions that produce ^{60}Fe as calculated by TALYS. A natural abundance of Ni is assumed. The blue line shows protons incident on Ni, and the orange line shows neutrons incident on Ni. TALYS-calculated cross-sections are used up to 200 MeV (solid lines), after which we assume a constant cross-section for higher energies (dashed lines). Data points show the $^{\text{nat}}\text{Ni}(p, X)^{60}\text{Fe}$ reaction presented in Merchel et al. (2000).

Given that CR nucleosynthesis is such a slow process, the natural isotopic abundance is assumed to be accurate for asteroids. As in the model presented by Leya et al. (2000), it is assumed that α particles are shattered into their components after undergoing their first inelastic reaction. Therefore, they have a very small depth and do not contribute largely to the production of ^{60}Fe, regardless of their cross-section. While penetration and flux of α depth have not been measured, the reaction is included here out of both interest and completeness. Should the machinery to handle α particle reactions be developed in the future, the underlying cross-sections have already been calculated and are ready to include.

2.2.4 ^{60}Fe *production and comparison*

With both the CR energy and the cross sections, Eqn. 2.6 can be used to calculate the equilibrium abundance of ^{60}Fe.

During this calculation of ^{60}Fe production, we keep track of which reactions are the most significant. In Fig. 2.3(a), we show the depth profile of ^{60}Fe production out to 170 cm. The initial increase around $0 - 20$ cm is due to the secondary neutrons being generated by primary cosmic rays. The neutron reactions are clearly more significant than the proton reactions at every depth. In Fig. 2.3(b), we integrate over depth to get the total surface density for each reaction. The two most important reactions are that of neutrons interacting with ^{62}Ni and ^{64}Ni. The proton reactions produce a full two orders of magnitude less ^{60}Fe. This result is further justification for separating proton depth and energy: a more detailed calculation that did not involve separation would be very similar for neutron reactions. Proton reactions only contribute $\sim 1\%$ to the total ^{60}Fe, and so can be safely ignored.

These calculations for the production of ^{60}Fe in stony material have been done for ^{60}Fe by several groups (Ammon et al., 2009; Knie et al., 1999b; Merchel et al., 2000), often for small asteroids of size ≤ 100 cm. In Figure 2.4, we plot their ^{60}Fe production of large asteroids, compared to our calculated ^{60}Fe production using CR fluxes from Michel et al. (1991). Our results show less ^{60}Fe production than other studies. In the case of Ammon et al. (2009), this difference is due to the type of material, as they calculate secondary CR particle fluxes for iron meteorites and therefore have more neutrons available for reactions.

2.3 Constraints with Ni

In order to produce the measured amount of ^{60}Fe, any number of appropriately-sized impactors could suffice. To constrain this problem, we compare the ratio of ^{60}Fe to Ni abundance. Along with Fe and ^{60}Fe abundances, Wallner et al. (2016) also measures Ni abundance. This measured Ni abundance places an upper limit on how much Ni impactors can bring. In the extreme case, we assume that all Ni in this layer is meteoritic rather than terrestrial. By examining how many impactors are needed to reconstruct both the Ni and ^{60}Fe values, we aim to find a number and radius

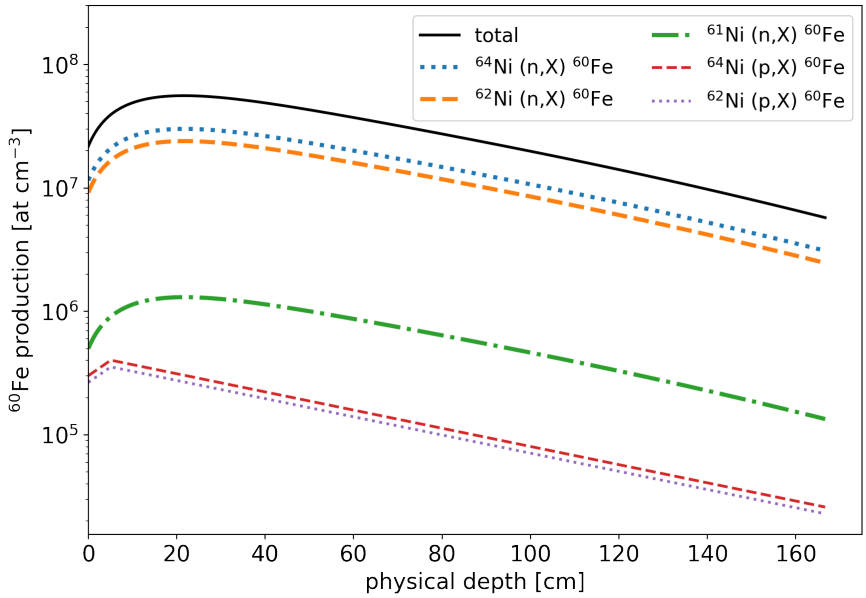

(a)

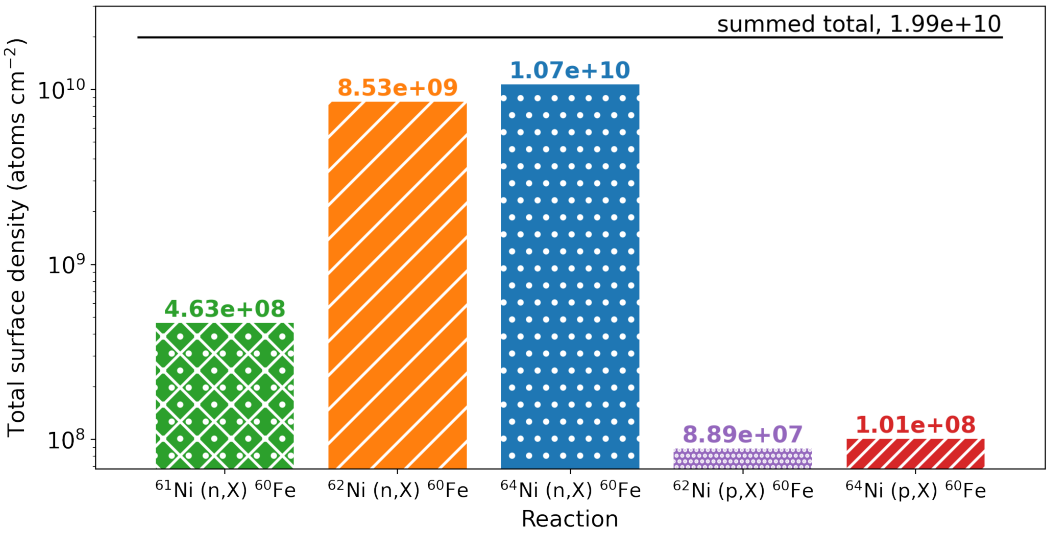

(b)

Figure 2.3: Amount of ^{60}Fe generated by CRs in stony asteroids split by nuclear reaction. (a) shows this amount as a function of depth out to 170 cm. The sum of all reactions is shown as the solid black line. (b) shows the integrated surface density with the sum as the solid black line. The color scheme between (a) and (b) is the same.

of impactors required to satisfy both conditions. In reality, these impactors have a distribution of sizes and shapes, which we will discuss further in section 2.4.1.

We assume all Ni is distributed evenly throughout the impactor so that it scales with volume.

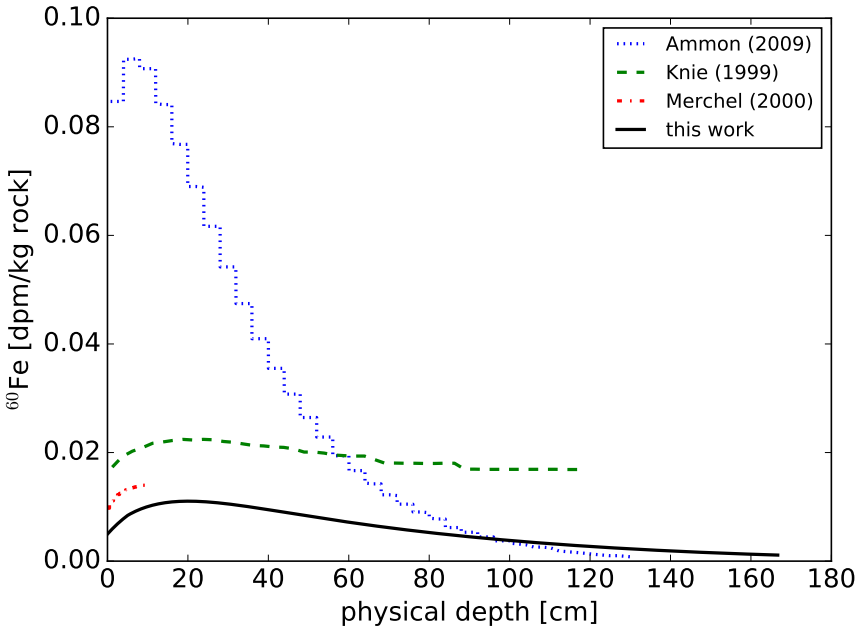

Figure 2.4: Activity of ^{60}Fe vs depth into an impactor, assuming a density of 3 g cm^{-3}. For consistency, we normalize to a CR flux of $J_0 = 1$ cm^{-2} s^{-1}. Data from Ammon et al. (2009) is much higher because they use metallic meteoroids rather than stony ones.

But ^{60}Fe is generated by CRs only on the outer ∼100 cm, as shown in Fig. 2.4. Assuming the impactor is spread evenly over the surface area of the Earth, the number of impactors needed to reproduce the given amount of Ni is

$$\mathcal{N}^{\rm Ni} = \frac{3R_\oplus^2(60u)}{\rho_i X_{\rm Ni}} \frac{\Sigma^{\rm Ni}}{r_i^3}\,, \tag{2.7}$$

where r_i is the radius of the impactor, $X_{\rm Ni}$ is the mass fraction of Ni, and $\Sigma^{\rm Ni}$ is the measured surface density of Ni in the same sediment samples that contain ^{60}Fe.

The ^{60}Fe from impactors is divided into two regimes depending on the size compared to the penetration depth of CRs. For a small impactor, CRs uniformly permeate the entire asteroid, so the ^{60}Fe abundance scales with volume, the same as Ni. This abundance is

$$\mathcal{N}^{\rm 60Fe} = \frac{3R_\oplus^2(60u)}{\rho_i X_{\rm Fe} \frac{\rm [60Fe]}{\rm [Fe]}} \frac{\Sigma^{\rm 60Fe}}{r_i^3} \qquad (r_i < d_{\rm pen})\,, \tag{2.8}$$

where $d_{\rm pen}$ is the penetration depth of CRs.

In the regime where the impactor is equal to or larger than the penetration depth, one must

slightly modify the volume to account for the unexposed inner core of the impactor:

$$\mathcal{N}^{60\mathrm{Fe}} = \frac{3R_{\oplus}^2(60u)}{\rho_i X_{\mathrm{Fe}} \frac{[60\mathrm{Fe}]}{[\mathrm{Fe}]}} \frac{\Sigma^{60\mathrm{Fe}}}{(r_i^3 - (r_i - d_{\mathrm{pen}})^3)} \qquad (r_i > d_{\mathrm{pen}})\,. \tag{2.9}$$

Note that in the limit $r_i \gg d_{\mathrm{pen}}$, this equation will scale as surface area rather than volume.

Extensive work has been done by eg. Ammon et al. (2009) to examine the ^{60}Fe production rate as a function of depth for impactors of multiple different sizes, from 5 cm to the outer 1.3 m of a 10 m sphere. We use this latter ^{60}Fe production rate since we are interested in large impactors, noting that this may introduce a factor of ∼2 for smaller impactors into our calculations.

2.4 Results

We show the results of our calculations to reproduce both the ^{60}Fe and Ni signals using parameters chosen in Table 2.1, in which sediment data comes from Wallner et al. (2016). Table 2.2 shows the given impactor parameters, as shown in Fimiani et al. (2016). The values used are chosen specifically to make this impactor hypothesis seem possible, such as assuming all impactors are metal-rich. Indeed, some of these values are different than those chosen by Wallner et al. (2016) in their analysis described above. We choose parameters in favor of this impactor model so that, if we still cannot make it feasible, we can safely dismiss the theory and conclude that the ^{60}Fe must have been from a supernova.

Variable	**Symbol**	**Value**	**Uncertainty factor**
impactor mass fraction of Ni	X_{Ni}	0.1	1.5
sediment density	ρ^{sed}	1.16 g cm^{-3}	(none given)
mass fraction of Fe	$X_{\mathrm{Fe}}^{\mathrm{sed}}$	0.2×10^{-2}	1.5
Ni to Fe ratio	$\frac{[\mathrm{Ni}]}{[\mathrm{Fe}]}$	0.025	1.2
sedimentation rate	$\frac{dh}{dt}$	0.32×10^{-3} cm yr^{-1}	1.15
time length of signal	Δt	1 Myr	1
number of impactors for Ni	$\mathcal{N}^{\mathrm{Ni}}$		**factor of 2.70**
impactor mass fraction of Fe	X_{Fe}	0.8	1.2
mass ratio of ^{60}Fe to Fe	$\frac{[60\mathrm{Fe}]}{[\mathrm{Fe}]}$	3×10^{-15}	2
surface density of ^{60}Fe	$\Sigma^{60\mathrm{Fe}}$	0.5×10^{8} at cm^{-2}	2
number of impactors for ^{60}Fe	$\mathcal{N}^{60\mathrm{Fe}}$		**factor of 3.07**

Table 2.1: A list of the necessary parameters to determine impactor number vs. radius as shown in Wallner et al. (2016).

Variable	Value	Source
Impactor density	3 g cm^{-3}	estimate
Ni mass fraction	0.1	Fimiani S. Table 3
Fe mass fraction	0.8	Fimiani S. Table 3
^{60}Fe/Fe mass fraction	3×10^{-15}	Fimiani S. Table 1

Table 2.2: A list of necessary parameters of the impactors, also meant to determine impactor number vs radius. These values come from Fimiani et al. (2016).

Upon inserting these values into Eqn. 2.9, we plot the impactor number against radius in order to reproduce the observed ^{60}Fe signal as detected by Wallner et al. (2016) in Figure 2.5. As expected, the Ni from impactors scales with volume, $\mathcal{N}^{\mathrm{Ni}} \propto r_i^{-3}$. For large radii, the ^{60}Fe line follows a $\mathcal{N}^{60\mathrm{Fe}} \propto r_i^{-2}$ down to a depth of $r \approx d_{pen}$. Impactors smaller than this are fully penetrated by CRs and so scales proportional to volume. Again, to achieve an upper limit for the amount of Ni, we assume all observed Ni is meteoritic. This places a hard upper limit to the total amount of meteoritic material found in sediment.

Instead of finding a single region where these lines cross, we find that they overlap only because of error in the measured quantities. There is no single values for radius and number that successfully reproduce both the Ni and ^{60}Fe data. Instead, a narrow range of impactor parameters is barely acceptable. Even these cases assume that all Ni in the sediment layers came from impactors, which is a bold and unsubstantiated claim. Fig. 2.5 also shows a 1-Myr sum of meteoritic infall, assuming the present-day rate. The Ni abundance is 100 times higher than this, meaning that not all Ni is extraterrestrial, as expected.

Any impactors larger than $r \sim 1000$ cm cannot be responsible for the detected ^{60}Fe signal. Even at a size of $r = 1000$ cm, the number of impactors needed nearly reaches a staggering 10^9. This result indicates that, if true, one thousand 10 meter-sized impactors fell to Earth every year for a time span of one million years. There is no astronomical or geological precedent for this bombardment. Although this scenario of 1000 cm impactors can be ruled out, smaller impactors may still be plausible, as the two lines in Figure 2.5 overlap at smaller radii. However, as they overlap in the $\mathcal{N} \propto r_i^{-3}$ part of the graph, the total mass of impactor material remains constant at any location along the overlap. Impactors too small to leave craters are essentially micrometeorites, and the contribution of micrometeorites is already discarded by Wallner et al. (2016). Therefore, we can safely dismiss the multiple impactor hypothesis as the source of ^{60}Fe signal.

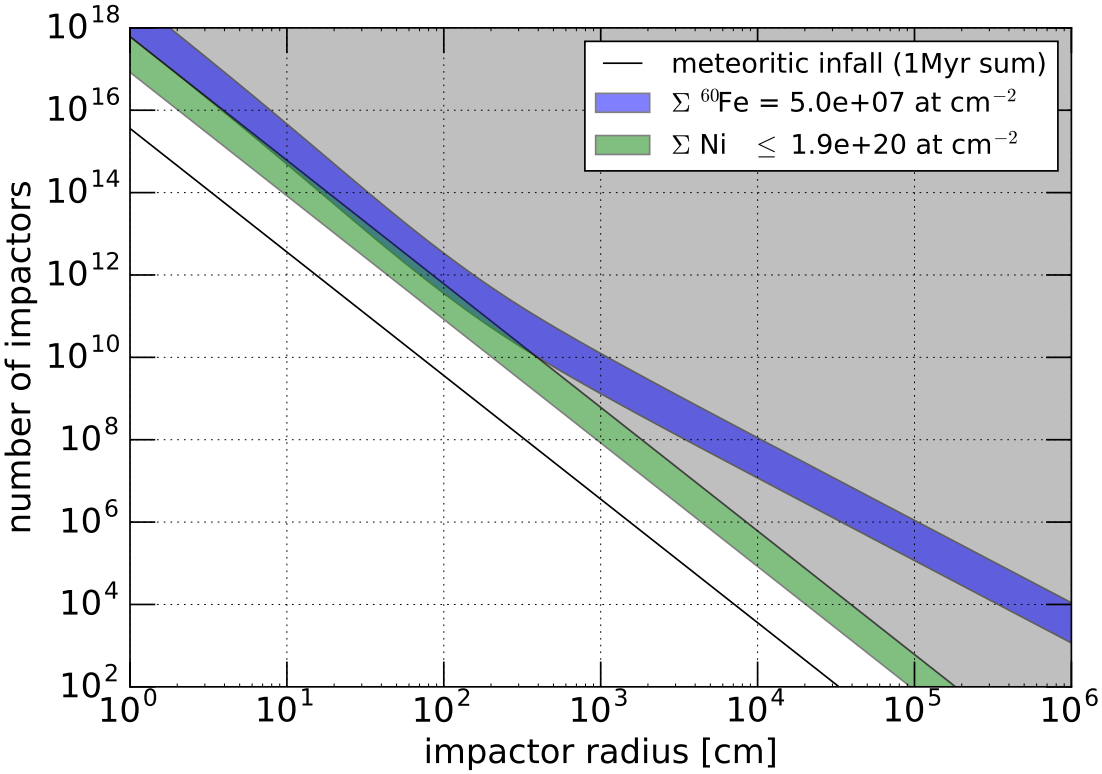

Figure 2.5: A plot of the number of impactors vs. the impactor size needed to reproduce the Ni and ^{60}Fe signals measured by Wallner et al. (2016). The green bar shows the number of impactors for Ni and the blue bar is for ^{60}Fe. The bars' widths are due to uncertainties shown in Table 2.1. The solid black line is the meteoritic infall rate today (50,000 tons per year) summed over 1 Myr. The gray region is "excluded" and places an upper limit based on the amount of Ni observed in the sediment. Note the extremely logarithmic axes.

2.4.1 Different sizes of impactors

Although we have explored an ideal case for many impactors of the same size, we can generalize to a more realistic case by considering impactors with a distribution of sizes. Since CRs generate ^{60}Fe on the outermost $\sim$ 100 cm of asteroids, all impactors smaller than this penetration depth are very nearly the same in terms of ^{60}Fe and Ni abundances, notably the [^{60}Fe/Ni] ratio. For a large distribution of sizes, many impactors will be larger than 100 cm. These larger impactors serve to increase the Ni/^{60}Fe ratio. As seen in Figure 2.5, this pushes the number of impactors further into the excluded region. As a result, considering a distribution of sizes does not make the impactor hypothesis more plausible, it can only serve to make it even less likely.

2.4.2 Lunar cratering

One could question whether such a bombardment of impactors would leave a mark on Earth. Certainly, the outer layers will burn away in the atmosphere. The amount depends on size and composition. It is possible that some larger bodies will reach the surface, where they will leave craters. Even if no evidence were apparent on Earth due to erosion over time, these impactors would also bombard the Moon and certainly leave a visible cratering effect there that would endure for at least the 3 Myr since the ^{60}Fe signal.

To see how many craters this would entail, we note that the Earth and Moon must have received approximately the same asteroid flux. The number of impactors each large body receives increases with cross section (πr^2) and is distributed by surface area ($4\pi r^2$). By taking the ratio of these two quantities (and neglecting gravitational attraction), the crater surface density is constant regardless of the size of the body, and therefore the Earth and Moon will have the same surface density.

For 10^{10} impactors, the resulting surface density is 19.6 km^{-2}. Using a rule-of-thumb to relate crater and impactor size as $R_c \approx 10R_i$, we calculate an upper limit of the fraction of the body covered by craters of 0.075%. While this is not a significantly large fraction of the body, such cratering would surely be noticed on the Moon. While further calculations of lunar crating distributions could be made, the overwhelming majority of lunar craters are older than 3 Myr (see, e.g., Hiesinger et al., 2012; Ivanov, 2018). We therefore rule out the possibility of $\sim$1 m-sized asteroids contributing to the ^{60}Fe supernova signal.

2.4.3 Meteoritic contribution to ^{60}Fe surface density

We can place limits on how much ^{60}Fe in the deep-sea sediment data came from CR nucleosynthesis on impactors. This factor will be relevant going forwards as more precise data becomes available. Assuming a constant rate of meteoritic infall of 30,000 tons per year and a Ni abundance of $\sim$1% (a typical value for CI chondrites), we calculate a surface density of ^{60}Fe on Earth as 0.0056 atoms cm^{-2} yr^{-1}. This result is a full order of magnitude below that presented in Wallner et al. (2016) (0.06 atoms cm^{-2} yr^{-1}). The discrepancy may be due to a different Ni abundance, or potentially surface effects where a surviving fragment is more likely to be from the outer layers of the meteor where CR nucleosynthesis is more prevalent. Either way, the expected meteoritic ^{60}Fe abundance is

far less than the > 20 atoms cm^{-2} yr^{-1} attributed to the supernovae.

We note that in the earliest time range of less than 0.2 Myr, Wallner et al. (2016) placed a limit of < 0.2 atoms cm^{-2} yr^{-1}. This limit is approaching their own calculation of meteoritic ^{60}Fe. With further AMS precision, it may be possible to measure the meteoritic component directly, though it remains to be seen if this precision can be achieved.

2.4.4 Impactor constraints from other isotopes

The solar wind implants ^{3}He on the surface of rocky interplanetary bodies. Since CR nucleosynthesis occurs on the outer layers as well, the surface should contain roughly a fixed ^{3}He/^{60}Fe ratio. Thus a meteoritic ^{60}Fe pulse should come with a ^{3}He pulse. Measurements of ^{3}He show no spike of this sort around 3 Myr; a spike at 8 Myr is attributable to a break-up of an asteroid (Farley et al., 2006).

Any iron-containing impactors can also host CR production of ^{53}Mn. The ^{53}Mn/^{60}Fe ratio is proportional to the Fe/Ni ratio – this method was how the supernova ^{60}Fe excess was found over the background produced by cosmic rays in lunar samples (Fimiani et al., 2016). Korschinek et al. (2020) claims to detect ^{53}Mn from the supernova 3 Myr ago – if true, this detection would represent a ^{53}Mn/^{60}Fe ratio of 14. In contrast, Fimiani et al. (2016) calculates a meteoritic ratio of 370. The observed value is a factor of ~ 20 below the meteoritic one, therefore we agree that the ^{53}Mn abundance does not show a meteoritic origin.

2.5 Extension: ^{92}Nb and the K-Pg layer

In light of these calculations of surface ^{60}Fe, it may be possible to trace the amount of interplanetary dust falling onto Earth over Myr timescales. Of course, this is only feasible when looking at global distributions of infall summing over many asteroids and dust grains. But there is one exciting possibility for examining the global deposition from a single event.

It may be possible to find radioisotopes from the asteroid that caused the K-Pg event that extincted all non-avian dinosaurs 66 Myr ago (Alvarez et al., 1980). Few radioisotopes have ideal half-lives of $\sim 10 - 100$ Myr. Shorter-lived isotopes like ^{60}Fe and ^{26}Al will have undergone too many half-lives to be detectable. However, longer-lived ones like ^{235}U will still exist from solar system formation, potentially making them difficult to disentangle from this specific event. Table 2.3 shows

the short list of isotopes with half-lives in the range of about $10 - 100$ Myr as well as their decay method. Many of these elements are a direct result of the r-process, such as the actinides.

Radioisotope	$t_{1/2}$ **(Myr)**	**Decay mode**
^{92}Nb	34.7	e^- capture
^{129}I	15.7	β^-
^{146}Sm	103	α
^{205}Pb	17.3	e^- capture
^{236}U	23.4	α
^{244}Pu	81.1	α
^{247}Cm	15.6	α

Table 2.3: A list of radioisotopes with half-lives between 10 and 100 Myr. Data from the NNDC.

Using a similar methodology to that described above for ^{60}Fe, the cosmic ray production of ^{92}Nb on the surface of an asteroid can be calculated. The cosmic ray flux analysis is already shown, so we again use TALYS to calculate the relevant cross-sections for reactions that produce ^{92}Nb. The cross-sections are summarized in Fig. 2.6. Several reactions are dominant at various incident energies. However, the most promising reaction by far is $^{93}\mathrm{Nb}(n, 2n)^{92}\mathrm{Nb}$, which peaks at just over 1 barn around 10-20 MeV.

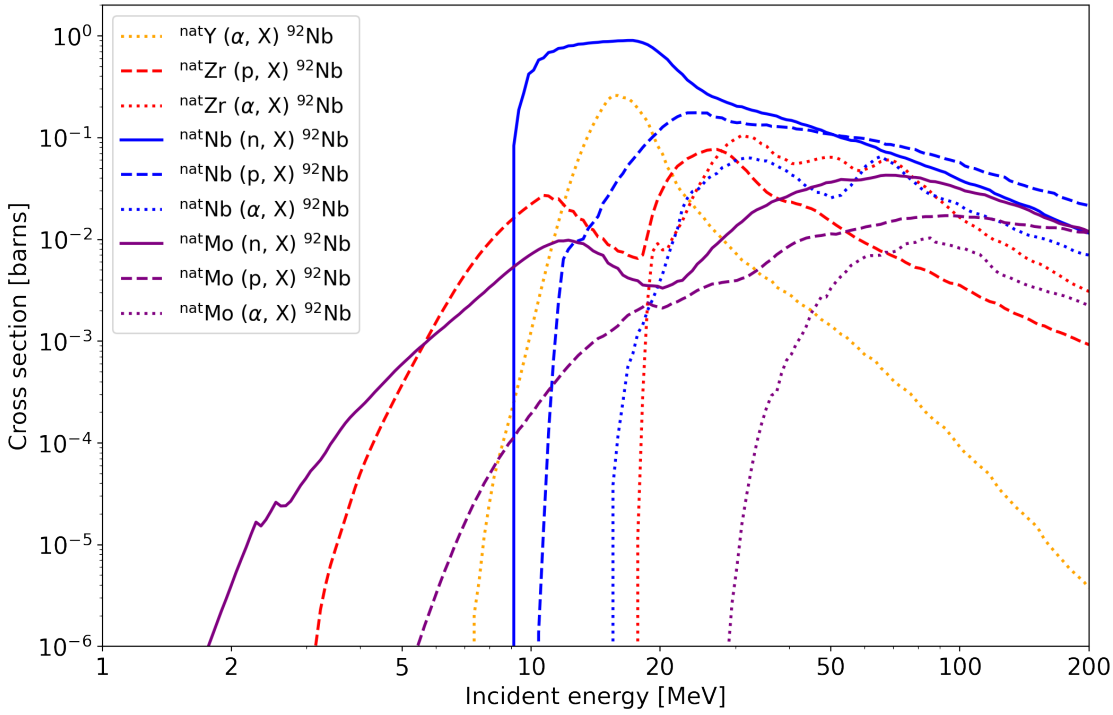

Figure 2.6: Cross-sections for the main reactions that produce ^{92}Nb calculated by TALYS. Natural isotopes are weighted by abundance.

The ^{93}Nb$(n, 2n)^{92}$Nb reaction is shown in more detail in Fig. 2.7. There is good agreement between TALYS and the experimental data. Unfortunately, this reaction also generates a significant amount of ^{92m}Nb, the excited state of ^{92}Nb. ^{92m}Nb decays to ^{92}Zr with a half-life of 10.15 days, essentially instantaneous on Myr timescales. The only useful amount of ^{92}Nb is from the ground state, which accounts for $60 - 70\%$ of ^{92}Nb from this reaction.

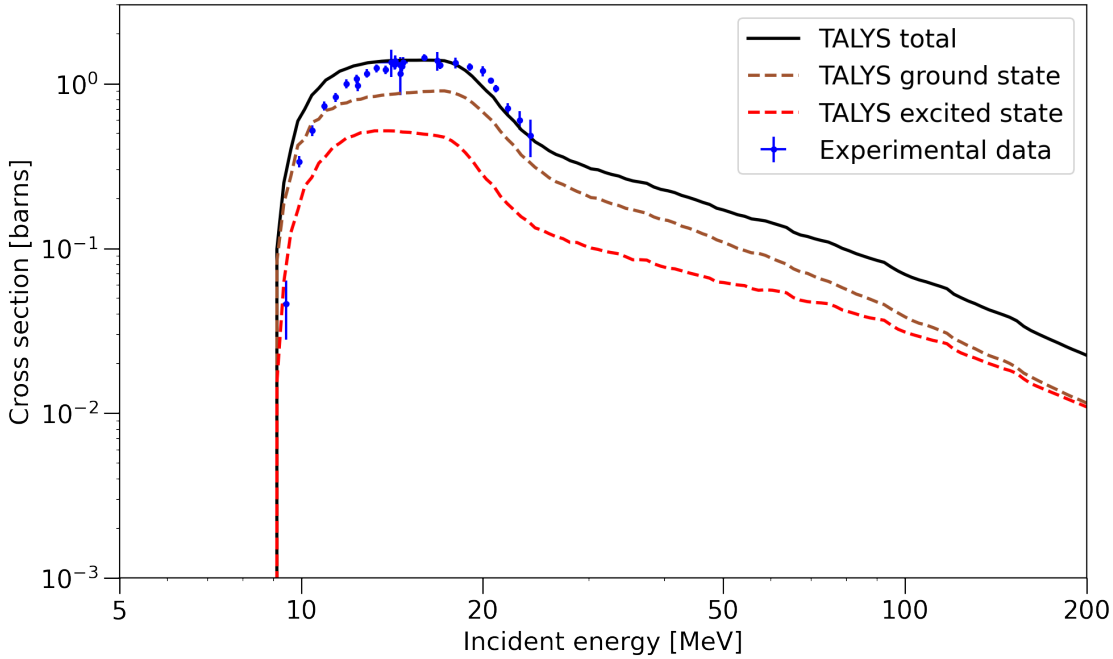

Figure 2.7: Cross-sections for the ^{93}Nb(n,2n)^{92}Nb reaction. Lines show the cross-section leading to the ^{92}Nb ground state (brown dashed), excited state (red dashed), and the total (blue solid). Experimental data compiled by the NNDC from the following sources: Frehaut et al. (1980); Mather et al. (1972); Häring et al. (1971); Lychagin et al. (1984); Hermsdorf et al. (1973); Kozyr' & Prokopets (1977); Veeser et al. (1977); Paulsen & Widera (1970); Prokopets (1980).

In order to predict the total amount of extant ^{92}Nb from the asteroid, we need only apply these cross sections to equation 2.6 (again assuming separation of depth and energy). The total amount of ^{92}Nb is expected to be very low, and AMS precision similar to that used for ^{60}Fe will be needed. Currently, only one attempt to measure ^{92}Nb/^{93}Nb using AMS (Guozhu et al., 2013), yielding a value of about 10^{-11}. Unfortunately, the typical ^{60}Fe/Fe ratio even for the elevated supernova rate is $\sim 10^{-15}$. Should the ^{92}Nb/^{93}Nb ratio be similar, it may not be detectable unless truly heroic efforts are made by the AMS community.

2.6 Discussion & conclusions

The goal of this work was to examine whether a barrage of Earth impactors bringing ^{60}Fe through CR nucleosynthesis on their surfaces could imitate the ^{60}Fe signal commonly attributed to a near-Earth supernova. Our model for CR nucleosynthesis is based on the one presented in Michel et al. (1991). After calculating ^{60}Fe production as a function of depth, we used Ni abundance to constrain the problem and calculate a number and size of impactors. Even assuming generous values (such as letting all impactors be metal-rich and all measured Ni in sediment be extraterrestrial), we find that the only result consistent with ^{60}Fe and Ni data calls for $\sim 10^{12}$ meter-sized asteroids over $\sim$1 Myr. This scenario is completely unprecedented: geological records, lunar impact cratering, and ^{53}Mn measurements do not show any indications of this bombardment. Therefore, we conclude that such an asteroid bombardment did not occur, and the measured ^{60}Fe is in fact from a supernova.

A more direct tracing of meteoritic material in sediment is to measure the abundance of ^{3}He in the same sediment as Ni and ^{60}Fe. ^{3}He comes from the solar wind getting trapped in asteroids, which can then bring it with them all the way to the ocean floor. While we did not need to consider this process to eliminate the impactor hypothesis, we note that it is an alternative method to examine meteoritic material in the relevant sediment. Similarly, ^{53}Mn measurements rule out a meteoritic origin as well.

As precise measurements of ^{60}Fe continue to improve, the contribution of meteoritic ^{60}Fe will become increasingly important. At the moment, the detection of supernova ^{60}Fe is several orders of magnitude over that of a meteoritic origin ($\sim$ 20 vs 0.06 atoms cm^{-2} yr^{-1}). However, these samples have been taken at the peak of the supernova signal. If more data were measured away from the peak, especially in the most recent sediment and crust samples, then meteoritic ^{60}Fe will play a larger role.

Chapter 3

Supernova triggers for end-Devonian extinctions

The Late Devonian was a protracted period of low speciation resulting in biodiversity decline, culminating in extinction events near the Devonian-Carboniferous boundary. Recent evidence indicates that the final extinction event may have coincided with a dramatic drop in stratospheric ozone, possibly due to a global temperature rise. Here we study an alternative possible cause for the postulated ozone drop: a nearby supernova explosion that could inflict damage by accelerating cosmic rays that can deliver ionizing radiation for up to ~ 100 kyr. We therefore propose that the end-Devonian extinctions were triggered by supernova explosions at ~ 20 pc, somewhat beyond the "kill distance" that would have precipitated a full mass extinction. Such nearby supernovae are likely due to core-collapses of massive stars; these are concentrated in the thin Galactic disk where the Sun resides. Detecting either of the long-lived radioisotopes ^{146}Sm or ^{244}Pu in one or more end-Devonian extinction strata would confirm a supernova origin, point to the core-collapse explosion of a massive star, and probe supernova nucleosythesis. Other possible tests of the supernova hypothesis are discussed.

3.1 Features of the end-Devonian extinction

The late Devonian biodiversity crisis is characterized by a protracted decline in speciation rate occurring over millions of years (Stigall, 2012; Fan et al., 2020), punctuated by an extinction pulse

The following chapter has been published in PNAS with the citation: Fields, B., et al. (2020), *PNAS*, 117:35, pp. 21008–21010. doi:10.1073/pnas.2013774117.

(Kellwasser event) followed $\sim$ 10 Myr later by a more moderate extinction (Hangenberg event) around the Devonian-Carboniferous boundary (DCB) $\sim$ 359 Myr ago (Kaiser et al., 2016; Bond & Grasby, 2017). Marshall et al. (2020) recently suggested that the Hangenberg event was associated with ozone depletion (see also Cockell, 1999), in light of evidence such as malformations persisting in palynological assemblages on the order of many thousands of years. Racki (2020) argued that volcanic eruption and a large igneous province (LIP) triggered ozone depletion, whereas Marshall et al. (2020) instead linked it to an episode of global warming not caused by LIP.

Previous work has not considered astrophysical sources of ionizing radiation, which are known to be possible causes of ozone depletion and concomitant UV-B increase that could trigger elevated extinction levels (see, e.g., Melott & Thomas, 2011), as well as direct genetic damage. Here we consider whether astrophysical sources could account for the data in Marshall et al. (2020), and whether any additional evidence could test for their occurrence.

The precise patterns prevalent during the DCB are complicated by several factors including difficulties in stratigraphic correlation within and between marine and terrestrial settings and the overall paucity of plant remains (Prestianni et al., 2016). However, a general consensus seems to be emerging that there was first a loss of diversity in spores and pollen followed after about 300 kyr (Myrow et al., 2014) by a pulse of extinctions of many plants including proto-trees, armored fish, trilobites, ammonites, conodonts, chitinozoans and acritarchs, possibly coeval with the Hangenberg Crisis; this seems to have largely left intact sharks, bony fish and tetrapods with five fingers and toes. The fact that these species disappeared over multiple beds indicates that the extinction extended over at least thousands of years.

Filipiak & Racki (2010); Prestianni et al. (2016); Marshall et al. (2020) also report the discovery of spores from this episode with distinct morphologies including malformed spines and dark pigmented walls, features consistent with severely deteriorating environmental conditions, and UV-B damage following destruction of the ozone layer (Filipiak & Racki, 2010). However, more quantitative data are needed to study their variation during quiescent times in the fossil record.

3.2 Heating mechanism for ozone depletion

Marshall et al. (2020) proposes an ozone depletion mechanism involving increased water vapor in

the lower stratosphere caused by enhanced convection due to higher surface temperatures. Water vapor contributes to a catalytic cycle that converts inorganic chlorine (primarily HCl and $ClONO_2$) to free radical form (ClO). The ClO then participates in an ozone-destroying catalytic cycle. A similar set of cycles involving Br contributes to ozone depletion, but to a lesser extent (Anderson et al., 2012). Increased ClO and decreased ozone following convective injection of water into the lower stratosphere has been verified by observation and modeling (Anderson et al., 2012, 2017). Marshall et al. (2020) argues that a period of exceptional and sustained warming would lead to the loss of the protective ozone layer via this mechanism.

This mechanism is important for lower stratosphere ozone depletion, and may have consequences for ground-level UV-B exposure (Anderson et al., 2012). More detailed study is warranted. Until then, it is unclear whether this change would be sufficient to cause an extinction. There are several reasons for this.

First, the vertical extent of this ozone depletion mechanism should be limited to the lower stratosphere ($\sim 12 - 18$ km altitude) and does not overlap with the largest concentration of ozone, which occurs around 20-30 km. So, while depletion may be significant in the lower stratosphere, the bulk of the ozone layer lies above this region and would not be affected. The total column density would be reduced, but not to the extent of a complete loss of the protective ozone layer.

Secondly, the duration of the effect should be relatively short, $\lesssim 1$ week (Anderson et al., 2012), since the injected water vapor is photolyzed and ClO is converted back to HCl and $ClONO_2$. Thus, unless convective transport of water vapor to the lower stratosphere, e.g., by storms, is continuous (on week timescales) the ozone reduction will be episodic, not sustained. The effect is also seasonal, since strongly convective storms tend to be limited to the spring/summer. While this is likely detrimental to surface life, most organisms have repair mechanisms that can cope with some short-duration UV-B exposure.

Thirdly, the effect is likely to be limited geographically, since strongly convective storms are not uniformly distributed and the enhanced water vapor is likely only to spread over ~ 100 km horizontally (Anderson et al., 2012).

Finally, there is significant uncertainty as to the ozone depletion level needed to induce aberrations in pollen morphology and even more critically, large-scale extinction. While the anthropogenic ozone "hole" over Antarctica has led to increased UV-B exposure, no crash in the ecosystem has resulted.

This may partly be due to the seasonal nature of the change, as would be the case here as well. Recent work (Neale & Thomas, 2016) has shown that short-term exposure to significant increases in UV-B does not result in large negative impacts on the primary productivity of ocean phytoplankton, and other organisms show a wide range of sensitivity (Thomas et al., 2015; Thomas, 2017). The amount of column depletion over a given location in those cases was $\sim 50\%$. The depletion caused by the mechanism considered in Marshall et al. (2020) seems unlikely to be that large. Hence, the convective transport of water vapor to the lower stratosphere may not be sufficient to induce a substantial extinction. It is thus worth considering other mechanisms for global ozone depletion.

3.3 Astrophysical agents of ozone destruction and biosphere damage

Astrophysical mechanisms for biosphere damage include bolide impacts, solar proton events, supernova (SN) explosions, gamma-ray bursts, and neutron star mergers (kilonovae). Bolide impacts, gamma-ray bursts and solar proton events are essentially impulsive, and recovery of the ozone layer takes $\lesssim 10$ yr (Thomas et al., 2005), which is likely to avert lasting biosphere destruction. Moreover, these events and kilonovae are unlikely to recur frequently. Accordingly, we focus on SNe.

Supernovae (SNe) are prompt sources of ionizing photons: extreme UV, X-rays, and gamma rays. Over longer timescales, the blast collides with surrounding gas, forming a shock that drives particle acceleration. In this way, SNe produce cosmic rays, i.e., atomic nuclei accelerated to high energies. These charged particles are magnetically confined inside the SN remnant, and are expected to bathe the Earth for ~ 100 kyr.

The cosmic-ray intensity would be high enough to deplete the ozone layer and induce UV-B damage for thousands of years (Ruderman, 1974; Ellis & Schramm, 1995; Gehrels et al., 2003; Melott et al., 2017). In contrast to the episodic, seasonal, and geographically limited ozone depletion expected from enhanced convection, ozone depletion following a SN is long-lived and global (see, e.g., Gehrels et al., 2003; Melott et al., 2017; Thomas, 2017) and is therefore much more likely to lead to an extinction event, even given uncertainties around the level of depletion necessary. (We note that, as well as the induced UV-B damage, cosmic rays could also cause radiation damage via muons produced when they impact the atmosphere (Melott et al., 2018)). The SN blast itself is unlikely to wreak significant damage on the biosphere, but may deposit detectable long-lived

nuclear isotopes that could provide distinctive signatures, as we discuss later.

There are two main types of SNe: (1) massive stars ($\gtrsim 8 M_\odot$) that explode as core-collapse SNe (CCSNe), and (2) white dwarfs that accrete from binary companions and explode as Type Ia SNe. These SN types have similar explosion energies, and both produce ionizing radiation able to damage the biosphere. However, different nucleosynthesis outputs lead to different radioisotope signatures.

Near-Earth CCSNe are more likely than Type Ia SNe. We estimate the nearby CCSN frequency using a Galactic rate $\mathcal{R}_{\rm CCSN} = (30 \text{ yr})^{-1}$ and placing the Sun at a radius $R_\odot = 8.7$ kpc in a thin disk of scale radius 2.9 kpc and height 0.1 kpc (Adams et al., 2013). This gives a CCSN rate $\mathcal{R}_{\rm SN} = e^{-R_\odot/R_0}\, r^3/3R_0^2 h_0 \sim 4\ r_{20}^3$ Gyr^{-1} within $r_{20} = r/20$ pc from Earth. Hence a CCSN at a distance ~ 2 times the "kill radius" of 10 pc is a plausible origin of the end-Devonian event(s). In contrast, the Type Ia SN rate is an order of magnitude smaller, as these events are spread over the ~ 8 times larger volume of the thick disk.

Massive stars are usually born in clusters (OB associations), and are usually in binaries with other massive stars. Thus, if one CCSN occurred near the DCB, likely there were others. This could explain the Kellwasser and other enigmatic Devonian events, in addition to the Hangenberg event.

3.4 Possible radioisotope signatures of supernovae

A CCSN close enough to cause a significant extinction would also deliver SN debris to the Earth as dust grains–micron or sub-micron sized particles created early after the explosion. Grains in the explosion would decouple from the plasma (gas) and propagate in the magnetized SN remnant until they are stopped or destroyed by sputtering during collisions (Fields et al., 2019).

The portion that reaches the Earth would deposit in the atmosphere live (undecayed) radioactive isotopes. There is very little pre-existing background for radioisotopes whose lifetimes are much shorter than the age of the Earth. Those with lifetimes comparable to the time since the event would provide suitable signatures. The discoveries of live ^{60}Fe in the deep ocean, the lunar regolith and Antarctic snow provide one such signal, which is interpreted as due to at least one recent nearby CCSN 2–3 Myr ago at a distance $\sim 50 - 100$ pc, which is compatible with the rate estimate given above (Fields et al., 2019).

Possible relic SN radioisotopes from the end-Devonian period with an age 360 Ma include ^{146}Sm

(half-life 103 Myr), ^{235}U (half-life 704 Myr) and ^{244}Pu (half-life 80.0 Myr). The most promising signature may be provided by ^{244}Pu, which has also been discovered in deep-ocean crust and sediment samples deposited over the last 25 Myr (Wallner et al., 2015b). Moreover, it is absorbed into bones and retained during life (Takizawa, 1982), whereas uranium is absorbed during fossilization (Koul, 1979) and ^{146}Sm is soluble. There is a significant ^{235}U background surviving from before the formation of the solar system, with $(^{235}\mathrm{U}/^{238}\mathrm{U})_\oplus = 0.721 \pm 0.001\%$, so a significant detection above this background requires deposition attaining $^{235}\mathrm{U}_{\mathrm{SN}}/^{238}\mathrm{U}_\oplus \gtrsim 3 \times 10^{-5}$. U-Pb dating has been used to date the end-Devonian extinction, but with an uncertainty in the ^{235}U/^{238}U ratio that is much larger than this target sensitivity, but even a few atoms of non-anthropogenic ^{244}Pu in end-Devonian fossils would be unambiguous evidence for the r-process in SNe.

We have estimated the terrestrial deposition of ^{146}Sm, ^{235}U and ^{244}Pu by a nearby SN. ^{146}Sm is a proton-rich ("p-process") nucleus that might be produced by CCSNe or Type Ia SNe (Arnould & Goriely, 2003). Models for the p-process (Arnould & Goriely, 2003) give $^{146}\mathrm{Sm}/^{144}\mathrm{Sm} \sim 0.01 - 2.5$, with the predicted core-collapse abundance typically around 0.2. Assuming a CCSN that produced a solar $^{144}\mathrm{Sm}/^{16}\mathrm{O}$ ratio, and ejected $M_{\mathrm{ej}}(^{16}\mathrm{O}) = 2M_\odot$, we estimate a total yield of ^{146}Sm in the ejecta of $\mathcal{N}(^{146}\mathrm{Sm}) \sim 1.6 \times 10^{47}$ atoms. On the other hand, ^{244}Pu and ^{235}U are neutron-rich nuclei that are made by the rapid capture of neutrons, the r-process, whose astrophysical sites are uncertain. There is evidence that kilonovae make at least *some* of the lighter r-process nuclei (Abbott et al., 2017a), but it is uncertain whether these events make the heavier nuclei of interest here. Assuming that CCSNe are the dominant r-process sites, we estimate yields of $\mathcal{N}(^{235}\mathrm{U}, ^{244}\mathrm{Pu}) \sim (3, 1.6) \times 10^{47}$ atoms per explosion.

The journey of SN-produced radioisotopes from explosion to seafloor is complex. Ejecta in dust most readily reaches the Earth (Fry et al., 2015). The fraction of atoms in dust f_{dust} should be high for the refractory species of interest. Due to their high speeds, SN dust grains will easily overcome the solar wind and reach Earth (Fry et al., 2016). The fallout on Earth favors deposition at mid-latitudes; additional dispersion occurs due to ocean currents (Fry et al., 2016). The global-average surface density of isotope i with half-life $t_{1/2}$ is $N_i = f_{\mathrm{dust}}\mathcal{N}_{\mathrm{ej},i}2^{-t/t_{1/2}}/16\pi r^2$ (Fry et al., 2015), with t the time since the explosion. We thus find global-averaged end-Devonian surface densities of SN material

$$N(^{146}\mathrm{Sm}, ^{235}\mathrm{U}, ^{244}\mathrm{Pu}) \sim f_{\mathrm{dust}}(1, 9, 0.3) \times 10^5 \mathrm{atoms/cm}^2 \; r_{20}^{-2}$$

after including the decay factors for each species. Unfortunately, this estimate implies a ratio of SN-produced ^{235}U to the background level in the Earth's crust of $\mathcal{O}(10^{-10})$, which is undetectably small. On the other hand, there is no natural background to the prospective ^{244}Pu signal, which may be detectable in fossiliferous material. Its detectability depends on the temporal resolution of the available geological sample, whereas the possible detectability of the prospective ^{146}Sm signal depends also on the degree of dilution due to its solubility. Finally, if more than one SN occurred before the DCB, then each of these could deposit radioisotope signals.

3.5 Other tests for supernovae

Some hundreds or thousands of years after the optical and ionizing outburst, the cosmic-ray and dust bombardment of the Earth would begin, with several possible effects.

Cosmic-ray ionization of the atmosphere and accompanying electron cascades may lead to more frequent lightning, increased nitrate deposition, and wildfires (Melott & Thomas, 2019). The increased nitrate flux might have led to CO_2 drawdown via its fertilization effect (Melott et al., 2018), thereby cooling the climate. There is evidence for cooling during the first stage of the DCB, though this occurred an estimated 300 kyr before the radiation damage attested by the data on pollen and spores (Marshall et al., 2020). Any increases in soot and carbon deposits during the end-Devonian could have been generated by increases in wildfires (Melott & Thomas, 2019).

Cosmic rays striking the atmosphere produce energetic muons that can penetrate matter to a much larger depth than UV-B radiation. The radiation dose due to muons at the Earth's surface (Thomas et al., 2016) and in the oceans at depths $\lesssim 1$ km (Melott et al., 2018) could exceed for many years the current total radiation dose at the Earth's surface from all sources. Therefore, in addition to comparing the effects of muons and UV-B radiation at or near the surface, they could be considered in end-Devonian extinctions of megafauna living at depth.

Finally, if there was one CCSN at the DCB, there may have been more, which may have been responsible for the Kellwasser and additional events. Thus, there should be associated evidence for ozone depletion and the other signatures above.

These could show evidence for ozone depletion and the other signatures above.

Chapter 4

Heliospheric compression due to recent nearby supernova explosions

The widespread detection of ^{60}Fe in geological and lunar archives provides compelling evidence for recent nearby supernova explosions within ~ 100 pc around 3 Myr and 7 Myr ago. The blasts from these explosions had a profound effect on the heliosphere. We perform new calculations to study the compression of the heliosphere due to a supernova blast. Assuming a steady but non-isotropic solar wind, we explore a range of properties appropriate for supernova distances inspired by recent ^{60}Fe data, and for a 20 pc supernova proposed to account for mass extinctions at the end-Devonian period. We examine the locations of the termination shock decelerating the solar wind and the heliopause that marks the boundary between the solar wind and supernova material. Pressure balance scaling holds, consistent with studies of other astrospheres. Solar wind anisotropy does not have an appreciable effect on shock geometry. We find that supernova explosions at 50 pc (95 pc) lead to heliopause locations at 16 au (23 au) when the forward shock arrives. Thus, the outer solar system was directly exposed to the blast, but the inner planets—including the Earth—were not. This finding reaffirms that the delivery of supernova material to the Earth is not from the blast plasma itself, but likely is from supernova dust grains. After the arrival of the forward shock, the weakening supernova blast will lead to a gradual rebound of the heliosphere, taking $\sim$ 100s of kyr to expand beyond 100 au. Prospects for future work are discussed.

This chapter has been submitted and accepted for publication in *The Astrophysical Journal*.

4.1 Introduction

The local neighborhood of the Sun is an ever-changing environment, as a result of our residence in a star-forming galaxy with a dynamic interstellar medium. The heliosphere must therefore evolve with time in response (Müller et al., 2006, 2009; Frisch & Slavin, 2006; Frisch et al., 2011). Indeed, events on Galactic scales may have an impact on Earth. Terrestrial ice ages have been linked to our passage through the Galaxy's spiral arms (Gies & Helsel, 2005), and our vertical motion through the Galactic disk may have affected the cosmic ray flux on Earth and have corresponding biological signatures (Medvedev & Melott, 2007). The Sun's passage through a dense cloud could compress the heliosphere to 1 au or smaller (Yeghikyan & Fahr, 2003, 2004); it has even been suggested that a recent such event could have occurred, and the corresponding compression could have ultimately had an effect on human evolution (Opher & Loeb, 2022). In this work, we explore the hydrodynamic effects of near-Earth supernovae, in which the blast wave moves at a velocity much greater than the Sun's typical speed through the local interstellar medium (ISM).

There is now abundant evidence of multiple recent near-Earth supernovae within $\lesssim 100$ pc. The most compelling is the discovery of live (undecayed) samples of ^{60}Fe ($t_{1/2} = 2.6$ Myr). This radioactive isotope is found in geological records such as ocean sediments and crusts (Knie et al., 1999b, 2004; Fitoussi et al., 2008; Wallner et al., 2016; Ludwig et al., 2016; Wallner et al., 2021), Antarctic snow (Koll et al., 2019), and even lunar samples returned by *Apollo* astronauts (Fimiani et al., 2016). ^{60}Fe has also been found in cosmic rays (Binns et al., 2016), which show a low-energy excess Fe flux that could be evidence for a recent nearby source (Boschini et al., 2021). Wallner et al. (2021) also detected ^{244}Pu coincident with the ^{60}Fe signals. In addition, Korschinek et al. (2020) reports a detection of ^{53}Mn, and ^{26}Al has been studied but not yet separated from the overwhelming terrigenic component (Feige et al., 2018).

Further evidence of a nearby supernova comes from the proton, antiproton, and positron cosmic-ray spectra and anisotropy (Kachelrieß et al., 2018; Savchenko et al., 2015), the existence of the Local Bubble (Smith & Cox, 2001; Frisch & Dwarkadas, 2017), and the observed distribution of Galactic ^{26}Al (Fujimoto et al., 2020). By tracing back the motion of runaway stars and neutron stars, Neuhäuser et al. (2020) suggested stars in a binary progenitor system for these supernovae; similarly, Tetzlaff et al. (2013) also suggested a progenitor for the nearby Antlia supernova remnant

(McCullough et al., 2002). The short ^{60}Fe lifetime demands that it was produced recently and thus nearby. These data are consistent with a nearby supernova ∼3 Myr ago, and the ^{60}Fe abundance implies a supernova distance of $60 - 130$ pc (Fry et al., 2015).

The observed ^{60}Fe came to us in the form of dust; ^{60}Fe ions would have been a component of the plasma that gets deflected by the heliosphere. The dynamics of dust grains in the outer heliosphere have received considerable theoretical study (e.g., Belyaev & Rafikov, 2010; Sterken et al., 2012), especially for the present-day heliosphere. Wallis (1987) found that during the passage through a dense cloud, dust can penetrate the heliosphere to Earth with little deflection due to the heliosphere's small size. Athanassiadou & Fields (2011); Fry et al. (2016) found that dust grains from near-Earth supernovae are typically deflected less than 1° by the heliosphere, due to their high speeds $v_{\rm dust} \gg v_{\rm esc}(1\,{\rm au}) = 42$ km/s far exceeding the escape speed at 1 au. The simulations we perform here may also contribute to our understanding of dust grain dynamics from near-Earth supernovae.

Wallner et al. (2021) has recently found ^{60}Fe from a second pulse due to an earlier supernova ∼7 Myr ago, showing that nearby supernovae are relatively commonplace on geological and astrophysical timescales. These two known events are at roughly similar distances, too far to cause mass extinctions of species on Earth, although possible damage to the biosphere is an open question under study (Melott & Thomas, 2019; Melott et al., 2017; Thomas et al., 2016). Closer events should occur, but less frequently. With this in mind, Fields et al. (2020) proposed that one or more supernovae at ~ 20 pc could have triggered extinctions at the end of the Devonian period 360 Myr ago, leading to observed global ozone depletion reflecting ionizing radiation damage from the explosion.

Motivated by these data, we consider the case of a near-Earth explosion, one of the most dramatic events the heliosphere can experience. This scenario is relevant for both the distant past and recent well-documented events. In the aftermath of a supernova, the supernova remnant (SNR) rapidly expands outwards, sweeping up the interstellar medium and eventually engulfing many surrounding stars. As the blast wave encounters these stars, it drives back their stellar winds, compressing their astrospheres. We aim to study the extent of this compression as applied to own heliosphere with a suite of numerical simulations to determine the innermost distance the supernova blast penetrates in our solar system.

To date, the only simulations of supernovae interacting with the heliosphere has been done in

Fields et al. (2008), which lays the foundations for our work here. This earlier study examined the impact of supernovae out to at most 30 pc, closer than current estimates suggest for the 3 Myr event Fry et al. (2015). Our work will for the first time study blasts from supernovae out to 126 pc, in line with the results from analyses of the ^{60}Fe data. We also perform detailed comparisons of our solar wind model against *in situ* measurements from *Voyager 2* and *Ulysses*. In addition, we study the scaling of the heliosphere dimensions with the supernova blast properties in a more detailed manner. We then use these scalings to estimate the evolution of heliosphere compression with the arrival of the supernova shock and subsequent rebound towards its present boundary.

The structure of this chapter is as follows: section 4.2 describes the formalism and initialization of the simulations as well as expectations; section 4.3 presents the results of the simulations; section 4.4 discusses these results; and section 4.5 gives concluding remarks.

4.2 Simulation model

Our goal is to examine how our heliosphere is compressed by a supernova blast wave. Since the most recent time this occurred was ∼3 Myr ago, present-day observations of this phenomenon are impossible. Therefore, we must turn to numerical simulations. We begin with the basic fluid equations, and then show that they produce a solar wind that roughly agrees with observations. Next we apply the Sedov model for a supernova remnant as the input for the blast wave. Finally we explore scaling laws for how these flows should interact.

4.2.1 Fluid equations

The modern heliosphere enjoys a variety of complex physics that deviates from standard hydrodynamics, such as magnetic fields, multi-fluid flows, charge exchange, and cosmic ray propagation (Pauls et al., 1995; Zank, 1999). Our goal, however, is to investigate the broad changes induced by the supernova blast. Consequently, we do not attempt to compete with the sophisticated models that include these effects, such as those presented in, e.g., Pogorelov et al. (2004), Izmodenov et al. (2008), and Opher et al. (2015, 2020).

Indeed, some of the relevant physics for the modern heliosphere may not be applicable for the case of an incoming supernova blast. For example, charge exchange occurs when neutral ISM atoms

penetrate into the heliosphere (Baranov & Malama, 1993; Pauls & Zank, 1997). As a result, the solar wind's ram pressure is weakened and the boundary between the solar wind and the present-day ISM is closer than it would be for a fully ionized ISM. But as we will show, we do not expect a SNR to contain a large population of neutrals, in which case the effects of charge exchange are not at play. Out to 30 au, the one-component model of the solar wind matches the observed density very well and the velocity to a difference of less than 10% (see Fig. 4.2 in Zank, 1999), a result we will confirm below.

To start, we assume that both solar wind and SNR flows can be adequately described with the basic equations of hydrodynamics,

$$\frac{\partial \rho}{\partial t} + \boldsymbol{\nabla} \cdot (\rho \boldsymbol{v}) = 0 \tag{4.1}$$

$$\frac{\partial \rho \boldsymbol{v}}{\partial t} + \boldsymbol{\nabla} \cdot (\rho \boldsymbol{v}\boldsymbol{v} + p) = 0 \tag{4.2}$$

$$\frac{\partial E}{\partial t} + \boldsymbol{\nabla} \cdot [(E + p)\boldsymbol{v}] = 0 \tag{4.3}$$

where $p = nkT$ for an ideal gas. We use an adiabatic equation of state with $\gamma = 5/3$.

We solve these equations with the `Athena++` code (Stone et al., 2020). `Athena++` is a grid-based magnetohydrodynamics framework, though we only make use of its hydrodynamics and neglect magnetic fields. We use the built-in HLLE Riemann solver, well-suited for our case where the kinetic energy of the flow dominates. While this solver can be diffusive, especially around contact discontinuities, it suppresses the Carbuncle instability and the "odd-even decoupling" that can appear when using other solvers (Sutherland et al., 2003; Quirk, 1994). While performing our simulations, we do not see evidence for substantial diffusion around any contact discontinuities.

4.2.2 Solar wind initialization

The solar wind is the complex flow of gas launched from the solar corona and streaming outwards through the solar system, first predicted by Parker (1958). While the real solar wind varies with time according to solar activity (Provornikova et al., 2014; Izmodenov et al., 2008), for these simulations we adopt a constant, steady outflow. Spacecraft near Earth's orbit such as *ACE* and *DSCOVR* have taken an abundance of solar wind data. Our main interest is in how the solar wind interacts far away from the Sun, so we input the wind at 1 au using a rough average of solar wind density, speed,

and thermal pressure. All grid cells within 1 au are overwritten with constant values every timestep.

The real solar wind not only varies in time, but also location: it is launched differently in the plane of the solar system than towards the poles. We use data from *Ulysses*'s close approach in 1995 to approximate these parameters as a step function in angle, shown in Table 4.1. For comparison, we also show the values adopted in Fields et al. (2008), which is spherically symmetric.

Table 4.1: Solar wind input values at 1 AU

Region	Density ($g\ cm^{-3}$)	Velocity ($km\ s^{-1}$)	Ram pressure (ρv^2) ($erg\ cm^{-3}$)	Thermal pressure ($erg\ cm^{-3}$)
Fields et al. (2008) comparison, global	1.02×10^{-23}	464	2.19×10^{-8}	2.00×10^{-10}
equatorial, $\lvert\theta\rvert < 25°$	1.06×10^{-23}	434	2.00×10^{-8}	6.68×10^{-10}
polar, $\lvert\theta\rvert > 25°$	4.18×10^{-24}	643	1.73×10^{-8}	9.91×10^{-10}

While a reasonable wind initialization is made across the grid at the start of the simulation, the solar wind is allowed to relax to its steady-state profile before the supernova blast is introduced.

With our steady one-fluid model, we must check to ensure our simulated solar wind still accurately represents the observed heliosphere. To this end, we compare our relaxed solar wind in the equatorial region to *Voyager 2* plasma data. Figure 4.1 shows density, velocity, and thermal and ram pressures of both our model and *Voyager 2* data. A 240-day running average of *Voyager 2* data is also shown. Our model tracks *Voyager 2*'s density, velocity, and ram pressure well, though not accounting for temporal variations. The thermal pressure clearly has a different profile. We attribute this in part to the assumption of the adiabatic evolution of our model, whereas the real solar wind is not adiabatic. Since the thermal pressure approximately matches in the region from 5–40 au, we consider it to be sufficiently accurate in the most relevant region. Furthermore, the thermal pressure is still several orders of magnitude below the ram pressure, which will dominate the large-scale structure of the simulations.

In Figure 4.2 we plot the velocity as a function of heliolatitude during *Ulysses*' close approach. Although initially a polar step function, the abrupt change in velocity is slightly smoothed out as the wind propagates. Data from our model is taken from a distance of 2 au in order to allow the solar wind time to relax and give a better description of the distant solar wind than the input step function. The largest discrepancy here is due to temporal variability, which we do not model. The averages over time are a close match.

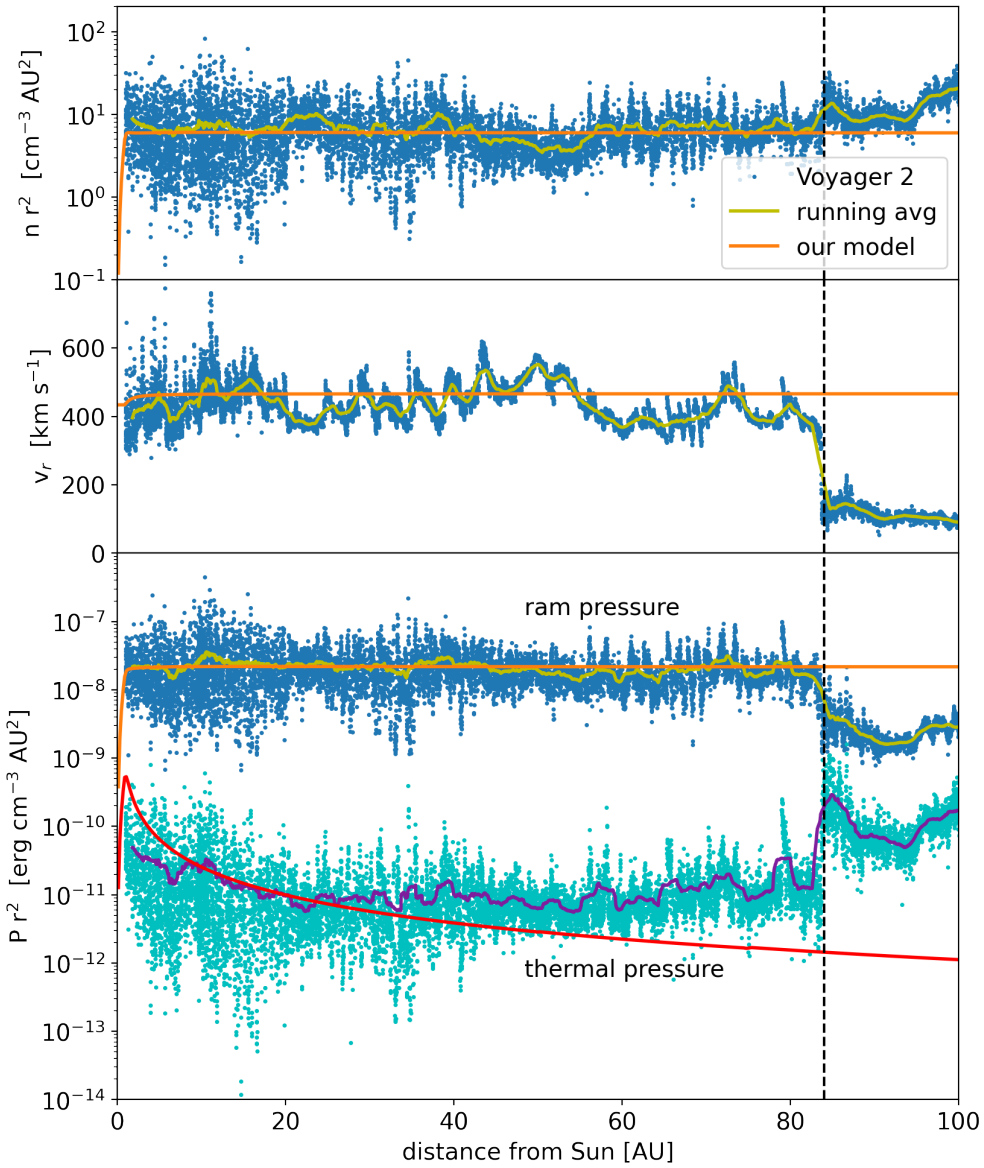

Figure 4.1: Comparison of our equatorial solar wind quantities (orange/red line) to daily averages of measurements made by *Voyager 2* (blue/cyan points) and a 240-day running average of *Voyager 2* (yellow/violet line). The black dashed line shows where *Voyager 2* crossed the termination shock, beyond which our model is not expected to match the data. The top panel shows density (scaled by r^2), the middle panel shows velocity, and the bottom panel shows ram and thermal pressure (scaled by r^2).

Currently, it is an open question as to where the supernova 3 Myr ago exploded, and therefore which direction the blast wave would come from. Proposed clusters include the Sco-Cen association (Benítez et al., 2002) and the Tuc-Hor association (Mamajek, 2015; Hyde & Pecaut, 2018). Sørensen et al. (2017) traced back nearby stellar clusters and statistically examined which ones were most

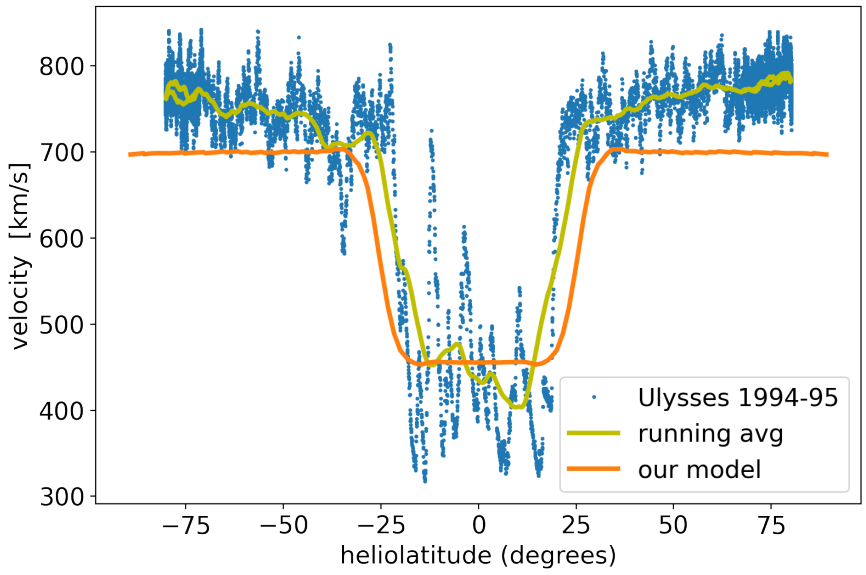

Figure 4.2: Comparison of our solar wind velocity to measurements made by *Ulysses* during its close approach of the solar minimum of 1995. We use the same color scheme as in Figure 4.1. Solar wind velocity does not change appreciably with distance (Fig. 4.1) but simulations are for a distance of 2 au; data follow the *Ulysses* elliptical orbit and sample distances from 1.3 to 2.8 au.

likely to produce a nearby supernova explosion. In addition, this supernova could have been a companion to a previous star that exploded, and could have been flung outwards with orbital velocity and exploded away from its home cluster. Given these uncertainties in location, we do not assume a single place of the supernova, but instead examine the effect of solar wind orientation with respect to the supernova.

In order to increase computational efficiency, we perform our simulations in 2D cylindrical coordinates in the r-z plane, with rotational symmetry imposed about the z axis. We use two different orientations depending on whether the blast wave enters orthogonal or parallel to the plane of the solar system. Figure 4.3 shows a schematic geometric interpretation of these orientations. When the blast comes perpendicular to the axis of rotation as shown in panel (a), the rotational symmetry of our simulation captures the solar wind behavior, which we model with the step function in angle described above; this is the polar orientation. When the blast comes in along the plane (striking the outer planets' orbits first) as in panel (b), we use a spherically symmetric wind; we refer to this as the equatorial orientation. Both orientations have similar ram pressures, so we do not expect great differences in heliospheric structure between the orientations.

Our base mesh resolution is 256×512 cells for all but the comparison to Fields et al. (2008),

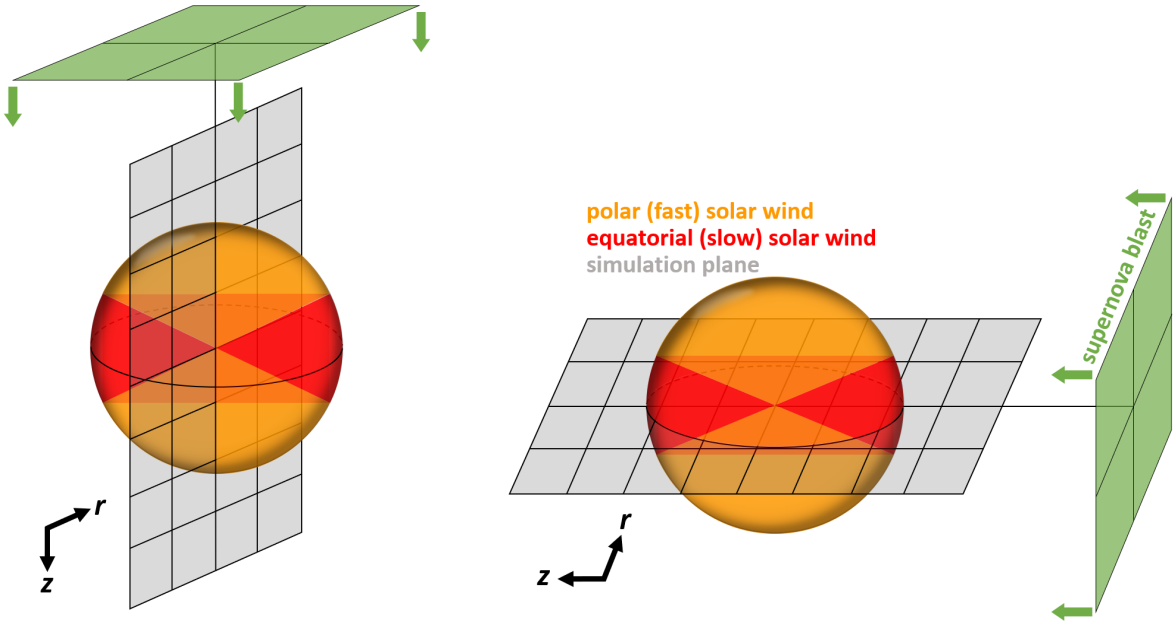

(a) (b)

Figure 4.3: Schematic of the two orientations. The equatorial solar wind (red) is slow and dense, while the polar solar wind (yellow) is fast and sparse. The gray region shows the 2D plane of the simulation domain. (a) In the polar orientation, the simulated wind is polar along the **z** direction and equatorial along **r**. (b) In the equatorial orientation, the entire solar wind in the simulation is equatorial, resulting in an isotropic wind.

which is 1024×1536. If kept uniform across the grid, several of our larger simulations would make the region within 1 au only a few cells across, resulting in a poorly-defined flow. To ensure a smooth spherical outflow, we refine the solar wind injection region for the entirety of the simulation (known as static mesh refinement, SMR). The amount of refinement depends on the outer boundaries of the mesh. Figure 4.4 shows the the relaxed solar wind and corresponding meshblocks in the polar orientation. Each refinement level increases resolution by a factor of 2.

4.2.3 Supernova blast initialization

Supernova remnants evolve over time. After the initial free expansion phase, supernova remnant morphology roughly follows a Sedov-Taylor profile (Sedov, 1946; Taylor, 1950) for much of its evolution. The remnant expands quasi-spherically over many parsecs until thermal emission becomes important. For SNRs several tens of parsecs across, a spherical forward shock is well-approximated as plane wave on the scale of the solar system. Since the most important parameter in our simulations

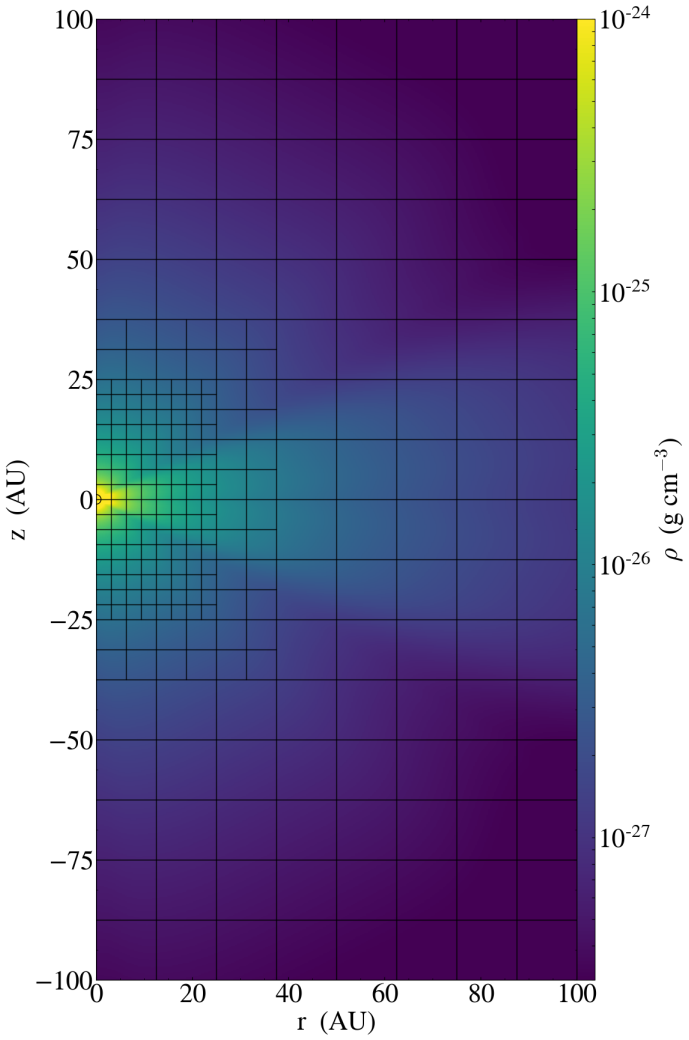

Figure 4.4: Density plot of the initialized, relaxed solar wind in the polar orientation. Color shows density on a log scale. The black grid shows `Athena++` meshblocks.

is the distance to the supernova, $R_{\rm SN}$, we invert the usual Sedov equation for distance to solve for time as

$$t = \sqrt{\frac{R_{\rm SN}^5 \rho_0}{\beta^5 E_{\rm SN}}} = 27 \text{ kyr } \left(\frac{n_0}{0.01 \text{ cm}^{-3}}\right)^{1/2} \left(\frac{R_{\rm SN}}{50 \text{ pc}}\right)^{5/2}, \tag{4.4}$$

where $R_{\rm SN}$ is the radius of the remnant, ρ_0 is the ambient medium density, β is a numerical factor of 1.1517 for the typical $\gamma = 5/3$, and $E_{\rm SN}$ is the energy of the supernova, taken to be 10^{51} ergs. By applying the Rankine-Hugoniot conditions, we find the density, velocity, and thermal pressure of

the gas immediately post-shock, which are

$$\rho_1 = \rho_0 \frac{\gamma+1}{\gamma-1} \tag{4.5}$$

$$v_1 = \frac{2}{\gamma+1} v_s \tag{4.6}$$

$$p_1 = \frac{2}{\gamma+1} \rho_0 v_s^2, \tag{4.7}$$

where the subscripts 0 and 1 indicate the ambient medium and immediate post-shock gas, respectively. γ is the adiabatic index, and v_s is the shock velocity, given by

$$v_s = \frac{2}{5}\frac{R_{\rm SN}}{t} = \frac{2}{5}\sqrt{\frac{E_{\rm SN}}{\beta^5 \rho_0}} R_{\rm SN}^{-3/2} \tag{4.8}$$

$$= 730 \text{ km/s } \left(\frac{n}{0.01 \text{ cm}^3}\right)^{-1/2} \left(\frac{R_{\rm SN}}{50 \text{ pc}}\right)^{-3/2}. \tag{4.9}$$

Our current local interstellar environment is dominated by the Local Bubble, a region of low-density carved out by multiple supernovae (Smith & Cox, 2001). While the density varies greatly with location, we use an average value of $n = 0.005$ cm^{-3}, rather than a typical Galactic ISM. The earliest supernovae to explode did so in a denser environment, and later ones encounter the swept-out low-density region from the past explosions. (Fuchs et al., 2006) estimated that 14-20 supernovae have exploded in the Local Bubble, and (Schulreich et al., 2017) and Breitschwerdt et al. (2016) performed hydrodynamic simulations showing how 16 supernovae can generate this environment. We will show that the ambient density has no effect on the distance of closest approach in our solar system, a feature of using the Sedov model. But the low density of the medium extends the duration of the Sedov phase, which should be a reasonable approximation for the supernova distances of interest here.

Furthermore, we can calculate the temperature of the post-shock material assuming an ideal gas. This yields a remarkably high temperature of

$$T = \frac{2\beta^5}{25 k_B (\gamma+1)} \frac{E_{\rm SN}}{r_s^3 n_1} \tag{4.10}$$

$$T = 1.5 \times 10^6 \left(\frac{R_{\rm SN}}{100 \text{ pc}}\right)^{-3} \left(\frac{n_0}{0.01 \text{ cm}^{-3}}\right)^{-1} \text{ K}. \tag{4.11}$$

For the low density observed in the Local Bubble, this model predicts that the temperature post-shock will remain over 10^6 K for 100 pc, the approximate size of the Local Bubble. In the past, it was accepted that Local Bubble consisted of a large hot component with $T \sim 10^6$ K, though such assumptions have recently been challenged (Welsh & Shelton, 2009; Linsky & Redfield, 2021). Despite the hot environment of supernova remnants, the quick formation of dust and even molecules in SN 1987A (Matsuura et al., 2017) suggest that some component of the remnant may be neutral. We do not account for multi-fluid hydrodynamics here, instead interpreting the Sedov equations to indicate complete ionization at the forward shock.

The most important parameter for the supernova is the distance, which directly affects the strength of the blast wave, with ram pressure scaling as $P_{\rm ram} \sim E_{\rm SN}/R_{\rm SN}^3$. The supernova 3 Myr ago is estimated to have occurred somewhere between 60-130 pc away (Fry et al., 2015). Recently, Fields et al. (2020) proposed that a supernova at $\sim$ 20 pc could have contributed to biological extinctions at the end-Devonian period. To cover this range of distances, we use supernova distances of 25.3, 50.0, 63.3, 75.9, 94.9, 110.0, and 126.5 pc. Looney et al. (2006) proposed that a very nearby supernova within $\sim$ 1 pc exploded in the early stages of the solar nebula; we limit our simulations to the fully-formed solar system and so do not consider this case here.

From a single point in space, SNRs weaken over tens of thousands of years. Our simulations cover at most the first few years of the initial blast; this timescale is a multiple of the $\sim$ 0.5 yr crossing time for a flow of 100 km/s to travel 10 au. Therefore, we do not allow the remnant to weaken during our simulation. Since we are primarily interested in the closest approach of the blast wave in our solar system, we restrict ourselves to modelling the strongest part of the blast, the forward shock. See §4.4.2 for discussion of the behavior over longer timescales.

The supernova blast is implemented as a boundary condition in `Athena++`. We first let the solar wind evolve until it has reached a steady state across the entire domain. Then the boundary condition at $-z_{\rm max}$ is changed to be the incoming supernova blast, flowing in the $+z$ direction. This new boundary condition is kept constant for the duration of the simulation. All times shown in our figures define $t = 0$ as the introduction of the blast.

4.2.4 Expected heliosphere structure and stagnation distance

Our work draws upon insights from the many studies of the *present-day* heliosphere's interaction with the very local ISM (e.g., Opher et al., 2020; Frisch et al., 2011). In addition, several studies of stellar winds interacting with the ISM have been carried out, both observational and numerical (Meyer et al., 2021; Henney & Arthur, 2019; Kobulnicky et al., 2016). These studies show that the solar wind-ISM interaction region consists of three main features: the termination shock (TS), where the solar wind slows to a subsonic velocity, the heliopause (HP), where the solar wind and in-flowing ISM meet, and the bow shock (BS), where the ISM transitions from supersonic to subsonic. In the modern day, the *Voyager 1* and *Voyager 2* missions have passed the HP at distances of 121.6 and 119.0 au, respectively (Burlaga et al., 2019). There is increasing evidence that there is no BS (McComas et al., 2012), indicating that the Sun's motion through the ISM is barely subsonic. This is not the case for a very rapidly-moving supernova blast.

We expect that the closest approach of the blast wave, directly on-axis, will be the point of pressure balance. (As we will show in section 4.4, pressure balance is instead an excellent predictor of the TS rather than the HP.) This point, also called the stagnation distance, is relevant for astrospheres and their bow shocks (Wilkin, 1996; Comerón & Kaper, 1998). While commonly written as a function of a star's mass loss rate as

$$r_{\rm stag} = \sqrt{\frac{\dot{M} v_w}{4\pi \rho_0 v_*^2}}, \tag{4.12}$$

where v_w is the stellar wind velocity and v_* is the speed of the star relative to the ISM (Comerón & Kaper, 1998), our model of the Sun has both an equatorial and polar region with slightly different mass loss rates. In order to relate the stagnation distance to our input parameters, we write it as a balance of thermal and ram pressure between the Sun and the supernova remnant. This stagnation distance is

$$r_{\rm stag} = \sqrt{\frac{P_{\rm sw} + \rho_{\rm sw} v_{\rm sw}^2}{P_{\rm SNR} + \rho_{\rm SNR} v_{\rm SNR}^2}} \text{ au} \tag{4.13}$$

where solar wind properties are evaluated at 1 au. Fields et al. (2008) found good agreement with this (for the TS) for very nearby supernovae. Given that the SNR gas parameters depend completely

on distance, $r_{\rm stag}$ could equivalently be written in terms of the Sedov supernova distance as

$$r_{\rm stag} = \left(\frac{25(\gamma-1)}{8\beta^5} \frac{R_{\rm SN}^3}{E_{\rm SN}} \left(P_{\rm sw} + \rho_{\rm sw} v_{\rm sw}^2 \right) \right)^{1/2} \tag{4.14}$$

$$= A \left(\frac{R_{\rm SN}}{100 \text{ pc}} \right)^{3/2} \left(\frac{E_{\rm SN}}{10^{51} \text{ erg}} \right)^{-1/2} \tag{4.15}$$

where $A = 24.97$ (23.50) au in the equatorial (polar) orientation. This final equation allows us to write the stagnation distance solely in terms of the supernova distance, given an explosion energy.

Qualitatively, different supernova distances should yield the same large-scale heliospheric shape and features among the simulations. Nearby supernovae will produce a much larger velocity than distant ones, which may affect the production of Kelvin-Helmholtz instabilities that form on the HP.

4.3 Results

We run 13 simulations, numbered with respect to supernova distance. Model 1 is a comparison to model 12 of Fields et al. (2008) for a 20 pc supernova. Here, the solar wind follows their parameters, rather than the updated ones for the rest of our models. Models 2-4 are for a 25.3 pc and 50 pc supernova in the equatorial and top-down orientations. Models 5a, 5b, and 5c are all a 63.3 pc supernova in the equatorial orientation, but with higher ambient medium densities representing a more dense Local Bubble before multiple supernovae carved it out. Models 6-11 are for supernovae at larger distances in both equatorial and polar orientations. A summary of the results is given in Table 4.2, which lists the initial conditions for the supernova and the distances of closest approach for the TS, HP, and BS. The location of the BS is not stated for the cases where it has retreated off the grid domain.

In Figure 4.5 we show three density plots from the last timestep of models 6, 8, and 11. We see the qualitative expected upwind structure including the TS, HP, and BS. Any turbulence happens across the HP, seen most easily in model 8. The high-density equatorial solar wind gets bent back and is incorporated into the rest of the flow. It does not appear to be a source of turbulence. Instead, the HP drives Kelvin-Helmholtz instabilities.

Figure 4.5 and all of our simulations show that for supernova distances consistent with recent ^{60}Fe measurements, the closest approach of the blast is > 10 au away. Certainly the blast can

Table 4.2: Supernova-heliosphere collision simulation results

Label	# of SMR Levels	Orientation*	R_{SN} (pc)	ρ_{SNR} (g cm^{-3})	v_{SNR} (km s^{-1})	p_{SNR} (erg cm^{-3})	r_{stag} (au)	r_{TS} (au)	r_{HP} (au)	r_{BS} (au)
1†	0	E	20.0	6.40e-25	688	1.00e-9	2.34	2.47	3.37	8.90
2	1	E	25.3	3.34e-26	2141	5.11e-10	3.18	3.43	4.75	14.47
3	1	P	25.3	3.34e-26	2141	5.11e-10	2.99	3.08	3.60	12.25
4	1	E	50.0	3.34e-26	771	1.99e-10	8.83	9.72	15.97	—
5a	1	E	63.3	3.34e-26	541	3.26e-11	12.56	13.72	23.88	—
5b‡	1	E	63.3	1.34e-25	271	3.26e-11	12.56	13.82	23.97	—
5c‡	1	E	63.3	6.68e-25	121	3.26e-11	12.56	13.82	22.61	38.18
6	1	P	63.3	3.34e-26	542	3.26e-11	11.82	12.94	18.90	39.94
7	1	E	75.9	3.34e-26	412	1.89e-11	16.51	17.53	29.98	—
8	2	P	94.9	3.34e-26	295	9.68e-12	21.72	22.31	23.10	64.26
9	2	E	110.0	3.34e-26	236	6.22e-12	28.80	30.76	44.63	86.33
10	2	P	110.0	3.34e-26	236	6.22e-12	27.11	26.07	27.05	80.08
11	2	E	126.5	3.34e-26	192	4.09e-12	35.53	37.21	52.15	97.27

* E = equatorial, P = polar orientation. Solar wind parameters for these are given in Table 4.1.
† Fields et al. (2008) model 12 comparison, different solar wind parameters.
‡ Models 5b and 5c use ISM densities of $n = 0.02$ and 0.1 cm^{-3}, respectively.

only arrive at 1 au for supernovae at extinction-level distances. But Fry et al. (2015) showed that ^{60}Fe abundances measured in terrestrial and lunar archive over the past 10 Myr imply a supernova distance of 50-100 pc. This reaffirms the conclusions of Fields et al. (2008) that these radioisotopes must arrive in the form of dust that can decouple from the blast at the supernova-solar wind interface. The dust must then travel ~ 10 au, which requires large or fast grains to avoid repulsion from the solar light pressure (Athanassiadou & Fields, 2011; Fry et al., 2016).

4.3.1 Comparison to previous work

In model 1, we use the same input parameters as Fields et al. (2008) model 12 in order to compare our two codes. We find excellent agreement with the overall structure of the heliosphere and the locations of the TS and HP upwind. The largest difference between the two is the amount of Kelvin-Helmholtz instabilities at the HP present in the previous work. We attribute this abundance to the use of adaptive mesh refinement in the previous work. This refinement was not used here in favor of static mesh refinement that resolved the solar wind at 1 au over much larger scales. While further refinement is needed to study instabilities and downwind mixing in detail, the two results are otherwise consistent.

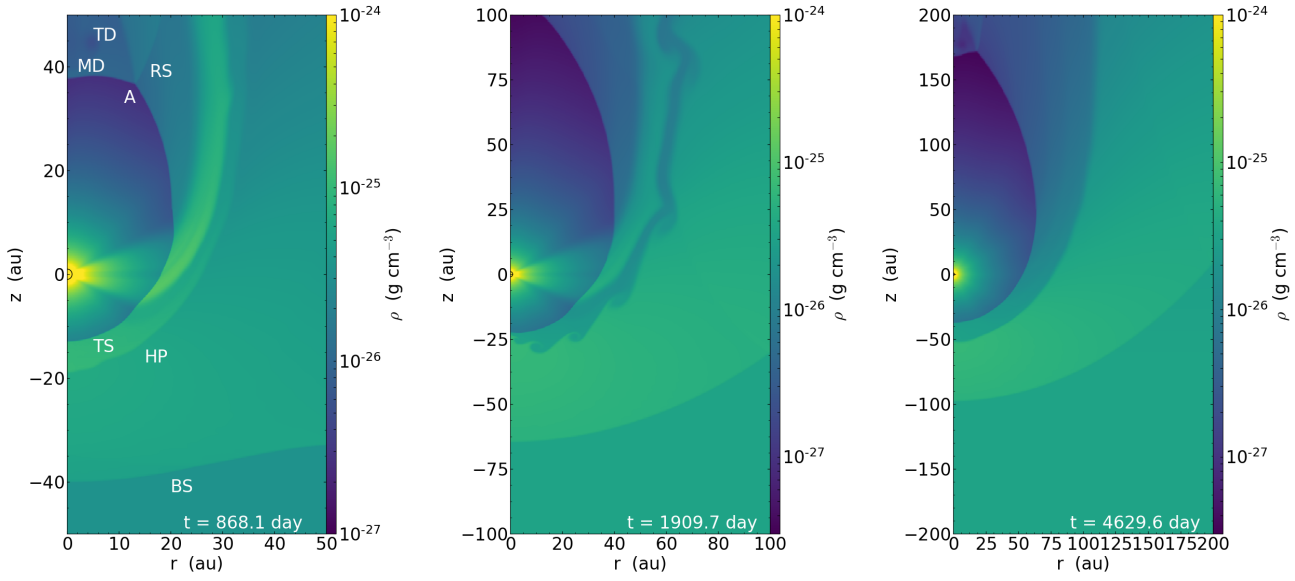

(a) (b) (c)

Figure 4.5: Density plots of models 6, 8, and 11, from left to right. Note the different distance and color scales. Both (a) and (b) are in the polar orientation and (c) is in the equatorial orientation. Labelled features in (a) use the abbreviations from Baranov & Malama (1993) and correspond to the bow shock (BS), heliopause (HP), termination shock (TS), Mach disk (MD), secondary tangential discontinuity (TD), reflected shock (RS), and the point at which the TS splits (A).

4.3.2 Time-dependent features

A characteristic timescale for these simulations is the time for the blast wave to cross the simulation domain, $t_{\rm cross}$. When $t \sim t_{\rm cross}$, the heliosphere directly upwind is in its most compressed state. Over multiple $t_{\rm cross}$, several processes continue to shape the heliosphere: Kelvin-Helmholtz instabilities along the HP, rebounding of the HP and BS, and downwind TS splitting.

The HP is a tangential discontinuity formed by solar wind and supernova fluids flowing along a surface of contact with a velocity tangential to this surface. This condition is ripe for Kelvin-Helmholtz instabilities, as we see in our simulations. Spiral features begin close to the axis of symmetry and grow as they are pushed downwind. The appearance of these instabilities is, in part, due to the resolution of our simulations, as high-resolution runs promote more instabilities and greater mixing. Since our goal is primarily to determine the innermost penetration of the SNR, we do not extend additional layers of resolution to the Kelvin-Helmholtz ripples.

4.3.3 Discontinuity locations

Tracking the location of the discontinuities (TS, HP, and BS) over time can be used to determine their stability. The Mach number M is an excellent indicator of the location of strong shocks. Both the solar wind and blast wave are initially supersonic and must decrease below $M = 1$ in order to interact head-on along the axis of symmetry. We note that as the blast first enters the domain, the BS does not immediately develop. Instead, there is a smooth gradient over M until it sharpens into a single location after approximately $t \sim t_{\text{cross}}$.

Figure 4.6 shows the Mach number along the z-axis for models 5a, 8, and 11. In this plot, the locations of the TS and BS are clear, marked by the near-vertical jump in the Mach number as it crosses $M = 1$. In 5a, the BS has receded out of the simulation frame, so is only marked by a small uptick at the domain boundary.

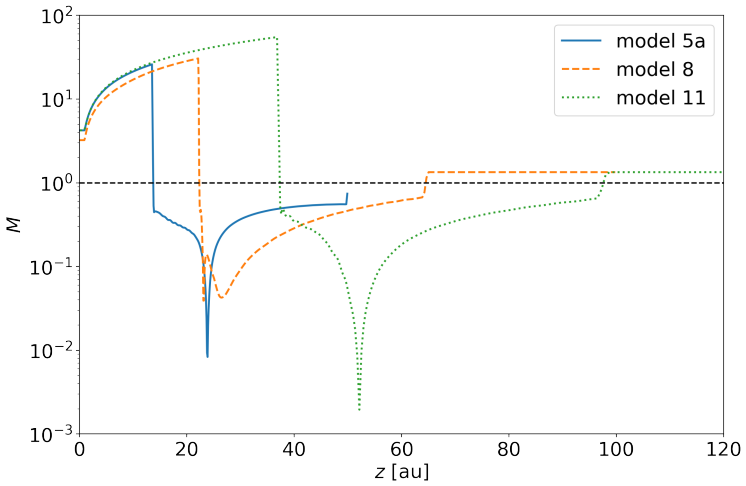

Figure 4.6: Profile plot of Mach number along the z-axis starting at the Sun and extending towards the upwind ($-z$) direction for models 5a, 8, and 11 (solid blue, dashed orange, and dotted green lines, respectively). The horizontal dashed line is at $M = 1$.

The HP is located where the two flows meet, which should be near-zero velocity along this axis. Models 5a and 11 clearly show this sharp downwards spike. The HP in model 8 is more difficult to locate. In this simulation, Kelvin-Helmholtz instabilities form close to the axis of symmetry. These ripples cause the location of the HP to change each frame, even after several t_{cross} have passed. We attribute this to the polar orientation of both models: the polar solar wind is lower density, and the greater density contrast appears to promote the growth of Kelvin-Helmholtz instabilities close

to the axis of symmetry. Nonetheless, we still use the minimum value for M as the HP with the understanding that this value has some error of $\sim 10\%$ for models 8 and 10.

4.3.4 Discontinuities over time

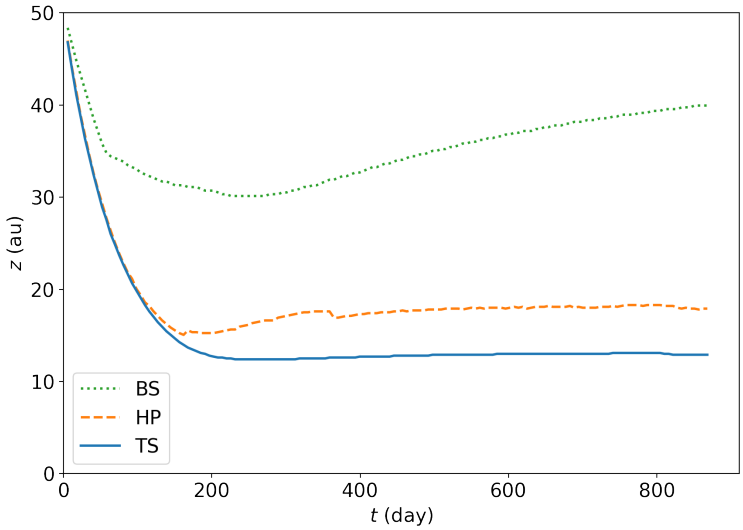

Figure 4.7: Location of upwind heliosphere features over the full ∼900 day simulation for model 6. The TS, HP, and BS are given by the solid blue, dashed orange, and dotted green lines, respectively.

We can apply this Mach number analysis over the duration of the simulation to examine the evolution of discontinuities over time. Figure 4.7 shows the locations of the TS, HP, and BS for model 6. Upon reaching the closest approach at $t \sim 250$ days, the TS remains extremely stable. The HP has some small motion, mostly due to the effect of Kelvin-Helmholtz instabilities. The BS approaches an innermost position, then slowly retreats upstream over the duration of the simulation. This is a numerical artifact, largely due to an unintended interaction of the BS with the outer r-axis. By widening the boundary to capture the full extent of the shock so that the BS falls off the $+r$-direction, we find that the BS retreat is not as dramatic. However, doing so is both computationally more intensive and does not affect the other heliosphere features.

4.3.5 Downstream features

When the TS meets itself at a point in the downwind side of the simulation, it splits into three features labelled in Baranov & Malama (1993). These are (from the inside outwards) the Mach disk, the secondary tangential discontinuity, and the reflected shock (as shown in Figure 4.5. In

model 1, we even see the appearance of Kelvin-Helmholtz instabilities in this secondary tangential discontinuity. The appearance of these features is a qualitative way to verify the accuracy of this code, as they are expected in the case of a fully-ionized ISM. More detailed models that include a neutral ISM component do not see evidence of these features.

4.3.6 Local Bubble density

For our Sedov supernova blast, we use a uniform ISM density of $n = 0.005$ cm^{-3}. Of course, the Local Bubble does not have that same density everywhere, as evidenced by the Complex of Local Interstellar Clouds. Due to self-similarity in the Sedov blast, the ram pressure does not depend on the ambient density. Therefore, the distance of closest approach should not depend on the ambient density. This relation is also reflected in eq. (4.15), in which ambient density does not appear in the expression for stagnation distance. To verify this relation and examine any other differences beyond stagnation distance, we ran three simulations changing only the ISM ambient density in models 5a-c. The ambient densities used here are $3.34 \times 10^{-26}, 1.34 \times 10^{-25}$ and 6.68×10^{-25} g cm^{-3} (i.e., ρ_0, $4\rho_0$, and $16\rho_0$) for models 5a, 5b, and 5c, respectively.

We show these simulations after the same amount of time has passed since the introduction of the blast in Figure 4.8 (all are in the isotropic equatorial orientation). The most significant output of these simulations, the distance of closest approach, remains unchanged independent of the ambient ISM density, as expected. Kelvin-Helmholtz instabilities are seen in the low density simulation, but are not as apparent in the higher density cases. Larger ambient densities slow the blast, resulting in a smaller velocity difference that hinders the growth of these instabilities. Other features are largely the same, though the smaller blast wave velocity means evolution takes place on a longer timescale. Qualitatively, in Fig. 4.8(c), we see a clear bow shock and lack of features in the downstream termination shock, but these will continue evolving as the simulation advances.

We conclude that the ambient density does not have a large impact on our simulations. The greatest effect is on the timescale of the heliosphere compression, with a larger ambient density slowing the compression. Larger ISM densities will also increase the time for the blast wave to reach the solar system after the inciting supernova explosion.

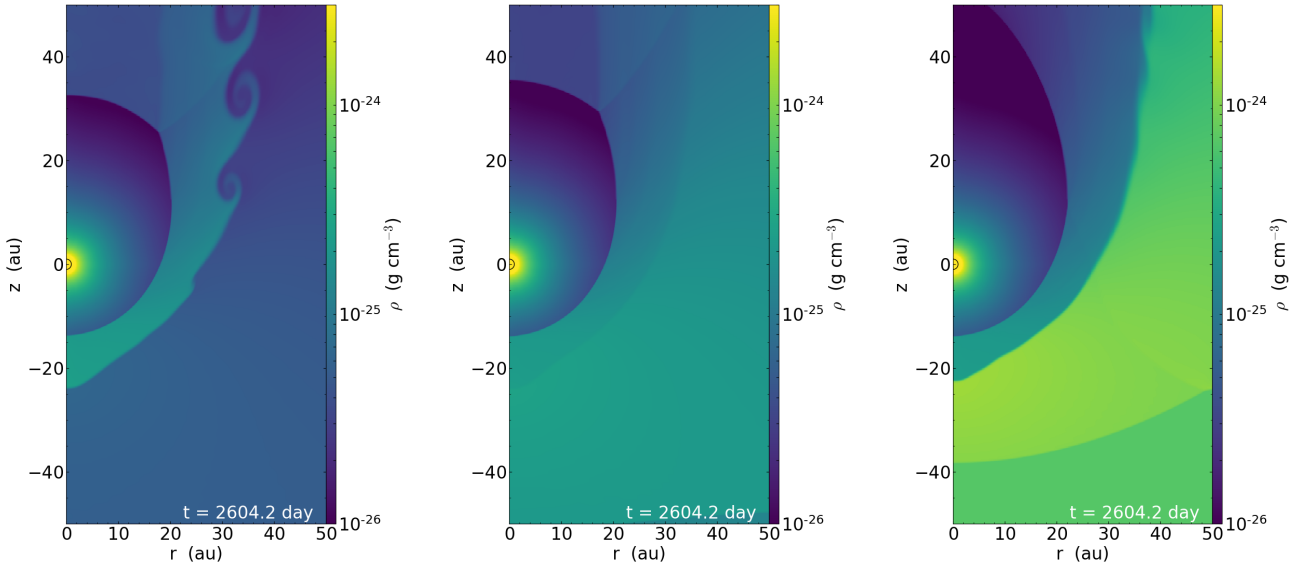

(a) (b) (c)

Figure 4.8: Density plots of models 5a, 5b, and 5c for supernovae 63.3 pc at the same time for three different ambient ISM densities: $3.34 \times 10^{-26}, 1.34 \times 10^{-25}$ and 6.68×10^{-25} g cm^{-3}, from left to right.

4.3.7 Orientation effects

These simulations are performed in two orientations depending on the location of the supernova compared to the equatorial solar wind. The polar wind has a lower density but higher velocity, making the ram pressures similar (see Table 4.1). The overall structure of the heliosphere is the same for both orientations. The main difference is that, in the polar orientations, the equatorial wind is bent back through the heliosheath. It does not appear to be a source of instabilities, but reacts to those produced along the HP, as seen in Figure 4.5(b).

We ran three polar orientations with equatorial counterparts (numbers 3, 6, and 10; model 8 is polar but does not have a corresponding equatorial simulation at the same distance). As expected from the weaker ram pressure, the polar orientation compresses the heliosphere more. This ∼10% difference in the TS, however, is dwarfed by the different values for the supernova distance. We conclude that the supernova distance is more important than its orientation for heliosphere compression.

4.4 Discussion and analysis

These simulations of a supernova blast wave colliding with the heliosphere assume idealized hydrodynamics. Although the real situation is surely more complex, we expect that the gross features of the perturbed heliosphere are captured in our simulation. The apparent lack of a large neutral component to supernova blasts implies that our single-fluid treatment is a reasonable approximation. Thus, scaling laws and analytical arguments can be formed.

If one assumes a thin region for the heliosheath, the position of the bow shock should follow a simple analytical expression as a function of angle. As derived by Wilkin (1996), the position is

$$r(\theta) = r_{\rm stag} \csc\theta \sqrt{3(1 - \theta\cot\theta)}. \tag{4.16}$$

Our simulations do not show a thin heliosheath, instead showing a well-separated TS, HP, and BS. Accordingly, this equation is only accurate for small values of θ directly upstream.

4.4.1 Discontinuity scaling

Given the final locations of the TS, HP, and BS in each of these simulations, relations between these values and the supernova blast waves can be examined. This comparison will test the usefulness of $r_{\rm stag}$ scaling.

In Figure 4.9, we compare the location of the TS and HP to two parameters: the stagnation distance from Equation 4.13 in (a) and the supernova distance in (b). When comparing to $r_{\rm stag}$, the TS has a very tight relation along the $y = x$ line. According to this relation, $r_{\rm stag}$ is an excellent predictor of the location of the TS rather than the HP. This effect is also noted in, e.g., Comerón & Kaper (1998) and Comerón & Pasquali (2007). The location of the HP appears to be dependent on orientation, approaching much closer in the polar orientations (particularly models 8 and 10) than in the equatorial one. We note that these two models also suffered from Kelvin-Helmholtz instabilities near the axis of symmetry. It is possible that the increased grid resolution of these models is responsible for this difference, though it does not affect the models in the equatorial orientation similarly.

Similarly to Figure 4.9(a), we can plot the TS and HP distances as a function of $R_{\rm SN}$, shown in

Figure 4.9(b). We also plot eq. (4.15) for both equatorial and polar orientations, though the small difference between these two lines emphasizes how solar orientation is a less significant parameter than supernova distance. We again see the tight correlation between the TS and $r_{\rm stag}$, as well as the very apparent $r_{\rm stag} \propto R_{\rm SN}^{3/2}$ relation.

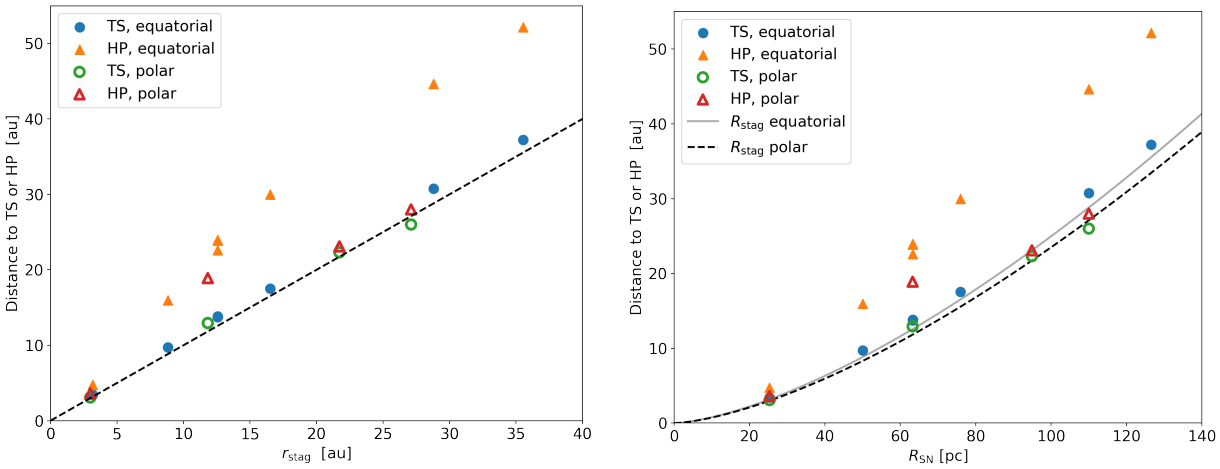

(a) (b)

Figure 4.9: (a) Termination shock and heliopause locations vs stagnation distance from equation 4.15. The solid blue circles and orange triangles show the TS and HP (respectively) for simulations in the equatorial orientation. The empty green circles and red triangles show the TS and HP from the polar orientation. The dashed black line is a $y = x$ line for reference. (b) The same as (a), but vs $R_{\rm SN}$. The solid grey and dashed black lines are the stagnation distances from Eqn. 4.15 for both equatorial and polar orientations.

The locations of the HP shown in Figure 4.9(a) seem to suggest a correlation between TS and HP distances. To examine this, we plot these two distances against each other in Figure 4.10. We fit a line to all these points, forcing it to go through the origin. The slope of the best-fit line is 1.389 ± 0.067, in very good agreement with Fields et al. (2008) who found a slope of 1.41. The smaller slope we find is primarily due to models 8 and 10, which lie well below the line. As discussed above, this departure from the trend is likely due to the increased resolution, allowing instabilities to form close to the axis of symmetry. The other models show decent agreement with the fit, though more points would show how well this fit holds over a larger range.

This relation does not hold for the present-day heliosphere, where the TS and HP are ~100 and ~120 au, respectively. The derived relation comes from purely fluid dynamics, and the present-day heliosphere requires a variety of more complex physical process to model correctly. Therefore, the

present heliosphere is not required or even expected to fit among this trend.

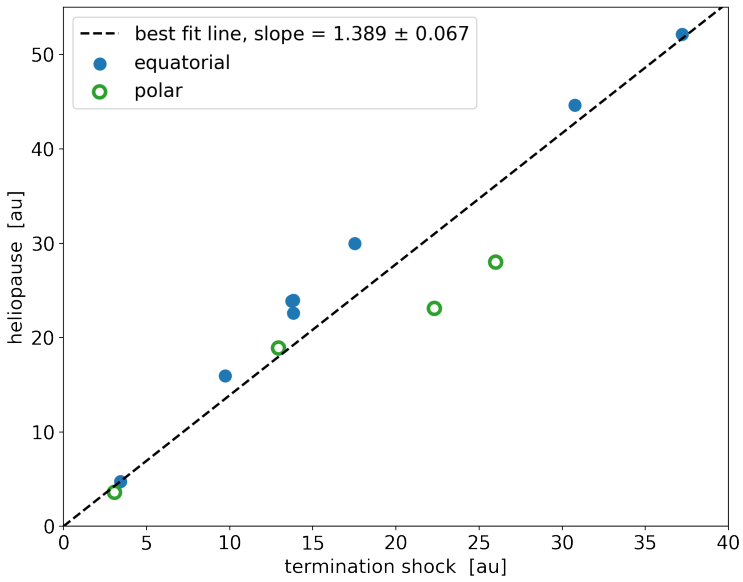

Figure 4.10: Distance to the heliopause vs termination shock. The simulations in the equatorial orientation are shown with a filled blue circle; the ones in the polar orientation are shown with a empty green circle. The dashed line is the best-fit line to all points, forced to go through the origin.

4.4.2 Blast weakening over time

The strength of the supernova blast will weaken over time as the remnant expands. The duration of this process depends on the explosion distance and local density, but certainly takes $\gg 1$ kyr. This timescale is far longer than the ~ 1 yr duration of our simulations. Accordingly, supernova blast properties change on similarly long timescales. We can study the effect of the weakening supernova blast by considering "snapshots" of the blast properties at different times.

We have shown that $r_{\rm stag}$ is an excellent predictor for the distance to the TS. By taking advantage of this relation, we can extend this analysis over the whole passage of the blast rather than just the leading edge.

The Sedov-Taylor model for supernova remnant evolution can be used to calculate the pressure balance distance for longer time scales. Normally, the Sedov solution is solved in terms of the outermost blast wave. In this instance, we wish to solve for the gas parameters for a stationary observer at a constant location from the origin.

We employ a Sedov blast wave verification code[1] to calculate the Sedov profile over the first 300 kyr after the blast. The chosen ambient density is still that of the Local Bubble, $n_{\rm amb} = 0.005$ cm^{-3}. At each timestep, we obtain the thermal and ram pressure and use Eqn. 4.13 to calculate $r_{\rm stag}$ (indicating the TS position). We show the results of these calculations in Fig. 4.11. The vertical lines correspond to the initial arrival of the blast; their spacing in time reflects the duration of the blast travel to the solar system for different supernova distances (eq. 4.4). Note that on the timescales plotted, our hydrodynamic simulations cover a thin ~ 1 yr at the innermost region upon the blast arrival; the rest of the curves use pressure balance to find the closest approach of the supernova. Maximum heliospheric compression lasts on the order of ∼kyr, however, it takes > 100 kyr for the blast to weaken enough so that the heliosphere fully rebounds.

Figure 4.11 has important implications for delivery of ^{60}Fe and other radioisotopes to the Earth and Moon. We see that the closest approach of the blast recedes quite rapidly at first. If the supernova ejecta is well-mixed into and carried by the blast, this means that the distance it must travel through the heliosphere rapidly becomes larger over time. If instead the ejecta is not well-mixed but located well behind the forward shock, it has even farther to travel in the heliosphere than in the well-mixed case. This again points to the need for the radioisotopes to arrive on dust grains having large sizes or high speeds.

After the forward shock arrival, much of the solar system will be exposed to the blast wave. Fig. 4.11 also shows the region of the Kuiper belt from 30 to 55 au (Sanctis et al., 2001; Chiang et al., 2003). Even for the most distant 100 pc supernova, the entirety of the Kuiper belt is exposed for ∼10 kyr.

It is interesting to note that due to the slightly sharper weakening of the closer supernovae, the outer Kuiper belt at 55 au is exposed to the supernova blast for approximately 70 kyr regardless of distance. In contrast, the inner Kuiper belt at 30 au is more sensitive to the distance, resulting in a nearly linear relation with distance.

4.4.3 Other solar system effects

Given the extent to which the heliosphere can be compressed, parts of the outer solar system are directly exposed to the supernova blast. This exposure may have numerous effects on the outer

[1] originally written by Frank Timmes, ported to Python by J. Moskal and J. Workman

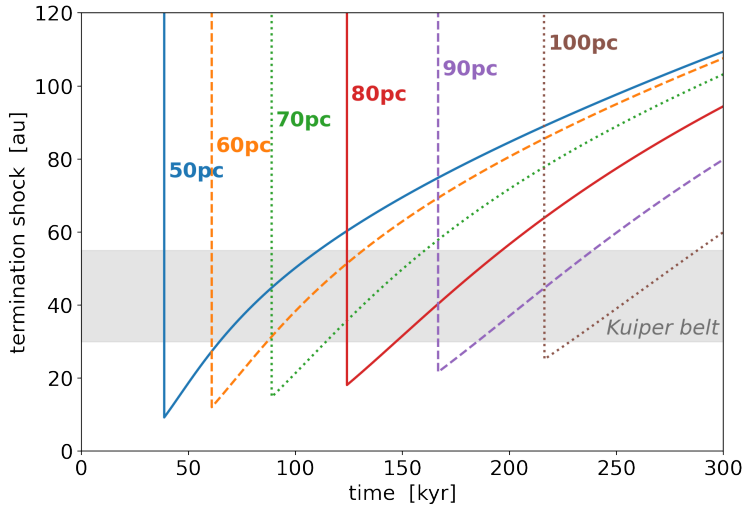

Figure 4.11: Location of pressure balance for several supernovae at 50-100 pc as the supernova remnant evolves, assuming a Sedov phase and an ISM density of $n_{\rm amb} = 0.005$ cm^{-3}. Vertical line corresponds to the arrival of the forward shock and indicates the blast arrival delay after the explosion. The rebound of the heliosphere thereafter follows the drop in blast ram pressure behind the forward shock. The shaded band shows the extent of the Kuiper belt.

bodies. Stern & Shull (1988) investigated how the light from a nearby supernova could melt the outermost surface of comets. Stern (1990) calculated the erosion of these bodies due to SNRs and how small particles with radius $\lesssim 100$ μm would be ejected from the solar system. Both of these studies can now be re-contextualized in light of the known supernovae detected by terrestrial ^{60}Fe: the most recent 3 Myr supernova may have "cleaned" the Oort cloud of small dust grains but left larger comet orbits unperturbed.

Due to the increased abundance of cosmic rays, the cosmic ray exposure ages of asteroid surfaces may be affected. While typical isotopes of interested for exposure ages have half-lives of less than $\lesssim$ 1 Myr (see, e.g., Michel et al., 1997), some of the longer-lived radioisotopes like ^{60}Fe, ^{53}Mn, and ^{26}Al could have high abundances. This effect would be more apparent in metallic meteoroids, which are exposed for longer than stony meteoroids (Ammon et al., 2009).

Potential links between SNRs and planets have so far been almost wholly unexplored. A significant challenge is to suggest not only how a supernova affects planets, but also find what observable features could remain after millions of years. We leave these investigations to future studies.

4.4.4 Supernova effects on astrospheres

In these simulations, we examine the supernova blast wave's effect on our own heliosphere. These simulations can be generalized to examine the effect of supernovae on astrospheres, which are driven by stellar winds from other stars.

Astrospheres are commonly observed by their bow shocks in the IR part of the spectrum. They are most commonly seen in surveys, either by the rapidly-moving runaway stars (Peri et al., 2012) or in the dusty environment of the Galactic plane (Kobulnicky et al., 2016). Red supergiants in particular, such as Betelgeuse, are expected to have enormous astrospheres nearly a parsec wide (Meyer et al., 2021). As of yet, no bow shocks have been associated with a star located within an SNR. Indeed, supernovae are prolific destroyers of ISM dust, so it is perhaps expected that astrospheres in SNRs would not be detectable in the IR due to a lack of dust. However, if discovered, they would be a novel form of stellar-interstellar interaction.

Astrospheres present an interesting complementary aspect to our own heliosphere: though we can directly probe our own heliosphere, the overall shape of the heliopause is still debated. It may have a comet-like tail 1000s of au long (e.g., Izmodenov & Alexashov, 2015) or it may be truncated much closer (Opher et al., 2015). In contrast, known astrospheres cannot be probed directly, but their shape can be seen by their bow shocks.

Both the solar system penetration distance and the increase in cosmic rays may alter the potential habitability of astrospheres. The proximity of stellar systems to supernovae affects the Galactic Habitable Zone (Gonzalez et al., 2001; Lineweaver et al., 2004; Morrison & Gowanlock, 2015; Spinelli et al., 2021). With these simulations, more accurate calculations of cosmic ray exposure during supernova blasts can be made in order to better ascertain astrosphere viability.

4.4.5 Effects of solar motion

We have assumed the solar system is at rest relative to the supernova explosion. In general one expects the Sun will move relative to the supernova progenitor and blast center. A nonzero solar velocity relative to the blast would change the ram pressure seen by the heliosphere, and the impact of this change scales at $\delta P_{\rm ram}/P_{\rm ram} \sim v_\odot/v_{\rm blast}$. The Sun's present motion with respect to the stellar Local Standard of Rest is 18 km/s (Schönrich et al., 2010; Zbinden & Saha, 2019) and our

speed relative to the very local ISM is 27 km/s; for such values $v_\odot / v_{\rm blast} \ll 1$ when blast arrives, and the perturbation is small.

At late times, the blast speed slows and Earth's speed could become important; these effects are discussed in (Chaikin et al., 2021) in the context of ^{60}Fe deposition and the local environment encountered by the solar system. It remains for future work to model such effects on the heliosphere, including the possibility that the Earth's velocity is misaligned with that of the supernova blast.

4.5 Conclusions

Motivated by terrestrial detections of ^{60}Fe as evidence for near-Earth supernovae in the recent past, we have presented hydrodynamic simulations of the heliosphere's response to a supernova blast wave at various distances. We match our steady solar wind to that observed by space missions and test the effect of solar wind orientation. The supernova blast is assumed to be in the Sedov phase.

The broad structure of the heliosphere is reproduced, albeit at much smaller scales than the present-day heliosphere. We verified that pressure balance gives the location of the TS over a range of distances. We applied this relation to analytically examine the heliosphere throughout the duration of the supernova remnant evolution far longer than the hydrodynamic simulations could run.

Taking advantage of rotational axisymmetry allowed for two orientations of how the blast wave strikes the heliosphere: polar, in which the blast approaches from the poles of the Sun, and equatorial, in which the blast arrives from the side. We apply a steady fast and slow solar wind originating from the poles and equator, respectively. Due to their density differences, the ram pressures of these winds are very similar. Appropriately, since the penetration distance depends chiefly on ram pressure, the orientation is found to have little influence on the global structure of the heliosphere.

This work reaffirms and builds upon the conclusions of Fields et al. (2008) that the supernova blast plasma is strongly excluded from 1 au for any plausible distance to the recent ^{60}Fe-depositing supernovae. The observed ^{60}Fe deposits on the Earth and Moon must have arrived in a form other than the plasma–namely, in dust grains. The dynamics of dust grains in the outer heliosphere are well-studied (e.g., Belyaev & Rafikov, 2010), especially for the present-day heliosphere. Wallis (1987) found that during the passage through a dense cloud, dust can penetrate the heliosphere to Earth

with little deflection due to the heliosphere's small size. Athanassiadou & Fields (2011); Fry et al. (2016) found that dust grains from near-Earth supernovae are typically deflected less than 1° by the heliosphere. Our work shows provides the location of closest approach of the supernova material and thus the initial conditions for studies of the dust propagation within the compressed heliosphere to Earth.

As the SNR evolves, the blast wave will weaken and allow the heliosphere to rebound. According to our scaling laws, this process is expected to take several 100 kyr to rebound to 100 au. Our simulations do not account for supernova-formed dust dynamics, but their propagation through the heliosphere is modified by the decreased heliosphere size. This effect is especially significant for any grains that arrive within the first 100 kyr after the blast wave arrival. Grains that arrive later will need to traverse progressively more of the heliosphere in order to reach the Earth and Moon.

The principal shocks in our simulations (BS and TS) can accelerate particles through diffusive Fermi acceleration to produce anomalous cosmic rays (Zank et al., 1996; Lazarian & Opher, 2009). Cosmic rays accelerated in these shocks would have an effect on the amount of radiation impinging on Earth. For very nearby supernovae, there could even be biological effects, either as a mass extinction (Gehrels et al., 2003) or lesser extinction events (Melott et al., 2017; Thomas et al., 2016). Tracking how these shocks evolve over the passage of the blast wave furthers our understanding of potential biological responses to the supernova.

The proposed Interstellar Probe mission[2] plans to launch a spacecraft several hundred au into the very local ISM in the coming decades. Such a probe would be sent out to the remains of an ancient supernova remnant, and may thus contribute to the study of how old SNRs evolve and fade into the Galactic medium.

The simulations presented here could be expanded upon in many ways, including developing a more careful treatment of non-hydrodynamic physics like magnetic fields and charge exchange. Solar activity represented as a time-varying solar wind may also be relevant for determining how instabilities affect the distance of closest approach. Such inclusions would allow for more realistic non-axisymmetric simulations, allowing us to probe how our own solar system responds to dramatic nearby events such as supernovae.

[2] https://interstellarprobe.jhuapl.edu/

Chapter 5

r-process radioisotopes from near-Earth supernovae and kilonovae

The astrophysical sites where r-process elements are synthesized remain mysterious: it is clear that neutron star mergers (kilonovae (KNe)) contribute, and some classes of core-collapse supernovae (SNe) are also possible sources of at least the lighter r-process species. The discovery of ^{60}Fe on the Earth and Moon implies that one or more astrophysical explosions have occurred near the Earth within the last few million years, probably SNe. Intriguingly, ^{244}Pu has now been detected, mostly overlapping with ^{60}Fe pulses. However, the ^{244}Pu flux may extend to before 12Myr ago, pointing to a different origin. Motivated by these observations and difficulties for r-process nucleosynthesis in SN models, we propose that ejecta from a KN enriched the giant molecular cloud that gave rise to the Local Bubble, where the Sun resides. Accelerator mass spectrometry (AMS) measurements of ^{244}Pu and searches for other live isotopes could probe the origins of the r-process and the history of the solar neighborhood, including triggers for mass extinctions, e.g., that at the end of the Devonian epoch, motivating the calculations of the abundances of live r-process radioisotopes produced in SNe and KNe that we present here. Given the presence of ^{244}Pu, other r-process species such as ^{93}Zr, ^{107}Pd, ^{129}I, ^{135}Cs, ^{182}Hf, ^{236}U, ^{237}Np, and ^{247}Cm should be present. Their abundances and well-resolved time histories could distinguish between the SN and KN scenarios, and we discuss

The following chapter has been published in ApJ with the citation: Wang, X., et al. (2021), *ApJ*, 923:219. doi:10.3847/1538-4357/ac2d90.

prospects for their detection in deep-ocean deposits and the lunar regolith. We show that AMS ^{129}I measurements in Fe-Mn crusts already constrain a possible nearby KN scenario.

5.1 Introduction

Astrophysical explosions such as supernovae (SNe) within $\mathcal{O}(10)$ pc would be close enough to endanger life on Earth (Ruderman, 1974; Ellis & Schramm, 1995), and SN explosions within $\mathcal{O}(100)$ pc would have been close enough to deposit detectable amounts of live (undecayed) radioactive isotopes (Ellis et al., 1996). Over the past two decades, many experiments have detected live ^{60}Fe in deep-ocean sediments and ferromanganese (Fe-Mn) crusts (Knie et al., 1999a, 2004; Fitoussi et al., 2008; Ludwig et al., 2016; Wallner et al., 2016, 2020, 2021), in the lunar regolith (Fimiani et al., 2016), in cosmic rays (Binns et al., 2016), and in Antarctic snow (Koll et al., 2019). The ^{60}Fe is best understood as evidence for explosion of one or more nearby and recent SNe, and the deep-ocean data point to an epoch ~ 3 Myr ago and a distance $\lesssim 120$ pc away (Fields & Ellis, 1999; Fields et al., 2005; Fry et al., 2015). Recent evidence for ^{53}Mn in Fe-Mn crusts (Korschinek et al., 2020) adds support to the picture of a nearby SN, and we note that multiple nearby SNe are postulated when modeling the Local Bubble (Smith & Cox, 2001; Breitschwerdt et al., 2016; Schulreich et al., 2017). The wealth and variety of ^{60}Fe detections establish that near-Earth explosions indeed occurred in the geological past. These results bring home the environmental hazards facing citizens of star-forming galaxies such as ours.

Intriguingly, there also have been several reports of non-anthropogenic ^{244}Pu in deep-ocean deposits from the past 25 Myr (Paul et al., 2001; Wallner et al., 2004; Raisbeck et al., 2007; Wallner et al., 2015b, 2021), which are of particular interest because ^{244}Pu originates in the astrophysical r-process. Whereas previous ^{244}Pu detections were tentative, the recent measurements by Wallner et al. (2021) are definitive and presumably represent injections from one or more extrasolar explosions, and it is important to consider their profound implications for potential r-process sites in the solar neighborhood. Therefore, in this chapter we study potential near-Earth r-process events that could possibly explain the ^{244}Pu detections: their astrophysical sources, means of delivery to Earth, and radioisotope signatures.

The most important sites for the r-process are currently a subject of debate (Cowan et al., 2021).

Certainly neutron star mergers (kilonovae (KNe)) provide inevitable sites, and the recent observation of a KN associated with the GW190521 gravitational-wave signal (Abbott et al., 2017a,b) suggests encouraging prospects for more detailed studies of similar events in the future (Zhu et al., 2018; Barnes et al., 2021; Korobkin et al., 2020; Wang et al., 2020b; Zhu et al., 2021). However, neutron star mergers may be only partially responsible for the Galactic tally of r-process elements (Kyutoku & Ioka, 2016; Côté et al., 2019; Kobayashi et al., 2020; Yamazaki et al., 2021), and a variety of other sites have been proposed, including both standard and rare types of core-collapse SNe (see, e.g., Hoffman et al. (1997); Wanajo (2006); Fujimoto et al. (2008); Winteler et al. (2012); Mösta et al. (2018); Siegel et al. (2019); Miller et al. (2020); Choplin et al. (2020); Reichert et al. (2021); Fujimoto & Nagakura (2021)). In support of this possibility, we note that Yong et al. (2021) recently discovered an r-process-enriched (and actinide-enhanced or -boosted) halo star with a very low metallicity [Fe/H] $= -3.5$, which implies very early production suggestive of an SN origin, perhaps in magnetohydrodynamic jets. The radioisotopes produced by various r-process sites have also been studied: see, e.g., early work by Seeger & Schramm (1970) and Blake & Schramm (1973); Meyer (1993) on pre-solar abundances; Goriely & Janka (2016) on SN neutrino-driven winds; the ^{244}Pu yields and ratios in Tsujimoto et al. (2017); and recent work by Beniamini & Hotokezaka (2020) and Côté et al. (2021).

As ^{244}Pu is among the heaviest of the r-process actinides, its production requires the most robust of r-process conditions. Modern simulations do not find these conditions in regular core-collapse SNe (Fischer et al., 2010; Hüdepohl et al., 2010; Arcones & Janka, 2011). Indeed, in most recent models, *no* actinides are produced at all, and ^{244}Pu is absent. On its face, this would indicate a KN scenario as the origin for the observed ^{244}Pu. However, there are still significant uncertainties in the extreme physical conditions of SNe, particularly (1) in the physics of neutrinos and their impact on the neutron abundance (McLaughlin et al., 1999; Duan et al., 2011; Roberts et al., 2012; Johns et al., 2020; Abbar et al., 2021), and (2) in the effects of relativistic magnetohydrodynamic jets that can expel neutron-rich material from the proto-neutron star (Winteler et al., 2012; Mösta et al., 2018; Reichert et al., 2021). In some scenarios these effects can lead to SN actinide production. We study possible SN sources as well as KNe, and study the ability of the ^{244}Pu detection to discriminate among these scenarios.

We have also been motivated to calculate the possible yields of other r-process nuclei in both SN

and KN sites and compare their abundances relative to ^{244}Pu. These may be measurable in both deep-ocean deposits and the lunar regolith, where ^{60}Fe has already been detected (Fimiani et al., 2016). Of particular interest are layers of ages ~ 2.5 and ~ 7 Myr where there are peaks in the deep-ocean ^{60}Fe signal, as discovery of one or more r-process isotopes there would confirm that at least one SN was an r-process site. However, other layers are also of interest, particularly because there is some evidence for deep-ocean ^{244}Pu atoms deposited earlier than the two ^{60}Fe peaks, which points to one or more other sources of unknown astrophysical origin. Another motivation is the possibility that one or more other astrophysical explosions may have occurred at closer distances in the more distant past. Specifically, it has been suggested (Fields et al., 2020) that one or more extinction events toward the end of the Devonian ~ 360 Myr ago might have been caused by SN explosions. These events probably occurred too long ago to have left detectable deposits of ^{60}Fe, in view of its relatively short half-life of 2.6 Myr, but might have left detectable deposits of longer-lived r-process isotopes such as ^{244}Pu (half-life 80 Myr).

In order to lay a basis for a systematic study of the live isotopes from possible nearby astrophysical explosions and r-process sites, we survey all the nuclear isotopes with half-lives between 1 Myr and 1 Gyr, identifying the nucleosynthesis processes that might produce them and commenting on the results of previous searches on the Earth and Moon and on the prospects for their future detection.

Three timescales are of particular interest. First, the widespread detection of live ^{60}Fe shows that at least one nearby SN injected ^{60}Fe into the interstellar medium (ISM) at a time

$$t_{\rm Plio} \simeq 3.2 \text{ Mya} \,, \tag{5.1}$$

where Mya = Myr ago. This is derived from the sediment data of Wallner et al. (2016) and Ludwig et al. (2016), where Wallner et al. (2016) report the earliest ^{60}Fe detection. The peak of the ^{60}Fe deposition on Earth due to this event was ~ 2.5 Mya, around the end of the Pliocene epoch, and a linkage to a coincident mass extinction has been proposed in Melott et al. (2018). We note also that the ferromanganese crust data from Wallner et al. (2016, 2021) provides evidence of a potential second peak at about 7 Mya that has not yet been detected in sediment data.

A second important timescale is the lifespan of Local Bubble, a $\gtrsim 100$ pc region of hot, low-density gas in which the Sun resides (Frisch, 1981; Crutcher, 1982; Paresce, 1984; Frisch et al., 2011).

Multiple supernovae are required to account for this structure (Smith & Cox, 2001; Berghöfer & Breitschwerdt, 2002), and the ^{60}Fe pulses are likely to be among the most recent and nearest such events. As we will discuss, the timescale for the creation of the bubble and the subsequent deaths of the massive stars within it can be as long as

$$t_{\rm LB} \lesssim \mathcal{O}(50)\ \text{Mya} \tag{5.2}$$

Possibly related, geological indications of live ^{244}Pu imply a flux on Earth that stretches farther back, with the earliest potential detection in a layer deposited 12–25 Mya. It is thus of interest to consider an event at least this long ago. We will see in Section 5.6.5 that existing ^{244}Pu and ^{129}I data suggest a timescale comparable to that in eq. (5.2).

Finally, Marshall et al. (2020) have recently found evidence of a dramatic loss of stratospheric ozone 359 Myr ago in the so-called Hangenberg crisis, the last of several poorly understood mass extinction events that punctuated the end of the Devonian period. This raises the possibility that one or more nearby SNe were responsible for the Hangenberg event and possibly others as well (Fields et al., 2020), roughly at

$$t_{\rm Devo} \simeq 360\ \text{Mya}\,. \tag{5.3}$$

We highlight in the following the yields and isotope ratios at these epochs. We note also that other extinction events may be connected to astrophysical explosions. For example, Melott et al. (2004) have suggested a gamma-ray burst origin for the late Ordovician mass extinction ~ 440 Myr ago.

The layout of this chapter is as follows. In Section 5.2 we survey the radioisotopes with half-lives between 1 Myr and 1 Gyr that are candidates for providing interesting signatures of nearby astrophysical explosions due to SNe and/or KNe. In Section 5.3 we review the available measurements of ^{60}Fe and ^{244}Pu in deep-ocean deposits, and in Section 5.4 we introduce the SN and KN models we use to illustrate the range of possible astrophysical r-process sites that fit the data on isotope abundances of representative metal-poor stars and also match solar abundances. Then, in Section 5.5 we present detailed calculations of the ratios of the abundances of live isotopes and their time evolution in these models. In light of these results, we discuss in Section 5.6 the

observability of r-process isotopes in deep-ocean sediments and crusts and on the Moon. Finally, in Section 5.7 we discuss the prospects for terrestrial and lunar searches for live isotopes, and how they might cast light on r-process sites and the history of the solar neighborhood, and we summarize our conclusions and suggest directions for future work in Section 5.8.

5.2 A survey of radioisotope signatures of astrophysical explosions

An SN or KN within $\mathcal{O}(10)$ pc would be near enough to pose a threat to life on Earth. Fortunately, SN explosions within $\mathcal{O}(10)$ pc of Earth are expected to occur only on intervals of a billion years or so, and nearby KN explosions are thought to be even rarer. However, SNe are estimated to occur within $\mathcal{O}(100)$ pc every few million years, and it was suggested in Ellis et al. (1996) that live radioisotopes would be the premier signatures of such events. The detection of such signatures can cast light on the history of the Local Bubble and SN nucleosynthesis mechanisms (Breitschwerdt et al., 2016; Schulreich et al., 2017), refine estimates of the SN threat to life on Earth, and possibly serve as markers of past SN effects on the biosphere.

The existence of the well-studied ^{60}Fe peak at 3 Myr ago, and the Wallner et al. (2021) reports of another peak at 7 Myr ago and ^{244}Pu possibly extending to 10 Myr ago, focus interest on the search for other live isotopes deposited around those times. But there is also interest in looking for earlier radioisotope deposits, e.g., from the epochs of mass extinctions, many examples of which are known in the fossil record. The famous Cretaceous–Paleogene extinction, which included the death of non-avian dinosaurs, was triggered by a different type of astrophysical event, namely an asteroid impact, whereas the end-Permian extinction is thought to be due to large-scale vulcanism. However, there are other events in the fossil record whose origins are unknown as yet, and detection of coincident radioisotope signatures could provide evidence for any astrophysical origins. Candidate extinctions whose origins could be explored in this way include those at the end of the Devonian epoch ~ 360 Mya (Fields et al., 2020).

In view of the timings of these target events, radioisotopes of interest are those with half-lives between 1 Myr and 1 Gyr. We have therefore identified all nuclides with half-lives from $t_{1/2} = 1$ Myr to 1 Gyr. We display in Fig. 5.1 scatterplots of all radioisotopes with half-lives $> 10^6$ yr, ordered by their atomic weights A, and separated according to their respective dominant nucleosynthesis

mechanisms. More relevant information about these isotopes is given in Table 5.2, including their half-lives $t_{1/2}$, their dominant decay modes, the nucleosynthesis mechanisms dominating their production, and comments on the prospects for their detectability, which we develop in more detail later in this chapter. The half-lives are from the NUBASE2016 evaluation (Audi et al., 2017) and, unless otherwise noted, the nucleosynthesis processes are from Lugaro et al. (2018) and the accelerator mass spectrometry (AMS) detection information is from Kutschera (2013).

We now discuss relevant features of the various isotopes listed in Table 5.2. As noted, there is a large background of ^{10}Be production by cosmic-ray interactions, so this is not a promising signature of a nearby astrophysical explosion. There is expected to be copious ejection of ^{53}Mn and ^{60}Fe by Type-Ia (Lugaro et al., 2018; Kobayashi et al., 2020) and core-collapse SNe, respectively, rather than by the r-process, and these isotopes are not expected to be prominent in KN debris. The main mechanism for producing the proton-rich isotopes ^{92}Nb and ^{97,98}Tc is expected to be the p-process, [1] while there may be p-, r- and s-process contributions to ^{93}Zr production. Most of the heavier isotopes with $A > 100$ are expected to be produced mainly via the r-process, exceptions being ^{146}Sm, ^{150}Gd, ^{154}Dy and ^{205}Pb. [2] In the cases of the actinide isotopes, one must be mindful of the possible presence of terrestrial anthropogenic contamination by nuclear accidents or bomb debris, which was an issue for the analysis of ^{236}U and ^{237}Np in *Apollo* lunar regolith samples (Fields et al., 1972, 1976). The ambient terrestrial level of ^{244}Pu has been measured in Winkler et al. (2004), and the detection of ^{244}Pu in deep-ocean deposits by Wallner et al. (2015b) is thought to be free of this background, which was considered in detail in Wallner et al. (2021).

We focus in the following on the long-lived radioisotopes that could be synthesized through the r process, as listed in the top panel of Fig. 5.1, and their production by SNe and KNe alongside ^{244}Pu. Since several of these isotopes have multiple avenues of astrophysical production while ^{244}Pu is an r-only species, we emphasize that the r-process production ratios we present in the following are lower limits.

[1] As mentioned in Table 5.2, ^{97,98}Tc may be produced by SN neutrino interactions in molybdenum, via the reactions $\nu_e + ^{98}\text{Mo} \rightarrow ^{97}\text{Tc} + e^- + n$ and $\nu_e + ^{97,98}\text{Mo} \rightarrow ^{97,98}\text{Tc} + e^-$. Searches for ^{97,98}Tc in molybdenum ore could be interesting complementary ways to search for evidence of recent nearby SN explosions (Haxton & Johnson, 1988; Nguyen & Johnson, 2007; Lazauskas et al., 2009)

[2] We do not include in Table 5.2 or in our subsequent considerations the long-lived state ^{210}Bi*, an excitation lying 271 keV above the ground state, which is expected to have a low production rate in all the models studied.

5.3 Searches for explosion ejecta on the Earth and Moon

The Earth and the Moon serve as natural archives that store any debris from nearby explosions that reach within 1 au from the Sun. This provides a great opportunity to bring samples of ejecta to the laboratory and analyze their content, which can be realized after finding suitable deposition sites and favorable samples by then identifying the signals within them. Live radioisotopes have the advantage of minimizing the natural background, which may render the search possible, even if the measurements remain difficult. As noted in Eqs. (5.1) - (5.3) and the surrounding discussion, the three timescales of particular interest are $\sim (3, 50, and 360)$ Mya, corresponding to the best-observed ^{60}Fe pulse, the ^{244}Pu half-life (approximately), and the end of the Devonian epoch.

5.3.1 Sensitivities to radioisotopes of interest

A challenge common to terrestrial and lunar searches is the tiny abundance of any radioisotope that one may wish to seek. The widespread ^{60}Fe detections summarized in the introduction provide a model for successful detection of an extraterrestrial species. As discussed above, the r-process components of any reasonable signal are expected to have fluences smaller than the established ^{60}Fe signal, implying that only AMS techniques may have the needed sensitivity, i.e., the capability of separating and identifying the isotopes of interest given the expected number of atoms per gram in a sample. At present, ^{60}Fe measurements can find isotope fractions with a sensitivity down to $^{60}\text{Fe/Fe} \sim (0.3 - 1) \times 10^{-16}$ (Wallner et al., 2020). However, this sensitivity may be impaired in the cases of isotopes with a significant cosmic-ray-induced background. For example, in the case of the recently reported evidence for the terrestrial deposition of ^{53}Mn, the apparent excess of the signal over the background is $^{53}\text{Mn/Mn} \sim 1.5 \times 10^{-14}$ (Korschinek et al., 2020). [3]

When a natural terrestrial background is absent or small, AMS sensitivities are often limited by the ability to remove or discriminate an interfering stable isobar with the same A and thus nearly the same mass as the species of interest; this is important for many of the r-process signals that may reside within these samples. Removal of this interference is typically performed through both chemical processing and ion identification techniques, but limitations still remain. Recent advances

[3] See also Feige et al. (2018) for a recent example of a study in deep-ocean sediments of ^{26}Al, an isotope with a significant background.

suggest that it is possible to reach $^{93}Zr/^{92}Zr \sim 6 \times 10^{-11}$ (Hain et al., 2018; Pavetich et al., 2019), though this hinges on successful removal of the stable isobar ^{93}Nb. In the case of ^{107}Pd, Korschinek et al. (1994) reported an AMS sensitivity $^{107}Pd/^{106}Pd \sim 10^{-8}$; here the interfering stable isobar is ^{107}Ag. In the case of ^{129}I there is a natural background level $^{129}I/^{127}I \sim 1.5 \times 10^{-12}$ (Ji et al., 2015b). Sensitivities down to $^{129}I/^{127}I \lesssim 10^{-14}$ are possible (Vockenhuber et al., 2015) since the interfering stable isobar ^{129}Xe is an inert gas, fortuitously, so it does not form negative ions and will not interfere. In the case of ^{135}Cs, Yin et al. (2015) were able to reduce stable isobar contamination to $^{135}Ba/^{133}Cs \sim 9 \times 10^{-12}$, and we adopt the same value for the prospective sensitivity to ^{135}Cs, namely $^{135}Cs/^{133}Cs \sim 9 \times 10^{-12}$. In the case of ^{182}Hf, Vockenhuber et al. (2004) reported a sensitivity $(^{182}Hf + ^{182}W)/^{180}Hf \sim 10^{-11}$; the ability to measure $^{182}Hf/^{180}Hf$ to this precision or better requires that techniques be developed to suppress further the stable isobar ^{182}W. In the case of ^{236}U, there are no isobaric contaminants, and the detection limits are set by the ability to discriminate the neighboring abundant uranium isotopes ^{235}U and ^{238}U. Efforts by Wilcken et al. (2008) estimate a detection limit of $^{236}U/^{238}U \sim 10^{-13}$.

In the cases of ^{237}Np, ^{244}Pu, and ^{247}Cm, there are no stable isotopes nor isobars, so searches can first focus simply on extracting the element, guarding against anthropogenic contamination, which could be orders of magnitude greater than a stellar signal (Wallner et al., 2004). In addition, these AMS samples must be "spiked" with a known quantity of shorter-lived isotopes of each species in order to calibrate the response. Both ^{236}Pu and ^{242}Pu have been used as calibration standards for ^{244}Pu (Wallner et al., 2004; Raisbeck et al., 2007; Wallner et al., 2015b). The other species have been studied less. In the case of ^{237}Np, sector-field inductively coupled plasma mass spectrometry studies have sensitivities down to a mass fraction of 10^{-15} within soil and sediment samples (Röllin et al., 2009), while systematic AMS studies suggest subfemtogram-per-sample detection limits as long as the ^{238}U content remains sufficiently low (Fifield et al., 1997; López-Lora & Chamizo, 2019). Initial AMS studies of ^{247}Cm made by Christl et al. (2014) suggest a detection limit of <0.1 femtogram in a typical sample, where limits were set by the impurities of the ^{244}Cm spike added for reference.

5.3.2 Plutonium measurements

We anchor our predictions for prospective r-process radioisotopes using the results of geological searches for ^{244}Pu in deep-ocean crusts and sediments that are displayed in Fig. 5.2 and are summarized in Table 5.2. [4] The most significant of these is the remarkable Wallner et al. (2021) study, which not only presented solid detections of astrophysical ^{244}Pu in an Fe-Mn crust from the deep Pacific, but also identified the two ^{60}Fe peaks.

Any claim of astrophysical ^{244}Pu detection must contend with anthropogenic contamination, and this is a major focus of Wallner et al. (2021). They searched not only for ^{244}Pu, which potentially contains an astrophysical signal, but also for the short-lived ^{239}Pu, ^{240}Pu, and ^{241}Pu isotopes, which measure anthropogenic contamination. All of the ^{239}Pu, ^{240}Pu and ^{241}Pu were found in the top layers of the crust, and exhibited ^{239}Pu/^{240}Pu and ^{239}Pu/^{241}Pu ratios consistent with anthropogenic fallout. This shows that some uptake has occurred in modern times. In the deeper layers corresponding to times $\mathcal{O}$(several) Mya, the ^{244}Pu/^{239}Pu ratio shows an excess over the value in the top layer. In contrast, the ^{240}Pu/^{239}Pu and ^{241}Pu/^{239}Pu ratios do not show significant variation with depth. The fact that, uniquely, ^{244}Pu exhibits an excess points to a source for this isotope distinct from anthropogenic production. There being no significant natural ^{244}Pu on Earth today, the signal must be extraterrestrial.

Wallner et al. (2021) inferred the extraterrestrial ^{244}Pu incorporation rate into the crust, after subtracting the anthropogenic ^{244}Pu contribution. An incorporation efficiency or uptake of $U_{\rm Pu} = 0.17$ is adopted, the same as that found for ^{60}Fe in the same crust. For the two layers below the top, fluxes are evaluated as follows (see also Table 5.2):

$$\Phi_{244}^{\rm interstellar}(0 - 4.76\ {\rm Myr}) = (1.67 \pm 0.35) \times 10^3\ {\rm atoms\ cm^{-2}\ Myr^{-1}}\,, \tag{5.4}$$

$$\Phi_{244}^{\rm interstellar}(0 - 9\ {\rm Myr}) = (0.98 \pm 0.18) \times 10^3\ {\rm atoms\ cm^{-2}\ Myr^{-1}}\,. \tag{5.5}$$

These fluxes will be central inputs to our study. We see that these timespans overlap with the ^{60}Fe pulses at ~ 3 and ~ 7 Myr ago. These data leave open the question of whether the flux is different in the earlier time bin versus the overall average; the reported difference of about 1.8σ is

[4] We also note that also Hoffman et al. (1971) reported a signal in Precambrian bastnäsite, but this claim was not confirmed subsequently by Lachner et al. (2012)

not decisive.

Other important ^{244}Pu measurements have been reported previously. An upper limit of $\Phi_{244}^{\text{interstellar}} < 2 \times 10^5$ atoms cm^{-2} Myr^{-1} on the rate of extraterrestrial deposition in young sediment was set by Paul et al. (2001). Subsequently, AMS measurements of crust VA13-2 by Wallner et al. (2004) and of sediment MD90-0940 by Raisbeck et al. (2007) each yielded one event, dated to $1 - 14$ Mya and $2.4 - 2.7$ Mya, respectively. Raisbeck et al. (2007) did not attribute their single event to a signal, but derived upper limits on the fluence assuming one count in each of three time bins. We follow this practice, noting that the flux inferred from the nonzero bin would vastly exceed the other limits and detections overlapping this time period. More recently, a search for ^{244}Pu by Wallner et al. (2015b) yielded a possible signal in three samples corresponding to three different epochs: sediments spanning $0.53 - 2.17$ Mya, and crust layers at $5 - 12$ Mya and $12 - 25$ Mya. In each of these samples, at most only a single ^{244}Pu count was found in each time bin, so these results must be treated with great caution.

The detections reported in Fig. 5.2 and Table 5.2 show that extraterrestrial ^{244}Pu deposition has occurred over at least over the last 9 Myr and possibly goes back to as far as 25 Myr. Taking the measurements at face value, it would seem that the ^{244}Pu flux history differs from the two ^{60}Fe pulses, which are each limited in time (though a small ^{60}Fe continues to the present). That is, the wide time ranges of the Wallner et al. (2021) detections both overlap with the ^{60}Fe pulses, but earlier indications of ^{244}Pu flux extend from nearly the present back to at least 12 to 25 Mya. Within the large uncertainties, it is unclear if the flux varies over this time. The data could accommodate–but within uncertainties do not demand–a larger flux around the time of the ^{60}Fe pulse(s) at ~ 3 Mya (and ~ 7 Mya). The possible difference between the ^{60}Fe and ^{244}Pu deposition histories suggests a different origin for at least some of the ^{244}Pu, a point also made in previous studies, e.g., Wallner et al. (2015b).

5.4 Modeling r-process production in SNe and KNe

We can link the observed ^{244}Pu flux with that of other r-process radioisotopes through theoretical calculations of r-process nucleosynthesis. These calculations depend on the nature of the candidate nucleosynthesis event, and on the nuclear inputs one adopts. The results are constrained by the

observed r-process pattern in solar system material and in stars. Here we describe our calculations and their uncertainties.

The production ratios of radioactive isotopes resulting from an r-process event can be estimated by the extraction and post-processing of ejected matter trajectories from astrophysical simulations of the event. The trajectories contain the time history of $(\rho, T, and Y_e)$, where ρ is the density, T is the temperature, and the electron fraction $Y_e = n_e/n_B = \langle Z/A \rangle$ measures the neutron richness $Y_n = 1 - Y_e = \langle N/A \rangle$. The evolution of the nuclear material along this trajectory is then calculated using a network of the relevant nuclear reactions. This procedure brings with it significant challenges, starting from the identification and characterization of the appropriate nucleosynthesis sites within the candidate event.

SNe were the first type of event suggested for r-process production (Burbidge et al., 1957), and for many decades the core-collapse SN neutrino-driven wind was considered the leading candidate site. However, modern simulations show that the neutrino-driven wind is unlikely to be sufficiently neutron-rich to synthesize the actinides (Fischer et al., 2010; Hüdepohl et al., 2010; Arcones & Thielemann, 2013), though it may produce $A \sim$ 80-100 species through a weak r-process (Bliss et al., 2018) or a νp-process (Fröhlich et al., 2006). The ultimate extent of nucleosynthesis in this environment depends on neutrino physics that is not fully understood (Balantekin & Yüksel, 2005; Duan et al., 2011; Johns et al., 2020; Xiong et al., 2020). Rare types of core-collapse events may also generate neutron-rich outflows, with promising candidates including magneto-rotational (MHD) SNe (Winteler et al., 2012; Mösta et al., 2018; Reichert et al., 2021) and collapsars (Pruet et al., 2003; Surman et al., 2006; Fujimoto et al., 2008; Siegel et al., 2019).

Studies of galactic chemical evolution suggest that, whilst collapsars might have been important early in the history of the universe during the epoch of Population III stars, they were less relevant during the epochs of interest for this study. For this reason, and given the uncertainty in how robust collapsar r-process calculations might be (Miller et al., 2020), we do not consider them further in this chapter. [5]

While neutron star mergers have recently been confirmed to produce r-process elements (Cowperthwaite et al., 2017; Kasen et al., 2017; Abbott et al., 2017a,c), exactly how, where, and how

[5] We note the suggestion that core-collapse SNe driven by the quark-hadron transition might also be rare r-process sites (Fischer et al., 2020), but also do not discuss this possibility here.

much have yet to be definitively worked out (see reviews in Cowan et al., 1991; Arnould et al., 2007; Kajino et al., 2019; Cowan et al., 2021, and references therein). Possible nucleosynthetic environments within a merger include the prompt ejecta—cold, very neutron-rich tidal tails and/or shock-heated ejecta from the neutron star contact interface (Bauswein et al., 2013; Hotokezaka et al., 2013; Rosswog et al., 2013; Endrizzi et al., 2016; Lehner et al., 2016; Sekiguchi et al., 2016; Rosswog et al., 2017)—and magnetic, viscous, and/or neutrino-driven outflows from the resulting accretion disk (Chen & Beloborodov, 2007; Surman et al., 2008; Dessart et al., 2009; Perego et al., 2014; Wanajo et al., 2014; Just et al., 2015; Martin et al., 2015; Siegel & Metzger, 2018). The composition and relative contributions of each type of mass ejection depend on quantities such as the physical parameters of the merging system and the still unknown microphysics of dense matter and its neutrino emission (see, e.g., Caballero et al., 2012; Foucart et al., 2015; Malkus et al., 2016; Kyutoku et al., 2018).

In view of the large astrophysical uncertainties in each candidate r-process site, our calculations of isotopic yields rely on illustrative models that indicate the ranges of possibilities. We choose matter trajectories from modern simulations that capture the rough characteristics (Y_e, entropy s/k, and dynamical timescale τ) expected for each site. Different combinations of (Y_e, s/k, and τ) lead to distinct nucleosynthetic pathways through the neutron-rich side of the nuclear chart, leading to different amounts of individual isotopes even when the final elemental yields are similar. We choose at least two distinct trajectories for each type of event so as to ensure production of both main ($A > 120$) and weak ($70 < A < 120$) r-process nuclei.

We adopt four illustrative r-process model combinations, using trajectories from a *forced* modification of a conventional SN neutrino-driven wind scenario (SA), an MHD SN model (SB), and two neutron star merger disk and dynamical ejecta combinations (KA and KB). We then combine and scale the resulting abundances to the elemental patterns of select r-process-enhanced stars. We scale to individual metal-poor stars rather than, e.g., the solar abundances, since these stars have experienced fewer generations of stellar nucleosynthesis and thus are cleaner representations of the yields from single r-process events. We choose one of the few stars for which elements in all three r-process peaks have been detected (Roederer & Lawler, 2012), and J0954+5246, the star with the largest enhancement in actinide elements ever detected (Holmbeck et al., 2018). We use a variety of r-process species measured in the above-discussed metal-poor stars to normalize our estimates,

including ytterbium, tellurium, cadmium and zirconium, and note the mixing fraction(s) f of the total mass(es) of the weak r-process trajectory (trajectories) relative to the most neutron-rich r-process trajectory that appears in the combined model fit. The total mass of the r-process ejecta for each model is normalized to unity. The details of each model combination and constraint are described below and summarized in Table 5.3.

Our nucleosynthesis calculations are made with the nuclear reaction network code Portable Routines for Integrated nucleoSynthesis Modeling (PRISM; Mumpower et al. (2018); Sprouse et al. (2021)), implemented as in Wang et al. (2020b) for the baseline calculation. We note that isotopic ratio estimates are shaped in addition by the nuclear physics properties of the thousands of exotic nuclei that participate in an r-process. Thus for each model we explore variations in the nuclear inputs for quantities for which experimental values are unavailable (masses from Goriely et al. (2009) (HFB), or β-decay rates from Marketin et al. (2016) (MKT) for both SN and KN models, and fission yields from Kodama & Takahashi (1975) for KN models), as in Wang et al. (2020a). Additionally, because of the general limitation of the network code for time step evolution at times $\gtrsim$ Myr, which results in large time steps comparable to the half-lives of the radioisotopes of interest in this work such as ^{93}Zr, we use PRISM to generate r-process abundance yields until 1 kyr for ^{182}Hf and lighter radioisotopes, and until 1 Myr for actinides (except for ^{248}Cm and ^{245}Cm, for which we run until 0.1 Myr), and then switch to a pure radioactive decay calculation for these radioisotopes. These calculations provide the relative abundance yields for the radioisotopes.

As commented above, the SN neutrino-driven wind scenario has fallen out of favor as a primary r-process site because modern simulations do not show that sufficiently neutron-rich conditions to reproduce the solar r-process pattern (Fischer et al., 2010; Hüdepohl et al., 2010; Arcones & Thielemann, 2013). Indeed, no actinides are produced at all. We are however motivated by the intriguing possibility of coincident identifications of ^{60}Fe and ^{244}Pu to consider here a *forced* neutrino-driven wind scenario, denoted in Table 5.3 by "$\nu\star$". We start with the neutrino-driven wind simulations of Arcones et al. (2007); Arcones & Janka (2011) and modify the initial Y_e in order to produce different r-process yields. The upper panel of Fig. 5.3 shows the final abundance pattern results at $t \sim 10$ Gyr for four values of $Y_e = 0.31$ (blue), 0.35 (yellow), 0.42 (green), and 0.48 (pink). We have found that results for $Y_e \leq 0.31$, following different trajectories, and using different nuclear networks, make qualitatively similar predictions for substantial production of isotopes with atomic

numbers $A \gtrsim 130$, up to and including the actinides. On the other hand, simulations with $Y_e \geq 0.38$ yield much less production of isotopes with $A \gtrsim 130$, as exemplified by the results shown in green and pink. The results shown in red are for a mixture (model SA) of the simulations for SN *forced* neutrino-driven wind with four different values of Y_e (see Table 5.3), whose relative normalizations are scaled to fit data on the abundances of ytterbium, tellurium, cadmium, and zirconium in the metal-poor star HD 160617 (Roederer & Lawler, 2012). The range of Y_e in the SA model is similar to that of the SN model with actinide production in Goriely & Janka (2016). These and other abundances are shown in gray in the upper panel of Fig. 5.3, and we see in the lower panel of Fig. 5.3 that model SA also matches the solar abundance data very well.

Fig. 5.4 shows analogous results using the Mösta et al. (2018) MHD SN model. In the upper panel, we show the abundance predictions of two trajectories (blue for the main r-process trajectory and green for the light r-process trajectory) and a combination (SB, red) fitted to the abundances of ytterbium and zirconium measured in the metal-poor star HD 160617 (Roederer & Lawler, 2012) (see Table 5.3). These and other abundances are shown in gray in the upper panel of Fig. 5.4, and we see in the lower panel of Fig. 5.4 that this mixture of simulations also matches the solar abundance data quite well in general, though it overestimates the structure seen in the solar data for $A \sim 130$, and falls off more rapidly for $A \gtrsim 190$. Indeed, almost all modern SN models struggle to produce actinides, displaying higher production of lighter r-process species relative to plutonium as described in the next section.

The upper panel of Fig. 5.5 shows results from representative simulations of the abundances of nuclei produced by the r-process (at $t \sim 10$ Gyr) in KN dynamical ejecta based on the work of Bovard et al. (2017) (blue), and in KN disk neutrino-driven wind based on the work of Just et al. (2015) (green). Also shown is a combination of these simulations (KA, red) fitted to the abundances of ytterbium and zirconium in the metal-poor star HD 160617 (Roederer & Lawler, 2012) (see Table 5.3). These and other abundances are shown in gray in the upper panel of Fig. 5.5, and we see in the lower panel of Fig. 5.5 that the KA model also matches the solar abundance data quite well, though with some deviations for $A \sim 140$.

As compared with Figure. 5.5, Figure. 5.6 shows analogous results obtained using the KN dynamical model with a relatively more neutron-rich trajectory from Bovard et al. (2017) (blue), and the disk neutrino-driven wind model of Just et al. (2015). Also shown are the predictions of

a combination (KB, red) fitted to the abundances of ytterbium and zirconium measured in the actinide-boost star J0954+5346 (Holmbeck et al., 2018). These and other abundances are shown in gray in the upper panel of Fig. 5.6, and we see in the lower panel of Fig. 5.6 that this combination model also matches the solar abundance data quite well in general, though with some deviations from the solar data for $A \sim 120$ and $A \sim 135$. The KA and KB models both exhibit robust production of actinides that subsequently fission, so fission yields play important roles in shaping the second peak in these models (Eichler et al., 2015; Giuliani et al., 2020; Vassh et al., 2019, 2020). The fission yields of most neutron-rich actinides have not been experimentally determined, so in addition to the simple symmetric-split fission yields adopted in the baseline calculation, we also implement the wide-Gaussian fission yields from Kodama & Takahashi (1975) to estimate the uncertainty range. We find that the fission yields from Kodama & Takahashi (1975) would bring a small boost to the left and right sides of the second peak ($A \sim 120$ and $A \sim 133$) for the KA model, while leaving the yields of the interesting r-process radioisotopes listed in Table 5.5 largely unchanged. For the KB model with boosted actinide production, fission deposition could potentially fill the gap around $A \sim 120$ and lower the bump around $A \sim 133$ to bring the abundance pattern closer to the solar pattern, thus resulting in a smaller ^{135}Cs yield. In a more extreme example of a wider distribution of fission fragments, the neutron star merger nucleosynthesis calculations in Shibagaki et al. (2016) exhibit a fission-recycling r-process pattern without a second peak, which could bring even smaller abundance yields of ^{129}I and ^{135}Cs. Additionally, spallation reactions that can occur when fast neutron star merger ejecta interact with the ISM may also affect the abundances of the radioisotopes located around r-process peaks (Wang et al., 2020a). These details do not influence the overall conclusion, however, that the KN models are predicted to produce actinides robustly, leading to lower ratios of lighter r-process species relative to plutonium, as described in the next section.

5.5 r-process radioisotope ratios and time evolution

We have already seen in Figs. 5.3, 5.4, 5.5, and 5.6 that the abundances of different r-process radioisotopes depend sensitively on the model of the SN or KN that is adopted. The same holds for actinide isotopes, even when attention is focused on hybrid models whose parameters are adjusted to yield ratios of the radioisotopes with $A \lesssim 200$ that are similar to those measured for

the metal-poor star HD 160617 or the actinide-boost star J0954+5346. Tables 5.4, 5.5, 5.6 and 5.7 show the production ratios for the r-process isotopes of interest after 10^5 yr (i.e., after the decays of short-lived isotopes), 3 Myr (as in eq. 5.1, corresponding to the ^{60}Fe detection from near the end of the Pliocene era: the ratios after 7 Myr corresponding to the other ^{60}Fe pulse reported in Wallner et al. (2021) are similar), 50 Myr (as in eq. 5.2, comparable with the half-life of ^{244}Pu), and 360 Myr (eq. 5.3; the time since the end-Devonian mass extinction(s)), respectively, as discussed in Section 5.1. These have been calculated from the SN and KN models studied in the previous Section 5.4, and are expressed as the abundance ratios relative to ^{244}Pu. Included for information are the production ratios for several r-process isotopes with half-lives > 500 Myr, namely ^{232}Th, ^{235}U, and ^{238}U. However, in view of the backgrounds from astrophysical processes before the formation of the solar system, we do not consider further these isotopes.

Also, we note that SNe in general produce ^{60}Fe by other nuclear mechanisms in addition to the r-process, such as by explosive burning, where the yield is expected to exceed greatly any possible r-process contribution, so the ^{60}Fe/^{244}Pu ratios for SN models SA and SB in these and subsequent tables are in general underestimates and could be viewed as lower limits on the actual ratio. If the ratio of the ^{60}Fe synthesized through the r-process to the total ^{60}Fe produced in a SN is $\sim f(^{60}\mathrm{Fe}, r)$, then the ^{60}Fe/^{244}Pu ratio for the SN model is boosted to $Y(^{60}\mathrm{Fe})/(f(^{60}\mathrm{Fe}, r)Y(^{244}\mathrm{Pu}))$. Additionally, our SN models provide the estimates per r-process event $Y_i(\mathrm{SN, r})$, implicitly assuming that all SNe are similar r-process sites. As only a small fraction of SNe may be r-process sites, we may account for SN heterogeneity by assuming, in the crudest picture, that the the r-process occurs in only a fraction $f_{\mathrm{SN,r}}$ of SNe. In this case, the probability that a given SN will eject r-process material is $f_{\mathrm{SN,r}}$, implying that, for the r-process yield per SN event, $Y_i(\mathrm{SN})$ must be lower, i.e., $Y_i(\mathrm{SN}) = f_{\mathrm{SN,r}} Y_i(\mathrm{SN, r})$.

Fig. 5.7 displays the subsequent time evolution of several radionuclides of interest (^{60}Fe, ^{93}Zr, ^{107}Pd, ^{129}I, ^{135}Cs, ^{182}Hf, ^{244}Pu and ^{247}Cm) from an r-process event only as calculated using the SN and KN models discussed in the previous section. The solid lines are obtained using our baseline r-process calculation, and the shaded bands are the ranges that result from the nuclear data variations described in Section 5.4. Also shown as vertical lines are the three timescales of interest, namely the age of the well-attested SN explosion ~ 3 Mya, an age of 50 Mya comparable with the half-life of ^{244}Pu, and the age of the end-Devonian extinction(s) ~ 360 Mya. We see that there are

substantial differences between the abundances of the radioisotopes calculated in different models. We note that the relative production rates of light (second peak and lighter) and heavy (third peak and higher) r-process nuclei depend strongly on the astrophysical conditions of the r-process sites. On the other hand, the relative ratios of the actinides themselves are largely insensitive to the site and thus have less discriminating power. The uncertainties in the relative yields of the actinides are dominated by large nuclear physics uncertainties in this region, so their yields depend sensitively on the choice of nuclear data adopted (as seen in Figure 5.7). Therefore measurements of radioisotope ratios, especially the ratios of light r-process nuclei to actinides, could provide useful diagnostic tools for the nature of any astrophysical explosion that occurred near Earth within the last few hundred million years.

As we have already discussed, measurements of terrestrial ^{60}Fe deposits indicate that at least one such explosion took place within $\sim$ 100 pc of Earth about 3 Mya, and there has also been deposition of ^{244}Pu on Earth that may extend back to 25 Mya. The presence of ^{244}Pu indicates that there has been at least one active r-process site close to Earth within the past 80 Myr or so. In the following, we treat the ^{244}Pu abundance as our reference, and predict the relative abundances of other r-process radioisotopes under different hypotheses about the nature of the site(s) and its (their) timing.

For this purpose, we follow the evolution of interesting radioisotopes over $\sim$ Gyr, using the calculations of the previous section as starting points and taking account of the possible production of the radioisotopes via the decays of heavier isotopes as well as their own decays. The left panels of Fig. 5.8 illustrate the abundances of the radioisotopes of principal interest, while the right panels show the ratios to ^{244}Pu. The upper panels show the results calculated in SN model SA, and the lower panels show the results in model SB. Most of the radioisotopes exhibit simple decay curves, but the effects of feedthrough from the decays of heavier isotopes are visible in ^{244}Pu, which is made in α-decays of ^{248}Cm, and in ^{236}U, which is a decay product of ^{244}Pu. We have included the r-process production of ^{60}Fe in these plots, although the r-process is not expected to dominate its production, at least in core-collapse SNe. Hence the ^{60}Fe curves should be regarded as (very) conservative lower bounds on the ^{60}Fe yields and ratios to ^{244}Pu production.

The vertical lines in Fig. 5.8 are at 3 Myr, corresponding to the time since the event that gave rise to the well-attested deep-ocean ^{60}Fe deposition; 50 Myr comparable with the half-life of ^{244}Pu; and

360 Myr, corresponding to the time since the end-Devonian extinction(s). The observation of ^{244}Pu signals overlapping the ^{60}Fe signals from 3 Mya and 7 Mya suggests that all radioisotopes with yields $Y \gtrsim Y(^{244}\mathrm{Pu})$ would be interesting targets for searches in the layers containing the ^{60}Fe signals. Depending on the model, these may include ^{93}Zr, ^{107}Pd, ^{129}I, ^{135}Cs, ^{182}Hf, ^{236}U, ^{237}Np and ^{244}Pu, and the abundance of ^{247}Cm may not be much smaller than that of ^{244}Pu, as seen in the right panels of Fig. 5.8 and in Table 5.5. The ratios ^{93}Zr/^{244}Pu, ^{107}Pd/^{244}Pu, ^{129}I/^{244}Pu, ^{135}Cs/^{244}Pu, and ^{182}Hf/^{244}Pu could be particularly useful for discriminating between models, followed by ^{236}U/^{244}Pu and ^{237}Np/^{244}Pu.

However, only a fraction of the reported ^{244}Pu may have been generated by the events producing the ^{60}Fe deposition peaks, with the remainder being due to one or more earlier astrophysical events. In this case it is natural to compare abundances on a time-scale of ~ 50 Myr, which is comparable with the half-life of ^{244}Pu, corresponding to the central vertical lines in the right panels of Fig. 5.8. On this time scale, as seen in this figure and in Table 5.6, the most interesting remaining isotopes are ^{107}Pd, ^{129}I, ^{182}Hf, ^{236}U, and ^{244}Pu, with the first three providing the greatest discriminating power, albeit with similar nuclear model uncertainties to those discussed above (not shown).

Finally, after 360 Myr, corresponding to the age of the end-Devonian mass extinctions, the ^{244}Pu abundance would have decreased by an order of magnitude, relatively few radioisotopes would have survived, and only uranium isotopes, ^{232}Th, and ^{129}I might have abundances comparable to that of ^{244}Pu, as seen in Table 5.7. Measurements of ^{129}I should be able to distinguish between SN models, but not other radioisotopes.

The results of analogous calculations for the KN models KA and KB are shown in the upper and lower panels of Fig. 5.9, respectively, with yields Y in the left panels and the ratios $Y/Y(^{244}\mathrm{Pu})$ in the right panels. As seen in this figure and in Table 5.5, the radioisotopes ^{93}Zr, ^{107}Pd, ^{129}I, ^{135}Cs, ^{182}Hf, ^{236}U, ^{237}Np, ^{244}Pu, and ^{247}Cm are again the most promising potential signatures after 3 Myr or 7 Myr, with ^{93}Zr, ^{107}Pd, ^{129}I and ^{182}Hf offering the greatest discriminating power between KN models, and also between them and the SNS models. After 50 Myr, as seen in Table 5.6, the most promising radioisotopes for detection are ^{129}I and ^{236}U. However, ^{236}U offers little discriminating power between the different KN models, nor between the SN and KN models. After 360 Myr, as also seen in Fig. 5.9 and in Table 5.7, the best prospects for detection are again offered by ^{236}U, which does not discriminate among the KN and SN models. We do not consider ^{232}Th and ^{238}U to

be promising search targets, in view of their long half-lives and the consequent large backgrounds from events before the formation of the solar system.

We recall that there are considerable variations in the isotope ratios calculated using the different nuclear models. In making comparisons, we have used the β-decay rates from Marketin et al. (2016), and the HFB model from Goriely et al. (2011), which assumes different nuclear masses, in addition to the baseline calculation. We note in brackets in Table 5.5 the ranges of isotope ratios σ found in all the models SA, SB, KA and KB. [6] The ranges of predictions that come from the nuclear model variations show some overlap between the four models. We also show the ranges due to nuclear data variations in the abundance ratios of the radioisotopes ^{60}Fe, ^{129}I, and ^{247}Cm to ^{244}Pu as shaded bands in the right panels of Fig. 5.8 and Fig. 5.9, to illustrate the uncertainty evolution for the ratios of light elements and actinides to ^{244}Pu. The absolute abundances of ^{129}I and lighter isotopes are relatively insensitive to the nuclear model used as shown in Fig. 5.7, so the uncertainties in their ratios to ^{244}Pu are largely due to those in the ^{244}Pu yield, and hence correlated. While the abundances of isotopes heavier than ^{236}U are sensitive to the nuclear variations, they have similar uncertainty trends; thus their abundances relative to that of ^{244}Pu vary over smaller uncertainty ranges, as quoted in Table 5.5.

The results of our calculations of interesting abundances after 100 kyr, 3 Myr and 7 Myr (also after 50 Myr for the KN models) for the different astrophysical r-process models described in Table 5.3 are summarized in Fig. 5.10, which shows scatterplots of the isotope abundance ratios of ^{93}Zr, ^{107}Pd, ^{129}I, ^{135}Cs,^{182}Hf, and ^{247}Cm over ^{244}Pu versus ^{60}Fe/^{244}Pu.The asymmetric uncertainty bars reflect the ranges of microphysics uncertainties shown in Table 5.5 and discussed above. Note that these ratios reflect the output purely of the r-process alone. In the case of a SN there can be additional synthesis of some of these species, and if there is mixing with multiple events this would also change the ratios.

Figure 5.10 shows that the ratios of all these isotopes relative to ^{244}Pu are highest in the SB SN model. However, the ordering of the abundance ratios of the other isotopes in the different models is not universal, with model SA being the lowest for ^{236}U/^{244}Pu and ^{247}Cm, and KB being the lowest for ^{93}Zr, ^{107}Pd, ^{129}I and ^{182}Hf/^{244}Pu. These and other differences between the model predictions

[6] There are similar uncertainties in the abundance ratios after $\sim$ 1 Myr, which are omitted for clarity in the corresponding tables.

offer prospects for distinguishing between the different r-process models by measurements in deposits up to 50 Myr old.

We emphasize that the predicted ratios in Table 5.3 and Fig. 5.10 are for r-process production only. For the KN models, this should be indicative of the typical ejected yields for these explosions. On the other hand, for the SN models there will be additional production of some species due to other processes, as summarized in Table 5.2. For example, ^{60}Fe production in hydrostatic and explosive burning will far exceed that made in any SN r-process, and ^{93}Zr, ^{107}Pd, ^{135}Cs, and ^{182}Hf could be also produced by an s-process in an earlier stage of stellar evolution and ejected in the SN event. Thus for these species the ratios to ^{244}Pu in the SN models should be viewed as *lower limits*. Even so, they retain their discriminatory power, particularly the ^{60}Fe/^{244}Pu ratio.

The vertical shaded band in Fig. 5.10 shows the the isotope ratios of ^{60}Fe/^{244}Pu measured at 3 Myr (1.34-4.57 Myr; dark gray) and 7 Myr (4.57-9.0 Myr; gray) time periods from Wallner et al. (2021). We see that, as discussed in Section 5.6.1, comparing this measurement to the ^{60}Fe/^{244}Pu ratios from our calculations excludes the KN models as the sole source of both isotopes. This is consistent with Fry et al. (2015), which excluded KNe as the source of the 3 Myr ^{60}Fe pulse.

To lend support to our conclusions, we compare our radioisotope ratios to those from Goriely & Janka (2016) and Côté et al. (2021). Our SA model's ^{247}Cm/^{244}Pu ratios at 1 Myr are consistent with the SN neutrino-driven wind calculations presented in Goriely & Janka (2016). We find our SB, KA, and KB model ratios to be largely consistent with the radioisotope abundances from the data sets for the analogous simulations reported in Côté et al. (2021) at 1 Myr, i.e., our combined KN models' radioisotope ratios are well within the uncertainty ranges of those data sets. The one notable difference is in the actinide abundances resulting from the adopted MHD SN models. The MHD SN model from Côté et al. (2021) shows more robust actinide production than our SB model, resulting in somewhat lower ratios to ^{244}Pu, while our SB model ratios are more consistent with recent simulation results from Reichert et al. (2021). Current MHD SN models exhibit conditions that only marginally reach the actinides, which results in a large astrophysical uncertainty in the ^{244}Pu yield and a distinct contrast to the KN models.

In order to make predictions for measurements of radioisotopes like ^{244}Pu we need, in addition to their abundances $Y_i(t)$ obtained from the network calculation, estimates of the total r-process yields or ejected masses $M_{\rm ej}$ from our SN and KN models, from which we can obtain the absolute yields

for the radioisotopes i at time t, namely $M_i(t) = M_{\rm ej} \times A_i Y_i(t)$. The nucleosynthetic outcome of our SA model is similar to that of the 2.2 $M_\odot$ neutrino-driven wind model from Wanajo (2013), where a total yield of $1.37 \times 10^{-5} M_\odot$ is reported; estimates of the mass ejected in SN neutrino-driven winds vary from $1 \times 10^{-5} M_\odot$ to $5 \times 10^{-4} M_\odot$ (see, e.g., Wanajo et al., 2001; Argast et al., 2004). The yield from the MHD SN simulation we adopt for our SB model is $\sim 0.03 M_\odot$ (Mösta et al., 2018), while a wide range of MHD SN yields are found in the literature, from $6.72 \times 10^{-3} M_\odot$ in Winteler et al. (2012) to $\sim 0.389 M_\odot$ in Reichert et al. (2021). For the KN models, the yield from our chosen Bovard et al. (2017) dynamical ejecta simulation is about $3.53 \times 10^{-3} M_\odot$, which is roughly consistent with the yield in, e.g., Radice et al. (2018) of $\sim 2 \times 10^{-3} M_\odot$. The disk wind yields from Just et al. (2015) range from $\sim 7 \times 10^{-3}$ to $6.68 \times 10^{-2} M_\odot$, similar to the range found in, e.g., Fernández et al. (2015), of ~ 0.03 to $0.22 M_\odot$. For our KB model, the disk and dynamical ejecta masses are similar, giving a total yield of $7 \times 10^{-3} M_\odot$, while for our KA model the disk wind mass is roughly four times that of the dynamical ejecta for a total yield of $1.7 \times 10^{-2} M_\odot$. The theoretical estimates quoted above give ranges for r-process yields of $\sim 5 \times 10^{-3} M_\odot - 0.1 M_\odot$, consistent with the values suggested by the observations of GW170817 (Côté et al., 2018).

Following this survey of r-process radioisotope production in SNe and KNe, we now turn to the prospects for searches in deep-ocean deposits and in the lunar regolith.

5.6 Models for eeep-ocean r-process radioisotopes from stellar explosions

We now have the tools in place to interpret the deep-ocean ^{244}Pu (and ^{60}Fe) in light of our SN and KN models.

5.6.1 ^{244}Pu radioactivity distance constraints on an event 3 Myr ago

We first consider the possibility that the ^{244}Pu flux coincident with the ^{60}Fe pulse ~ 3 Mya is due to the same event. Thus, any ^{244}Pu flux outside of this timespan must come from another process, such as that explored in the following section. We also assume that the radioisotope delivery is a *one-step* process, i.e., the terrestrial and lunar deposition of these species is a direct consequence of the propagation of the explosion ejecta.

Consider an explosion at distance r and time t in the past. If the explosion is isotropic, the

time-integrated flux, i.e., the fluence, of radioisotope i at the Sun's interstellar location is

$$\mathcal{F}_i^{\rm interstellar} = f_i \, \frac{M_{{\rm ej},i}/A_i m_u}{4\pi r^2} \, e^{-t/\tau_i} \,, \tag{5.6}$$

where the radioactive decay factor includes all decay in the interval t between the explosion and the present time t, i.e., including both travel time and the duration since arrival. Here the isotope's mass number is A_i, its mean life is τ_i, and $m_u \approx m_p$ is the atomic mass unit. Also $M_{{\rm ej},i}$ is the yield at the time of the explosion, i.e., the total mass of isotope i ejected, the total mass of isotopes ejected at explosion time is $M_{\rm ej} = \sum_i M_{\rm ej,i}$, and $f_i \leq 1$ is the fraction of atoms of i that are incorporated into dust particles that arrive at Earth (Benítez et al., 2002; Athanassiadou & Fields, 2011; Fry et al., 2016).

After fallout onto the Earth and accumulation into natural archives such as deep-ocean sediments and crusts, the present-day surface density is (Ellis et al., 1996; Fry et al., 2015)

$$N_i = \frac{U_i \mathcal{F}_i}{4} = U_i f_i \, \frac{M_{{\rm ej},i}/A_i m_u}{16\pi r^2} \, e^{-t/\tau_i} \,, \tag{5.7}$$

where the factor of 4 accounts for the ratio of the Earth's cross section to its surface area and we have included a decay factor. Here the uptake factor U_i measures the fraction of incident atoms of i that are incorporated into the sample. Fry et al. (2016) note that the fallout will not be uniform over the Earth, favoring midlatitudes at the expense of the poles and equator. Thus the effective uptake can be different at different sites for this reason alone, in addition to variations in geological conditions.

We can infer the ^{244}Pu yield for a given explosion distance within this picture. We focus here on the time interval ~ 3 Mya that contains the better-measured ^{60}Fe pulse, whose duration is at least equal to that of the nonzero ^{60}Fe signal seen in sediments, $\Delta t = 1.6$ Myr. Integrating the ^{244}Pu flux from eq. (5.4) over this time, we find an interstellar ^{244}Pu fluence $\mathcal{F}_{244}^{\rm interstellar} = 2670 \pm 560$ atoms cm^{-2}. Using this and the ^{244}Pu mass yields $M_{\rm ej,244}$ calculated within the SN and KN models, we can invert eq. (5.6) to infer the explosion distance:

$$D_{\rm rad}(^{244}{\rm Pu}) = \sqrt{f_{\rm dust} \frac{M_{\rm ej,244}/244 m_{\rm u}}{4\pi \mathcal{F}_{244}^{\rm interstellar}}} \; e^{t_{\rm exp}/2\tau_{244}} \,. \tag{5.8}$$

This "radioactivity distance" is the analog of a standard luminosity distance, with the yield playing the role of luminosity, and the fluence playing the role of flux (Ellis et al., 1996; Fry et al., 2015).

Figure 5.11 shows the radioactivity distance for our four r-process models, assuming that most of the ^{244}Pu is incorporated into dust, $f_{\rm dust}^{\rm Pu} \simeq 1$. We see that the central value of the distance estimate in the MHD model SB is ~ 100 pc, with an uncertainty of about an order of magnitude in either direction. The *forced* neutrino-driven wind model SA has somewhat larger yields and thus requires larger distances, but within uncertainties the distance range overlaps with the MHD model.

These ^{244}Pu-based distances are quite consistent with the explosion distance inferred (Fields et al., 2005; Fry et al., 2015; Breitschwerdt et al., 2016) for an SN that could have generated the well-established ^{60}Fe pulse ~ 3 Mya. This range, $D_{\rm rad}(^{60}{\rm Fe}) = 20 - 150$ pc, is represented by the yellow band in Fig. 5.11. Within the uncertainties, this distance estimate is also compatible with the distances to the Tucana-Horologium and Scorpius-Centaurus stellar associations, which have been proposed as possible locations of the SN that generated the ^{60}Fe pulse (Benítez et al., 2002; Breitschwerdt et al., 2012; Mamajek, 2015). Note that these results assume $f_{\rm dust}^{\rm Pu} \simeq 1$. Smaller distances would follow if a smaller value for dust efficiency is adopted; within the large yield uncertainties, these SN models remain consistent with ^{60}Fe for dust efficiency values down to $f_{\rm dust} \sim 0.01$.

Thus we see that the ^{244}Pu signal overlapping with the 3 Myr ^{60}Fe pulse can be explained by an SN explosion, but only one that is r-process-enhanced. As seen in Fig. 5.11, such an event can give consistent distance estimates or equivalently a consistent ^{60}Fe/^{244}Pu ratio. We also see that these distances lie between the "kill" radius $r_{\rm kill} \sim 10$ pc and the distance at which the remnant would fade away, $r_{\rm fade} \sim 160$ pc, which provide lower and upper bounds on the distance to a nearby SN event whose radioisotope signal would be detectable. We note that the earlier ^{60}Fe pulse at ~ 7 Myr has similar but somewhat smaller fluence, and so would give a similar but somewhat smaller radioactive distance range. This too could also in principle be explained by an SN, but must again have been an r-process-enhanced event. However, such events are at best atypical of SN explosions and, as we have noted, in most modern SN models there is *no actinide production at all*. It is, therefore, particularly unlikely to have two such events in close succession. We will return to this point in the next section.

We now turn to the possibility of a KN as the source of ^{244}Pu 3 Mya. The yields for our KA and

KB models are ~ 6 orders of magnitude larger than those in the SN models. As a result, Fig. 5.11 shows that they correspond to much larger radioactivity distances $\gg 1$ kpc. This would place the explosions implausibly far for any ejecta to reach the Earth. Indeed, the upper range of the distances extends beyond the size of our Galactic disk. Moreover, as seen in Fig. 5.10, the ^{60}Fe/^{244}Pu ratio for the KN models sharply disagrees with the data. This suggests a different scenario is needed for the KN case, to which we now turn.

5.6.2 ^{244}Pu *constraints on a KN enrichment of the Local Bubble*

As discussed above, the seemingly straightforward association of the ^{244}Pu signals with the ^{60}Fe pulses would require two consecutive rare, r-process-enhanced SN events. This coincidence seems unlikely, particularly because we know of no reason that r-process-enhanced SNe would occur in pairs or be clustered. Lacking such a reason, the two events are independently rare and thus their occurrence in close succession is exceedingly improbable. Moreover, we have seen that the ^{244}Pu data favor a persistent flux that may extend back to as early as 25 Mya, not necessarily an impulsive signal as seen in ^{60}Fe. This leads us to consider an r-process event that occurred earlier than the ^{60}Fe SNe, with a KN explosion being an obvious candidate. We have also seen above that a KN scenario requires that the ^{244}Pu was not injected directly and impulsively from a single event, but instead suggests that some form of dilution occurred between the explosion and injection in the solar system.

The requirements of early r-process creation and subsequent dilution are both met naturally if a KN exploded prior to or during the early formation of the Local Bubble, enriching the entire star-forming cloud that gave rise to the bubble. Indeed, Wallner et al. (2015b) have proposed such a scenario, and here we build on their analysis.

We thus envision a *two-step* process in which (1) the KN ejecta propagate to and mix into the proto-Local Bubble, followed by (2) the relative motion of the Earth and r-process-enriched dust leading to a flux of r-process radioisotopes onto Earth. Specifically, we envision the following sequence of events. (1a) More than ~ 25 Mya, a KN exploded, ejecting ^{244}Pu-bearing r-process material. (1b) Some of the KN ejecta collided with and was mixed into the molecular cloud giving rise to the Local Bubble. (1c) Some of the ^{244}Pu was incorporated into dust grains. (2) The ^{244}Pu-bearing dust subsequently bombarded the Earth.

Step 1: ^{244}Pu *injection into the proto-Local Bubble.* Let a KN explode at distance $r_{\rm KN}$ from the forming Local Bubble, ejecting a yield $M_{\rm ej}(^{244}{\rm Pu})$. If the molecular cloud progenitor of the bubble has radius $R_{\rm MC}$, then the mass intercepted by the bubble and becoming dust is

$$M_{244}^{\rm LB,dust} = \frac{\pi R_{\rm MC}^2}{4\pi r_{\rm KN}^2} f_{244} M_{\rm ej}(^{244}{\rm Pu}) = \pi R_{\rm MC}^2 \; m_{244} \; \mathcal{F}_{244}(r_{\rm KN})\,, \tag{5.9}$$

with $f_{244} < 1$ accounting for the fraction of incident ^{244}Pu stopped by the bubble and ultimately incorporated into grains. We see that this is just the expression in eq. (5.7), for the one-step interstellar KN fluence $\mathcal{F}_{244,KN}$ at $r_{\rm KN}$, multiplied by the cloud cross section and the atomic ^{244}Pu mass m_{244}. Below we use the data, and KN rate information, to estimate the distance $r_{\rm KN}$ and evaluate its reasonableness.

Step 2: ^{244}Pu *transport to Earth.* Given the ^{244}Pu mass in eq. (5.9), we now estimate the ^{244}Pu flux onto Earth. Within the bubble, the interstellar ^{244}Pu number flux is $\Phi_{244} = n_{244} v_{\rm rel}$, with n_{244} the number density and $v_{\rm rel}$ the relative velocity with respect to Earth. We expect both factors to vary with time, as ^{244}Pu-bearing dust moves in the turbulent medium constantly stirred by SNe. We do not attempt to capture these variations but only estimate average values. We then demand that these match the observed mean flux $\Phi_{244}^{\rm interstellar}$ in eq. (5.5), and use the results to constrain this model.

We describe the Local Bubble crudely, as a sphere of radius $R_{\rm LB}$, so that the ^{244}Pu average number density is $n_{244} = M_{244}^{\rm LB,dust}/(4\pi A_{244} m_u R_{\rm LB}^3/3)$. Let $v_{\rm rel}$ be the speed of the Local Bubble gas relative to the Sun, [7], so that the interstellar ^{244}Pu number flux is $\Phi_{244} = n_{244} v_{\rm rel} \propto M_{244}^{\rm LB,dust}/R_{\rm LB}^3$. Since this flux is now measured, we are in a position to evaluate the ^{244}Pu mass needed to be injected in the Local Bubble for our model, given the measured flux Φ_{244}:

$$\begin{aligned} M_{244}^{\rm LB,dust} &= \frac{4\pi}{3} A_{244} m_{\rm u} R_{\rm LB}^3 \frac{\Phi_{244}^{\rm obs}}{v_{\rm rel}} \\ &= 6\times 10^{-11} M_\odot \left(\frac{\Phi_{244}^{\rm obs}}{1670\ {\rm cm^{-2}\ Myr^{-1}}}\right) \left(\frac{R_{\rm LB}}{50\ {\rm pc}}\right)^3 \left(\frac{30\ {\rm km/s}}{v_{\rm rel}}\right). \end{aligned} \tag{5.10}$$

We use for the fiducial velocity in eq. (5.10) a value comparable to the Sun's present motion with respect to the local standard of rest. This is conservative in that SN blasts and turbulent motions

[7] Note that this relative speed encodes not only the Sun's motion with respect to the cloud's center of mass, but also turbulent motions within the cloud, which have dispersion $\sigma_v \sim 1-10$ km/s for clouds of size $R_{\rm MC} \gtrsim 10$ pc.

in the Local Bubble will in general add to the relative velocity.

We see from eq. (5.10) that the ^{244}Pu inventory is far below the levels of KN yields. This implies that the explosion was not contained in the Local Bubble, but occurred outside it with only a fraction of the yield intercepted by the locally. This dilution is the main motivation for the two-step model, allowing it to avoid the unphysically large KN distances seen in the one-step picture (Fig. 5.11).

We note that it is likely that KN ejecta are unable to form significant amounts of dust, due to their high velocities (Takami et al., 2014; Gall et al., 2017). This is expected as a continuation of the trend in which Type Ia SNe have smaller or no dust formation compared to core-collapse explosions, which have slower ejecta speeds (Nozawa et al., 2011; Gomez et al., 2012). In light of the need for dust grains to deliver ejecta to Earth, the lack of KN dust production argues against direct, one-step deposition of ejecta from these explosions. However, in the two-step model the KN ejecta are stopped and mixed into the proto-Local Bubble material and can then be incorporated into dust grains.

We can go further and estimate the distance from the KN to the Local Bubble. This is a variant of the radioactivity distance calculation, similar to the Looney et al. (2006) calculation of the SN injection of radioisotopes into the pre-solar nebula (see, e.g., Ouellette et al., 2009). We can then solve for the KN distance, finding

$$r_{\rm KN} = \sqrt{\frac{f_{244} M_{\rm ej}(^{244}{\rm Pu})}{4 M_{244}^{\rm LB,dust}}}\, R_{\rm MC} \tag{5.11}$$

$$= 2000 \text{ pc } f_{244}^{1/2} \left(\frac{M_{\rm ej}(^{244}{\rm Pu})}{10^{-4} M_\odot}\right)^{1/2} \left(\frac{10^{-10} M_\odot}{M_{244}^{\rm LB,dust}}\right)^{1/2} \left(\frac{R_{\rm MC}}{3 \text{ pc}}\right) . \tag{5.12}$$

For our fiducial quantities and $f_{244} < 1$, we have $r_{\rm KN} \lesssim 2$ kpc. This places the KN explosion at a distance that is more consistent with the expectation that KNe are rarer and further between than SNe. [8] We note that a KN is likely to be so distant that its ejecta blast would be weak when arriving in the solar neighborhood, and hence unlikely to destroy the local molecular cloud.

Estimates of KN and neutron star merger rates place consistency checks on our distance calculations (Hartmann et al., 2002; Scalo & Wheeler, 2002). The average rate for a KN within

[8] An incorporation efficiency as low as $f_{244} \sim 10^{-3}$ can be accommodated and still give a distance comparable to that estimated above for an SN remnant.

distance $r_{\rm KN}$ is $\Gamma(r_{\rm KN}) \approx \pi r_{\rm KN}^2\, Q_{\rm local}$ where $Q_{\rm local} = dN_{\rm KN}/dA\, dt$ is the KN rate per unit area of the Galactic disk at the solar location; we assume $r_{\rm KN} > h$, the scale height of KN progenitors, so that the problem is reduced to two dimensions. Using the usual approximation of an exponential disk with scale radius $R_0 = 2.9$ kpc (see, e.g., Girardi et al., 2005; Murphey et al., 2021), we have $Q(R) = \mathcal{R}_{\rm KN} e^{-R/R_0}/2\pi R_0^2$, where the total Galactic KN rate sets the normalization via the surface integral $\mathcal{R}_{\rm KN} = 2\pi \int Q(R)\ R\ dR$. We estimate the Galactic KN rate assuming the ratio to the Galactic core-collapse SN rate $\mathcal{R}_{\rm CC}$ is the same as the ratio of the local cosmic rate densities: $\mathcal{R}_{\rm KN}/\mathcal{R}_{\rm CC} = \dot\rho_{\rm KN}/\dot\rho_{\rm CC}$. Using $\mathcal{R}_{\rm CC} \approx 0.032\ {\rm yr}^{-1}$ (Adams et al., 2013), $\dot\rho_{\rm CC} = 1.1\times10^{-4}\ {\rm Mpc}^{-3}\,{\rm yr}^{-1}$ (Lien & Fields, 2009), and a binary neutron star merger rate as a measure of the underlying r-process source rate $\dot\rho_{\rm BNS} \gtrsim \dot\rho_{\rm KN} \sim 1500\ {\rm Mpc}^{-3}\,{\rm yr}^{-1}$ (consistent with estimates from Matteucci et al., 2014; Wehmeyer et al., 2015; Chruslinska et al., 2018; Côté et al., 2018; Della Valle et al., 2018; Jin et al., 2018; Andreoni et al., 2020, 2021), we find $R_{\rm KN} \sim 1.4\times10^{-2}\mathcal{R}_{\rm SN} \sim 440\ {\rm Myr}^{-1}$. Finally

$$\Gamma_{\rm KN} \sim 1.3\ {\rm events\ Myr}^{-1} \left(\frac{r_{\rm KN}}{1\ {\rm kpc}}\right)^2 \tag{5.13}$$

at the solar distance from the center of the galaxy, i.e., $r_{\rm KN} = R_\odot = 8.7$ kpc. We see that the typical KN recurrence time is $\Gamma_{\rm KN}^{-1} \sim 0.8$ Myr $(1\,{\rm kpc}/{\rm r_{KN}})^2$. Thus KN explosion times of $t_{\rm KN} = (10, 50)$ Myr correspond to mean distances of $r_{\rm KN} = (280, 120)$ pc. Our two-step ^{244}Pu-based radioactivity distances lie comfortably within this range, demonstrating overall consistency.

Two other issues constrain the timing of the KN explosion and subsequent r-process rain. One is the timescale for the Local Bubble to assemble and form stars; this timescale plus massive-star lifetimes sets an upper limit to the KN injection time. The Fuchs et al. (2006) fit to massive-star lifetimes gives 23 (18) Myr for masses $\geq 8(10)M_\odot$ at the threshold of core collapse, and the lifespans are nearly linearly dependent on the inverse of the mass. Estimates of the lifetimes of molecular clouds span a significant range from local solar neighborhood values of a few Myr (Hartmann et al., 2001) to ~ 30 Myr (Murray, 2011). For the Local Bubble itself, based on lifetimes of extant stars and pulsars, as well as on expansion dynamics, Breitschwerdt et al. (2009, 2016) estimate an age ~ 15 Myr and ~ 17 SNe, which is consistent with the Maíz-Apellániz (2001) argument for ~ 20 SNe during the last 10-12 Myr. On the other hand, Abt (2011) argues that some portions of the bubble could be as old as ~ 50 Myr, whereas Smith & Cox (2001) consider models with ages $\lesssim 10$ Myr and

three SNe. We therefore consider a range of KN injection timescales of $(10, 20, 50)$ Myr, as noted in eq. (5.2).

Finally, the r-process bombardment on Earth can begin only when the Sun enters the Local Bubble. This time is uncertain and depends on the evolving bubble morphology, but also sets an upper limit on the injection time.

We observe that this two-step process incurs larger uncertainties overall than the one-step SN mechanism. One of them is the timing of the KN: the further in the past, the greater the losses of shorter-lived species. If the ^{244}Pu event in the 12.5–25 Mya crust layer is real, it sets a lower limit on this time. The longest-lived r-process radioisotopes of interest, apart from ^{244}Pu, are ^{129}I, ^{182}Hf, and ^{247}Cm. These live long enough for their production in a KN to be potentially observable in this layer; also the secular equilibrium abundance of ^{236}U potentially provides a check on anthropogenic sources of actinides.

5.6.3 Predicting r*-process radioisotope signatures in terrestrial archives*

The previous two subsections show that it is possible to construct both SN and KN scenarios for some or all of the ^{244}Pu signal. We conclude that the ^{244}Pu flux in eqs. (5.4) and (5.5) could have an astrophysical origin, and use these to normalize our subsequent predictions for possible live isotope searches using AMS techniques. In this section we compute terrestrial signals for additional r-process radioisotopes, with a particular focus on Fe-Mn crusts. Our strategy is to pursue the consequences of the ^{244}Pu detection, using it to infer the abundances of other r-process radioisotopes predicted by our SN and KN models.

The available natural terrestrial archives that accumulate gradually over the longest periods of time, and thereby give the most complete dating information, are deep-ocean crusts and sediments. In the natural archives of interest, radioisotope abundances are usually presented as an isotope fraction $(N_i/N_j)_{\rm obs}$, the ratio of a radioisotope i to a stable isotope or element j. Here we derive predictions for the ratio $N_i^{\rm astro}/N_j^{\rm bg}$, i.e., the astrophysical signal relative to a stable "background" isotope.

The astrophysical signal can be expressed as the incident interstellar number flux $\Phi_i^{\rm interstellar} = dN_i/dAdt$, usually given without decay losses included. The measurable flux onto a terrestrial

sample is

$$\Phi_i^{\rm sample} = \frac{f_i U_i}{4} \Phi_i^{\rm interstellar} e^{-t/\tau_i} \,, \tag{5.14}$$

where the factor of 4 accounts for the ratio of the Earth's cross section to its surface area, f_i is the fraction of i in dust arriving at Earth, and U_i accounts for uptake into the sample. We have also accounted for radioactive decay. If the flux is measured for a time interval Δt, the corresponding surface density in the sample is $N_i^{\rm astro} = \Phi_i^{\rm sample}\, \Delta t$.

During this time interval, the sample accumulates a surface mass density $\rho\ \dot{h}\ \Delta t$, where ρ is the total density, and $\dot{h} = dh/dt$ is the rate of growth of the thickness. Let the background species j have mass fraction $X_j = \rho_j/\rho$ in the sample, and mass number A_j. Then the background atoms j have surface density $N_j = X_j \rho\, \dot{h}\ \Delta t/A_j m_u$, with $m_u = 1/N_{\rm Avo}$ the atomic mass unit. Thus

$$\frac{N_i^{\rm astro}}{N_j^{\rm bg}} = U_i f_i \frac{\Phi_i^{\rm interstellar}}{4 X_j \rho\, \dot{h}/A_j m_u} e^{-t/\tau_i} \tag{5.15}$$

is the desired isotopic ratio.

We anchor our predictions to the detections of ^{244}Pu discussed above. In this case we have

$$\frac{N_i^{\rm astro}}{N_j^{\rm bg}} = U_i\ \frac{f_i}{f_{\rm Pu}}\ \left(\frac{\mathcal{N}_i}{\mathcal{N}_{244}}\right)_{\rm astro}\ \frac{\Phi_{244,{\rm astro}}^{\rm interstellar}}{4 X_j \rho\, \dot{h}/A_j m_u} e^{-t/\tau_i} \,, \tag{5.16}$$

where we use the fact that the interstellar flux of a species is proportional to its (number) yield, $\Phi_i^{\rm interstellar} \propto \mathcal{N}_i$. Using values typical for crusts, we have

$$\frac{N_i^{\rm astro}}{N_j^{\rm bg}} = 2\times 10^{-13}\ U_i\ \frac{f_i}{f_{\rm Pu}}\ \left(\frac{\mathcal{N}_i}{\mathcal{N}_{244}}\right)_{\rm astro} e^{-t/\tau_i} \tag{5.17}$$

$$\times \left(\frac{\Phi_{244}^{\rm interstellar}}{1670\ {\rm cm^{-2}\,Myr^{-1}}}\right) \left(\frac{1\ {\rm ppm}}{X_j}\right) \left(\frac{A_j}{150}\right) \left(\frac{2\,{\rm g/cm^3}}{\rho}\right) \left(\frac{3\,{\rm mm/Myr}}{\dot{h}}\right) . \tag{5.18}$$

Note that the signal is inversely proportional to both the growth rate and the background abundance in the sample: $N_i^{\rm astro}/N_j^{\rm bg} \propto (X_j \dot{h})^{-1}$. This favors samples with low growth rates and hence Fe-Mn crusts. It also favors elements that are rare in crusts (so long as the uptake is not too small).

Tables 5.5-5.7 give the number ratios for various isotopes of interest $(\mathcal{N}_i/\mathcal{N}_{244})_{\rm astro} e^{-t/\tau_i}$, where we incorporate the decay factors corresponding to the different time scales of interest. For the

lighter species with stable isotopes, the candidates of particular interest are those with high ratios to ^{244}Pu.

Table 5.8 shows the time-integrated interstellar flux or *fluence*, as defined in eq. (5.6), for selected r-process radioisotopes in specific scenarios. The values are for the present day, and include the effects of decay. For the 3 Mya signal associated with an SN, the duration is 1 Myr. For the KN signal at 10 Myr, the duration is assumed to be 10 Myr. The fluences are the most direct results from the astrophysical calculations, but connecting them to geological and lunar measurements requires one to specify the abundances in particular samples.

Table 5.9 shows our predictions for selected radioisotope ratios following deposition in Fe-Mn crusts 3 Mya, normalized to a 10% uptake and $f_i/f_{\rm Pu} = 1$. These results also appear in Fig. 5.12, where use the ^{244}Pu flux inferred from sediments $0.5 - 2.2\,$Myr old (Wallner et al., 2015b) for normalization. In general we see that the SN predictions are as large as, and sometimes much larger than, those of the KN models. This reflects the difficulty of making actinides in SN models, which means that lower-mass species are more abundant relative to the ^{244}Pu isotope that anchors our results. Variations between the KN model predictions are generally within a factor of 10. In contrast, the SN predictions can span several orders of magnitude, with the SB model generally leading to larger low-mass abundances due to its particularly low ^{244}Pu output. Also shown in Table 5.9 and Fig. 5.12 are the prospective AMS sensitivities for ^{93}Zr (Hain et al., 2018; Martschini et al., 2019; Pavetich et al., 2019), ^{107}Pd (Korschinek et al., 1994), ^{129}I (Vockenhuber et al., 2015), ^{135}Cs (Yin et al., 2015), and ^{182}Hf (Vockenhuber et al., 2004). We see that, whereas predictions for the ^{93}Zr signal generally lie below the AMS sensitivity, those for ^{107}Pd, ^{135}Cs, and possibly ^{182}Hf in model SB lie above the AMS sensitivity, and the predictions for the ^{129}I signal lie above the AMS sensitivity in both SN scenarios and possibly also in the KN scenarios.

Figure 5.13 shows the Fe-Mn crust abundances for the actinides ^{236}U, ^{237}Np, and ^{247}Cm, for the same models as in Fig. 5.12. These are all elements with no stable isotopes, so we use ^{238}U as a reference standard for the ratios presented; we note that ^{238}U is also the source of ^{236}U background. We recall that natural uranium will far overwhelm any astrophysical contribution. For this reason, the ^{236}U signal may be masked by other production mechanisms. For ^{237}Np, suppression of the ^{238}U signal may be necessary before a signal can be seen. We thus conclude that ^{236}U and ^{237}Np detections likely await improvements in measurement techniques. For ^{247}Cm, uranium is not

anticipated to be a limitation, but detection will require establishing a pure curium reference spike. We urge further study of the experimental possibilities for all of these species.

To summarize, we have found that the ^{244}Pu evidence implies that the geological record should contain other r-process radioisotope signals. The abundances are in some cases within or close to the reach of existing AMS techniques, whereas improvements in the AMS sensitivity to key species are necessary in other cases.

We emphasize that the experimental program for these new species, as well as additional ^{60}Fe and ^{244}Pu searches, should have two related but distinct goals: sensitivity and time resolution.

- *Sensitivity.* High sensitivity, i.e., the ability to detect small extraterrestrial radioisotope abundances, obviously is critical. It allows for detection of additional species and more accurate abundances, both of which sharpen the probes of the potential nucleosynthesis sites.

- *Time resolution.* Time resolution offers another powerful means of distinguishing between models. A better determination of the ^{244}Pu time history can clarify whether it is exclusively coincident with the two ^{60}Fe pulses, suggesting a common SN origin, or it appears at other epochs, suggesting a distinct origin likely in a KN. The time behavior of additional radioisotopes can then be compared with that of ^{60}Fe and ^{244}Pu, which can further distinguish between these scenarios and potentially distinguish between SN and KN models.

These goals are in some tension, as finer time resolution implies smaller samples per time bin, reducing the available signal at a fixed sensitivity. As with the development of the ^{60}Fe measurements, a sensible strategy may be to first strive for the detection of new species, then follow up with better time resolution.

We now turn to considerations of sample collection for each of the radioisotopes of interest.

5.6.4 Terrestrial searches

In order to detect and preserve these signals, we emphasize that samples must be collected from well-chosen sites and suitable media, in the sense that the samples should have maintained a detectable abundance of the SN debris from the initial deposit to the present and that the samples should be accessible for collection and delivery to the laboratory. We consider these issues for the Earth in this section, and for the Moon in the next section.

Marine samples are the primary focus of interest as natural terrestrial archives, since continental material is subject to erosion, and radioisotope studies in ice cores do not extend so far into the past. [9] In general, deep-ocean deposits are essentially undisturbed, with very little disturbance from creatures at the ocean floor (bioturbation) to blur the time structure, and are largely free of anthropogenic contamination from nuclear debris, as well as backgrounds from cosmic-ray spallation in the atmosphere. Debris at the sea floor accumulates in sediments that stretch back beyond the ~ 10 Myr that has been studied so far, rendering it suitable for exploring possible astrophysical triggers of mass extinctions that occurred $\gtrsim 10^8$ ya ago in addition to the well-attested ^{60}Fe signal, evidence for ^{53}Mn from ~ 3 Mya, and reports of ^{244}Pu deposition over the past 25 Myr. Ultimately, deep-ocean sediments may harden to make sedimentary rock in geological strata reaching back to much longer timescales. In this section and Table 5.10 we highlight some of the key considerations from chemical oceanography that determine which astrophysical radioisotopes may have geologically favorable conditions for detection. We make heavy use in the following discussion of Broecker et al. (1982), Nozaki (2001), and the Geotraces database [10] and private communications with Craig Lundstrom and Tom Johnson.

In considering the prospects for detecting marine deposits of radionuclides, one must consider the sedimentation rates of the radionuclides of interest, focusing on those with a short residence time and discarding those that remain dissolved in seawater. Table 5.10 lists the elements discussed earlier in this chapter, together with their mean oceanic concentrations and the characteristics of their distributions, which provide the basis for our discussion of the possibilities of detecting their radioisotopes in view of the SN and KN model calculations above.

• Among the elements that may be produced by the r-process and are identified in the previous section as being of interest, we note that zirconium sinks in the ocean, attaches to solid particles, and may be scavenged at the water/sediment interface, similarly to iron. The half-life of ^{93}Zr (1.53×10^6 yr) is somewhat less than those of the isotopes ^{60}Fe and ^{53}Mn that have been reported in layers $\sim 2.5 \times 10^6$ yr old. Figs. 5.8 and 5.9 and Table 5.5 indicate that its r-process production rate, which is quite model-dependent, may be orders of magnitude higher than that of ^{60}Fe, or

[9] However, we recall that Antarctic ice dating back to 2.7 Mya has been recovered (Yan et al., 2019), potentially opening up prospects for the future.

[10] https://www.geotraces.org/

considerably lower. However, Table 5.9 and Fig. 5.12 indicate that the ^{93}Zr signal in 3 Myr old samples may lie below the estimated AMS sensitivity.

• Palladium has a distribution that increases with depth, but is not expected to bind to particles or be concentrated at the water/sediment interface. It has been detected in Fe-Mn crusts, but with low abundances (see Table 5.9), which is advantageous for our purposes. These low abundances imply that, as seen in Table 5.9 and Fig. 5.12, the relative abundances of ^{107}Pd predicted in some r-process models may be within reach of the AMS technique if a suitable 3 Myr old sample can be found.

• Most iodine is in the form of the IO_3^- ion, which is distributed conservatively, but a small fraction is in the form of the I^- ion, which may be scavenged, preferentially in anoxic basins such as the Black Sea. Fitoussi & Raisbeck (2007) attempted to measure ^{129}I in a relatively recent but pre-anthropogenic sediment, and found that care is needed to avoid anthropogenic contamination. Ji et al. (2015a) have presented the first AMS measurements of ^{129}I in Fe-Mn crusts. These data already reveal the power of ^{129}I to probe near-Earth explosions, particularly the possible KN enrichment of the Local Bubble, and the corresponding constraints are discussed in detail in the following Section 5.6.5.

• Cesium dissolves in water and has a conservative oceanic distribution, so ^{135}Cs offers poor prospects for deep-ocean detection. Moreover, as seen in Table 5.9 and Fig. 5.12, most of the models studied indicate that the fraction of ^{135}Cs may lie below the AMS sensitivity.

• Hafnium is an interesting target, particularly if production occurred more than 3 Mya, thanks to the ^{182}Hf half-life of 8.9 Myr. Most of our r-process models produce less ^{182}Hf than ^{93}Zr, while the oceanic distribution of hafnium is similar to that of zirconium. In a sediment, Vockenhuber et al. (2004) have established the upper limit $^{182}\mathrm{Hf}/^{180}\mathrm{Hf} < 10^{-6}$ using a 45 g sample, and quoted a total hafnium elemental abundance by dry weight of 8 ppm. Combining these numbers, we find an upper limit on the fraction by weight of ^{182}Hf of 8×10^{-12}. Martschini et al. (2020) showed that these limits could in principle be improved dramatically using a laser technique to remove stable isobars. They found $^{182}\mathrm{Hf}/^{180}\mathrm{Hf} = (3.4 \pm 2.1) \times 10^{-14}$, on the basis of which they estimated a sensitivity of $(^{182}\mathrm{Hf}/^{180}\mathrm{Hf})_{\mathrm{min}} \approx 6 \times 10^{-14}$. This would correspond to a mass fraction of $\sim 4 \times 10^{-18}$, which

could be achieved if the stable tungsten isobar ^{182}W is absent or can be removed.

For comparison, Wallner et al. (2021) estimated a range of $(0.1 - 100) \times 10^{-22}$ ^{244}Pu atoms per atom in the crust samples. It is important to note that one major improvement for these measurements was the use of the 1 MV accelerator Vega at Australia's Nuclear Science and Technology Organisation, which provided an improved ^{244}Pu detection efficiency from 1×10^{-4} (Wallner et al., 2015b) to 1.5%. These measurements correspond to a sensitivity to the fraction by weight of $\sim 10^{-22}$. In Table 5.5 we see ratios ^{182}Hf/^{244}Pu $< 8.7 \times 10^4$ (reached in model SB), suggesting that the model sensitivity of the ^{244}Pu detection by Wallner et al. (2021) is better than that of the ^{182}Hf search by Vockenhuber et al. (2004), though a more sensitive ^{182}Hf search may have interesting prospects. Vockenhuber et al. (2004) used their data to quote an upper limit on the ^{182}Hf flux into the sediment of 2×10^5 cm^{-2}yr^{-1}, to be compared with the estimated ISM flux of 0.05 cm^{-2}yr^{-1} assuming a global distribution of the infalling ISM and that all of the material is deposited in the sediment. Thus there is considerable scope for a more sensitive measurement to observe a signal above the expected background. Table 5.9 and Fig. 5.12 indicate that the fraction of ^{182}Hf may be within the AMS sensitivity range in model SB.

• Uranium has a natural background of ^{235}U and ^{238}U that far overwhelms any astrophysical perturbations we might hope to detect. The shorter-lived ^{236}U has no remaining proto-solar component, and so potentially could serve as an astrophysical signature. However, significant obstacles exist. In uranium ores, neutrons from fission can capture on ^{235}U to create ^{236}U. The resulting ^{236}U/^{235}U ratio will be strongly sensitive to local conditions, making this background challenging to estimate. Anthropogenic ^{236}U contamination is also a concern. Finally, uranium has a conservative oceanic distribution, so ^{236}U is likely difficult to use in sediments and crusts would be preferred.

• Neptunium is poorly studied as compared to other transuranic elements. Indeed, it has been called the "neglected actinide" (Thompson, 1982). Table 5.5 shows it is produced in abundances comparable to those of ^{244}Pu and thus is of great interest to search for as a cross-check on ^{244}Pu and potentially as a probe of the details of actinide synthesis. As for other transuranic elements, there are no stable isotopes, so elemental searches are viable. However, anthropogenic contamination is an issue. Lindahl et al. (2005) found that ^{237}Np has a conservative oceanic distribution, and so

does not readily precipitate. Thus, Fe-Mn crusts would seem to be a preferred terrestrial target. Future lunar measurements are also of interest; unfortunately, the initial report of ^{237}Np evidence in *Apollo* return samples (Fields et al., 1972) was subsequently found to be compromised by airborne anthropogenic contamination (Fields et al., 1976).

• Like iodine, plutonium may be scavenged, and it is encouraging that ^{244}Pu detection has been reported by multiple experiments, as seen in Table 5.2 and Fig. 5.7. [11] Measurements with higher sensitivity using deep-ocean deposits stretching back to ages comparable to the half-life of ^{244}Pu ($t_{1/2} = 81$ Myr) or further would be very interesting, as would sufficient time resolution to distinguish a possible ^{244}Pu pulse coincident with that observed for ^{60}Fe, and/or any earlier similar pulses. We encourage searches in anoxic basins where the concentration of ^{244}Pu may be higher.

• The model calculations in Table 5.5 indicate that an SN ~ 3 Mya could have deposited curium on Earth, with ^{247}Cm at levels comparable to those for ^{244}Pu, whereas most of the shorter-lived ^{248}Cm would have decayed. This isotope thus makes an important target for geological and lunar searches.

5.6.5 ^{129}I in Fe-Mn crusts and near-Earth KNe: present constraints and future opportunities

The AMS measurements of ^{129}I by Ji et al. (2015a) and Ji et al. (2015b) are from three ferromanganese crusts. For two of these, Ji et al. (2015a) tabulated ^{129}I profiles to depths of 8 cm. Table 5.11 gives the locations and elemental compositions of these crusts, which are both in the mid-Pacific, at locations separated by about 2300 km. The natural production of ^{129}I includes uranium fission products, as well as the daughters of spallation events between cosmic rays and atmospheric xenon. These give rise to a persistent flux of ^{129}I into the crusts, which represents an irreducible background.

Ji et al. (2015a) and Ji et al. (2015b) found that the crusts show an ^{129}I/^{127}I isotopic profile that drops with depth in a manner consistent with a background component undergoing radioactive decay, as seen in Fig. 5.14. Moreover, the most recent layer has an abundance consistent with the pre-bomb level found in sediments (Moran et al., 1998). Ji et al. (2015a) argue that this drop-off

[11] We note, however, that most of the shorter-lived isotope ^{242}Pu would have decayed on the time-scales discussed here.

with depth suggests that the results are free of anthropogenic contamination. We note that the crust data show no strong evidence for a "floor" of ^{129}I that persists as the background diminishes at increasing depth.

The crusts in which Ji et al. (2015a) measured ^{129}I lack independent measures of their growth rates, without which the depth profile cannot be transformed into a precise time history. Nonetheless we can use typical Fe-Mn growth rates to estimate the epochs probed: for a low growth rate $\dot{h} = 1$ mm/Myr, the crusts span 5–80 Myr, while a high growth rate $\dot{h} = 6$ mm/Myr would correspond to a range of 1-13 Myr. It is therefore not clear that these data include the 2-3 Mya range of the ^{60}Fe pulse, so that the SN (one-step) scenario may not be probed directly by these data. However, as seen in Fig. 5.12 and Table 5.9, the SB model predicts ^{129}I many orders of magnitude above the natural background, so that such a signal could be easily ruled out (or detected!) in a search coincident with the ^{60}Fe pulses in a crust. This is the case despite the significant model uncertainties, which are indicated in Fig. 5.12 but omitted in Fig. 5.14 for clarity. On the other hand, the SA model uncertainties are large enough that their lower extreme overlaps with the KN models.

On the other hand, it is clear that these data cover the timespan probed by the extended ^{244}Pu flux, and thus probe the two-step scenario of KN enrichment of the proto-Local Bubble. We illustrate the power of ^{129}I data in Fe-Mn crusts using the Ji et al. (2015a) data while emphasizing that, due to the lack of information on growth rate and uptake, our quantitative results are only crude estimates. Nevertheless, we hope that such order-of-magnitude estimates may stimulate further experimental work. In this spirit, we again assume a constant growth rate $\dot{h}_0$, so that a time t in the past corresponds to a depth $h(t) = \dot{h}_0\, t$. If the KN event occurred at a time $t_{\rm KN}$ ago, the signal can extend to a maximum depth $h_{\rm max} = \dot{h}_0\, t_{\rm KN}$.

All KN-produced radioisotopes would have decayed for the (unknown) $t_{\rm KN}$ duration since the explosion, regardless of the time history of their flux on Earth. Thus any KN-created flux will *not* show a radioactive decay pattern versus depth. This is in contrast to the natural ^{129}I background, which is due to ongoing production and so should show the effects of decay versus depth. Just such a pattern is evident in Fig. 5.14; any KN-produced signal would represent a "floor" underneath this natural background. Thus the deepest measurements have the most constraining power.

The KN signal in the crust is straightforward to calculate in the case where the growth rate

and r-process flux are both constant. In this case the ^{129}I profile versus depth h for KN model $\alpha = (\mathrm{KA}, \mathrm{KB})$ has a steplike structure:

$$\frac{^{129}\mathrm{I}}{^{127}\mathrm{I}}(h)_\alpha = \begin{cases} (^{129}\mathrm{I}/^{127}\mathrm{I})_{\alpha,0}\ e^{-t_{\mathrm{KN}}/\tau_{129}}\ , & h \le h_{\max} = t_{\mathrm{KN}}/\dot{h}_0\,, \\ 0\ , & h > h_{\max}\,, \end{cases} \tag{5.19}$$

where $(^{129}\mathrm{I}/^{127}\mathrm{I})_{\alpha,0} = N^{\alpha}_{129}/N^{\mathrm{bg}}_{127}$ from Eq. (5.17), which includes a factor f_{I} for dust formation and transport, and the uptake factor U_{I}. We see that the isotope ratio is constant with depth, and for increasing t_{KN} the level is progressively smaller but extends to greater depths.

In Fig. 5.14 we confront the data of Ji et al. (2015a,b) with some results from calculations based on the KN models KA and KB. For each of these, we show predictions for KN explosion time $t_{\mathrm{KN}} = (10, 20, 50)$ Myr, corresponding to a scenario in which an explosion at this time enriches and stirs the proto-Local Bubble, initiating a flux of r-process dust onto the Earth. The ^{244}Pu data in Fig. 5.7 shows that this flux extended at least to the earliest measured bin $12 - 25$ Mya, but neither excludes nor requires an earlier flux. Thus our constraints should apply only within this time window, though the explosion would have occurred earlier.

To predict the ^{129}I/^{127}I ratio in the crust, we assume a constant growth rate $\dot{h}_0 = 2$ mm/Myr and and a value $U_{\mathrm{I}} = 0.1$ of the uptake factor for iodine. [12] With these $(\dot{h}_0, U_{\mathrm{I}})$ values, model KA would be excluded if the KN occurred $\lesssim 50$ Mya, whereas model KB would be allowed for explosions $\gtrsim 20$ Mya. There are clearly many uncertainties in this analysis: the line heights scale as $(f_i/f_{\mathrm{Pu}})U_{\mathrm{I}}\ \exp(-t_{\mathrm{KN}}/\tau_{129})$ and they reach to maximum depths that scale as $h_{\max} = \dot{h}_0\ t_{\mathrm{KN}}$. Thus KA models can be accommodated with, for example, smaller uptake values.

The larger lesson is that it is of great interest to make additional ^{129}I measurements in Fe-Mn crusts, which could offer an important new probe of possible sources of r-process isotopes. Also, it would be of considerable interest to search at even greater depths and thus earlier times than those shown in Fig. 5.19, to see if the ^{129}I signal continues to drop as expected from a natural background, or whether a "floor" reveals itself and thereby indicates a scenario with a early injection time and

[12] According to Ji et al. (2015b), iodine is enriched in crusts relative to seawater, though much less so than iron. This would allow a range that includes the value of U_{I} that we assume, but with considerable uncertainty. For comparison, in Fe-Mn crusts the estimates of the iron uptake in different crusts have varied from $U_{\mathrm{Fe}} = 0.6\%$ (Knie et al., 2004) to 7% and 17% (Wallner et al., 2016), while Wallner et al. (2015b) estimated the ^{244}Pu incorporation efficiency at $U_{\mathrm{Pu}} = 21\% \pm 5\%$. Wallner et al. (2021) found for their crust a uptake efficiency of $17\% \pm 3\%$ for ^{60}Fe, and of $12\% \pm 4\%$ for ^{244}Pu; they adopted $U = 17\%$ for both.

thus a distant production epoch $t_{\rm KN}$. It would be of particular interest to measure ^{129}I in crusts with ^{60}Fe data, searching both inside and beyond the ^{60}Fe pulses; similarly, it would be useful to search for ^{129}I in the same crusts that show ^{244}Pu signals. Finally, we stress that independent measures of the growth rate, and of the iodine uptake, are as important as the additional ^{129}I data themselves. The ability to limit astrophysical perturbations to ^{129}I hinges on the precision and reliability of the ^{129}I profiles with time.

5.6.6 Lunar searches

A great advantage of lunar material is that it avoids geological and oceanographic effects that transport, mix, and dilute the signal. Moreover, the uptake is likely to be high, so that all of the favored radioisotopes among those that can be produced via the r-process, namely ^{93}Zr, ^{107}Pd, ^{129}I, ^{135}Cs, ^{182}Hf, ^{236}U, ^{237}Np, ^{244}Pu, and ^{247}Cm, are *a priori* interesting targets for searches in the lunar regolith (i.e., unconsolidated surface material). Fry et al. (2015) cautioned that some fast dust particles could lead to the vaporization and escape of some of the ejecta mass. However, the lunar detections of ^{60}Fe (Fimiani et al., 2016), with a fluence that is relatively high compared to terrestrial results, suggest that these effects are small. This could imply that much of the astrophysical dust slows to lower speeds by the time the particles arrive.

Thus the surface fluences of SN species should be close to the interstellar fluences estimated in Table 5.8, modulo a geometric factor of the cosine of the vertical angle. However, converting these values into predictions in, say, atoms per gram, requires one understands lunar surface processes over Myr timescales. Such a detailed analysis is beyond the scope of this work; we intend to visit this issue in a separate paper. Here we summarize some important considerations.

As impactors strike the lunar surface, the regolith gets continually reworked, a process known as gardening. Gardening mixes material more deeply over time, so that deeper material is less likely to have been disturbed recently, though it would have been disturbed in the more distant past. Shallow soil is continually turned over by the large flux of very small impactors. Costello et al. (2018) showed that there has been significant reworking down to ∼10 cm over the past 3 Myr, and significant reworking down to ∼40 cm over the past 400 Myr. Tables 5.6 and 5.7 suggest that ^{129}I, ^{236}U, and ^{244}Pu may be the most interesting search targets at lower depths. However, the gardening process implies that lunar samples cannot be time-stamped accurately, and we recall that

the *Apollo* lunar samples (Fimiani et al., 2016) have no direct timing information.

On the other hand, lunar samples may provide valuable information on the possible direction of any astrophysical source of live radioisotopes. If these arrive in dust grains that travel ballistically, their distributions could depend on the lunar latitude. The *Apollo* landing sites were all relatively close to the lunar equator. Therefore, in view also of their limited statistics, they provide limited information in this regard. However, the recent *Chang'e-5* sample return mission landed at a higher latitude, 43.1^o N (Qian et al., 2021), the *Artemis* program envisions landing at the lunar south pole (Smith et al., 2020), and various commercial lunar sample return missions are also planned. More information on the latitude distribution may therefore be available in the coming years, and could discriminate between origins in the Scorpius-Centaurus (Benítez et al., 2002; Breitschwerdt et al., 2012) and Tucana-Horologium (Mamajek, 2015) associations.

Even if dust propagation is not ballistic (as suggested by Fry et al., 2020), the lunar surface distribution of radioisotopes in general offers a unique measure of the directionality of the dust velocity distribution. This directly probes SN dust propagation that is otherwise inaccessible observationally.

We note, however, that there is an important source of radioisotope background on the Moon, namely cosmic-ray spallation on the lunar surface. This is an irreducible background, so the signal must be found above it. Spallation is less important for the heaviest isotopes, and is most effective when only one or a few nucleons are removed from a target nucleus. Thus a key issue is whether there are relatively abundant stable isotopes that have one or a few more nucleons than the radioisotope of interest. We note also that, although there is no anthropogenic background on the Moon, care must be taken after bringing samples to Earth, so as to avoid anthropogenic contamination, which was an issue for the evidence for ^{236}U and ^{237}Np on the Moon reported by Fields et al. (1972).

Cosmic-ray irradiation of the lunar regolith also produces a substantial neutron flux at depth. Neutron exposure would lead to a ^{236}U background that makes any extrasolar ^{236}U difficult to find, but ^{236}U searches could nonetheless be useful to establish which if either of these components is present. We note also that neutron captures on ^{236}U will lead to ^{237}Np, creating a background for that species.

It is therefore encouraging that the *Chang'e-5* mission has recently returned to Earth a new sample of lunar material, and that the future *Artemis* and other lunar missions have similar

objectives. We advocate efforts to replicate the *Apollo* results of ^{60}Fe and urge searches for the other radioisotopes discussed in this chapter. The *Apollo* samples were gathered relatively close to the lunar equator, whereas *Chang'e-5* landed in the northern hemisphere and *Artemis* is planned to land near the south pole. Measurements in their samples may therefore provide a measure of the dust arrival direction(s), and perhaps some indication of the latitude of their astrophysical sources. This would herald the dawn of radioisotope astronomy.

5.7 Discussion

We have found that the ^{244}Pu detection implies that there should also be measurable traces of other *r*-process radioisotopes, whose abundances and time history can shed important new light. Of these, ^{93}Zr, ^{107}Pd, ^{135}Cs, and ^{182}Hf are not only *r*-process species but can also be made in the *s*-process. Were these the only isotopes detected, this would lead to ambiguity about the nucleosynthesis site that led to their injection on Earth. But by comparing the time signature with those of ^{60}Fe and ^{244}Pu, one can see if they are associated with the production of these isotopes. It is conceivable as well that some species such as these could arise from a recent event distinct from the origins of both the ^{60}Fe and ^{244}Pu. For example, the *s*-process output of an AGB star could be delivered to Earth, perhaps via a two-step process within the proto-Local Bubble similar to what we have proposed for the KN injection of ^{244}Pu. Here again, the abundance patterns and time history of these species can test for such a model, and it would be of interest to investigate this scenario in more detail.

Our studies of live radioisotopes ejected from recent nearby explosions are closely linked with the long-studied question of now-extinct radioisotopes injected into the proto-solar nebula. As described in the excellent reviews by Meyer & Clayton (2000); Adams (2010); Lugaro et al. (2018), meteorites show evidence that more than a dozen of what we call "medium-lived" radioisotopes ("short-lived" in the cosmochemistry literature) were present in the nascent solar system. These include some *r*-process species (Meyer, 1993; Côté et al., 2021). Our calculations could be used to provide a new evaluation of pre-decay abundances for the early solar system.

The discovery of ^{60}Fe in deep-ocean deposits heralded a new era of laboratory astrophysics using relic live radioisotopes to explore events in the solar neighborhood, using them to understand quantitatively their contributions to nucleosynthesis. Previous studies have focused on nearby SNe

and their roles in forming the Local Bubble. The hints of discovery of ^{244}Pu carry these studies to a new level, including the possibility of gathering experimental information about sites of the r-process, extending the catalog of events of interest to include KNe, possibly out to a larger range surrounding the Local Bubble. This development also extends and expands the investigation of the potential repercussions on Earth of astrophysical events, including possible impacts on the biosphere. The longer half-life of ^{244}Pu (81 Myr) compared to ^{60}Fe (2.5 Myr) offers the possibility of studying the implications of such events in the more distant past, and exploring directly possible links to mass terrestrial extinctions, opening up a new frontier in astrobiology.

5.8 Conclusions and future directions

The Wallner et al. (2021) detection of a substantial ^{244}Pu signal in the deep ocean dramatically broadens the study of near-Earth explosions, because it demands that an r-process event occurred relatively recently and close by. Indeed, ^{244}Pu not only originates exclusively in the r process, but also is one of the heaviest nuclei it can produce. Thus the firm detection of ^{244}Pu not only opens a new window into the elusive r-process astrophysical site(s), but also points to an engine capable of synthesizing the fullest possible complement of species, extending to actinides. The ^{244}Pu coincidence in time with ^{60}Fe–now seen in two distinct events–suggests a common origin in SNe, yet modern SN models often struggle to host an r-process site, and typically yield no ^{244}Pu at all. Observationally, r-process abundances in halo stars and dwarf galaxies also demand that most SNe do not make the r-process. Thus one is driven also to consider a separate event–a neutron star merger, where theoretical calculations show robust synthesis of actinides including ^{244}Pu, now supported by evidence of substantial r-process production in the GW170817 KN.

We have therefore presented pairs of SN and KN models for r-process actinide production and delivery to Earth. The former illustrate scenarios for SN actinide production in a forced neutrino-driven wind model and in an MHD model; these are adjusted to fit the data on abundances measured in the metal-poor star HD160617. We have also presented two representative KN models, with different combinations of dynamical ejecta and disk wind contributions, chosen to fit the data on HD160617 and an actinide-boost star J0954+5246. These models indicate that radioisotopes of interest with half-lives between about 1 and 100 Myr include ^{93}Zr, ^{107}Pd, ^{129}I, ^{135}Cs, and ^{182}Hf.

As seen in Fig. 5.12, at least some of these may be detectable using AMS techniques, and their presence or non-detection could constrain significantly models of r-process nucleosynthesis.

The reported observations of ^{244}Pu are nicely compatible with the the direct (one-step) deposition of explosion debris of an r-process-enhanced SN within $\mathcal{O}(100)$ pc of Earth, the same distance range postulated to explain the observed ^{60}Fe signal. But most SNe do not make r-process radioisotopes and certainly not r-process actinides, so if the ^{244}Pu had been produced by two SNe, both must be rare events (and it must be possible for some SNe to produce actinides). If instead we try to account for the ^{244}Pu by direct (one-step) deposition by a KN, the required distances are unfeasibly large. As an alternative, we have proposed a two-step scenario, in which some of the ^{244}Pu produced by a more distant KN was absorbed into the ISM within the Local Bubble, before subsequently reaching Earth among the debris from a nearby SN.

We now summarize our conclusions. First, we reviewed the state of present and future r-process radioisotope observations.

- We have compiled a comprehensive list of possible signatures of near-Earth explosions in the form of medium-lived radioisotopes, summarizing their possible astrophysical origins and geological prospects, and assessing their detectability via AMS. Thereafter we have focused on r-process species, and presented new calculations of r-process radioisotope yields and uncertainties for selected SN and KN scenarios constrained to reproduce solar and actinide-boosted halo star abundance patterns.

- Turning to geological data, we reviewed data on deep-ocean ^{244}Pu in Fe-Mn crusts and sediments, combining searches by four groups. The published indications are intriguing: The published evidence for ^{244}Pu deposits spans an extended time period from 1 to between 12 and 25 Mya. The largest fluxes overlap the times of SN ^{60}Fe deposition, but the sustained flux over a much longer interval (if real) points toward a separate mechanism for r-process deposition on Earth.

We then performed r-process nucleosynthesis calculations, and linked them to astrophysical models for radioisotope delivery to Earth.

- We find that, for both SNe and KNe, ^{129}I is the most abundant product, with r-process mass fractions that are comparable in the different models we address here. The production of ^{107}Pd is similarly robust, but there are progressively larger variations in the yields of ^{93}Zr, ^{135}Cs, and ^{182}Hf. The rates of actinide production show the largest variations between the models, but their production ratios are relatively stable. Motivated by the discovery of live ^{244}Pu in the deep ocean, we have used these observations to anchor predictions for other actinide radioisotopes.

- For SNe, we have studied r-process radioisotope production in both a forced neutrino-driven wind scenario and a magnetohydrodynamic model. These SN scenarios struggle to make actinides at all unless neutrino processes are able to create low Y_e conditions. Thus the SN models, and particularly the unmodified MHD SN model, give high ratios of the lighter r-process radioisotopes relative to ^{244}Pu. On the other hand, KNe resulting from neutron star mergers show robust r-process actinide synthesis, and therefore have lower ratios of the lighter r-process radioisotopes relative to ^{244}Pu.

- We have studied the delivery to Earth by a nearby SN 3 Mya of ^{244}Pu and other r-process radioisotopes along with ^{60}Fe. In this one-step model, the inferred ^{244}Pu yields can be accommodated in both the forced neutrino-driven wind and MHD models. By contrast, such a one-step direct deposition of KN products is strongly inconsistent with both ^{60}Fe and ^{244}Pu data. We therefore constructed a two-step model for r-process delivery to Earth in which a KN explosion ~ 10 to ~ 50 Mya enriched the molecular cloud that gave rise to the Local Bubble. Dust grains seeded thereby with r-process radioiostopes would have bombarded the Earth thereafter. This model can account for the observed ^{244}Pu with plausible KN distances and rates.

Finally we presented a series of predictions for specific isotope ratios and discussed their observability.

- We have presented predictions for AMS searches for r-process radioisotopes in deep-ocean Fe-Mn crusts, in both the one-step SN and two-step KN scenarios. With the current AMS sensitivities, ^{129}I is the most promising. Potential AMS advances could make ^{182}Hf another

very interesting target. Additional AMS improvements would be needed to detect ^{93}Zr, ^{107}Pd, and ^{135}Cs. Whilst alternative production mechanisms may elevate the ^{236}U background, measurements of ^{236}U, ^{237}Np, and ^{247}Cm may serve as important complementary measurements to the ^{244}Pu data.

- We have also reviewed the Moon's fossil record of radioisotopes, where the systematics are very different from, and complementary to, those of geological searches. We recall that ^{60}Fe has already been discovered in the *Apollo* samples of the lunar regolith, and have discussed opportunities for the new generation of lunar sample return missions to yield evidence for r-process radioisotopes.

Our work and its larger context suggest many directions for future work, which we summarize here.

Astrophysical models:

- Explosion models remain essential, and we urge that radioisotope yields be reported for calculations within models of both SNe and KNe and in studies of their r-process outputs. An improved treatment of neutrino interactions is critical, particularly for evaluating whether realistic neutrino physics allows for SN actinide production at all in the absence of jets. Similarly, more realistic SN jet models are needed to assess their ability and frequency of actinide production.

- We urge continued work on models of SN dust formation, propagation, and injection into the heliosphere. Astrophysical models of the Local Bubble are critical, and it would be of particular interest to study the effects of injection of debris from a nearby KN. To establish the broader context of the Local Bubble and recent radioisotope production, we urge continued studies of chemical evolution models for the larger solar neighborhood. Of particular importance is the distribution of radioisotopes including r-process species, as well as their variation.

Geological and lunar studies with AMS:

- We urge geological searches for r-process radioisotopes in deep-ocean Fe-Mn crusts, most pressingly ^{129}I. There is also a clear need for more sensitive searches in deep-ocean sediments

for other live radioisotopes, coincident with the ^{60}Fe pulses and the putative ^{244}Pu signals in sediments. Improved time resolution for ^{244}Pu, including additional searches earlier than 10 Mya, is critical to determine if its flux history is coincident with or distinct from that of ^{60}Fe. Time resolution for additional radioisotopes will be similarly illuminating.

- We urge searches for r-process isotopes in the regolith samples brought to Earth recently by the *Chang'e-5* lunar mission and upcoming missions including *Artemis*.

- We urge efforts to improve the AMS sensitivities for r-process radioisotopes, especially for ^{93}Zr, ^{107}Pd, ^{182}Hf, and ^{244}Pu.

- Probes of possible live radioisotope deposits in the more distant past would also be interesting. In particular, the end of the Devonian epoch $\sim$ 360 Mya experienced an extinction event coincident with radiation UV-B damage to plant spores (Marshall et al., 2020). This could have been due to destruction of the ozone layer during cosmic-ray bombardment following an SN explosion $\sim$ 20 pc away (Fields et al., 2020). ^{244}Pu and possibly also ^{236}U can provide evidence of an SN connection to the extinction if the event produced the r-process.

Nuclear experiments and theory:

- We look forward to new data on unstable, neutron-rich nuclides whose properties set the abundance ratios described here, from experiments at current and upcoming radioactive beam facilities such as CARIBU (Savard et al., 2008) and the $N = 126$ factory (Savard et al., 2020) at ATLAS, RIBF at RIKEN (Motobayashi & Sakurai, 2012), ISAC/ARIEL at TRIUMF (Dilling et al., 2014a,b), FAIR at GSI (Kester et al., 2012), and FRIB (Gade & Sherrill, 2016; Horowitz et al., 2019). [13]

- Some key nuclear properties—particularly those of very neutron-rich species close to the neutron drip line—will remain inaccessible to experiment for the foreseeable future. Thus, advances in nuclear structure and reaction theory will also be required to improve estimates of masses, reaction rates, and fission properties and reduce yield prediction uncertainties.

We have entered an era of multi-messenger astrophysics, with the advent of gravitational wave, cosmic ray, and neutrino measurements that complement the many decades of the electromagnetic

[13] See also https://groups.nscl.msu.edu/frib/rates/fribrates.html.

spectrum that were already being explored. In particular, a new window into r-process nucleosynthesis opened with the simultaneous detection of a neutron star merger gravitational-wave event GW170817 and the electromagnetic discovery of the associated KN outburst (Abbott et al., 2017a,b). To these multi-messenger observations may be added the detection of live radioisotopes, which cast light not only on nucleosynthesis, but also on the history of the solar neighborhood and the potential impacts of nearby astrophysical events on the terrestrial environment and life. The first observations of deep-ocean deposits of live ^{60}Fe have been confirmed by many other experiments, extending to measurements of ^{60}Fe in samples of the lunar regolith, Antarctic ice, and cosmic rays. This wealth of data firmly establishes that nearby SNe occurred about 3 and 7 Myr ago, and ^{244}Pu deposition on similar time scales has now been established.

The detection of deep-ocean ^{244}Pu represents a novel probe of the r-process, one that is complementary to observations of neutron star mergers and stellar abundance patterns. Geophysical samples of live ^{244}Pu, and potentially other r-process radioisotopes, offer new laboratory-based probes of fresh nucleosynthesis products. These measurements are highly sensitive and isotopically specific, tied to a single nucleosynthesis event, and capable of helping us to infer the nature of the source–though only indirectly. In contrast, in neutron star merger observations the basic nature of the event is known, but the nucleosynthesis output may only be inferred indirectly and without isotopic or even elemental specificity. The abundances of r-process species in low-metallicity halo and dwarf galaxy stars offer a wealth of elemental information but generally no isotopic information. In general, stellar abundances sum over multiple synthesis events and, like geo-radioisotopes, do not directly identify the source(s). Clearly the most fruitful strategy is to use all of these r-process probes together, and now deep-ocean data contributes to this holistic approach.

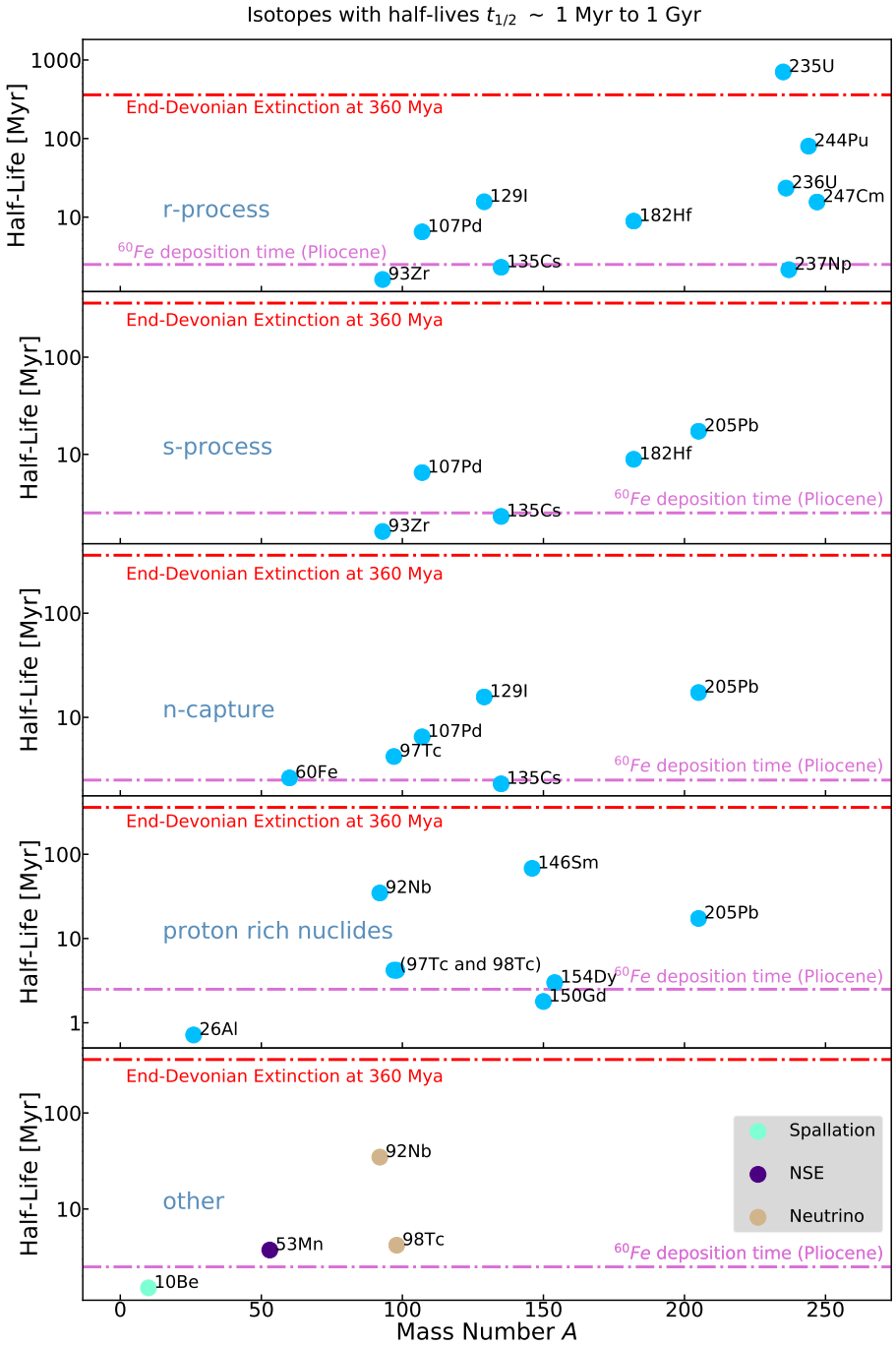

Figure 5.1: *Radioisotopes with half-lives of interest to searches for nearby SN and KN explosions. The horizontal orchid-colored lines indicate the age of the SN explosion ∼ 3 Mya attested by discoveries of deposits of* ^{60}Fe*, and the horizontal red lines mark the end-Devonian time scale. These five panels represent different nucleosynthesis channels, with the proton-rich nuclide panel including both p-process and γ-process isotopes, which are ordered by isotope mass number A.*

Table 5.1: Radioisotopes with Half-lives $t_{1/2} \sim 1$ Myr to 1 Gyr: Astrophysical Production and Geological Detection

Isotope	Half-Life (Myr)	Decay Mode	Nucleosynthesis Process (Lug18)	AMS (Kut13)	Background Measured	Notes on Extrasolar Evidence and Terrestrial Backgrounds (Section 5.3)
^{10}Be	1.51*	β^-	CR (Gos01,Mas99)	yes	yes	used as chronometer
^{26}Al	0.717	β^+, EC	proton capture	yes	yes	searches in Fe-Mn crusts
^{53}Mn	3.74	EC	NSE	yes	yes	evidence in Fe-Mn crusts (Kor20)
^{60}Fe	2.62	β^-	neutron capture	yes	no	detection in Fe-Mn crusts and nodules, deep-ocean sediments, Antarctic snow, lunar regolith, cosmic rays
^{92}Nb	34.7	β^+	α-rich freeze-out, p, ν	yes (Guo13)	no	
^{93}Zr	1.61	β^-	s (She20), r, α-rich freeze-out	yes	no	
^{97}Tc	4.2	EC	p (Nis18), n capture	no	no	possible SN ν production in Mo ore (Hax88,Ngu05)
^{98}Tc	4.2	β^-	p (Nis18), ν (Hay18)	no	no	possible SN ν production in Mo ore (Hax88,Ngu05)
^{107}Pd	6.5	β^-	s, r, n capture	yes	no	
^{129}I	15.7*	β^-	r (Dil08,Dav19) n capture	yes	yes	pre-anthropogenic background seen in Fe-Mn crusts
^{135}Cs	1.33	β^-	s, r, n capture	yes	no	
^{146}Sm	68	α	p (Nis18)	yes	no	
^{150}Gd	1.79	α	p (How93)	no	no	
^{154}Dy	3.0	α	p	no	no	
^{182}Hf	8.9	β^-	s, r (Voc04), n capture	yes	no	
^{205}Pb	17.3	EC	s, n capture	yes	no	
^{235}U	704	α	r	yes	yes	high natural background
^{236}U	23.4	α	r	yes	yes	natural and anthropogenic background
^{237}Np	2.14	α	r	yes	yes	anthropogenic background seen
^{244}Pu	80*	α 99.88% SF 0.12%	r	yes	yes	detection in Fe-Mn crusts, anthropogenic signature from global fallout (Ste13)
^{247}Cm	15.6	α	r	yes	no	possible anthropogenic background

Notes:
Our calculations use half-lives from NUBASE2016 (Audi et al., 2017) as implemented in Mumpower et al. (2018) and Sprouse et al. (2021). As indicated by asterisks, the recent NUBASE2020 update (Kondev et al., 2021) has small changes to some values, including those of the r-process species ^{129}I and ^{244}Pu.
Decay mode: β^- = β-decay, β^+ = positron emission, EC = electron capture, α = α-decay, SF = spontaneous fission
Nucleosynthesis process: CR = cosmic-ray spallation; NSE = nuclear statistical equilibrium; s = weak/limited or main slow neutron capture (s) process; p = p-process, synthesis of p-rich species by proton capture and/or γ-processes, ν = neutrino (ν) process; r = weak/limited or main rapid neutron capture (r) process; and n capture = neutron captures on preexisting species.
AMS: Accelerator mass spectrometry demonstrated for this isotope.
Background measured: Natural or anthropogenic levels detected.
References: [Dav19] Davila et al. (2019), [Dil08] Dillmann (2008), [Gos01] Gosse & Phillips (2001), [Guo13] Guozhu et al. (2013), [Hax88] Haxton & Johnson (1988), [Hay18] Hayakawa et al. (2018), [How93] Howard et al. (1993), [Kor20] Korschinek et al. (2020), [Kut13] Kutschera (2013), [Lug18] Lugaro et al. (2018), [Mas99] Masarik & Beer (1999), [Ngu05] Nguyen & Johnson (2007), [Nis18] Nishimura et al. (2018), [She20] Shetye et al. (2020), [Ste13] Steier et al. (2013), and [Voc04] Vockenhuber et al. (2004).

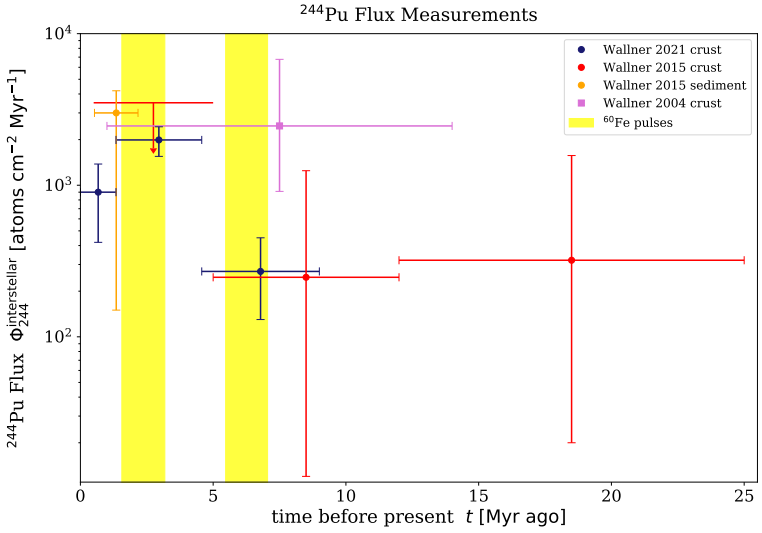

Figure 5.2: *Geological searches for* ^{244}Pu*, in deep-ocean crusts (Wallner et al., 2004, 2015b) and sediments (Paul et al., 2001; Raisbeck et al., 2007; Wallner et al., 2015b). The* ^{244}Pu *flux is* expressed as a measurement when the count is nonzero, and as a limit for zero counts and for the first (Raisbeck et al., 2007) time bin as described in the text.

Table 5.2: Geological Searches for Natural ^{244}Pu

Study	Sample	Time [Mya]	^{244}Pu Counts [at]	Flux $\Phi_{244}^{\text{interstellar}}$ [at cm^{-2} Myr^{-1}]	Fluence $\mathcal{F}_{244}^{\text{interstellar}}$ [at cm^{-2}]
Paul et al. (2001)	Sediment 92SAD01	$0-0.3$	1*	$< 2\times10^{5}$	$< 2\times10^{4}$
Wallner et al. (2004)	Crust VA13-2	1–14	1	2500	1.6×10^{4}
Raisbeck et al. (2007)	Sediment MD90-0940	2.4–2.7	1	$< 3\times10^{7}$	$< 3\times10^{6}$
Wallner et al. (2015b)	Crust 273KD	0.5–5	0	< 3500	< 800
		5–12	1	247^{+1000}_{-235}	
		12–25	1	320^{+1250}_{-300}	
	Sediment TR149-217	0.53–2.17	1	3000^{+12000}_{-850}	
Wallner et al. (2021)	Crust-3/A	0 - 1.34	34 ± 17	930 ± 480	1200 ± 600
	Crust-3/B	1.34 - 4.57	141 ± 19	1990 ± 440	6400 ± 1400
	Crust-3/C	4.57 - 9.0	$6.3^{+4.3}_{-3.2}$	270^{+180}_{-140}	1200^{+800}_{-600}

*Paul et al. (2001) argue that their detection could be due to anthropogenic contamination.

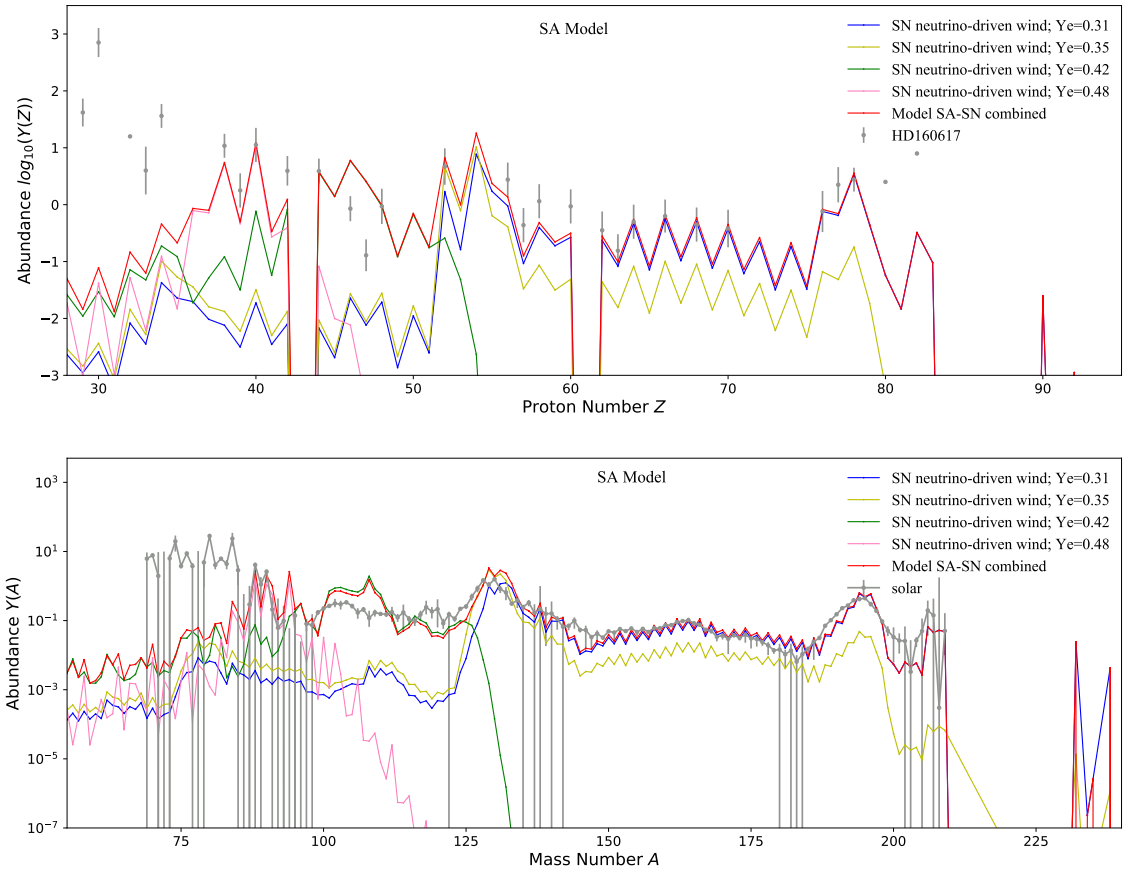

Figure 5.3: *Upper panel: The abundances at* $t \sim 10$ Gyr *of* r*-process nuclei produced in SN* forced *modifications of neutrino-driven wind simulations from Arcones et al. (2007) and Arcones & Janka (2011) with the electron fractions* $Y_e = 0.31$ *(blue),* 0.35 *(yellow),* 0.42 *(green), and* 0.48 *(pink), and a combination (SA, red) fitted to abundances measured in the metal-poor star HD 160617 (Roederer & Lawler, 2012), plotted as functions of the atomic number* Z*. Lower panel: A comparison with the corresponding solar abundance data (Arnould et al., 2007), plotted as functions of the atomic weight* A*.*

	SN Models		KN Models	
Label	SA ($\nu\star$)	SB (MHD)	KA	KB
Simulations	SN *forced* neutrino-driven wind: four trajectories from Arcones et al. (2007) and Arcones & Janka (2011) with modified $Y_e = 0.31$, 0.35, 0.42, and 0.48	MHD SN: two trajectories from Mösta et al. (2018)	KN dynamical ejecta: two trajectories from Bovard et al. (2017) diskwind: two trajectories from Just et al. (2015)	
Scaling	HD 160617: Yb, Te, Cd and Zr	HD 160617: Yb and Zr	HD 160617: Yb and Zr	J0954+5246: Yb and Zr
Mixing fractions f	$f_{0.35}$=0.757, $f_{0.42}$=1.778, and $f_{0.48}$=0.770	3.137	3.980	0.819

Table 5.3: *Combinations of* Forced *Modifications of Neutrino-driven SN Models (Arcones et al., 2007; Arcones & Janka, 2011) and MHD Models (Mösta et al., 2018) Constrained by Observations of the Metal-poor Star HD160617 (Roederer & Lawler, 2012) (SA and SB, Respectively), and Combinations of KN Dynamical Ejecta Models (Bovard et al., 2017) with Disk Neutrino-driven Wind Models from Just et al. (2015), Constrained by Observations of HD160617 (KA) or the Actinide-boost star J0954+5246 (Holmbeck et al., 2018) (KB).*

Table 5.4: r-Process Isotope Production Ratios after 10^5 yr

Radioisotope Ratio	SN Model		KN Model	
	SA	SB	KA	KB
^{60}Fe/^{244}Pu	0.39	2.5×10^4	8.6×10^{-3}	4.5×10^{-5}
^{93}Zr/^{244}Pu	35	6.4×10^5	28	1.1
^{107}Pd/^{244}Pu	1.4×10^2	3.9×10^5	18	1.8
^{129}I/^{244}Pu	7.1×10^2	4.5×10^6	1.8×10^2	41
^{135}Cs/^{244}Pu	48	1.2×10^6	2.6	13
^{182}Hf/^{244}Pu	7.5	1.2×10^4	1.5	0.28
^{232}Th/^{244}Pu	2.7	24	1.7	0.65
^{235}U/^{244}Pu	2.9	15	3.1	1.7
^{236}U/^{244}Pu	3.8	23	3.7	2.4
^{238}U/^{244}Pu	2.2	9.6	2.4	1.5
^{237}Np/^{244}Pu	3.3	8.9	3.4	2.6
^{242}Pu/^{244}Pu	1.9	2.6	1.9	1.9
^{247}Cm/^{244}Pu	1.1	1.2	0.97	1.0
^{248}Cm/^{244}Pu	1.1	1.5	0.86	1.1

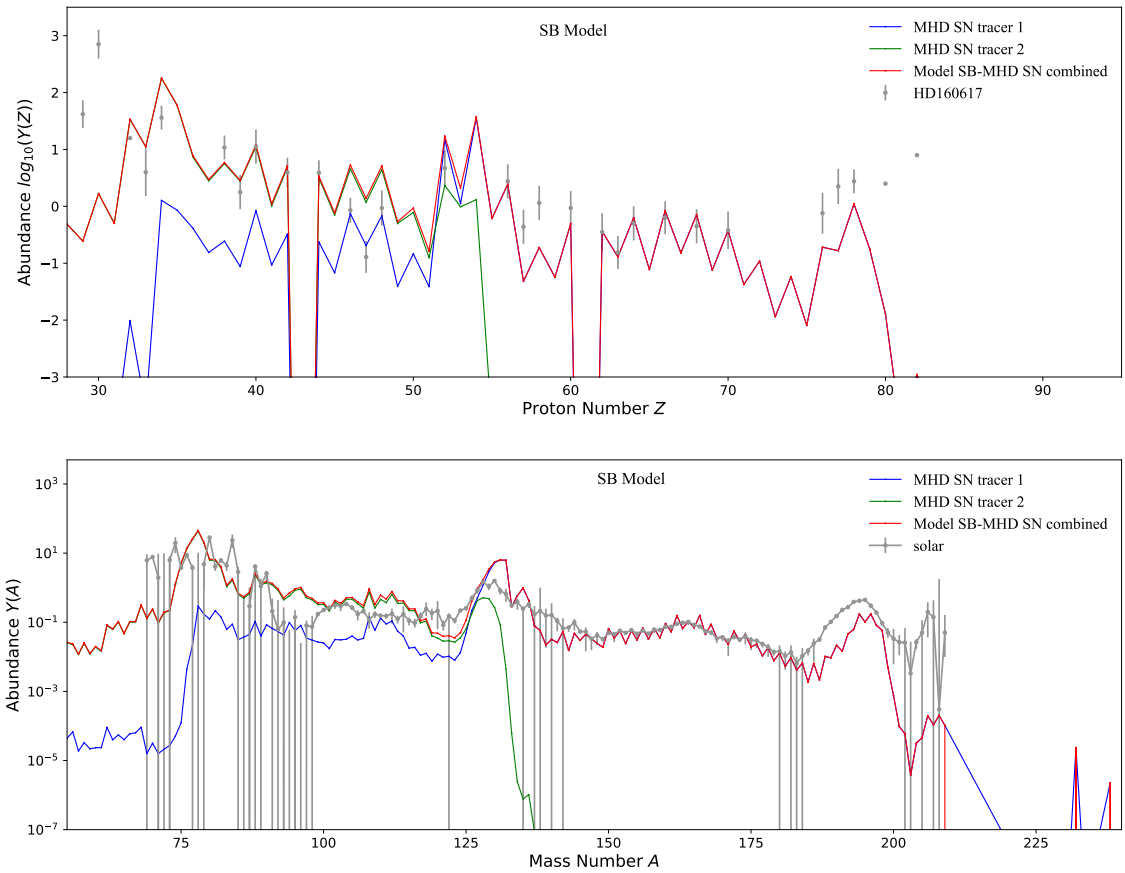

Figure 5.4: *Upper panel: The abundances at* $t \sim 10$ Gyr *of r-process nuclei produced in MHD SN simulations from Mösta et al. (2018) with two different tracers 1 (blue) and 2 (green) and a combination (SB, red) fitted to the abundances of ytterbium and zirconium measured in the metal-poor star HD 160617 (Roederer & Lawler, 2012), plotted as functions of the atomic number* Z*. Lower panel: A comparison with the corresponding solar abundance data (Arnould et al., 2007), plotted as functions of the atomic weight* A*.*

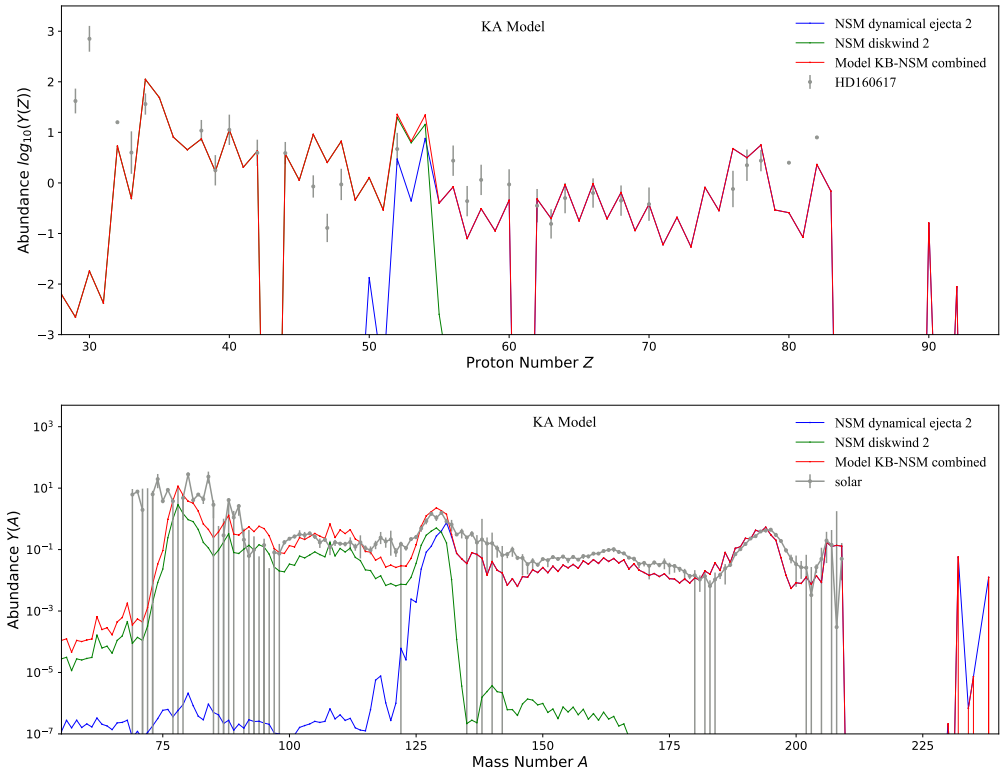

Figure 5.5: *Upper panel: The abundances at* $t \sim 10$ Gyr *of r-process nuclei produced in simulations of KN dynamical ejecta from Bovard et al. (2017) (blue) and of disk neutrino-driven wind from Just et al. (2015) (green), and a mixture (KA, red) fitted to measurements of the metal-poor star HD 160617 (Roederer & Lawler, 2012), plotted as functions of the atomic number* Z*. Lower panel: The corresponding abundance pattern of model KA compared with solar abundance data (Arnould et al., 2007), plotted as functions of the atomic weight* A*.*

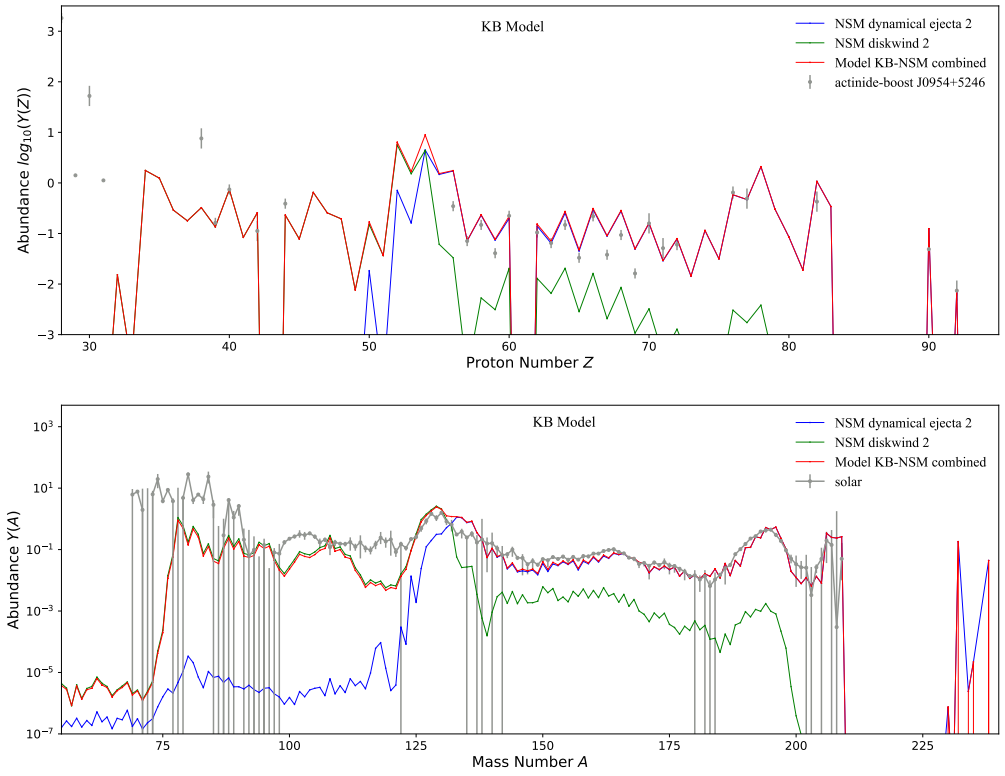

Figure 5.6: *Upper panel: The abundances (at* $t \sim 10Gyr$*) of r-process nuclei produced in simulations of KN more neutron-rich dynamical ejecta from Bovard et al. (2017) (blue) and of disk neutrino-driven wind from Just et al. (2015) (green), and a mixture (KB, red) fitted to the measurements of the actinide-boost star J0954+5346 (Holmbeck et al., 2018), plotted as functions of the atomic number Z. Lower panel: The corresponding abundance pattern of model KB compared with solar abundance data (Arnould et al., 2007), plotted as functions of the atomic weight A.*

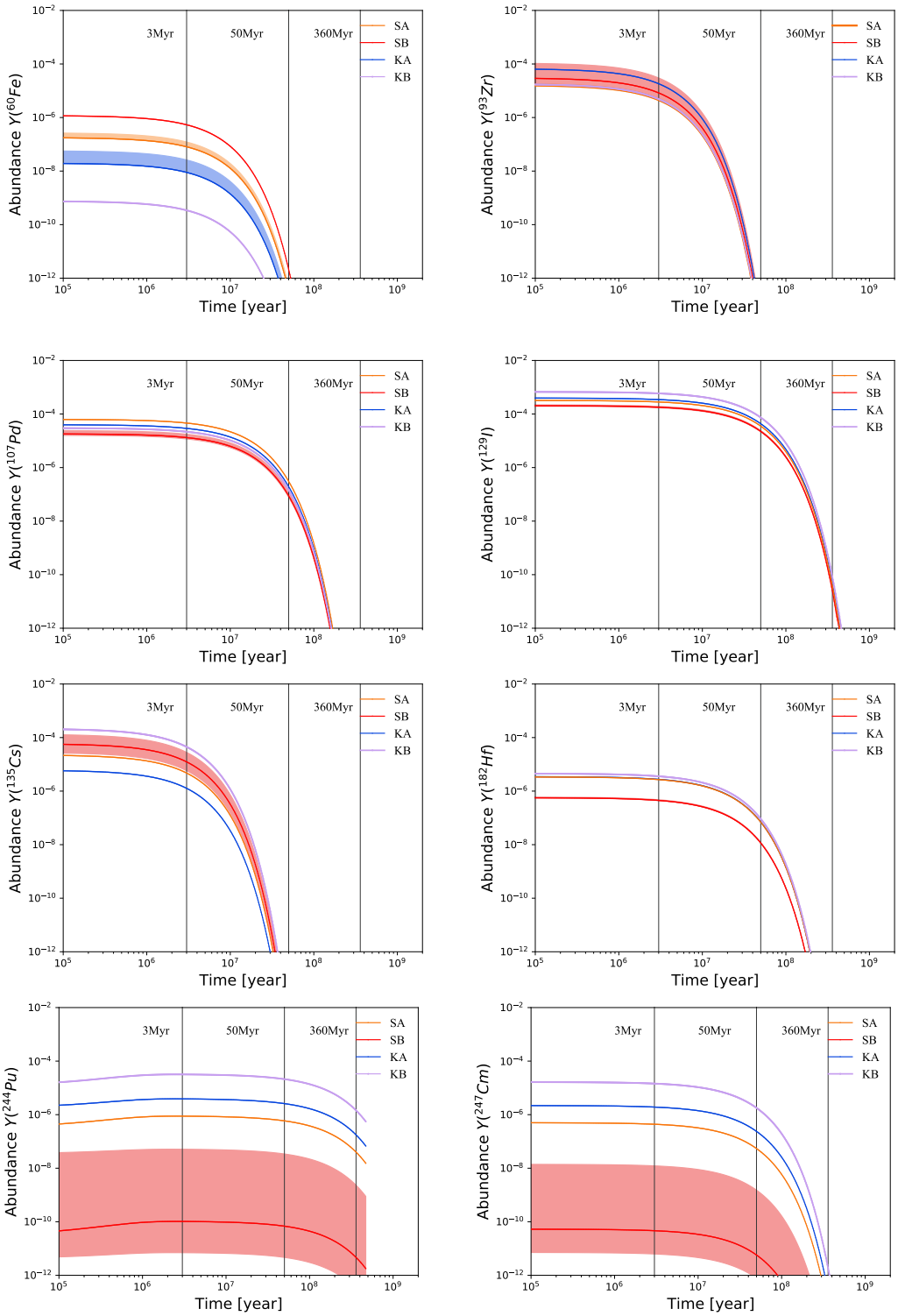

Figure 5.7: *The time evolutions of the relative abundances of* ^{60}Fe, ^{93}Zr, ^{107}Pd, ^{129}I, ^{135}Cs, ^{182}Hf, ^{244}Pu, *and* ^{247}Cm *from an r-process event as calculated with the different astrophysical models described in Table 5.3, with the total mass of r-process species normalized to unity for each model. The solid lines were obtained using our baseline r-process calculation, and the shaded bands are the ranges due to uncertainties resulting from the adoption of different nuclear data (HFB masses from Goriely et al. (2009) or β-decay rates from Marketin et al. (2016) for both SN and KN models, or fission yields from Kodama & Takahashi (1975) for KN models, in addition to the baseline nuclear data) in this calculation (orange: SA; red: SB; blue: KA; and light purple: KB). The vertical lines indicate the age of the supernova explosion* ~ 3 *Mya attested by discoveries of deposits of* ^{60}Fe, *an age of* 50 *Mya comparable with the half-life of* ^{244}Pu, *and the age of the end-Devonian extinction(s)* ~ 360 *Mya.*

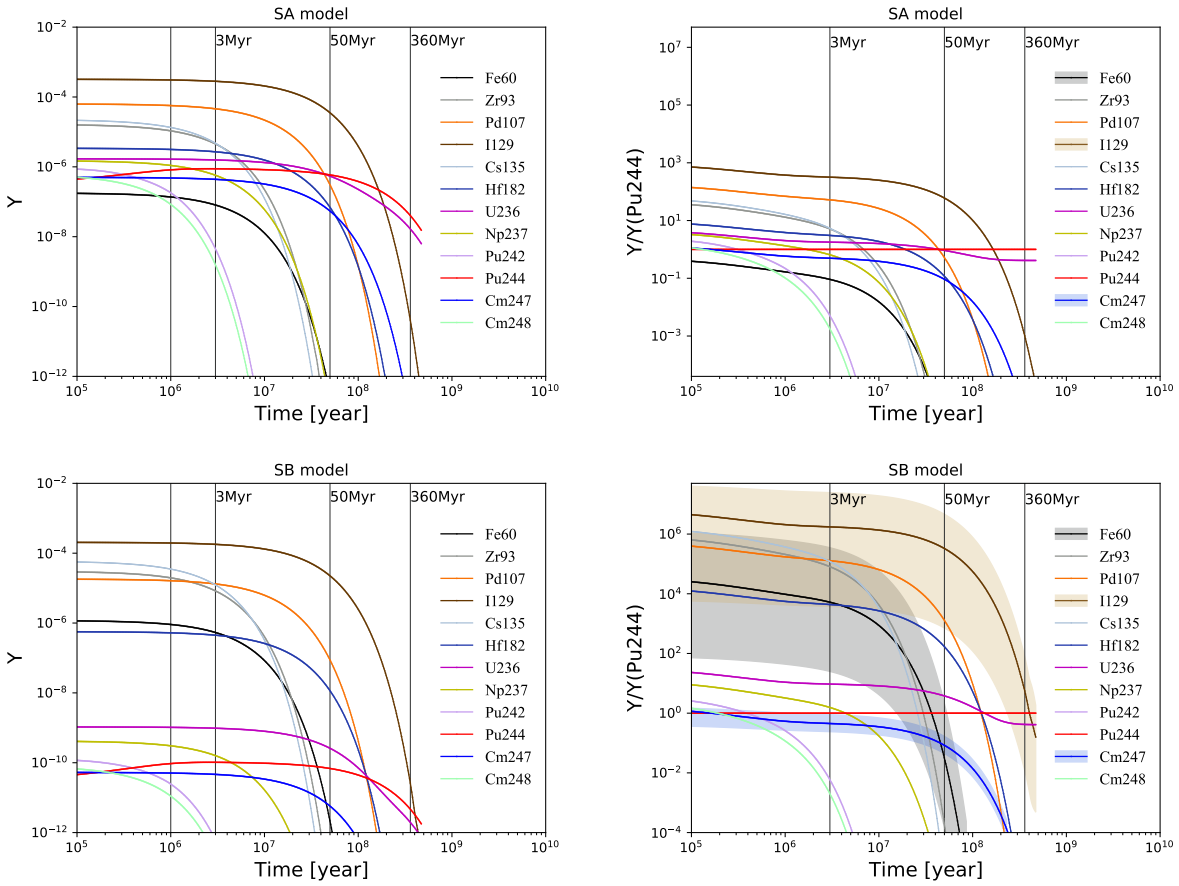

Figure 5.8: *The time evolution of the abundances Y (left) and ratios $Y/Y(^{244}\mathrm{Pu})$ (right) of r-process nuclei of interest from SN model SA (top panels) and MHD SN model SB (bottom panels). The vertical lines indicate the age of the SN explosion ~ 3 Mya attested by discoveries of deposits of ^{60}Fe, 50 Mya comparable with the half-life of ^{244}Pu, and the age(s) of the end-Devonian extinction(s) ~ 360 Mya. The ratio ranges due to the nuclear variations as described in the text for ^{60}Fe, ^{129}I and ^{247}Cm to ^{244}Pu are shown in shaded bands of black, brown, and blue, respectively.*

Table 5.5: r-Process Isotope Ratios after 3 Myr, Corresponding to the Event near the end of the Pliocene Era, together with Their Ranges σ Found in the Different Nuclear Models Adopted (HFB Masses from Goriely et al. (2009) and β-Decay Rates from Marketin et al. (2016) for Both SN and KN Models, as well as Fission Yields from Kodama & Takahashi (1975) for KN Models), in addition to the Baseline Calculations in the r-Process Simulations.

Radioisotope Ratio	SN Model		KN Model	
	SA	SB	KA	KB
^{60}Fe/^{244}Pu	9.2×10^{-2}	5.3×10^{3}	2.3×10^{-3}	1.1×10^{-5}
σ (^{60}Fe/^{244}Pu)	9.2×10^{-2} - 5.6×10^{2}	25 - 3.5×10^{5}	1.4×10^{-3} - 1.3×10^{-2}	$(1.1 - 4.0) \times 10^{-5}$
^{93}Zr/^{244}Pu	5.2	8.2×10^{4}	4.8	0.15
σ(^{93}Zr/^{244}Pu)	5.2 - 2.4×10^{4}	93 - 4.3×10^{6}	0.59 - 14	0.15 - 0.97
^{107}Pd/^{244}Pu	52	1.3×10^{5}	7.5	0.69
σ(^{107}Pd/^{244}Pu)	50 - 2.0×10^{5}	3.4×10^{2} - 1.7×10^{6}	2.4 - 7.5	0.69 - 1.5
^{129}I/^{244}Pu	3.2×10^{2}	1.7×10^{6}	89	19
σ(^{129}I/^{244}Pu)	2.8×10^{2} - 7.3×10^{5}	3.8×10^{3} - 2.4×10^{7}	46 - 89	19 - 38
^{135}Cs/^{244}Pu	5.4	1.2×10^{5}	0.33	1.4
σ(^{135}Cs/^{244}Pu)	5.4 - 1.9×10^{4}	1.2×10^{2} - 4.1×10^{6}	0.33 - 1.4	0.30 -3.9
^{182}Hf/^{244}Pu	3.1	4.4×10^{3}	0.71	0.11
σ(^{182}Hf/^{244}Pu)	3.1 - 2.6×10^{4}	8.7 - 6.8×10^{4}	0.71 - 9.0	0.11 - 2.3
^{232}Th/^{244}Pu	1.5	11	1.2	0.43
σ(^{232}Th/^{244}Pu)	0.23 - 6.0	0.31 - 16	0.36 - 1.2	0.27 - 0.63
^{235}U/^{244}Pu	1.6	7.0	1.9	0.99
σ(^{235}U/^{244}Pu)	1.2 - 7.2	2.0 - 21	1.4 - 4.6	0.99 - 1.7
^{236}U/^{244}Pu	1.8	9.5	2.0	1.1
σ(^{236}U/^{244}Pu)	1.2 - 4.1	2.0 - 9.5	1.2 - 2.5	0.79 - 1.1
^{238}U/^{244}Pu	2.1	5.4	2.5	1.8
σ(^{238}U/^{244}Pu)	2.1 - 3.2	3.2 - 6.9	2.0 - 2.7	1.7 - 1.8
^{237}Np/^{244}Pu	0.66	1.6	0.78	0.53
σ(^{237}Np/^{244}Pu)	0.66 - 1.9	1.0 - 2.6	0.78 - 1.9	0.53 - 2.0
^{242}Pu/^{244}Pu	5.3×10^{-3}	6.2×10^{-3}	6.0×10^{-3}	5.2×10^{-3}
σ(^{242}Pu/^{244}Pu)	$(5.3 - 6.7) \times 10^{-3}$	$(6.2 - 8.8) \times 10^{-3}$	$(5.0 - 6.1) \times 10^{-3}$	$(5.0 - 5.6) \times 10^{-3}$
^{247}Cm/^{244}Pu	0.50	0.45	0.50	0.46
σ(^{247}Cm/^{244}Pu)	0.48 - 0.87	0.24 - 0.90	0.62 - 1.2	0.46 - 1.4
^{248}Cm/^{244}Pu	1.9×10^{-3}	2.1×10^{-3}	1.6×10^{-3}	1.9×10^{-3}
σ(^{248}Cm/^{244}Pu)	$(1.3 - 1.9) \times 10^{-3}$	$(1.0 - 2.1) \times 10^{-3}$	$(1.5 - 2.3) \times 10^{-3}$	$(1.9 - 2.2) \times 10^{-3}$

Table 5.6: r-Process Isotope Ratios after 50 Myr, comparable with the half-life of ^{244}Pu.

Radioisotope	SN Model		KN Model	
Ratio	SA	SB	KA	KB
^{60}Fe/^{244}Pu	5.9×10^{-7}	3.2×10^{-2}	1.4×10^{-8}	6.6×10^{-11}
^{93}Zr/^{244}Pu	1.5×10^{-7}	2.0×10^{-4}	1.2×10^{-8}	3.8×10^{-10}
^{107}Pd/^{244}Pu	0.53	1.3×10^{3}	7.6×10^{-2}	6.9×10^{-3}
^{129}I/^{244}Pu	60	3.3×10^{5}	17	3.5
^{135}Cs/^{244}Pu	2.0×10^{-10}	4.5×10^{-6}	1.2×10^{-11}	5.4×10^{-11}
^{182}Hf/^{244}Pu	0.12	1.7×10^{2}	0.028	4.4×10^{-3}
^{232}Th/^{244}Pu	4.6	28	4.2	2.1
^{235}U/^{244}Pu	2.9	11	3.4	2.0
^{236}U/^{244}Pu	0.93	3.8	1.0	0.68
^{238}U/^{244}Pu	3.2	8.1	3.8	2.6
^{247}Cm/^{244}Pu	9.3×10^{-2}	8.4×10^{-2}	9.2×10^{-2}	8.5×10^{-2}

Table 5.7: r-Process Isotope Ratios after 360 Myr, corresponding to the time since the end-Devonian mass extinction(s).

Radioisotope	SN Model		KN Model	
Ratio	SA	SB	KA	KB
^{129}I/^{244}Pu	4.1×10^{-3}	30	1.3×10^{-3}	2.3×10^{-4}
^{232}Th/^{244}Pu	85	4.4×10^{2}	81	49
^{235}U/^{244}Pu	30	1.1×10^{2}	34	20
^{236}U/^{244}Pu	0.41	0.42	0.41	0.41
^{238}U/^{244}Pu	41	1.0×10^{2}	48	33

Table 5.8: Predicted Interstellar Fluences for r-Process Radioisotopes based on ^{244}Pu

	$\mathcal{F}$(3 Myr)				$\mathcal{F}$(10 Myr)		$\mathcal{F}$(20 Myr)		$\mathcal{F}$(50 Myr)	
Isotope	SA	SB	KA	KB	KA	KB	KA	KB	KA	KB
^{93}Zr	5.1(3)	8.0(7)	4.7(3)	1.5(2)	2.3(3)	7.5(1)	7.1(1)	2.3(0)	5.8(-4)	1.9(-5)
^{107}Pd	5.1(4)	1.3(8)	7.4(3)	6.7(2)	3.7(4)	3.4(3)	2.8(4)	2.5(3)	3.7(3)	3.4(2)
^{129}I	3.1(5)	1.7(9)	8.7(4)	1.8(4)	6.8(5)	1.4(5)	9.6(5)	2.0(5)	8.3(5)	1.7(5)
^{135}Cs	5.3(3)	1.2(8)	3.2(2)	1.4(3)	8.5(1)	3.7(2)	1.1(0)	4.7(0)	6.0(-7)	2.7(-6)
^{182}Hf	3.0(3)	4.3(6)	7.0(2)	1.1(2)	4.3(3)	6.7(2)	4.3(3)	6.8(2)	1.4(3)	2.1(2)
^{236}U	1.8(3)	9.3(3)	2.0(3)	1.1(3)	1.7(4)	1.0(4)	3.0(4)	1.8(4)	4.9(4)	3.4(5)
^{237}Np	6.4(2)	1.5(3)	7.6(2)	5.2(3)	8.1(2)	5.5(2)	7.2(1)	4.9(1)	1.5(-2)	1.0(-2)
^{247}Cm	4.9(2)	4.4(2)	4.9(2)	4.5(2)	3.8(3)	3.5(3)	5.3(3)	4.9(3)	4.5(3)	4.2(3)

Notes. The interstellar fluences $\mathcal{F}^{\text{interstellar}}$ *are normalized relative to the fluence of* ^{244}Pu*, and are expressed in units of* [atoms cm^{-2}]*, using the notation* $A(B) \equiv A \times 10^{B}$*. All results are for the present day, and include the effects of decay. The signal at 3 Mya assumes a flux duration of 1 Myr, and the others assume a constant flux after the event.*

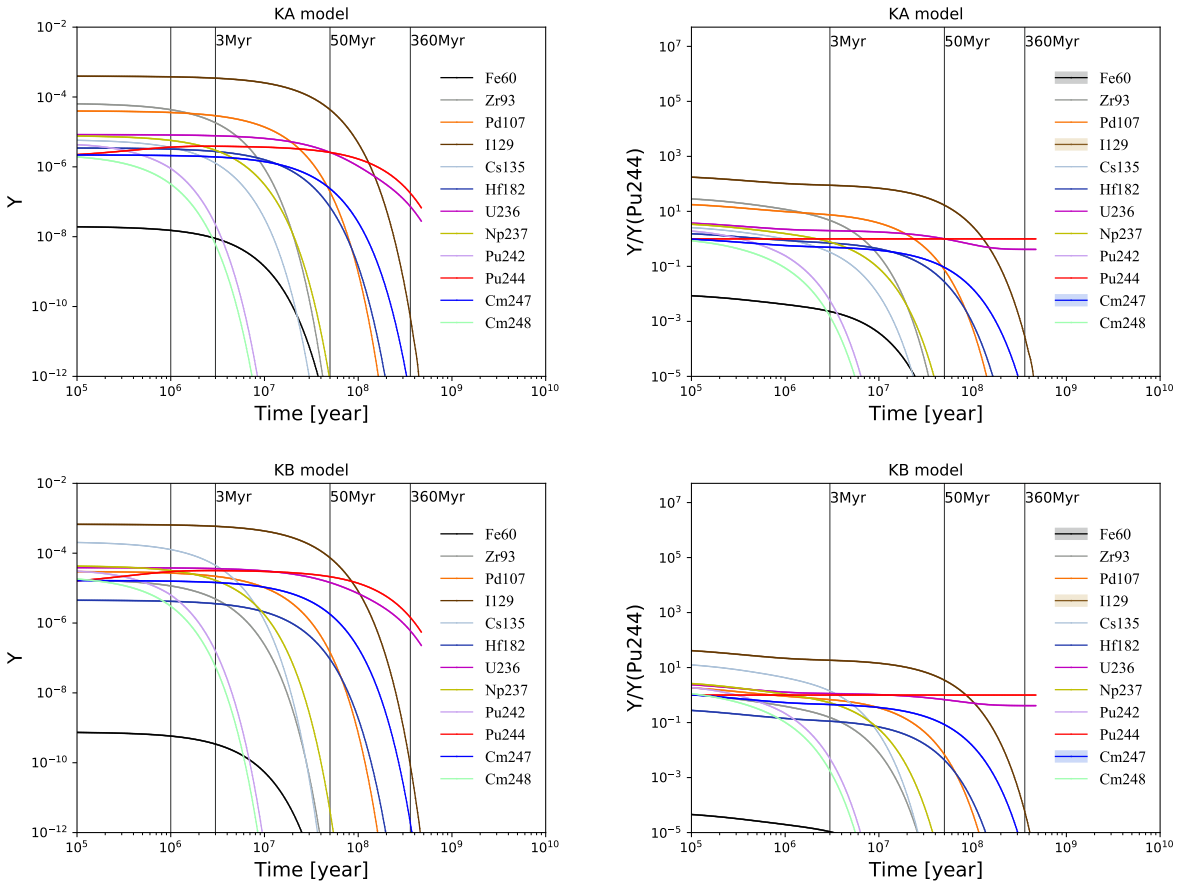

Figure 5.9: *The time evolution of the abundances Y (left) and ratios $Y/Y(^{244}\mathrm{Pu})$ (right) of r-process nuclei of interest from KM models KA (top) and KB (bottom). The vertical lines correspond to the age of the SN explosion ~ 3 Mya attested by discoveries of deposits of ^{60}Fe, ~ 50 Mya comparable with the half-life of ^{244}Pu, and the time since the end-Devonian extinction(s) ~ 360 Mya. The ratio ranges due to the nuclear variations as described in the text for ^{60}Fe, ^{129}I and ^{247}Cm to ^{244}Pu are shown in shaded bands of black, brown, and blue, respectively.*

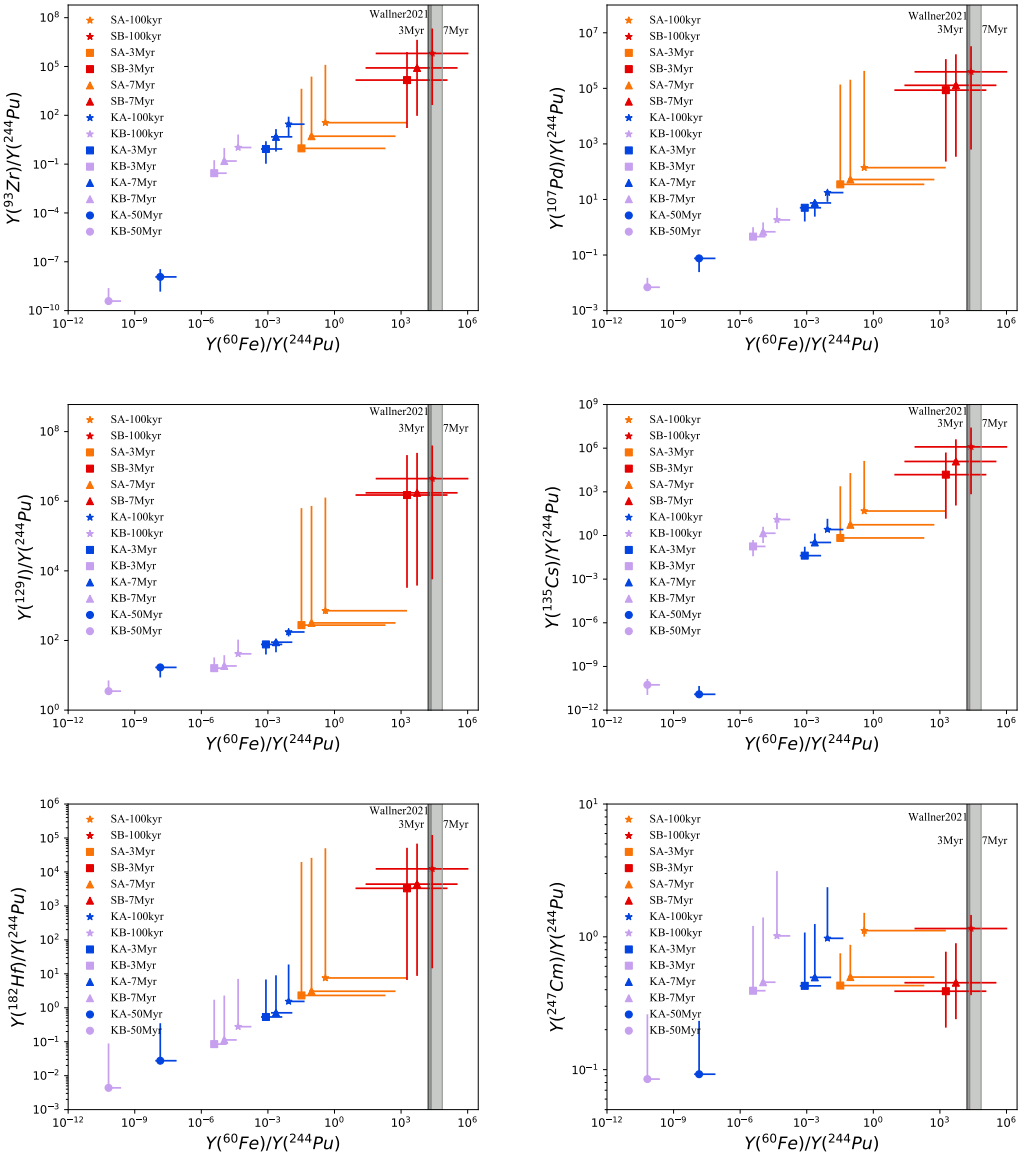

Figure 5.10: *Scatterplots of the isotope abundance ratios of* ^{93}Zr, ^{107}Pd, ^{129}I, ^{135}Cs,^{182}Hf, *and* ^{247}Cm/^{244}Pu *versus* ^{60}Fe/^{244}Pu *after times 100 kyr, 3 Myr and 7 Myr (also 50 Myr for the KN models KA and KB), as calculated with the different astrophysical* r*-process models described in Table 5.3. The points are the isotope ratios obtained from the baseline r-process calculations, and the error bars denote the variations due to the different sets of nuclear models (HFB masses from Goriely et al. (2009) or β-decay rates from Marketin et al. (2016) for both SN and KN models, or fission yields from Kodama & Takahashi (1975) for KN models, in addition to the baseline nuclear data) adopted in the r-process. Note that the isotope ratios presented here are only from the r-process nucleosynthesis. For SNe,* ^{60}Fe *is mainly produced in the pre-SN stage and through explosive nucleosynthesis; thus the isotope ratios of* ^{60}Fe/^{244}Pu *in the plot are actually the lower limit for SN models SA and SB. The shaded bands are the measured isotope ratios of* ^{60}Fe/^{244}Pu *at ∼3 Myr (1.34-4.57 Myr; dark gray) and ∼7 Myr (4.57-9.0 Myr; gray) time periods from Wallner et al. (2021).*

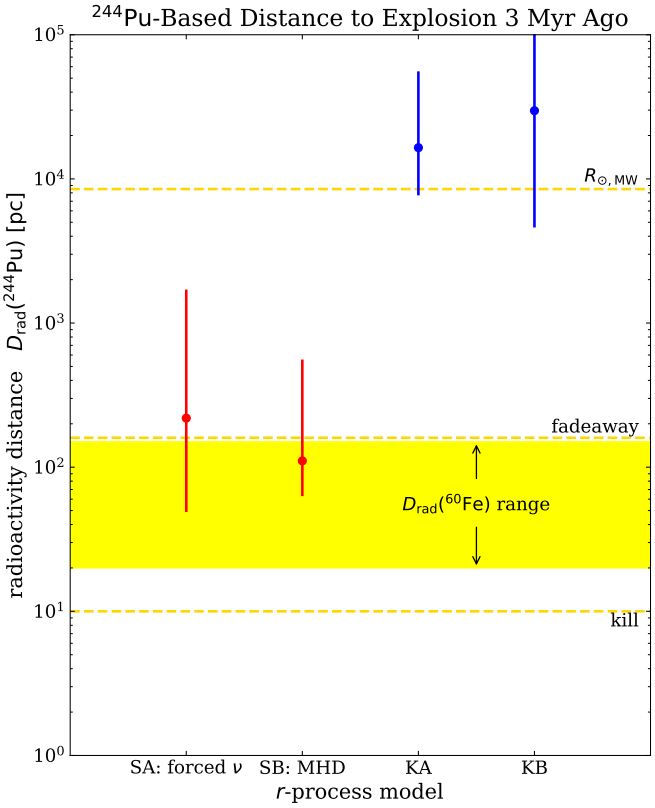

Figure 5.11: *The estimated radioactivity distances to possible events that are candidates for having produced* ^{244}Pu *3 Mya. The distance* $D_{\rm rad} \sim (f_{\rm dust} M_{\rm ej,244}/\mathcal{F}_{244}^{\rm interstellar})^{1/2}$ *depends on the dust fraction, the model yield of* ^{244}Pu*, and the interstellar flux. We see that SN models lead to distances consistent with that inferred from* ^{60}Fe *data, shown in the yellow band, and lie between the "kill" and "fadeaway" distances. On the other hand, KN models lead to distances far too large to allow for* ^{244}Pu *transport, namely distances similar to or larger than the Sun's distance* $R_{\odot,\rm MW}$ *from the Galactic center. Here we assume* $f_{\rm dust} = 1$*; smaller values lead to smaller inferred distances.*

Table 5.9: Predictions for r-Process Radioisotopes in Fe-Mn Crusts based on ^{244}Pu after 3 Myr

	Concentration [atoms g^{-1}]				Ratio	Measure-ment	Crust Elemental Abundance	Predicted Signal Ratio			
Isotope	SA	SB	KA	KB	$N_i^{\rm astro}/N_j^{\rm bg}$	Limit	X_j	SA	SB	KA	KB
^{93}Zr	6.5(2)	1.0(7)	5.9(2)	1.9(1)	^{93}Zr/^{92}Zr	2×10^{-11}	6.5×10^{-4}	8.9(-16)	1.4(-11)	8.2(-16)	2.7(-17)
^{107}Pd	6.5(3)	1.6(7)	9.4(2)	8.6(1)	^{107}Pd/^{106}Pd	10^{-8}	1.7×10^{-9}	2.5(-9)	6.1(-6)	3.6(-10)	3.3(-11)
^{129}I	4.0(4)	2.2(8)	1.1(4)	2.3(3)	^{129}I/^{127}I	10^{-14}	5×10^{-6}	1.7(-11)	9.2(-8)	4.7(-12)	9.8(-13)
^{135}Cs	6.8(2)	1.5(7)	4.2(1)	1.8(2)	^{135}Cs/^{133}Cs	9×10^{-12}	1.5×10^{-6}	1.0(-13)	2.2(-9)	6.1(-15)	2.6(-14)
^{182}Hf	3.8(2)	5.5(5)	8.9(1)	1.4(1)	^{182}Hf/^{180}Hf	10^{-11}	8×10^{-6}	4.5(-14)	6.4(-11)	1.0(-14)	1.7(-15)
^{236}U	2.2(2)	1.2(3)	2.5(2)	1.4(2)	^{236}U/^{238}U	10^{-13}	10^{-5}	8.9(-15)	4.7(-14)	1.0(-14)	5.7(-15)
^{237}Np	8.2(1)	2.0(2)	9.7(1)	6.6(1)	^{237}Np/^{238}U	5×10^{-11}	10^{-5}	3.3(-15)	7.8(-15)	3.9(-15)	2.6(-15)
^{247}Cm	6.2(1)	5.6(1)	6.2(1)	5.7(1)	^{247}Cm/^{238}U	-	10^{-5}	2.5(-15)	2.3(-15)	2.5(-15)	2.3(-15)

Notes. The values are expressed as $A(B) \equiv A\times10^B$. *The crust abundances are taken from Merchel et al. (2000), and we assume* $\Phi^{\rm interstellar}(^{244}{\rm Pu})$ *fluxes in eqs. (5.4) and (5.5). The uptake is assumed to be* $U = 0.10$ *in all cases. The isotopic concentration* $n_i^{\rm astro}/\rho$ *is the number of atoms of isotope* i *per gram of crust. The crust elemental abundances* X_j *are mass fractions; for* ^{237}Np *and* ^{247}Cm, *the uranium abundance is given. The measurement limits are the AMS sensitivities for* ^{93}Zr *(Hain et al., 2018; Martschini et al., 2019; Pavetich et al., 2019),* ^{107}Pd *(Korschinek et al., 1994),* ^{129}I *(Vockenhuber et al., 2015),* ^{135}Cs *(Yin et al., 2015) and* ^{182}Hf *(Vockenhuber et al., 2004); see discussion in §5.6.4.*

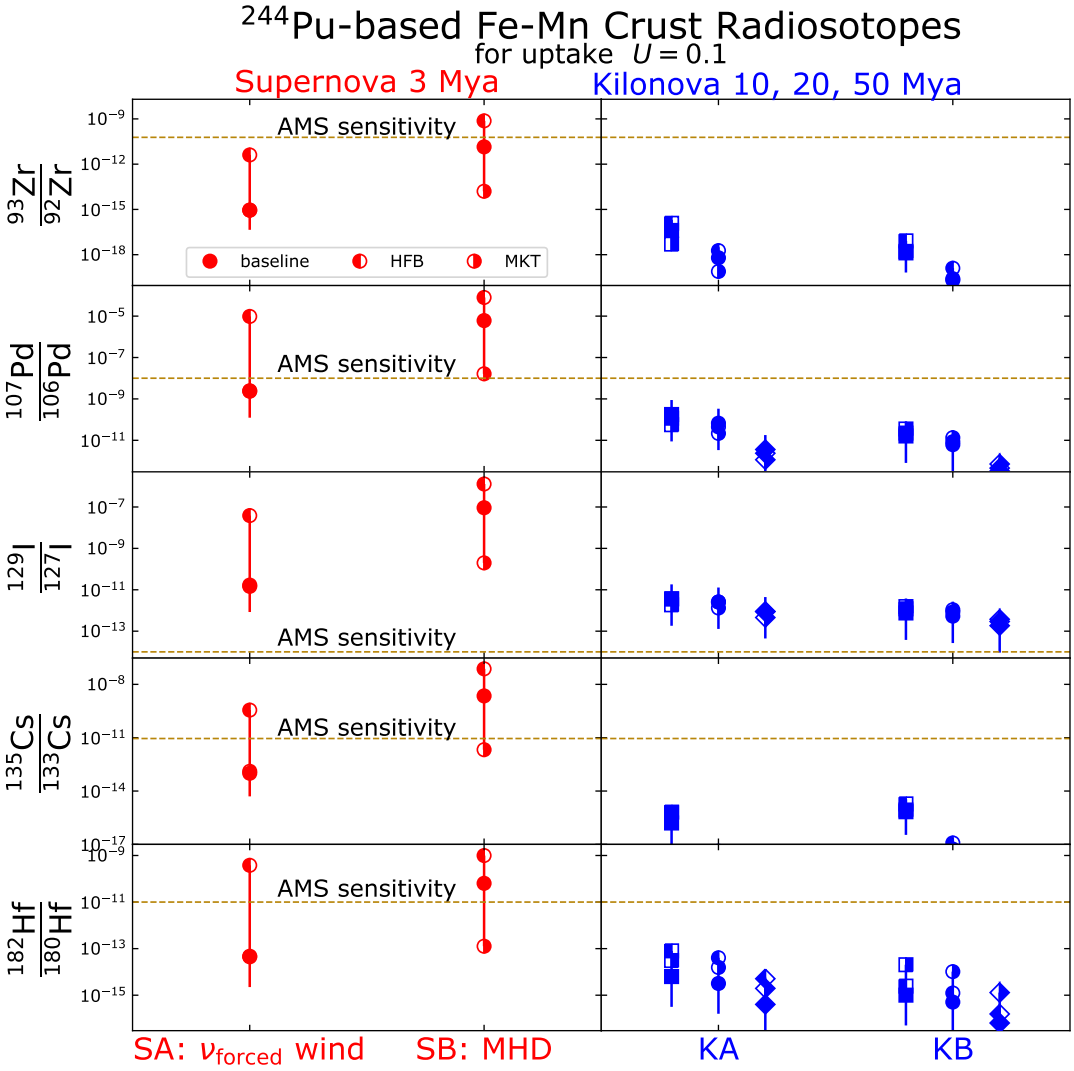

Figure 5.12: *Radioisotope predictions normalized to the Wallner et al. (2015b)* ^{244}Pu *flux from Eqs. (5.4) and (5.5). The predictions are normalized to a 10% uptake, and assume dust efficiency equal to that of Pu; for other values multiply by* $U_i f_i / f_{\rm Pu}$*. The uncertainties are only those due to the* ^{244}Pu *flux, and the measurement limits are those listed in Table 5.9. The predictions are from (left panels) the SN* r*-process models after 3 Myr and (right panels) the KN* r*-process models after 10, 20, and 50 Myr. The results from our baseline calculations are shown as full symbols, and the half-filled symbols are results from HFB and MKT calculations. A minor change to the figure should be made for* ^{93}Zr/^{92}Zr *from* 6×10^{-11} *to a new value of* 2×10^{-11} *in light of a new citation that has been added to the text.*

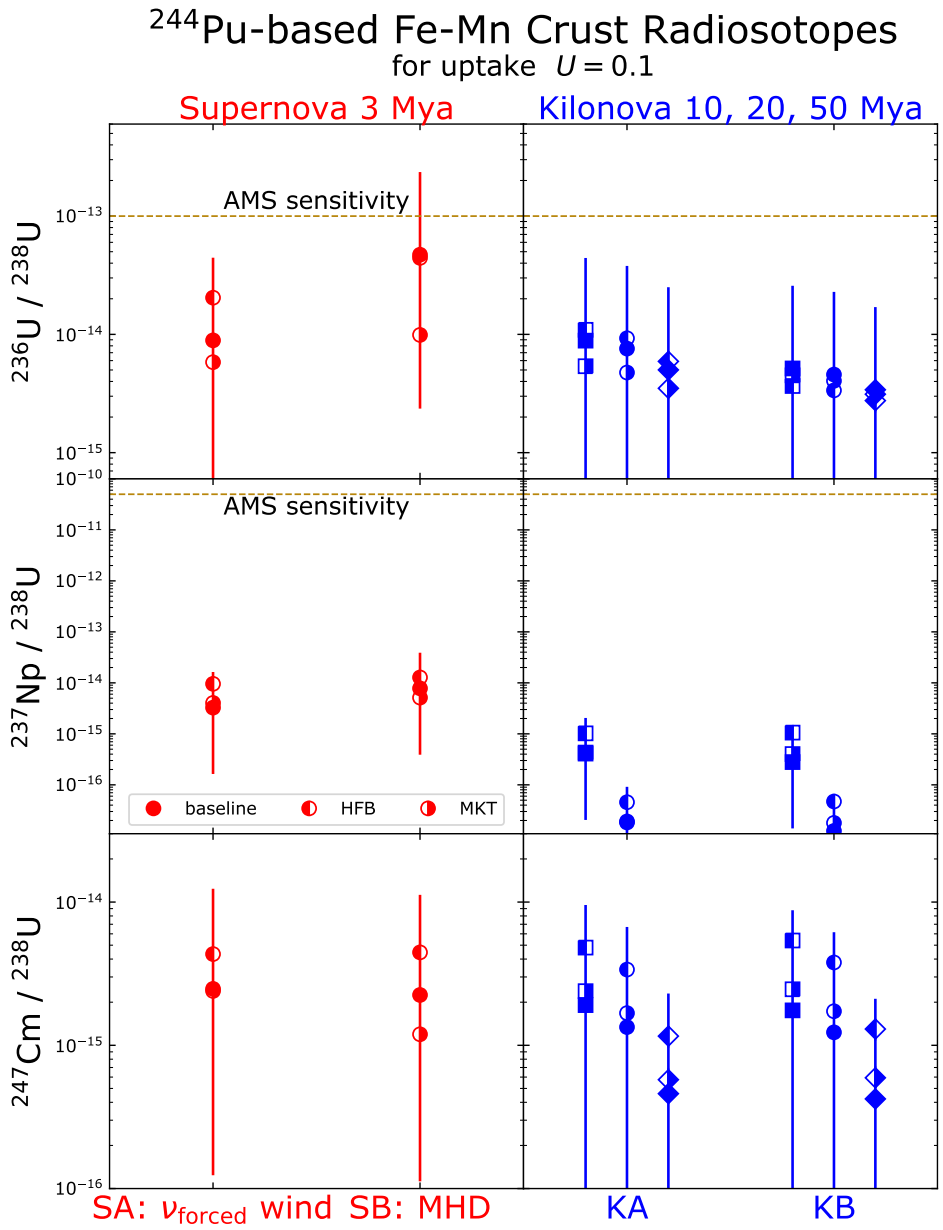

Figure 5.13: *Predicted abundances of the actinides* ^{236}U, ^{237}Np, *and* ^{247}Cm *in Fe-Mn crusts, shown for the same SN and KN models as in Fig. 5.12. We use* ^{238}U *as the reference standard for all three species. The results from our baseline calculations are shown as full symbols, and the half-filled symbols are results from HFB and MKT calculations.*

Table 5.10: Estimated mean oceanic concentrations of selected elements, adapted from Nozaki (2001)

Element	Mean oceanic mass fraction ($\times 10^{-12}$)	Type of Distribution	Leaves Solution Rapidly
Mn	20	s	yes
Fe	30	s + n	yes
Zr	15	s + n	yes
Pd	0.06	n	yes
I (IO_3^-)	5.8×10^4	c	no
I (I^-)	4.4	r + s	yes
Cs	310	c	no
Hf	0.07	s + n	yes
U	3.2×10^3	c	no
Np	$\sim 10^{-5}$	c	no
Pu	-	r + s	yes
Cm	-	s?	?

Notes. In this Table c denotes an element whose distribution is conservative, in the sense that it follows the salinity of the ocean water, n denotes a distribution that increases with depth, like that of typical nutrients in the water, s denotes an element that attaches to particulate matter and may be concentrated ("scavenged") at the water/sediment interface, and r denotes an element whose distribution is controlled by reduction and oxidation reactions ("redox-controlled") and may be formed in oceanic basins that are depleted in oxygen ("anoxic") (Nozaki, 2001). ^{237}Np *results are from Lindahl et al. (2005). We note also that there may be other geochemical and biological processes that affect the rates of uptake of different radionuclides in various materials. For example, "magnetotactic" bacteria that orientate themselves along magnetic fields* secrete iron and therefore concentrate ^{60}Fe, as discussed in Ludwig et al. (2016), and certain sorts of organic matter may absorb plutonium effectively (J. Marshall, private communication, 2021), specifically in anoxic environments. Schneider & Livingston (1984) measured anthropogenic ^{242}Cm and ^{244}Cm in Scottish coastal sediments, and summarized data indicating that ^{244}Cm has also been detected in fish and seaweed but not in seawater; we also note that curium adheres very tightly to soil particles.

Table 5.11: Ferromanganese Crusts with Measured ^{129}I Profiles (Ji et al., 2015a,b)

Crust Name	Crust Location	Elemental Mass Fractions X(Fe)	Elemental Mass Fractions X(I)	^{129}I/^{127}I Ratio/10^{-12}	^{129}I/Fe
CDX80-1	(19°57.9′ N, 172°55.1′ E)	$0.05 - 0.20$	$(2.7 - 7.7) \times 10^{-5}$	≤ 1.27	$\leq 10^{-15}$
MDP5D44	(10°20.24′ N, 167°26.5′ W)	$0.10 - 0.20$	$(3.8 - 10.9) \times 10^{-5}$	≤ 0.48	$\leq 10^{-15}$

The ranges of the iron and iodine fractions in the crust sample CDX80-1 (MDP5D44) shown are for depths $\in (0.5, 4)$ *cm* ($\in (1.6, 5)$ *cm) and the iodine isotope ratios shown are for depths* > 0.5 *cm* (> 1 *cm).*

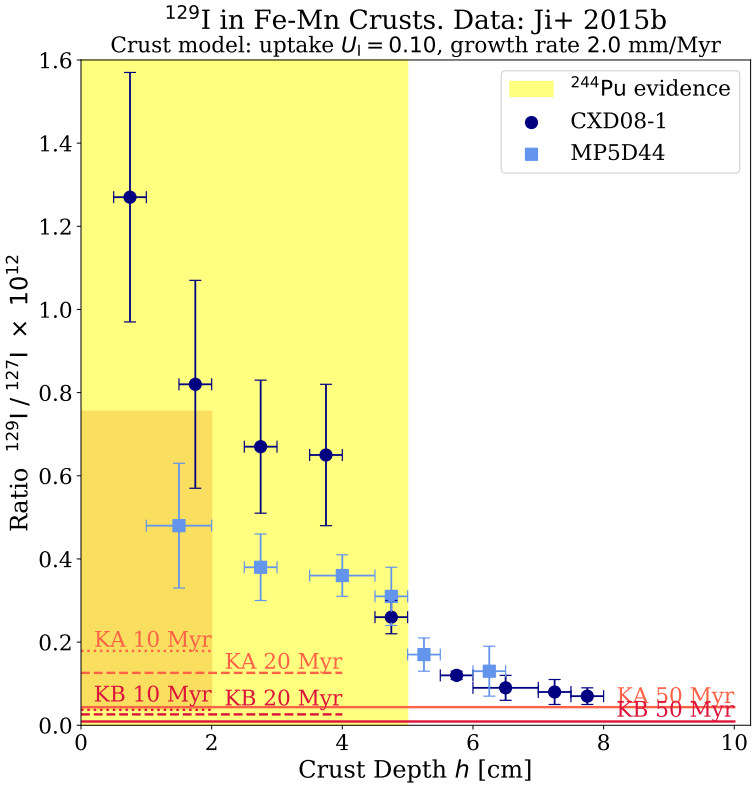

Figure 5.14: *An example of the potential power of* ^{129}I *measurements. We show an estimate of the evolution with depth of the* ^{129}I/^{127}I *isotope ratio, based on the AMS data of Ji et al. (2015a). The horizontal lines represent the ratio* ^{129}I/^{127}I *that would be generated within the KA and KB models occurring at the the indicated times* $t_{\rm KN}$ *in the past; these represent a floor below which the natural* ^{129}I *background cannot fall. The KA curves for* $t_{\rm KN} = (10, 20)$ Myr *are off-scale. These model lines assume a crust iodine uptake* $U_{\rm I} = 0.1$ *and a constant growth rate* $\dot{h}_0 = 2\,{\rm mm/Myr}$. *Model uncertainties for* $t({\rm KB}) = 10$ Myr *are shown as a red band; similar ranges apply to the other cases. Model line heights scale as* $U_{\rm I}\,\exp(-t_{\rm KN}/\tau_{129})$, *and maximum depth scales as* $h_{\rm max} = \dot{h}_0 t_{\rm KN}$. *The yellow band shows the extent of* ^{244}Pu *evidence using the assumed* $\dot{h}_0$.

Chapter 6

Supernova modification of Oort cloud orbits

A nearby supernova blast wave entering the solar system will likely have some effects on rocky or gas bodies. In this chapter, we explore how the blast wave may alter the orbits of Oort cloud objects by imparting an impulse. This work is the fruitful result of an undergraduate, Leeanne Smith, who worked under my direct supervision as part of the Undergraduate Research Apprenticeship Program (URAP) at UIUC. While the final code written was hers, I guided this project from initial concepts to testing to results.

One way in which supernovae affect Oort cloud bodies was examined by Stern (1990), who explored the effects of erosion and dynamical drag on these bodies due to both supernovae and two phases of the interstellar medium (ISM). For a supernova 40 pc away, it was found that the remnant will erode comet surfaces only 0.01 g/cm^{-2}, a negligible amount compared to the $\sim 3 \times 10^2$ g/cm^{-2} from molecular and atomic clouds. Other studies (e.g., Seab, 1987) show that dust grains smaller than ~ 100 μm will be destroyed by shock effects. However, the supernova would eject all particles < 0.3 mm. A previous paper (Stern & Shull, 1988) studied the thermal surface effects of supernovae and passing stars on Oort cloud bodies, but does not consider their orbits.

The Oort cloud, named after the astronomer who first predicted its existence (Oort, 1950), is a reservoir of comets located far away from the planets and only tenuously gravitationally bound to the Sun. The inner structure is dominated by passing stars and Galactic tidal forces (Heisler & Tremaine, 1986; Wiegert & Tremaine, 1999; Rickman et al., 2008), though molecular clouds may also play a role (Mazeeva, 2004; Jakubík & Neslušan, 2008).

Due to their extreme distance from the Sun, Oort cloud objects are rarely seen, so most of the efforts to understand its structure must be theoretical. Indeed, we only see objects on highly eccentric orbits ($e \gtrsim 0.999$) that, upon approaching the Sun, become sufficiently bright enough to be detected. Our goal is to understand the overall effect on the Oort cloud rather than a few specific comets, so we randomly generate orbital properties rather than use observed ones.

6.1 Setup

Our goal is to examine how supernovae may have altered the orbits of Oort cloud comets. We approach this task with purely Keplerian mechanics in mind. While orbits in our solar system have a variety of complexity that deviate from Keplerian mechanics (e.g., radiation pressure, gas drag, multi-body gravitation, the Yarkovsky and YORP effects, and other relativistic effects), all these processes are far less important than standard gravity-based orbits. Additionally, we assume that the size of the supernova remnant (SNR) is large compared to the Oort cloud, that is, $R_{\rm SNR} \gg R_{\rm Oort}$. On the scale of the solar system, then, the blast is well-approximated as a plane wave.

Keplerian orbits are exactly solvable in only three cases: the Kepler problem (two-body orbits), the Euler three-body problem, and the Stark (accelerated Kepler) problem (Lantoine & Russell, 2011). This third case is the most relevant, in which a point mass orbiting a larger body feels a constant linear force. Initially used to examine the orbits of electrons around nuclei in the presence of an external magnetic field, this corresponds well to the case of an orbiting Oort cloud body subject to a steady supernova blast. The Stark problem has long been studied (Lantoine & Russell, 2011), and exact solutions are attainable. However, an additional simplification can be made by comparing the orbital period to the SNR evolution timescale.

Given the long timescale of SNR evolution, it may take $\sim 10^5$ years for the blast to deposit most of its energy as it sweeps over the solar system. SNRs fade away after their radiation-dominated phase as they slowly dissolve into the ISM, a process that may take $\sim 10^6$ years. For timescales this long, most objects in the solar system complete many orbits around the Sun. However, at the distance of the Oort cloud, orbital periods are extremely long. Using the classic Kepler's Third Law

for our solar system, semimajor axis is related to period by

$$a^3 = P^2 \tag{6.1}$$

where a is the semimajor axis in au and P is the period in years. The Oort cloud is predicted to extend from approximately $a = 10^4$ au to perhaps $a = 10^5$ au, corresponding to periods of $P = 10^6 - 10^{7.5}$ years. Therefore, we can use the approximation that the blast wave from a SNR is short compared to the orbital period of bodies in the Oort cloud. Oort cloud bodies would therefore feel the entire duration of SNR evolution as a single impulse.

This assumption provides another benefit as well: by working with the Oort cloud rather than the asteroid belt, we make no assumptions about how compressed the heliosphere became. As examined thoroughly in Miller & Fields (2022) and Fields et al. (2008), a supernova needs to be within $\lesssim 30$ pc to expose the asteroid belt. A supernova at 100 pc could still expose the Kuiper belt, but the momentum imparted by the remnant could not be well-approximated by an impulse. Given that the Oort cloud already exists far outside the bounds of the heliosphere, the response of the solar wind is irrelevant in this setting.

6.1.1 Coordinates and transformation

When working with orbits, we are typically interested in the parameters of the orbit far more than the coordinate basis we apply. A natural description of orbits is given in the Keplerian elements, or orbital elements. These elements are listed in Table 6.1, and Fig. 6.1 gives a visual interpretation of the Keplerian elements (beyond semimajor axis and eccentricity). a and e define the size and shape of the orbit; i and Ω define the plane of the orbit; ω defines the rotation within that plane; and finally, any of the three anomalies (true, mean, or elliptical) are needed to give the object's position within that orbit.

Of these three anomalies, the true anomaly ν, the angle from the direction of periapsis to the orbiting body, is the most useful here. We also make use of the mean anomaly M, which describes the temporal fraction of the orbit, scaled from 0 to 2π, as in $M = 2\pi(t/P)$ with $t = 0$ at periapsis. The three anomalies can be converted between each other, though not always exactly. The mean

anomaly is related to the eccentric anomaly by Kepler's equation:

$$M = E - e \sin E, \tag{6.2}$$

which must be solved numerically. The true anomaly can be written as an exact function of the eccentric anomaly as

$$\cos \nu = \frac{\cos E - e}{1 - e \cos E}. \tag{6.3}$$

With these relations, we can convert between all three anomalies to a sufficient degree of precision.

Table 6.1: List of Keplerian elements

Symbol	Meaning
a	semi-major axis
e	eccentricity
i	angle of inclination
Ω	right ascension of the ascending node (RAAN)
ω	argument of periapsis
ν	true anomaly
M	mean anomaly
E	eccentric anomaly

The Keplerian orbital elements can be converted to Cartesian coordinates $(\boldsymbol{r}, \dot{\boldsymbol{r}})$. This process is shown in e.g., Gurfil (2005), eqn. 4:

$$\boldsymbol{r} = \frac{a(1-e^2)}{1 + e\cos\nu} \begin{bmatrix} \cos(\nu+\omega)\cos\Omega - \cos i \sin(\nu+\omega)\sin\Omega \\ \cos\Omega\cos i\sin(\nu+\omega) + \cos(\nu+\omega)\sin\Omega \\ \sin i \sin(\nu+\omega) \end{bmatrix} \tag{6.4}$$

$$\dot{\boldsymbol{r}} = \sqrt{\frac{\mu}{a(1-e^2)}} \begin{bmatrix} -\cos\Omega\sin(\nu+\omega) - \sin\Omega\cos i\cos(\nu+\omega) - e(\cos\Omega\sin\omega + \sin\Omega\cos\omega\cos i) \\ \cos\Omega\cos i\cos(\nu+\omega) - \sin\Omega\sin(\nu+\omega) - e(\sin\Omega\sin\omega - \cos\Omega\cos\omega\cos i) \\ \sin i(\cos(\nu+\omega) + e\cos\omega) \end{bmatrix} \tag{6.5}$$

where $\mu = GM_\odot$ is the standard gravitational parameter, a constant in our solar system.

The conversion from Cartesian back to Keplerian is a more involved process, and so is not detailed here.

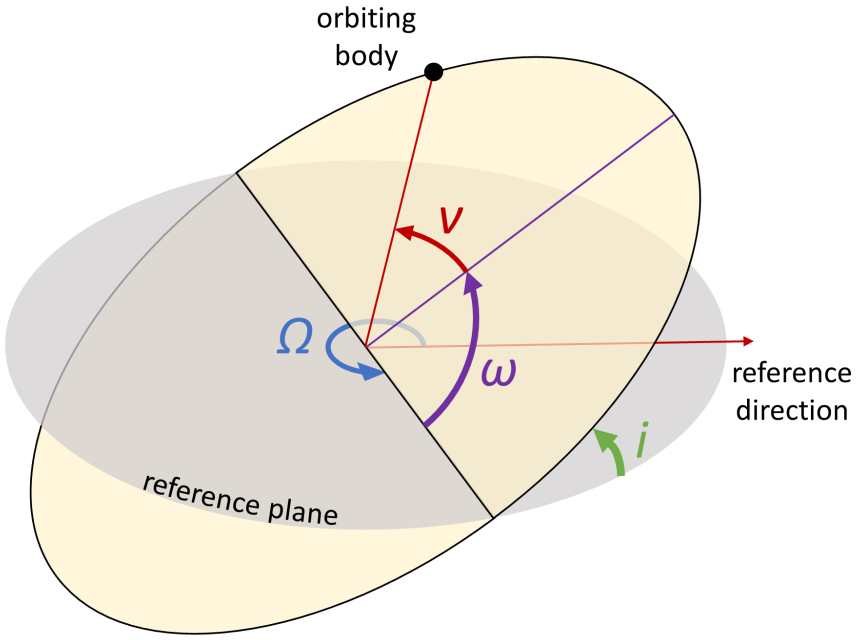

Figure 6.1: Schematic of the Keplerian elements (except semimajor axis and eccentricity), adapted from: https://en.wikipedia.org/wiki/File:Orbit1.svg.

6.1.2 Physical equations

As the SNR interacts with an Oort cloud body, its energy will be deposited in several ways: kinetic energy, thermal energy, and cosmic ray nucleosynthesis, to name a few. As an approximation, we assume that all energy striking the surface of the comet is converted into kinetic energy of the comet. The comet absorbs this energy based on its cross-section. Given that an impulse approximation is being used for the time duration, the phase of the SNR is irrelevant. In addition, the SNR is assumed to be isotopic, depositing energy equally across space. The energy increase in the comet is therefore

$$\Delta E_{\text{comet}} = \left(\frac{\pi r_c^2}{4\pi d_{\text{SN}}^2}\right) E_{\text{SN}} = \left(\frac{r_c}{d_{\text{SN}}}\right)^2 \frac{E_{\text{SN}}}{4} \tag{6.6}$$

where r_c is the radius of the comet, d_{SN} is the distance to the supernova, and E_{SN} is the energy of the supernova, taken to be the canonical 10^{51} ergs.

We give the comets a velocity "kick" with a magnitude

$$v_{\text{kick}} = \sqrt{\frac{3}{8\pi}\frac{E_{\text{SN}}}{\rho_c r_c d_{\text{SN}}^2}} \tag{6.7}$$

in an arbitrary direction. In this work, the $+\hat{x}$-direction was chosen, though any other direction will yield the same results.

In short, we use a three-step process:

1. Convert coordinates from Keplerian to Cartesian.
2. Add velocity in a specific direction.
3. Convert coordinates back to Keplerian.

With this process, we can see how the orbital elements change when getting a velocity change from the supernova blast.

6.1.3 Initial orbits

Assuming a spherical Oort cloud, we uniformly randomize all the Keplerian elements as shown in Fig. 6.2 for 10^6 comets. We pick random values for the mean anomaly, assuming that comets are at a random time in their orbit. When converting this to true anomaly, most objects are clustered around $\nu = \pi$, the location of their aphelion. They spend little time near their perihelion as one would expect from Kepler's laws.

Comet size and density are also necessary to calculate v_k, as shown in Eqn. 6.7. The radius is chosen randomly (on a log scale) from $10^{-3} - 10^5$ cm. This wide range of values will capture the dynamics of everything from large dust grains to km-sized comets. When applying the kick velocity, the comet absorbs energy according to its cross-section. The comet is assumed to be spherical; a good approximation for large bodies, but notably poor for smaller ones. Given that Oort cloud objects are likely rotating faster than the ~ 10 kyr passage of the supernova blast, some of the discrepancies due to shape may be averaged out over time.

Comet densities are assigned randomly from $0.5 - 2$ g/cm^3 to mimic loosely-packed ice balls and rocky material. A more precise calculation may assign a density that depends on size or even perihelion and semimajor axis (if it approaches close enough to the Sun to evaporate the ice, which we do not account for here).

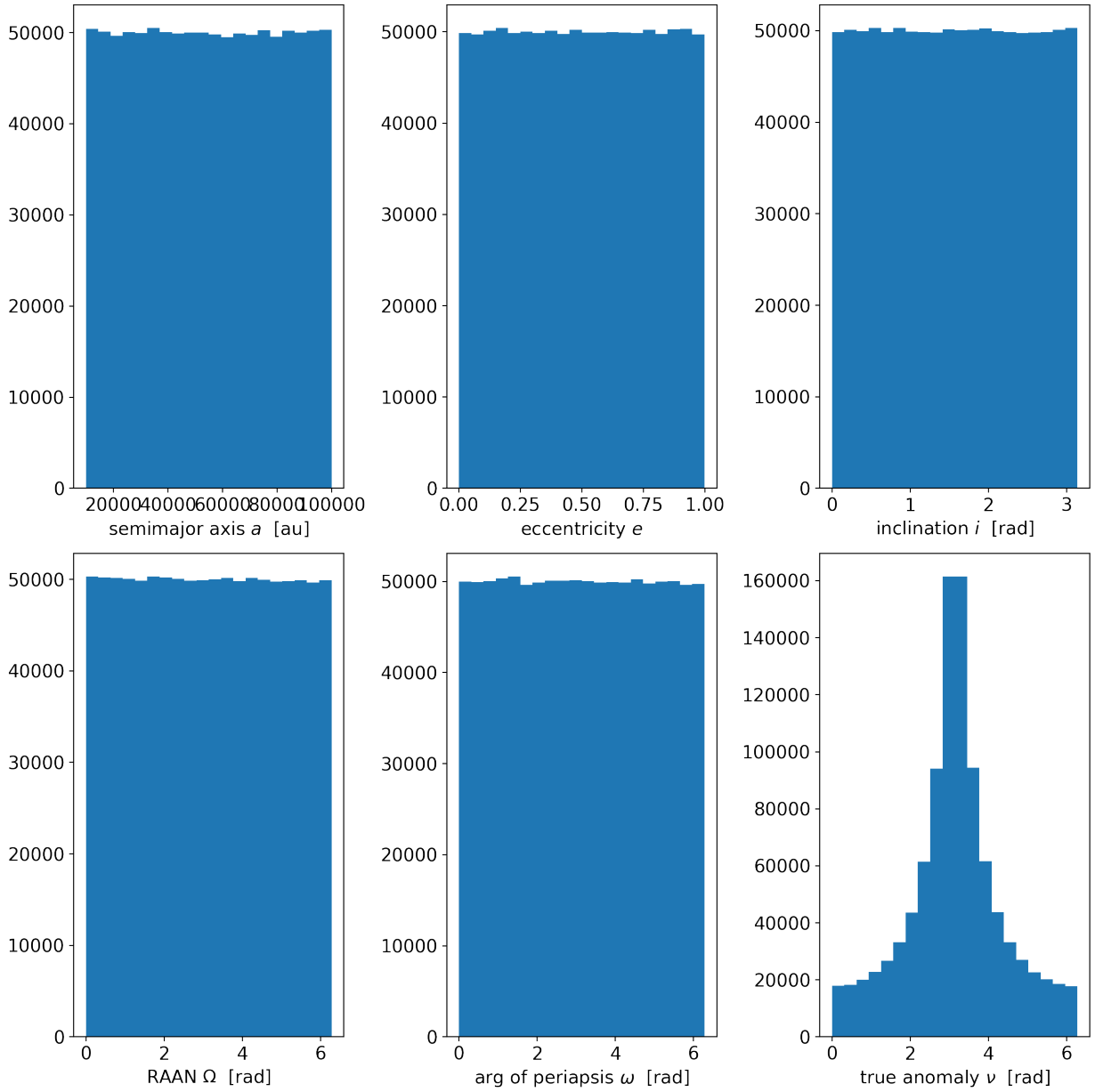

Figure 6.2: Initial Keplerian orbital elements of the Oort cloud for 10^6 comets. Note than an even distribution in the mean anomaly leads to a peaked distribution in the true anomaly.

6.1.4 Kick velocities

We apply the kick velocity in Eqn. 6.7. This velocity depends primarily on the comet's size and density. A histogram of kick velocities is shown in Fig. 6.3 for a very close 10 pc supernova. The majority of comets have a kick in the range 10^3 cm/s $< v_k < 10^6$ cm/s.

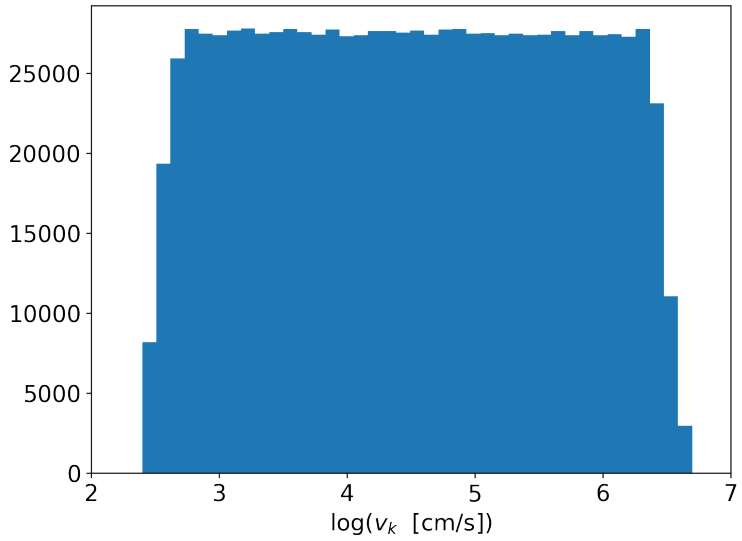

Figure 6.3: A histogram of kick velocities for a very close 10 pc supernova. Note that the velocity is on a logarithmic scale.

6.2 Results

6.2.1 Orbital effects

After applying the kick and transforming back into the Keplerian orbital elements, we can see how the orbits have changed due to the supernova blast. The more massive comets have not changed their orbit significantly; the greatest differences come from the very small objects that received a large v_k. Many of these small bodies were ejected (59.5% for a 10 pc supernova).

We show the post-supernova orbital elements in Fig. 6.4. The semimajor axis and eccentricity plots only show the value in the range of the initial orbits; ejected bodies are not shown in these two plots. There is a tendency for still-bound bodies to have lower a and higher e. However, the most prominent differences between the two states appear in Ω and ω, which show strong peaks at even fractions of π. The even fractions are due to the velocity direction chosen, which was in the $\hat{x}$-direction. These orbits correspond to unbound bodies with a much greater kick velocity than their orbital velocity. These peaks indicate that small dust from the Oort cloud will be scattered in a preferential direction from its orbit, with its new trajectory pointing back to the location of the supernova. In the true anomaly, the large leftward bulge is due to the these same unbound bodies: the large v_k puts them at the periapsis of their orbit with a true anomaly near zero.

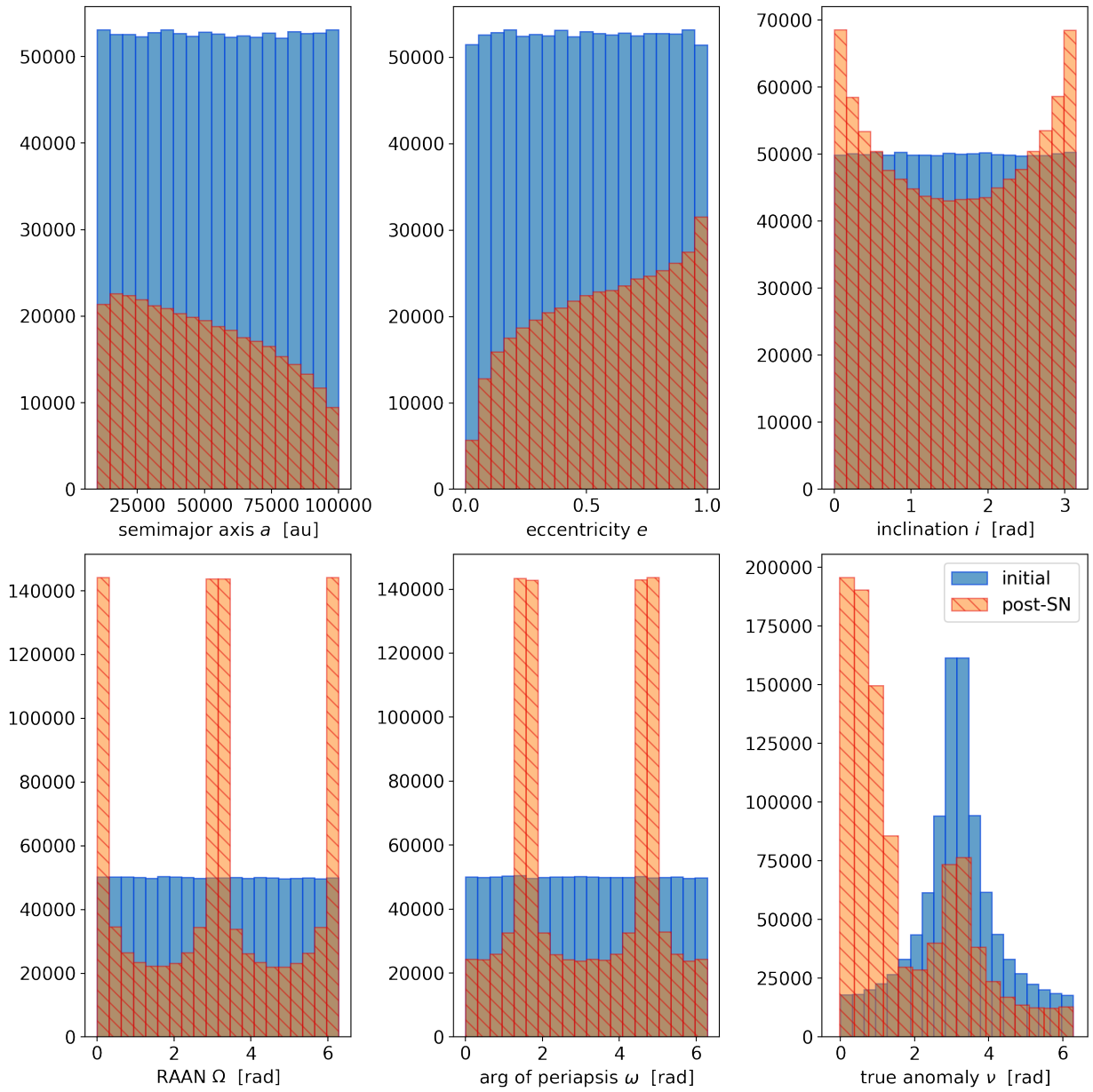

Figure 6.4: Similar to Fig. 6.2. Blue bars are the initial parameters, striped orange bars are after applying v_k from a 10 pc supernova. The histograms for a and e have been contained to show only values in the initial range.

For any observations of these comets to be made, they need to approach the inner solar system at their periapsis. Fig. 6.5 shows the periapsis (or perihelion) distances of the comets. We see that the supernova scatters the comets towards a larger periapsis. As stated above, this mainly affects the small mm-sized comets over the large visible ones.

Unfortunately, judging by the periapses alone, comets are not scattered towards the inner solar

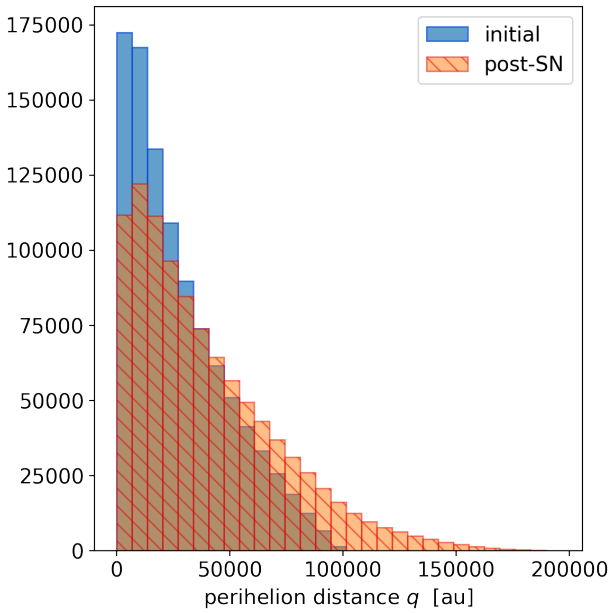

Figure 6.5: A histogram of initial and post-SN perihelia. As in fig. 6.4, initial values are blue and modified values are orange.

system and so may be difficult to detect. The small bodies would need to be directly between the supernova and the Sun, which is statistically very unlikely. While this is surely the case for some bodies, it is an extreme minority in the entirety of the Oort cloud.

6.2.2 Variation with supernova distance

The above sections assumed a startlingly close 10 pc supernova to highlight the orbital differences. The supernova 3 Myr ago is more likely to have been around $60 - 130$ pc (Fry et al., 2015). The only difference is that the comets would receive a smaller kick velocity, reducing the amount of orbital change.

In addition to the previous analysis focused on the magnitude of the orbital change, we can examine how many objects become unbound from the solar system and how that depends on size. In Fig. 6.6, we show the fraction of unbound comets as a function of size for four supernova distances. As expected, the smallest bodies are always unbound, while the largest ones remain bound (and in a very similar orbit). In the case of a supernova at 100 pc, about half of all bodies smaller than 1 m become unbound.

Fig 6.6 can be directly compared against Stern (1990), who finds that a 40 pc supernova ejects

all particles < 0.3 mm across. In contrast, our model shows that much fewer comets are ejected. In addition, there is not a single cutoff radius, but a gradual decline in probability. At 0.3 mm, all particles are ejected for the 10, 20, and 50 pc supernovae, and $\sim 98\%$ are ejected for the 100 pc supernova. For a 40 pc supernova, 50% of particles smaller than 3 cm will be ejected.

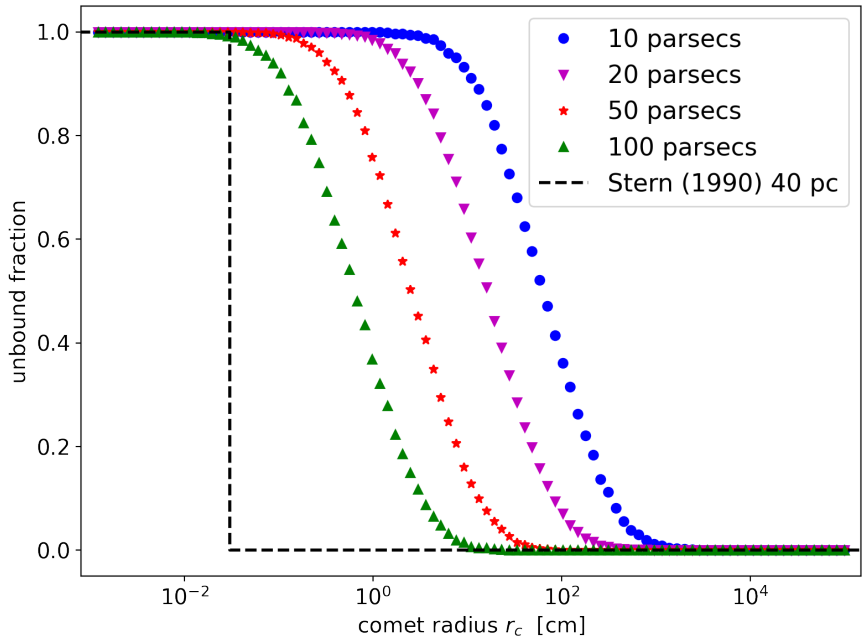

Figure 6.6: Fraction of orbits that become unbound after a supernova blast. The black dashed line comes from Stern (1990), who estimate a 40 pc supernova will eject particles with a critical radius of 0.3 mm.

If there were an accurate count of Oort cloud object down to the ∼cm level, it could give an indication of the distance to a recent supernova blast. A 10 pc supernova would unbind all 10 cm objects, but a 100 pc supernova would not unbind any. Sadly, such a complete survey of Oort cloud bodies is not likely to be achieved anytime soon.

6.2.3 Comparison to other modifiers

The Oort cloud is not affected by only supernovae, of course. The main processes responsible for shaping its structure over several Gyr are passing stars and the Galactic tides (Heisler & Tremaine, 1986). Because passing stars affect the Oort cloud in such a stochastic manner, direct comparisons between their effects and those of supernovae are challenging.

Here, we compare our results for a 10 pc supernova to that of Jakubík & Neslušan (2008), who

examine the dynamics of the Oort cloud affected by a passing giant molecular cloud (GMC). In their model, they explore only the gravitational effects and neglect dynamical forces; size and density are irrelevant. A direct comparison is therefore necessarily incomplete, but can still be illuminating.

A comparison between our results and those of Jakubík & Neslušan (2008) is shown in Fig. 6.7 (note the different quantities being plotted to match their model). These two models show striking differences, though have notably almost identical semimajor axes. The main function of GMCs is to reduce the number of comets in the Oort cloud by 12% (in this particular calculation) but otherwise change orbits in only a minor way. Comet size is irrelevant in their model, so a direct comparison to our $\sim 60\%$ unbound fraction is approximate at best.

6.3 Conclusions and future work

In our simple model for how a supernova blast affects Oort cloud orbits, we approximated the blast as an impulsive velocity kick to the Oort cloud. Although the blast did not change the orbital properties of large bodies significantly, many smaller ones were significantly altered to the point of becoming unbound. As expected, closer supernovae are able to unbind larger objects than more distant ones.

GMCs also affect the orbital properties of the Oort cloud. In comparison, GMCs affect all bodies regardless of size, whereas supernovae preferentially impact smaller bodies. However, given the sharp impulse nature of supernova blasts, the resulting orbital changes are highly directional, and both Ω and ω have clearly-defined peaks. Comparison to passing stars and Galactic tidal forces remains a challenge.

Our model can have increasing layers of complexity introduced. One potentially interesting aspect is to examine the effect of multiple supernovae to see how they could affect the Oort cloud over the 4.5 Gyr history of our solar system. Alternatively, real comet data could be used for the known Oort cloud bodies with extremely eccentric orbits ($e > 0.999$). Due to their extreme eccentricity, they would have a very low orbital velocity at their aphelion and therefore be more sensitive to a large velocity impulse.

Another direction is to sum the ejected bodies for all stars that a supernova remnant sweeps over to determine how the SNR can populate the Galaxy with bodies ejected from exo-Oort clouds. This

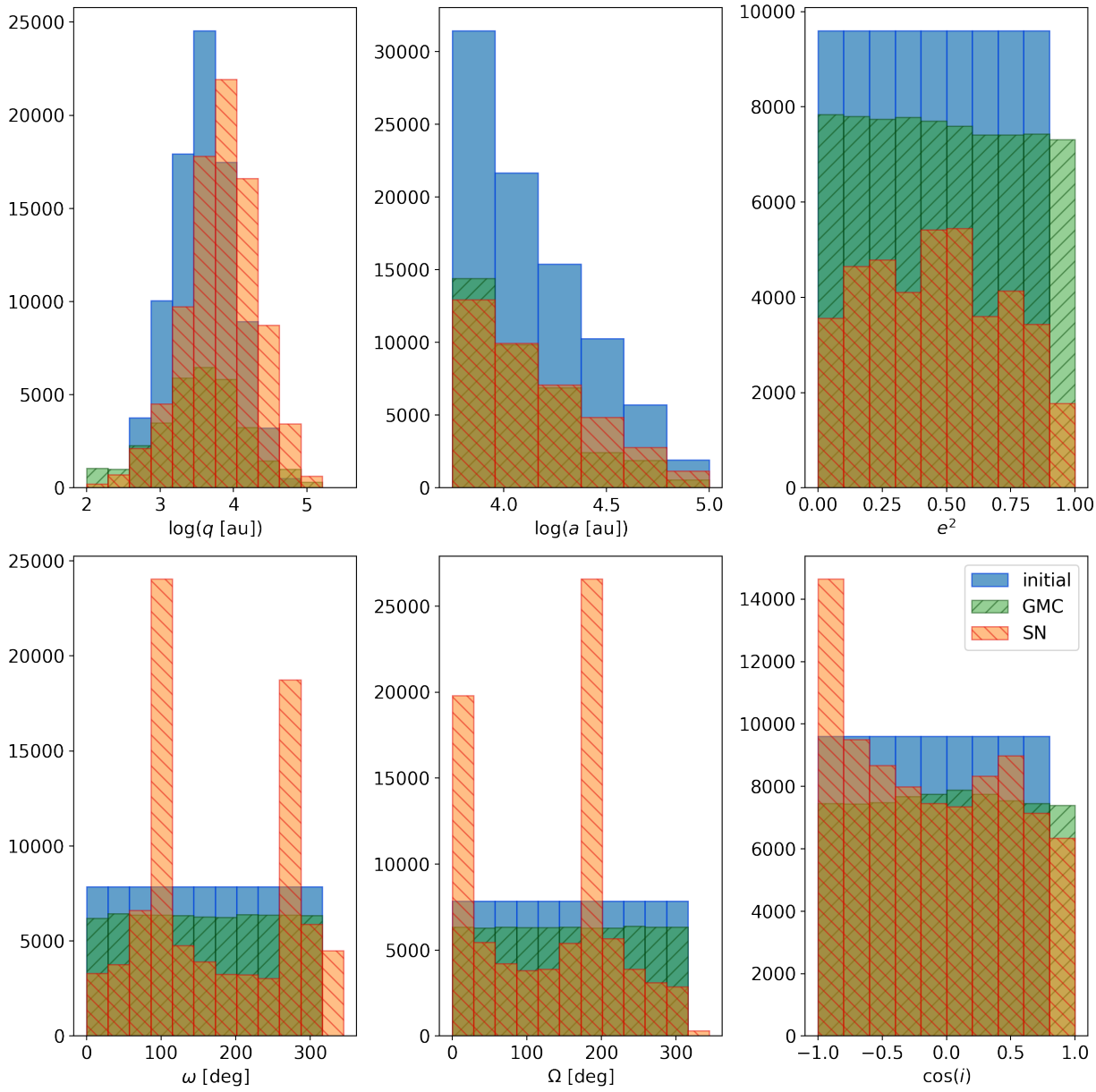

Figure 6.7: Comparison to Jakubík & Neslušan (2008) for a 10 pc SN. Initial values for both studies are shown in blue, changes due to a GMC are in green, and those due to a supernova are in orange. Quantities being shown are different than in figs. 6.2 and 6.4: here, we show perihelion distance, semimajor axis, square of the eccentricity, argument of periapsis, right ascension of the ascending node, and cosine of inclination angle.

amount could potentially be compared to early stellar system formation during planet formation. Orbital dynamics in this chaotic era also eject small bodies, so a potentially interesting comparison could be made.

Finally, more research is needed to determine how supernova shocks destroy dust grains, and

whether it is more likely for the small grains to be ejected or be ablated by the shock. As mentioned previously, Seab (1987) suggests that all grains smaller than ~ 100 μm should be vaporized. More study is needed to determine the dynamics of these grains as they undergo continual spallation in the SNR.

Chapter 7

Conclusions

7.1 Summary

Thanks to the work of numerous scientists across many disciplines, we can start to put together a cohesive picture of near-Earth supernova activity over the past few million years: a nearby cluster of stars (likely Sco-Cen) formed, containing some very massive stars. The most massive of these stars exploded, cavitating the ISM and making the Local Bubble. Two of these supernovae exploded 3 and 7 Myr ago, when the solar system happened to be within ~ 100 pc. Over the next $1-2$ Myr, supernova dust containing ^{60}Fe peppered our solar system, falling onto Earth and becoming incorporated into geological records.

This dissertation has focused on understanding the effects of nearby supernovae on the Earth, the heliosphere, and the rest of the solar system. We have shown that the ^{60}Fe signal has not been significantly contaminated by background cosmic ray nucleosynthesis on asteroid surfaces. However, current AMS experiments may soon reach the sensitivity needed to measure this background directly. The heliosphere protects the Earth from the supernova blast wave, though the outer planets are exposed. As a result, Earth did not receive any supernova plasma; the observed ^{60}Fe must have arrived as dust in order to punch through the heliosphere.

Based on the discovery of ^{244}Pu concurrent with ^{60}Fe, the two known supernovae may have both been the rare types to produce the r-process. We find it more likely that the local ISM was enriched by a neutron star merger before the stellar cluster formed. We also proposed that evidence pertaining to the late Devonian mass extinction is consistent with a supernova cause, and how

long-lived radioisotope abundances can confirm or negate this hypothesis. Finally, we showed how nearby supernovae can clear dust and other small bodies from the Oort cloud and eject them into interstellar space.

7.2 Future work

7.2.1 Heliosphere collisions

The blast waves from the SNRs ripped through the ISM and collided with our heliosphere, greatly compressing it and exposing the outer solar system to the blast. While a simplified model was the focus of Chapter 4, several extensions can be made to include a wider array of physics beyond axisymmetric steady-state hydrodynamics. For example, employing a full 3D model and a variable solar wind could alter the penetration distance.

A preliminary version of this simulation is shown in Fig. 7.1. The time-varying wind around the equator is driven with data from the *ACE* and *DSCOVR* satellites[1] and the polar wind is kept constant. The blast wave approaches slightly closer with the variable wind than in the steady-state, advancing during brief periods of low ram pressure and being forced back by high ram pressure. And yet, the heliopause in the equatorial plane is thinner and more focused than in the polar region. What are the roles of additional effects like magnetic fields and charge exchange? Though this work is yet to be done in detail, it represents one way in which a more accurate characterization of the heliosphere benefits our understanding of the consequences of nearby supernovae.

Modelling the heliosphere in an extreme environment has implications for other stars as well. Other stars were certainly closer to the supernova when it exploded, so their astrospheres were compressed even more than our own heliosphere. This has implications for the vulnerability of life near a supernova and adds to the discussion of the Galactic Habitable Zone (Gonzalez et al., 2001; Lineweaver et al., 2004; Morrison & Gowanlock, 2015; Spinelli et al., 2021). Beyond supernovae, another extreme stellar environment is the region very close to our Galaxy's central supermassive black hole, Sgr A*. Nearby stellar winds power Sgr A*'s accretion (Cuadra et al., 2006). Recently, a 2.2 $M_\odot$ star named S62 was discovered to have a periapsis velocity of 10% the speed of light

[1]Data obtained via the Space Weather Prediction Center (SWPC) at: http://www.swpc.noaa.gov/products/real-time-solar-wind.

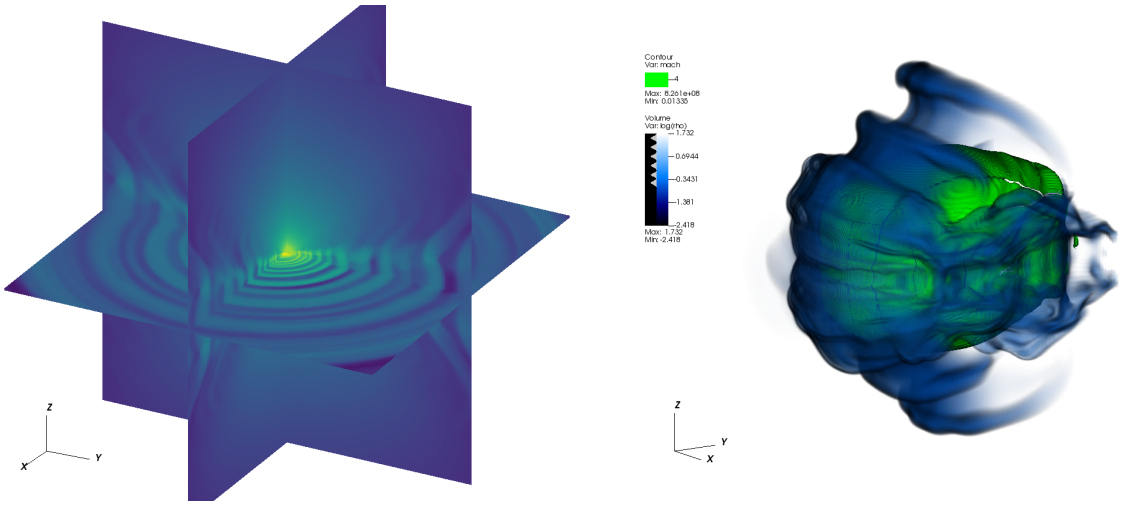

(a) (b)

Figure 7.1: A 50 pc supernova striking a 3D, active (time-dependent) solar wind driven with data from *DSCOVR*. (a) shows the initial condition of a steady polar wind with a variable equatorial wind. Post-collision, (b) shows a volume render of density, with the termination shock as the inner green surface.

(Peißker et al., 2020a,b). Studying this interaction may even lead to a greater understanding of the region around Sgr A*.

7.2.2 The future of near-Earth supernovae

Looking ahead, new ^{60}Fe data with improved precision and time resolution will always be useful, and it will continue to be the gold standard for characterizing the flux of dust from near-Earth supernovae. The detection of other isotopes will allow for abundance ratios, which in turn can constrain models of supernova or kilonova nucleosynthesis. ^{244}Pu, ^{53}Mn, and ^{26}Al (if it can be disentangled from the atmospheric background) could all prove useful in this regard. In particular, comparing the time profile of different isotopes could tell us how the composition of dust and grain dynamics evolve in SNRs. Longer-lived radioisotopes such as ^{92}Nb or ^{129}I could potentially be valuable for searching back further in the geological record for older supernovae. The precision these measurements require is extremely difficult to achieve, and will take significant improvements to current AMS sensitivity.

One aspect that certainly deserves further study is to examine the effects of nearby supernovae on planetary and rocky bodies throughout the solar system, which has been almost wholly unexplored.

Stern & Shull, 1988 and Stern, 1990 explored some effects on bodies in the Oort cloud, and Fry et al. (2016) postulated a latitude-dependent lunar deposition – beyond this, no other links to planetary sciences have been studied. How could the nearby supernovae have affected the surface of Kuiper belt objects? Outer planet ring structures or atmospheres? Any potential observables must have had an appreciable effect at the time, last for at least 3 Myr, and be measurable without too much difficulty (such as a uniquely dedicated mission[2]). The initial photon blast, especially γ- and X-rays, may have left a traceable effect in the atmosphere, though it seems to be difficult to separate from the background caused by solar activity. Given that SNRs produce so many cosmic rays, some of the longest-lived isotopes used in cosmic ray exposure age analysis could be affected.

The field of near-Earth supernovae can expand in a multitude of directions, with room for growth in theoretical, computational, and experimental domains. One of the great strengths (and joys!) of this field is its interdisciplinarity, spanning across astrophysics, geology, and biology. This field has the potential to expand enormously as scientists with different backgrounds contribute progressively more creativity.

[2]As exciting as it would be to extract a core from under the methane lakes of Titan and return it to Earth to search for ^{60}Fe, such a specialized and costly mission may not be within NASA's top priorities.

Bibliography

Abbar, S., Capozzi, F., Glas, R., Janka, H.-T., & Tamborra, I. 2021, Physical Review D, 103, 063033, doi: 10.1103/PhysRevD.103.063033

Abbott, B. P., Abbott, R., Abbott, T. D., et al. 2017a, The Astrophysical Journal, 848, L12, doi: 10.3847/2041-8213/aa91c9

—. 2017b, The Astrophysical Journal, 848, L13, doi: 10.3847/2041-8213/aa920c

—. 2017c, Physical Review Letters, 119, 161101, doi: 10.1103/PhysRevLett.119.161101

Abt, H. A. 2011, The Astronomical Journal, 141, 165, doi: 10.1088/0004-6256/141/5/165

Adams, F. C. 2010, Annual Review of Astronomy and Astrophysics, 48, 47, doi: 10.1146/annurev-astro-081309-130830

Adams, S. M., Kochanek, C. S., Beacom, J. F., Vagins, M. R., & Stanek, K. Z. 2013, The Astrophysical Journal, 778, 164, doi: 10.1088/0004-637X/778/2/164

Alexashov, D. B., Katushkina, O. A., Izmodenov, V. V., & Akaev, P. S. 2016, Monthly Notices of the Royal Astronomical Society, 458, 2553, doi: 10.1093/mnras/stw514

Alvarez, L. W., Alvarez, W., Asaro, F., & Michel, H. V. 1980, Science, 208, 1095, doi: 10.1126/science.208.4448.1095

Ammon, K., Masarik, J., & Leya, I. 2009, Meteoritics and Planetary Science, 44, 485, doi: 10.1111/j.1945-5100.2009.tb00746.x

Anderson, J. G., Wilmouth, D. M., Smith, J. B., & Sayres, D. S. 2012, Science, 337, 835, doi: 10.1126/science.1222978

Anderson, J. G., Weisenstein, D. K., Bowman, K. P., et al. 2017, Proceedings of the National Academy of Sciences, 114, E4905, doi: 10.1073/pnas.1619318114

Andreoni, I., Kool, E. C., Sagués Carracedo, A., et al. 2020, The Astrophysical Journal, 904, 155, doi: 10.3847/1538-4357/abbf4c

Andreoni, I., Coughlin, M. W., Kool, E. C., et al. 2021, The Astrophysical Journal, 918, 63, doi: 10.3847/1538-4357/ac0bc7

Arcones, A., & Janka, H.-T. 2011, Astronomy & Astrophysics, 526, A160, doi: 10.1051/0004-6361/201015530

Arcones, A., Janka, H.-T., & Scheck, L. 2007, Astronomy & Astrophysics, 467, 1227, doi: 10.1051/0004-6361:20066983

Arcones, A., & Thielemann, F. K. 2013, Journal of Physics G Nuclear Physics, 40, 013201, doi: 10.1088/0954-3899/40/1/013201

Argast, D., Samland, M., Thielemann, F.-K., & Qian, Y.-Z. 2004, Astronomy & Astrophysics, 416, 997, doi: 10.1051/0004-6361:20034265

Arnould, M., & Goriely, S. 2003, Physics Reports, 384, 1, doi: 10.1016/S0370-1573(03)00242-4

Arnould, M., Goriely, S., & Takahashi, K. 2007, Physics Reports, 450, 97, doi: 10.1016/j.physrep.2007.06.002

Athanassiadou, T., & Fields, B. D. 2011, New Astronomy, 16, 229, doi: 10.1016/j.newast.2010.09.007

Audi, G., Kondev, F. G., Wang, M., Huang, W. J., & Naimi, S. 2017, Chinese Physics C, 41, 030001, doi: 10.1088/1674-1137/41/3/030001

Balantekin, A. B., & Yüksel, H. 2005, New Journal of Physics, 7, 51, doi: 10.1088/1367-2630/7/1/051

Baranov, V. B., Lebedev, M. G., & Malama, I. G. 1991, The Astrophysical Journal, 375, 347, doi: 10.1086/170194

Baranov, V. B., & Malama, Y. G. 1993, Journal of Geophysical Research: Space Physics, 98, 15157, doi: 10.1029/93JA01171

Barnes, J., Zhu, Y. L., Lund, K. A., et al. 2021, The Astrophysical Journal, 918, 44, doi: 10.3847/1538-4357/ac0aec

Basu, S., Stuart, F. M., Schnabel, C., & Klemm, V. 2007, Physical Review Letters, 98, 141103, doi: 10.1103/PhysRevLett.98.141103

Bauswein, A., Goriely, S., & Janka, H. T. 2013, The Astrophysical Journal, 773, 78, doi: 10.1088/0004-637X/773/1/78

Belyaev, M. A., & Rafikov, R. R. 2010, The Astrophysical Journal, 723, 1718, doi: 10.1088/0004-637X/723/2/1718

Beniamini, P., & Hotokezaka, K. 2020, Monthly Notices of the Royal Astronomical Society, 496, 1891, doi: 10.1093/mnras/staa1690

Benítez, N., Maíz-Apellániz, J., & Canelles, M. 2002, Physical Review Letters, 88, 081101, doi: 10.1103/PhysRevLett.88.081101

Berghöfer, T. W., & Breitschwerdt, D. 2002, Astronomy & Astrophysics, 390, 299, doi: 10.1051/0004-6361:20020627

Binns, W. R., Israel, M. H., Christian, E. R., et al. 2016, Science, 352, 677, doi: 10.1126/science.aad6004

Blake, J. B., & Schramm, D. N. 1973, Nature Physical Science, 243, 138, doi: 10.1038/physci243138a0

Bliss, J., Witt, M., Arcones, A., Montes, F., & Pereira, J. 2018, The Astrophysical Journal, 855, 135, doi: 10.3847/1538-4357/aaadbe

Bond, D. P. G., & Grasby, S. E. 2017, Palaeogeography, Palaeoclimatology, Palaeoecology, 478, 3, doi: 10.1016/j.palaeo.2016.11.005

Boschini, M. J., Torre, S. D., Gervasi, M., et al. 2021, The Astrophysical Journal, 913, 5, doi: 10.3847/1538-4357/abf11c

Bovard, L., Martin, D., Guercilena, F., et al. 2017, Physical Review D, 96, 124005, doi: 10.1103/PhysRevD.96.124005

Breitschwerdt, D., de Avillez, M., Feige, J., & Dettbarn, C. 2012, Astronomische Nachrichten, 333, 486, doi: 10.1002/asna.201211692

Breitschwerdt, D., de Avillez, M. A., & Baumgartner, V. 2009, in American institute of physics conference series, Vol. 1156, The local bubble and beyond II, ed. R. K. Smith, S. L. Snowden, & K. D. Kuntz, 271–279, doi: 10.1063/1.3211826

Breitschwerdt, D., Feige, J., Schulreich, M. M., et al. 2016, Nature, 532, 73, doi: 10.1038/nature17424

Broecker, W. S., Peng, T.-H., & others. 1982, Tracers in the sea, Vol. 690 (Lamont-Doherty Geological Observatory, Columbia University Palisades, New York)

Burbidge, E. M., Burbidge, G. R., Fowler, W. A., & Hoyle, F. 1957, Reviews of Modern Physics, 29, 547, doi: 10.1103/RevModPhys.29.547

Burgess, C. P., & Zuber, K. 2000, Astroparticle Physics, 14, 1, doi: 10.1016/S0927-6505(00)00102-X

Burlaga, L. F., Ness, N. F., Berdichevsky, D. B., et al. 2019, Nature Astronomy, 3, 1007, doi: 10.1038/s41550-019-0920-y

Burrows, A. 2013, Reviews of Modern Physics, 85, 245, doi: 10.1103/RevModPhys.85.245

Caballero, O. L., McLaughlin, G. C., & Surman, R. 2012, The Astrophysical Journal, 745, 170, doi: 10.1088/0004-637X/745/2/170

Chaikin, E., Kaurov, A. A., Fields, B. D., & Correa, C. A. 2021, arXiv:2109.11242 [astro-ph]. http://arxiv.org/abs/2109.11242

Chen, W.-X., & Beloborodov, A. M. 2007, The Astrophysical Journal, 657, 383, doi: 10.1086/508923

Chiang, E. I., Jordan, A. B., Millis, R. L., et al. 2003, The Astronomical Journal, 126, 430, doi: 10.1086/375207

Choplin, A., Tominaga, N., & Meyer, B. S. 2020, Astronomy & Astrophysics, 639, A126, doi: 10.1051/0004-6361/202037966

Christl, M., Dai, X., Lachner, J., Kramer-Tremblay, S., & Synal, H.-A. 2014, Nuclear Instruments and Methods in Physics Research Section B: Beam Interactions with Materials and Atoms, 331, 225, doi: 10.1016/j.nimb.2013.11.045

Chruslinska, M., Belczynski, K., Klencki, J., & Benacquista, M. 2018, Monthly Notices of the Royal Astronomical Society, 474, 2937, doi: 10.1093/mnras/stx2923

Cockell, C. S. 1999, Paleobiology, 25, 212, doi: 10.1017/S0094837300026518

Cole, A. L., Boyd, R. N., Davis, M. E., et al. 2006, The Astrophysical Journal, 652, 1763, doi: 10.1086/503197

Comerón, F., & Kaper, L. 1998, Astronomy and Astrophysics, 338, 273. http://adsabs.harvard.edu/abs/1998A%26A...338..273C

Comerón, F., & Pasquali, A. 2007, Astronomy and Astrophysics, 467, L23, doi: 10.1051/0004-6361:20077304

Costello, E. S., Ghent, R. R., & Lucey, P. G. 2018, Icarus, 314, 327, doi: 10.1016/j.icarus.2018.05.023

Cowan, J. J., Sneden, C., Lawler, J. E., et al. 2021, Reviews of Modern Physics, 93, 015002, doi: 10.1103/RevModPhys.93.015002

Cowan, J. J., Thielemann, F.-K., & Truran, J. W. 1991, Physics Reports, 208, 267, doi: 10.1016/0370-1573(91)90070-3

Cowperthwaite, P. S., Berger, E., Villar, V. A., et al. 2017, The Astrophysical Journal, 848, L17, doi: 10.3847/2041-8213/aa8fc7

Crutcher, R. M. 1982, The Astrophysical Journal, 254, 82, doi: 10.1086/159707

Crutzen, P. J., & Brühl, C. 1996, Proceedings of the National Academy of Sciences, 93, 1582, doi: 10.1073/pnas.93.4.1582

Cuadra, J., Nayakshin, S., Springel, V., & Di Matteo, T. 2006, Monthly Notices of the Royal Astronomical Society, 366, 358, doi: 10.1111/j.1365-2966.2005.09837.x

Curtis, S., Ebinger, K., Fröhlich, C., et al. 2019, The Astrophysical Journal, 870, 2, doi: 10.3847/1538-4357/aae7d2

Côté, B., Fryer, C. L., Belczynski, K., et al. 2018, The Astrophysical Journal, 855, 99, doi: 10.3847/1538-4357/aaad67

Côté, B., Eichler, M., Arcones, A., et al. 2019, The Astrophysical Journal, 875, 106, doi: 10.3847/1538-4357/ab10db

Côté, B., Eichler, M., Yagüe López, A., et al. 2021, Science, 371, 945, doi: 10.1126/science.aba1111

Damon, P. E., Kocharov, G. E., Peristykh, A. N., Mikheeva, I. B., & Dai, K. M. 1995, 24th International Cosmic Ray Conference, 2, 311. https://ui.adsabs.harvard.edu/abs/1995ICRC...2..311D

Davila, N., Bojazi, M. J., & Meyer, B. S. 2019, AIP Conference Proceedings, 2076, 030005, doi: 10.1063/1.5091631

Della Valle, M., Guetta, D., Cappellaro, E., et al. 2018, Monthly Notices of the Royal Astronomical Society, 481, 4355, doi: 10.1093/mnras/sty2541

Dessart, L., Ott, C. D., Burrows, A., Rosswog, S., & Livne, E. 2009, The Astrophysical Journal, 690, 1681, doi: 10.1088/0004-637X/690/2/1681

Diehl, R. 2006, New Astronomy Reviews, 50, 534, doi: 10.1016/j.newar.2006.06.082

Diehl, R., Halloin, H., Kretschmer, K., et al. 2006, Nature, 439, 45, doi: 10.1038/nature04364

Dilling, J., Krücken, R., & Ball, G. 2014a, Hyperfine Interactions, 225, 1, doi: 10.1007/s10751-013-0877-7

Dilling, J., Krücken, R., & Merminga, L. 2014b, Hyperfine Interactions, 225, 253, doi: 10.1007/s10751-013-0906-6

Dillmann, I. 2008, in American institute of physics conference series, Vol. 1016, Origin of matter and evolution of galaxies, ed. T. Suda, T. Nozawa, A. Ohnishi, K. Kato, M. Y. Fujimoto, T. Kajino, & S. Kubono, 143–149, doi: 10.1063/1.2943564

Doherty, C. L., Gil-Pons, P., Lau, H. H. B., Lattanzio, J. C., & Siess, L. 2014, Monthly Notices of the Royal Astronomical Society, 437, 195, doi: 10.1093/mnras/stt1877

Draine, B. T. 2011, Physics of the Interstellar and Intergalactic Medium (Princeton University Press). https://ui.adsabs.harvard.edu/abs/2011piim.book.....D

Duan, H., Friedland, A., McLaughlin, G. C., & Surman, R. 2011, Journal of Physics G Nuclear Physics, 38, 035201, doi: 10.1088/0954-3899/38/3/035201

Eichler, M., Arcones, A., Kelic, A., et al. 2015, The Astrophysical Journal, 808, 30, doi: 10.1088/0004-637X/808/1/30

Ellis, J., Fields, B. D., & Schramm, D. N. 1996, The Astrophysical Journal, 470, 1227, doi: 10.1086/177945

Ellis, J., & Schramm, D. N. 1995, Proceedings of the National Academy of Sciences, 92, 235, doi: 10.1073/pnas.92.1.235

Endrizzi, A., Ciolfi, R., Giacomazzo, B., Kastaun, W., & Kawamura, T. 2016, Classical and Quantum Gravity, 33, 164001, doi: 10.1088/0264-9381/33/16/164001

Ertel, A. F., Fry, B. J., Fields, B. D., & Ellis, J. 2022, arXiv:2206.06464 [astro-ph], doi: 10.48550/arXiv.2206.06464

Fan, J.-x., Shen, S.-z., Erwin, D. H., et al. 2020, Science, 367, 272, doi: 10.1126/science.aax4953

Farley, K. A., Vokrouhlický, D., Bottke, W. F., & Nesvorný, D. 2006, Nature, 439, 295, doi: 10.1038/nature04391

Feige, J., Wallner, A., Altmeyer, R., et al. 2018, Physical Review Letters, 121, 221103, doi: 10.1103/PhysRevLett.121.221103

Fernández, R., Kasen, D., Metzger, B. D., & Quataert, E. 2015, Monthly Notices of the Royal Astronomical Society, 446, 750, doi: 10.1093/mnras/stu2112

Fesen, R. A., Drechsler, M., Weil, K. E., et al. 2021, The Astrophysical Journal, 920, 90, doi: 10.3847/1538-4357/ac0ada

Fields, B., Ellis, J. R., Binns, W. R., et al. 2019, Astro2020 Decadal Survey, 51, 410. http://adsabs.harvard.edu/abs/2019BAAS...51c.410F

Fields, B. D. 2004, New Astronomy Reviews, 48, 119, doi: 10.1016/j.newar.2003.11.017

Fields, B. D., Athanassiadou, T., & Johnson, S. R. 2008, The Astrophysical Journal, 678, 549, doi: 10.1086/523622

Fields, B. D., & Ellis, J. 1999, New Astronomy, 4, 419, doi: 10.1016/S1384-1076(99)00034-2

Fields, B. D., Hochmuth, K. A., & Ellis, J. 2005, The Astrophysical Journal, 621, 902, doi: 10.1086/427797

Fields, B. D., Melott, A. L., Ellis, J., et al. 2020, Proceedings of the National Academy of Sciences, 117, 21008, doi: 10.1073/pnas.2013774117

Fields, P. R., Diamond, H., Metta, D. N., & Rokop, D. J. 1976, in Lunar and planetary science conference, Vol. 7, Lunar and planetary science conference, 251

Fields, P. R., Diamond, H., Metta, D. N., Rokop, D. J., & Stevens, C. M. 1972, Lunar and Planetary Science Conference Proceedings, 3, 1637

Fifield, L. K., Clacher, A. P., Morris, K., et al. 1997, Nuclear Instruments and Methods in Physics Research Section B: Beam Interactions with Materials and Atoms, 123, 400, doi: 10.1016/S0168-583X(96)00428-4

Filipiak, P., & Racki, G. 2010, Geological Quarterly, 54, 1. https://gq.pgi.gov.pl/article/view/7535

Fimiani, L., Cook, D., Faestermann, T., et al. 2016, Physical Review Letters, 116, doi: 10.1103/PhysRevLett.116.151104

Firestone, R. B. 2014, The Astrophysical Journal, 789, 29, doi: 10.1088/0004-637X/789/1/29

Fischer, T., Whitehouse, S. C., Mezzacappa, A., Thielemann, F.-K., & Liebendörfer, M. 2010, Astronomy & Astrophysics, 517, A80, doi: 10.1051/0004-6361/200913106

Fischer, T., Wu, M.-R., Wehmeyer, B., et al. 2020, The Astrophysical Journal, 894, 9, doi: 10.3847/1538-4357/ab86b0

Fitoussi, C., & Raisbeck, G. M. 2007, Nuclear Instruments and Methods in Physics Research Section B: Beam Interactions with Materials and Atoms, 259, 351, doi: 10.1016/j.nimb.2007.01.179

Fitoussi, C., Raisbeck, G. M., Knie, K., et al. 2008, Physical Review Letters, 101, 121101, doi: 10.1103/PhysRevLett.101.121101

Foucart, F., O'Connor, E., Roberts, L., et al. 2015, Physical Review D, 91, 124021, doi: 10.1103/PhysRevD.91.124021

Frehaut, J., Bertin, A., Bois, R., & Jary, J. 1980, Status of (n,2n) cross section measurements at Bruyeres-le-Chatel, Tech. rep., CEA Centre d'Etudes de Bruyeres-le-Chatel, France

Frisch, P., & Dwarkadas, V. V. 2017, in Handbook of Supernovae, ed. A. W. Alsabti & P. Murdin (Cham: Springer International Publishing), 2253–2285, doi: 10.1007/978-3-319-21846-5-13

Frisch, P. C. 1981, Nature, 293, 377, doi: 10.1038/293377a0

Frisch, P. C., Redfield, S., & Slavin, J. D. 2011, Annual Review of Astronomy and Astrophysics, 49, 237, doi: 10.1146/annurev-astro-081710-102613

Frisch, P. C., & Slavin, J. D. 2006, Astrophys. Space Sci. Trans., 2, 53, doi: 10.5194/astra-2-53-2006

Frisch, P. C., Dorschner, J. M., Geiss, J., et al. 1999, The Astrophysical Journal, 525, 492, doi: 10.1086/307869

Fry, B. J., Fields, B. D., & Ellis, a. J. R. 2020, The Astrophysical Journal, 894, 109, doi: 10.3847/1538-4357/ab86bf

Fry, B. J., Fields, B. D., & Ellis, J. R. 2015, The Astrophysical Journal, 800, 71, doi: 10.1088/0004-637X/800/1/71

—. 2016, The Astrophysical Journal, 827, 48, doi: 10.3847/0004-637X/827/1/48

Fröhlich, C., Martínez-Pinedo, G., Liebendörfer, M., et al. 2006, Physical Review Letters, 96, 142502, doi: 10.1103/PhysRevLett.96.142502

Fuchs, B., Breitschwerdt, D., de Avillez, M. A., Dettbarn, C., & Flynn, C. 2006, Monthly Notices of the Royal Astronomical Society, 373, 993, doi: 10.1111/j.1365-2966.2006.11044.x

Fujimoto, S.-i., & Nagakura, H. 2021, Monthly Notices of the Royal Astronomical Society, 502, 2319, doi: 10.1093/mnras/stab171

Fujimoto, S.-i., Nishimura, N., & Hashimoto, M.-a. 2008, The Astrophysical Journal, 680, 1350, doi: 10.1086/529416

Fujimoto, Y., Krumholz, M. R., & Inutsuka, S.-i. 2020, Monthly Notices of the Royal Astronomical Society, 497, 2442, doi: 10.1093/mnras/staa2125

Gade, A., & Sherrill, B. M. 2016, Physica Scripta, 91, 053003, doi: 10.1088/0031-8949/91/5/053003

Gaisser, T. K., Engel, R., & Resconi, E. 2016, Cosmic Rays and Particle Physics (Cambridge University Press)

Gall, C., Hjorth, J., Rosswog, S., Tanvir, N. R., & Levan, A. J. 2017, The Astrophysical Journal Letters, 849, L19, doi: 10.3847/2041-8213/aa93f9

Gehrels, N., Laird, C. M., Jackman, C. H., et al. 2003, The Astrophysical Journal, 585, 1169, doi: 10.1086/346127

Gies, D. R., & Helsel, J. W. 2005, The Astrophysical Journal, 626, 844, doi: 10.1086/430250

Girardi, L., Groenewegen, M. a. T., Hatziminaoglou, E., & Costa, L. d. 2005, Astronomy & Astrophysics, 436, 895, doi: 10.1051/0004-6361:20042352

Giuliani, S. A., Martínez-Pinedo, G., Wu, M.-R., & Robledo, L. M. 2020, Physical Review C, 102, 045804, doi: 10.1103/PhysRevC.102.045804

Gomez, H. L., Clark, C. J. R., Nozawa, T., et al. 2012, Monthly Notices of the Royal Astronomical Society, 420, 3557, doi: 10.1111/j.1365-2966.2011.20272.x

Gonzalez, G., Brownlee, D., & Ward, P. 2001, Icarus, 152, 185, doi: 10.1006/icar.2001.6617

Goriely, S., Bauswein, A., & Janka, H.-T. 2011, The Astrophysical Journal Letters, 738, L32, doi: 10.1088/2041-8205/738/2/L32

Goriely, S., Chamel, N., & Pearson, J. M. 2009, Physical Review Letters, 102, 152503, doi: 10.1103/PhysRevLett.102.152503

Goriely, S., & Janka, H. T. 2016, Monthly Notices of the Royal Astronomical Society, 459, 4174, doi: 10.1093/mnras/stw946

Gosse, J. C., & Phillips, F. M. 2001, Quaternary Science Reviews, 20, 1475, doi: 10.1016/S0277-3791(00)00171-2

Green, D. A. 2019, Journal of Astrophysics and Astronomy, 40, 36, doi: 10.1007/s12036-019-9601-6

Green, D. A., & Stephenson, F. R. 2003, Supernovae and Gamma-Ray Bursters, 598, 7, doi: 10.1007/3-540-45863-8_2

Guozhu, H., Ming, H., Zuying, Z., et al. 2013, Nuclear Instruments and Methods in Physics Research Section B: Beam Interactions with Materials and Atoms, 294, 132, doi: 10.1016/j.nimb.2012.05.016

Gurfil, P. 2005, Journal of Guidance, Control, and Dynamics, 28, 1079, doi: 10.2514/1.14760

Hain, K., Deneva, B., Faestermann, T., et al. 2018, Nuclear Instruments and Methods in Physics Research Section B: Beam Interactions with Materials and Atoms, 423, 42, doi: 10.1016/j.nimb.2018.02.034

Harris, M. J., Knödlseder, J., Jean, P., et al. 2005, Astronomy and Astrophysics, Volume 433, Issue 3, April III 2005, pp.L49-L52, 433, L49, doi: 10.1051/0004-6361:200500093

Hartmann, D. H., Kretschmer, K., & Diehl, R. 2002, in Nuclear astrophysics, ed. W. Hillebrandt & E. Müller, 154–163

Hartmann, L., Ballesteros-Paredes, J., & Bergin, E. A. 2001, The Astrophysical Journal, 562, 852, doi: 10.1086/323863

Haxton, W. C., & Johnson, C. W. 1988, Nature, 333, 325, doi: 10.1038/333325a0

Hayakawa, T., Ko, H., Cheoun, M.-K., et al. 2018, Physical Review Letters, 121, 102701, doi: 10.1103/PhysRevLett.121.102701

Heisler, J., & Tremaine, S. 1986, Icarus, 65, 13, doi: 10.1016/0019-1035(86)90060-6

Henney, W. J., & Arthur, S. J. 2019, Monthly Notices of the Royal Astronomical Society, 486, 3423, doi: 10.1093/mnras/stz1043

Hermsdorf, D., Sassonoff, S., Seeliger, D., & Seidel, K. 1973, Journal of Nuclear Energy, 27, 747, doi: 10.1016/0022-3107(73)90113-5

Hiesinger, H., van der Bogert, C. H., Pasckert, J. H., et al. 2012, Journal of Geophysical Research: Planets, 117, n/a, doi: 10.1029/2011JE003935

Hoffman, D. C., Lawrence, F. O., Mewherter, J. L., & Rourke, F. M. 1971, Nature, 234, 132, doi: 10.1038/234132a0

Hoffman, R. D., Woosley, S. E., & Qian, Y. Z. 1997, The Astrophysical Journal, 482, 951, doi: 10.1086/304181

Holmbeck, E. M., Beers, T. C., Roederer, I. U., et al. 2018, The Astrophysical Journal, 859, L24, doi: 10.3847/2041-8213/aac722

Horowitz, C. J., Arcones, A., Côté, B., et al. 2019, Journal of Physics G Nuclear Physics, 46, 083001, doi: 10.1088/1361-6471/ab0849

Hotokezaka, K., Kiuchi, K., Kyutoku, K., et al. 2013, Physical Review D, 87, 024001, doi: 10.1103/PhysRevD.87.024001

Howard, W. M., Arnould, M., & Rayet, M. 1993, Meteoritics, 28, 365. https://ui.adsabs.harvard.edu/abs/1993Metic..28Q.365H

Hyde, M., & Pecaut, M. J. 2018, Astronomische Nachrichten, 339, 78, doi: 10.1002/asna.201713375

Häring, M., Vonach, H., & Feicht, E. J. 1971, Zeitschrift für Physik A Hadrons and nuclei, 244, 352, doi: 10.1007/BF01396795

Höfner, S., & Olofsson, H. 2018, The Astronomy and Astrophysics Review, 26, 1, doi: 10.1007/s00159-017-0106-5

Hüdepohl, L., Müller, B., Janka, H. T., Marek, A., & Raffelt, G. G. 2010, Physical Review Letters, 104, 251101, doi: 10.1103/PhysRevLett.104.251101

Ivanov, B. A. 2018, Solar System Research, 52, 1, doi: 10.1134/S0038094618010021

Iyudin, A. F. 2002, Journal of Atmospheric and Solar-Terrestrial Physics, 64, 669, doi: 10.1016/S1364-6826(02)00028-7

Izmodenov, V. V., & Alexashov, D. B. 2015, The Astrophysical Journal Supplement Series, 220, 32, doi: 10.1088/0067-0049/220/2/32

Izmodenov, V. V., Malama, Y. G., & Ruderman, M. S. 2008, Advances in Space Research, 41, 318, doi: 10.1016/j.asr.2007.06.033

Jakubík, M., & Neslušan, L. 2008, Contributions of the Astronomical Observatory Skalnate Pleso, 38, 33. http://adsabs.harvard.edu/abs/2008CoSka..38...33J

Ji, L., Liu, G., Chen, Z., et al. 2015a, Acta Oceanologica Sinica, 34, 31, doi: 10.1007/s13131-015-0718-4

Ji, L., Liu, G., Huang, Y., Xing, N., & Chen, Z. 2015b, Acta Oceanologica Sinica, 34, 13, doi: 10.1007/s13131-015-0704-x

Jin, Z.-P., Li, X., Wang, H., et al. 2018, The Astrophysical Journal, 857, 128, doi: 10.3847/1538-4357/aab76d

Johns, L., Nagakura, H., Fuller, G. M., & Burrows, A. 2020, Physical Review D, 102, 103017, doi: 10.1103/PhysRevD.102.103017

Jones, S. W., Möller, H., Fryer, C. L., et al. 2019, Monthly Notices of the Royal Astronomical Society, 485, 4287, doi: 10.1093/mnras/stz536

Joyce, M., Leung, S.-C., Molnár, L., et al. 2020, The Astrophysical Journal, 902, 63, doi: 10.3847/1538-4357/abb8db

Just, O., Bauswein, A., Ardevol Pulpillo, R., Goriely, S., & Janka, H. T. 2015, Monthly Notices of the Royal Astronomical Society, 448, 541, doi: 10.1093/mnras/stv009

Kachelrieß, M., Neronov, A., & Semikoz, D. 2018, Physical Review D, 97, 063011, doi: 10.1103/PhysRevD.97.063011

Kachelrieß, M., Neronov, A., & Semikoz, D. V. 2015, Physical Review Letters, 115, 181103, doi: 10.1103/PhysRevLett.115.181103

Kaiser, S. I., Aretz, M., & Becker, R. T. 2016, Geological Society, London, Special Publications, 423, 387, doi: 10.1144/SP423.9

Kajino, T., Aoki, W., Balantekin, A. B., et al. 2019, Progress in Particle and Nuclear Physics, 107, 109, doi: 10.1016/j.ppnp.2019.02.008

Karam, P. A. 2002, Radiation Physics and Chemistry, 64, 77, doi: 10.1016/S0969-806X(01)00454-6

Kasen, D., Metzger, B., Barnes, J., Quataert, E., & Ramirez-Ruiz, E. 2017, Nature, 551, 80, doi: 10.1038/nature24453

Kester, O., Spiller, P., & Stoecker, H. 2012, in Challenges and Goals for Accelerators in the XXI Century (WORLD SCIENTIFIC), 611–622, doi: 10.1142/9789814436403_0032

Knie, K., Korschinek, G., Faestermann, T., et al. 2004, Physical Review Letters, 93, doi: 10.1103/PhysRevLett.93.171103

—. 1999a, Physical Review Letters, 83, 18. https://journals.aps.org/prl/abstract/10.1103/PhysRevLett.83.18

Knie, K., Merchel, S., Korschinek, G., et al. 1999b, Meteoritics and Planetary Science, 34, 729, doi: 10.1111/j.1945-5100.1999.tb01385.x

Kobayashi, C., Karakas, A. I., & Lugaro, M. 2020, The Astrophysical Journal, 900, 179, doi: 10.3847/1538-4357/abae65

Kobulnicky, H. A., Chick, W. T., Schurhammer, D. P., et al. 2016, The Astrophysical Journal Supplement Series, 227, 18, doi: 10.3847/0067-0049/227/2/18

Kodama, T., & Takahashi, K. 1975, Nuclear Physics A, 239, 489, doi: 10.1016/0375-9474(75)90381-4

Koll, D., Korschinek, G., Faestermann, T., et al. 2019, Physical Review Letters, 123, 072701, doi: 10.1103/PhysRevLett.123.072701

Kondev, F. G., Wang, M., Huang, W. J., Naimi, S., & Audi, G. 2021, Chinese Physics C, 45, 030001, doi: 10.1088/1674-1137/abddae

Koning, A. J., Hilaire, S., & Duijvestijn, M. C. 2007, in Proceedings of the International Conference on Nuclear Data for Science and Technology (Nice, France: EDP Sciences), 211–214. http://www.talys.eu/more-about-talys/

Korobkin, O., Hungerford, A. M., Fryer, C. L., et al. 2020, The Astrophysical Journal, 889, 168, doi: 10.3847/1538-4357/ab64d8

Korschinek, G., Faestermann, T., Kastel, S., et al. 1994, Nuclear Instruments and Methods in Physics Research Section B: Beam Interactions with Materials and Atoms, 92, 146, doi: 10.1016/0168-583X(94)95995-1

Korschinek, G., Faestermann, T., Knie, K., & Schmidt, C. 1996, Radiocarbon, 68

Korschinek, G., Faestermann, T., Poutivtsev, M., et al. 2020, Physical Review Letters, 125, 031101, doi: 10.1103/PhysRevLett.125.031101

Koul, S. L. 1979, Radiation Effects, 43, 7, doi: 10.1080/00337577908226416

Kozyr', Y. E., & Prokopets, G. A. 1977, Sov. J. Nucl. Phys. (Engl. Transl.); (United States), 26, 927. https://www.osti.gov/biblio/6690445

Krassovskij, V. I., & Šklovskij, I. S. 1958, Il Nuovo Cimento (1955-1965), 8, 440, doi: 10.1007/BF02962552

Kretschmer, K., Diehl, R., Krause, M., et al. 2013, Astronomy & Astrophysics, 559, A99, doi: 10.1051/0004-6361/201322563

Kutschera, W. 2013, International Journal of Mass Spectrometry, 349-350, 203, doi: 10.1016/j.ijms.2013.05.023

Kyutoku, K., & Ioka, K. 2016, The Astrophysical Journal, 827, 83, doi: 10.3847/0004-637X/827/1/83

Kyutoku, K., Kiuchi, K., Sekiguchi, Y., Shibata, M., & Taniguchi, K. 2018, Physical Review D, 97, 023009, doi: 10.1103/PhysRevD.97.023009

Lachner, J., Dillmann, I., Faestermann, T., et al. 2012, Physical Review C, 85, 015801, doi: 10.1103/PhysRevC.85.015801

Lallement, R., & Bertaux, J. L. 2014, Astronomy & Astrophysics, Volume 565, id.A41, <NUMPAGES>8</NUMPAGES> pp., 565, A41, doi: 10.1051/0004-6361/201323216

Lantoine, G., & Russell, R. P. 2011, Celestial Mechanics and Dynamical Astronomy, 109, 333, doi: 10.1007/s10569-010-9331-1

Lazarian, A., & Opher, M. 2009, The Astrophysical Journal, 703, 8, doi: 10.1088/0004-637X/703/1/8

Lazauskas, R., Lunardini, C., & Volpe, C. 2009, Journal of Cosmology and Astroparticle Physics, 2009, 029, doi: 10.1088/1475-7516/2009/04/029

Lehner, L., Liebling, S. L., Palenzuela, C., et al. 2016, Classical and Quantum Gravity, 33, 184002, doi: 10.1088/0264-9381/33/18/184002

Leya, I., Lange, H.-J., Neumann, S., Wieler, R., & Michel, R. 2000, Meteoritics and Planetary Science, 35, 259, doi: 10.1111/j.1945-5100.2000.tb01775.x

Leya, I., & Masarik, J. 2009, Meteoritics and Planetary Science, 44, 1061, doi: 10.1111/j.1945-5100.2009.tb00788.x

Lien, A., & Fields, B. D. 2009, Journal of Cosmology and Astroparticle Physics, 2009, 047, doi: 10.1088/1475-7516/2009/01/047

Limongi, M., & Chieffi, A. 2006, The Astrophysical Journal, 647, 483, doi: 10.1086/505164

—. 2018, The Astrophysical Journal Supplement Series, 237, 13, doi: 10.3847/1538-4365/aacb24

Lindahl, P., Roos, P., Holm, E., & Dahlgaard, H. 2005, Journal of Environmental Radioactivity, 82, 285, doi: 10.1016/j.jenvrad.2005.01.011

Lineweaver, C. H., Fenner, Y., & Gibson, B. K. 2004, Science, 303, 59, doi: 10.1126/science.1092322

Linsky, J. L., & Redfield, S. 2021, The Astrophysical Journal, 920, 75, doi: 10.3847/1538-4357/ac1feb

Linsky, J. L., Redfield, S., & Tilipman, D. 2019, The Astrophysical Journal, 886, 41, doi: 10.3847/1538-4357/ab498a

Looney, L. W., Tobin, J. J., & Fields, B. D. 2006, The Astrophysical Journal, 652, 1755, doi: 10.1086/508407

Ludwig, P., Bishop, S., Egli, R., et al. 2016, Proceedings of the National Academy of Sciences, 113, 9232, doi: 10.1073/pnas.1601040113

Lugaro, M., Ott, U., & Kereszturi, A. 2018, Progress in Particle and Nuclear Physics, 102, 1, doi: 10.1016/j.ppnp.2018.05.002

Lychagin, A. A., Vinogradov, V. A., Grudzevich, O. T., et al. 1984, Soviet Atomic Energy, 57, 726, doi: 10.1007/BF01123646

López-Lora, M., & Chamizo, E. 2019, Nuclear Instruments and Methods in Physics Research Section B: Beam Interactions with Materials and Atoms, 455, 39, doi: 10.1016/j.nimb.2019.06.018

Malkus, A., McLaughlin, G. C., & Surman, R. 2016, Physical Review D, 93, 045021, doi: 10.1103/PhysRevD.93.045021

Mamajek, E. E. 2015, Proceedings of the International Astronomical Union, 10, 21, doi: 10.1017/S1743921315006250

Mann, I. 2010, Annual Review of Astronomy and Astrophysics, 48, 173, doi: 10.1146/annurev-astro-081309-130846

Marketin, T., Huther, L., & Martínez-Pinedo, G. 2016, Physical Review C, 93, 025805, doi: 10.1103/PhysRevC.93.025805

Marshall, J. E. A., Lakin, J., Troth, I., & Wallace-Johnson, S. M. 2020, Science Advances, 6, eaba0768, doi: 10.1126/sciadv.aba0768

Martin, D., Perego, A., Arcones, A., et al. 2015, The Astrophysical Journal, 813, 2, doi: 10.1088/0004-637X/813/1/2

Martschini, M., Fifield, L. K., Froehlich, M. B., et al. 2019, Nuclear Instruments and Methods in Physics Research Section B: Beam Interactions with Materials and Atoms, 438, 141, doi: 10.1016/j.nimb.2018.05.039

Martschini, M., Lachner, J., Merchel, S., et al. 2020, in European physical journal web of conferences, Vol. 232, European physical journal web of conferences, 02003, doi: 10.1051/epjconf/202023202003

Masarik, J., & Beer, J. 1999, Journal of Geophysical Research, 104, 12099, doi: 10.1029/1998JD200091

Mather, D. S., Bampton, P. F., Coles, R. E., James, G., & Nind, P. J. 1972, Measurement of (n,2n) cross sections for incident energies between 6 and14 MeV, Tech. Rep. AWRE-O–72/72; EANDC(UK)–142-AL, Atomic Weapons Research Establishment, Aldermaston (England). https://www.osti.gov/biblio/4570888

Matsuura, M., Indebetouw, R., Woosley, S., et al. 2017, Monthly Notices of the Royal Astronomical Society, 469, 3347, doi: 10.1093/mnras/stx830

Matteucci, F., Romano, D., Arcones, A., Korobkin, O., & Rosswog, S. 2014, Monthly Notices of the Royal Astronomical Society, 438, 2177, doi: 10.1093/mnras/stt2350

Mazeeva, O. A. 2004, Solar System Research, 38, 325, doi: 10.1023/B:SOLS.0000037467.03325.aa

Maíz-Apellániz, J. 2001, The Astrophysical Journal, 560, L83, doi: 10.1086/324016

McComas, D. J., Alexashov, D., Bzowski, M., et al. 2012, Science, 336, 1291, doi: 10.1126/science.1221054

McCullough, P. R., Fields, B. D., & Pavlidou, V. 2002, The Astrophysical Journal Letters, 576, L41. http://iopscience.iop.org/article/10.1086/343100/meta

McLaughlin, G. C., Fetter, J. M., Balantekin, A. B., & Fuller, G. M. 1999, Physical Review C, 59, 2873, doi: 10.1103/PhysRevC.59.2873

Medvedev, M. V., & Melott, A. L. 2007, The Astrophysical Journal, 664, 879, doi: 10.1086/518757

Melott, A. L., Marinho, F., & Paulucci, L. 2018, Astrobiology, 19, 825, doi: 10.1089/ast.2018.1902

Melott, A. L., & Thomas, B. C. 2011, Astrobiology, 11, 343, doi: 10.1089/ast.2010.0603

—. 2017, arXiv:1712.02730 [astro-ph, physics:physics, q-bio]. http://arxiv.org/abs/1712.02730

—. 2019, The Journal of Geology, 127, 475, doi: 10.1086/703418

Melott, A. L., Thomas, B. C., Kachelrieß, M., Semikoz, D. V., & Overholt, A. C. 2017, The Astrophysical Journal, 840, 105, doi: 10.3847/1538-4357/aa6c57

Melott, A. L., Lieberman, B. S., Laird, C. M., et al. 2004, International Journal of Astrobiology, 3, 55, doi: 10.1017/S1473550404001910

Merchel, S., Faestermann, T., Herpers, U., et al. 2000, Nuclear Instruments and Methods in Physics Research Section B: Beam Interactions with Materials and Atoms, 172, 806, doi: 10.1016/S0168-583X(00)00105-1

Meyer, B. S. 1993, Meteoritics, 28, 399. https://ui.adsabs.harvard.edu/abs/1993Metic..28Q.399M

Meyer, B. S., & Clayton, D. D. 2000, Space Science Reviews, 92, 133, doi: 10.1023/A:1005282825778

Meyer, D. M.-A., Mignone, A., Petrov, M., et al. 2021, Monthly Notices of the Royal Astronomical Society, 506, 5170, doi: 10.1093/mnras/stab2026

Michel, R., Dragovitsch, P., Cloth, P., Dagge, G., & Filges, D. 1991, Meteoritics, 26, 221. http://adsabs.harvard.edu/abs/1991Metic..26..221M

Michel, R., Bodemann, R., Busemann, H., et al. 1997, Nuclear Instruments and Methods in Physics Research Section B: Beam Interactions with Materials and Atoms, 129, 153, doi: 10.1016/S0168-583X(97)00213-9

Miller, J. A., & Fields, B. D. 2022, arXiv:2205.01746 [astro-ph, physics:physics]. http://arxiv.org/abs/2205.01746

Miller, J. M., Sprouse, T. M., Fryer, C. L., et al. 2020, The Astrophysical Journal, 902, 66, doi: 10.3847/1538-4357/abb4e3

Miyake, F., Nagaya, K., Masuda, K., & Nakamura, T. 2012, Nature, 486, 240, doi: 10.1038/nature11123

Moran, J. E., Fehn, U., & Teng, R. T. D. 1998, Chemical Geology, 152, 193, doi: 10.1016/S0009-2541(98)00106-5

Morrison, I. S., & Gowanlock, M. G. 2015, Astrobiology, 15, 683, doi: 10.1089/ast.2014.1192

Motizuki, Y., Takahashi, K., Makishima, K., et al. 2009, arXiv e-prints, doi: 10.48550/arXiv.0902.3446

Motobayashi, T., & Sakurai, H. 2012, Progress of Theoretical and Experimental Physics, 2012, 03C001, doi: 10.1093/ptep/pts059

Mumpower, M. R., Kawano, T., Sprouse, T. M., et al. 2018, The Astrophysical Journal, 869, 14, doi: 10.3847/1538-4357/aaeaca

Murphey, C. T., Hogan, J. W., Fields, B. D., & Narayan, G. 2021, Monthly Notices of the Royal Astronomical Society, 507, 927, doi: 10.1093/mnras/stab2182

Murray, N. 2011, The Astrophysical Journal, 729, 133, doi: 10.1088/0004-637X/729/2/133

Myrow, P. M., Ramezani, J., Hanson, A. E., et al. 2014, Terra Nova, 26, 222, doi: 10.1111/ter.12090

Möbius, E., Bochsler, P., Bzowski, M., et al. 2012, The Astrophysical Journal Supplement Series, 198, 11, doi: 10.1088/0067-0049/198/2/11

Mösta, P., Roberts, L. F., Halevi, G., et al. 2018, The Astrophysical Journal, 864, 171, doi: 10.3847/1538-4357/aad6ec

Müller, H.-R., Frisch, P. C., Fields, B. D., & Zank, G. P. 2009, Space Science Reviews, 143, 415, doi: 10.1007/s11214-008-9448-7

Müller, H.-R., Frisch, P. C., Florinski, V., & Zank, G. P. 2006, The Astrophysical Journal, 647, 1491, doi: 10.1086/505588

Neale, P. J., & Thomas, B. C. 2016, Astrobiology, 16, 245, doi: 10.1089/ast.2015.1360

Neuhäuser, R., Gießler, F., & Hambaryan, V. V. 2020, Monthly Notices of the Royal Astronomical Society, 498, 899, doi: 10.1093/mnras/stz2629

Nguyen, V. T., & Johnson, C. W. 2007, Astroparticle Physics, 27, 233, doi: 10.1016/j.astropartphys.2006.10.002

Nishimura, N., Rauscher, T., Hirschi, R., et al. 2018, Monthly Notices of the Royal Astronomical Society, 474, 3133, doi: 10.1093/mnras/stx3033

Nozaki, Y. 2001, Encyclopedia of Ocean Sciences, 4, 2354

Nozawa, T., Maeda, K., Kozasa, T., et al. 2011, The Astrophysical Journal, 736, 45, doi: 10.1088/0004-637X/736/1/45

Ogliore, R. C., Cohen, M., Wang, K., Chen, H., & Liu, N. 2020, 51st Lunar and Planetary Science Conference, 1695. https://ui.adsabs.harvard.edu/abs/2020LPI....51.1695O

Oort, J. H. 1950, Bulletin of the Astronomical Institutes of the Netherlands, 11, 91. http://adsabs.harvard.edu/abs/1950BAN....11...91O

Opher, M., Drake, J. F., Zieger, B., & Gombosi, T. I. 2015, The Astrophysical Journal, 800, L28, doi: 10.1088/2041-8205/800/2/L28

Opher, M., & Loeb, A. 2022, arXiv:2202.01813 [astro-ph]. http://arxiv.org/abs/2202.01813

Opher, M., Loeb, A., Drake, J., & Toth, G. 2020, Nature Astronomy, 4, 675, doi: 10.1038/s41550-020-1036-0

Ostdiek, K. M., Anderson, T. S., Bauder, W. K., et al. 2017, Physical Review C, 95, 055809, doi: 10.1103/PhysRevC.95.055809

Ouellette, N., Desch, S. J., Bizzarro, M., et al. 2009, Geochimica et Cosmochimica Acta, 73, 4946, doi: 10.1016/j.gca.2008.10.044

Paresce, F. 1984, The Astronomical Journal, 89, 1022, doi: 10.1086/113598

Parker, E. N. 1958, The Astrophysical Journal, 128, 664, doi: 10.1086/146579

—. 1965, Space Science Reviews, 4, 666, doi: 10.1007/BF00216273

Paul, M., Valenta, A., Ahmad, I., et al. 2001, The Astrophysical Journal, 558, L133, doi: 10.1086/323617

Pauls, H. L., & Zank, G. P. 1997, Journal of Geophysical Research: Space Physics, 102, 19779, doi: https://doi.org/10.1029/97JA01716

Pauls, H. L., Zank, G. P., & Williams, L. L. 1995, Journal of Geophysical Research: Space Physics, 100, 21595, doi: https://doi.org/10.1029/95JA02023

Paulsen, A., & Widera, R. 1970, Zeitschrift für Physik, 238, 23, doi: 10.1007/BF01399575

Pavetich, S., Carey, A., Fifield, L. K., et al. 2019, Nuclear Instruments and Methods in Physics Research B, 438, 77, doi: 10.1016/j.nimb.2018.07.019

Peißker, F., Eckart, A., & Parsa, M. 2020a, The Astrophysical Journal, 889, 61, doi: 10.3847/1538-4357/ab5afd

Peißker, F., Eckart, A., Zajaček, M., Ali, B., & Parsa, M. 2020b, The Astrophysical Journal, 899, 50, doi: 10.3847/1538-4357/ab9c1c

Perego, A., Rosswog, S., Cabezón, R. M., et al. 2014, Monthly Notices of the Royal Astronomical Society, 443, 3134, doi: 10.1093/mnras/stu1352

Peri, C. S., Benaglia, P., Brookes, D. P., Stevens, I. R., & Isequilla, N. L. 2012, Astronomy & Astrophysics, 538, A108, doi: 10.1051/0004-6361/201118116

Perlmutter, S., Aldering, G., Goldhaber, G., et al. 1999, The Astrophysical Journal, 517, 565, doi: 10.1086/307221

Pogorelov, N. V., Zank, G. P., & Ogino, T. 2004, The Astrophysical Journal, 614, 1007, doi: 10.1086/423798

Prestianni, C., Sautois, M., & Denayer, J. 2016, Geologica Belgica, doi: 10.20341/gb.2016.013

Prokopets, G. A. 1980, Yadernaya Fizika, 32, 37. https://inis.iaea.org/search/searchsinglerecord.aspx?recordsFor=SingleRecord&RN=13667878

Provornikova, E., Opher, M., Izmodenov, V. V., Richardson, J. D., & Toth, G. 2014, The Astrophysical Journal, 794, 29, doi: 10.1088/0004-637X/794/1/29

Pruet, J., Woosley, S. E., & Hoffman, R. D. 2003, The Astrophysical Journal, 586, 1254, doi: 10.1086/367957

Qian, Y., Xiao, L., Wang, Q., et al. 2021, Earth and Planetary Science Letters, 561, 116855, doi: 10.1016/j.epsl.2021.116855

Quirk, J. J. 1994, International Journal for Numerical Methods in Fluids, 18, 555, doi: 10.1002/fld.1650180603

Racki, G. 2020, Global and Planetary Change, 189, 103174, doi: 10.1016/j.gloplacha.2020.103174

Radice, D., Perego, A., Hotokezaka, K., et al. 2018, The Astrophysical Journal, 869, L35, doi: 10.3847/2041-8213/aaf053

Raisbeck, G., Tran, T., Lunney, D., et al. 2007, Nuclear Instruments and Methods in Physics Research Section B: Beam Interactions with Materials and Atoms, 259, 673, doi: 10.1016/j.nimb.2007.01.205

Reichert, M., Obergaulinger, M., Eichler, M., Aloy, M. A., & Arcones, A. 2021, Monthly Notices of the Royal Astronomical Society, 501, 5733, doi: 10.1093/mnras/stab029

Rickman, H., Fouchard, M., Froeschlé, C., & Valsecchi, G. B. 2008, Celestial Mechanics and Dynamical Astronomy, 102, 111, doi: 10.1007/s10569-008-9140-y

Riess, A. G., Filippenko, A. V., Challis, P., et al. 1998, The Astronomical Journal, 116, 1009, doi: 10.1086/300499

Roberts, L. F., Reddy, S., & Shen, G. 2012, Physical Review C, 86, 065803, doi: 10.1103/PhysRevC.86.065803

Roederer, I. U., & Lawler, J. E. 2012, The Astrophysical Journal, 750, 76, doi: 10.1088/0004-637X/750/1/76

Rood, R. T., Sarazin, C. L., Zeller, E. J., & Parker, B. C. 1979, Nature, 282, 701, doi: 10.1038/282701a0

Rosswog, S., Feindt, U., Korobkin, O., et al. 2017, Classical and Quantum Gravity, 34, 104001, doi: 10.1088/1361-6382/aa68a9

Rosswog, S., Piran, T., & Nakar, E. 2013, Monthly Notices of the Royal Astronomical Society, 430, 2585, doi: 10.1093/mnras/sts708

Rozwadowska, K., Vissani, F., & Cappellaro, E. 2021, New Astronomy, 83, 101498, doi: 10.1016/j.newast.2020.101498

Ruderman, M. A. 1974, Science, 184, 1079, doi: 10.1126/science.184.4141.1079

Rugel, G., Faestermann, T., Knie, K., et al. 2009, Physical Review Letters, 103, doi: 10.1103/PhysRevLett.103.072502

Röllin, S., Sahli, H., Holzer, R., Astner, M., & Burger, M. 2009, Applied Radiation and Isotopes, 67, 821, doi: 10.1016/j.apradiso.2009.01.041

Sanctis, M. C. D., Capria, M. T., & Coradini, A. 2001, The Astronomical Journal, 121, 2792, doi: 10.1086/320385

Savard, G., Brodeur, M., Clark, J. A., Knaack, R. A., & Valverde, A. A. 2020, Nuclear Instruments and Methods in Physics Research B, 463, 258, doi: 10.1016/j.nimb.2019.05.024

Savard, G., Baker, S., Davids, C., et al. 2008, Nuclear Instruments and Methods in Physics Research B, 266, 4086, doi: 10.1016/j.nimb.2008.05.091

Savchenko, V., Kachelrieß, M., & Semikoz, D. V. 2015, The Astrophysical Journal, 809, L23, doi: 10.1088/2041-8205/809/2/L23

Scalo, J., & Wheeler, J. C. 2002, The Astrophysical Journal, 566, 723, doi: 10.1086/338329

Schneider, D. L., & Livingston, H. D. 1984, Nuclear Instruments and Methods in Physics Research, 223, 510, doi: 10.1016/0167-5087(84)90700-2

Schulreich, M. M., Breitschwerdt, D., Feige, J., & Dettbarn, C. 2017, Astronomy & Astrophysics, 604, A81, doi: 10.1051/0004-6361/201629837

Schönrich, R., Binney, J., & Dehnen, W. 2010, Monthly Notices of the Royal Astronomical Society, 403, 1829, doi: 10.1111/j.1365-2966.2010.16253.x

Seab, C. G. 1987, in Interstellar Processes, ed. D. J. Hollenbach & H. A. Thronson, Astrophysics and Space Science Library (Dordrecht: Springer Netherlands), 490–512, doi: 10.1007/978-94-009-3861-8_18

Sedov, L. I. 1946, Prikl. Mat. Mekh, 10, 241

Seeger, P. A., & Schramm, D. N. 1970, The Astrophysical Journal, 160, L157, doi: 10.1086/180550

Sekiguchi, Y., Kiuchi, K., Kyutoku, K., Shibata, M., & Taniguchi, K. 2016, Physical Review D, 93, 124046, doi: 10.1103/PhysRevD.93.124046

Shetye, S., Eck, S. V., Goriely, S., et al. 2020, Astronomy & Astrophysics, 635, L6, doi: 10.1051/0004-6361/202037481

Shibagaki, S., Kajino, T., Mathews, G. J., et al. 2016, The Astrophysical Journal, 816, 79, doi: 10.3847/0004-637X/816/2/79

Shklovskii, I. S., & Sagan, C. 1966, Intelligent life in the universe (Holden-Day). https://ui.adsabs.harvard.edu/abs/1966ilun.book.....S

Shklovskij, I. S. 1969, Interscience Publishers. https://ui.adsabs.harvard.edu/#abs/1969supe.book.....S/abstract

Siegel, D. M., Barnes, J., & Metzger, B. D. 2019, Nature, 569, 241, doi: 10.1038/s41586-019-1136-0

Siegel, D. M., & Metzger, B. D. 2018, The Astrophysical Journal, 858, 52, doi: 10.3847/1538-4357/aabaec

Slavin, J. D., Dwek, E., Mac Low, M.-M., & Hill, A. S. 2020, The Astrophysical Journal, 902, 135, doi: 10.3847/1538-4357/abb5a4

Slavin, J. D., Frisch, P. C., Heerikhuisen, J., et al. 2010, AIP Conference Proceedings, 1216, 497, doi: 10.1063/1.3396301

Smith, M., Craig, D., Herrmann, N., et al. 2020, in 2020 IEEE Aerospace Conference, 1–10, doi: 10.1109/AERO47225.2020.9172323

Smith, R. K., & Cox, D. P. 2001, The Astrophysical Journal Supplement Series, 134, 283. http://iopscience.iop.org/article/10.1086/320850/meta

Sonett, C. P., Morfill, G. E., & Jokipii, J. R. 1987, Nature, 330, 458, doi: 10.1038/330458a0

Spinelli, R., Ghirlanda, G., Haardt, F., Ghisellini, G., & Scuderi, G. 2021, Astronomy & Astrophysics, Volume 647, id.A41, <NUMPAGES>11</NUMPAGES> pp., 647, A41, doi: 10.1051/0004-6361/202039507

Sprouse, T. M., Mumpower, M. R., & Surman, R. 2021, Physical Review C, 104, 015803, doi: 10.1103/PhysRevC.104.015803

Steier, P., Hrnecek, E., Priller, A., et al. 2013, Nuclear Instruments and Methods in Physics Research B, 294, 160, doi: 10.1016/j.nimb.2012.06.017

Sterken, V. J., Altobelli, N., Kempf, S., et al. 2012, Astronomy & Astrophysics, 538, A102, doi: 10.1051/0004-6361/201117119

Stern, S. A. 1990, Icarus, 84, 447, doi: 10.1016/0019-1035(90)90048-E

Stern, S. A., & Shull, J. M. 1988, Nature, 332, 407, doi: 10.1038/332407a0

Stigall, A. 2012, GSA Today, 22, 272

Stone, J. M., Tomida, K., White, C. J., & Felker, K. G. 2020, The Astrophysical Journal Supplement Series, 249, 4, doi: 10.3847/1538-4365/ab929b

Strub, P., Krüger, H., & Sterken, V. J. 2015, The Astrophysical Journal, 812, 140, doi: 10.1088/0004-637X/812/2/140

Strub, P., Sterken, V. J., Soja, R., et al. 2018, Astronomy & Astrophysics, doi: 10.1051/0004-6361/201832644

Stuart, F. M., & Lee, M. R. 2012, Chemical Geology, 322-323, 209, doi: 10.1016/j.chemgeo.2012.07.002

Sukhbold, T., Ertl, T., Woosley, S. E., Brown, J. M., & Janka, H.-T. 2016, The Astrophysical Journal, 821, 38, doi: 10.3847/0004-637X/821/1/38

Surman, R., McLaughlin, G. C., & Hix, W. R. 2006, The Astrophysical Journal, 643, 1057, doi: 10.1086/501116

Surman, R., McLaughlin, G. C., Ruffert, M., Janka, H. T., & Hix, W. R. 2008, The Astrophysical Journal, 679, L117, doi: 10.1086/589507

Sutherland, R. S., Bisset, D. K., & Bicknell, G. V. 2003, The Astrophysical Journal Supplement Series, 147, 187, doi: 10.1086/374795

Sørensen, M., Svensmark, H., & Jørgensen, U. G. 2017, arXiv:1708.08248 [astro-ph]. http://arxiv.org/abs/1708.08248

Tachibana, S., & Huss, G. R. 2003, The Astrophysical Journal, 588, L41, doi: 10.1086/375362

Takami, H., Nozawa, T., & Ioka, K. 2014, The Astrophysical Journal, 789, L6, doi: 10.1088/2041-8205/789/1/L6

Takizawa, Y. 1982, Journal of Radiation Research, 23, 198, doi: 10.1269/jrr.23.198

Taylor, G. 1950, Proceedings of the Royal Society of London. Series A, Mathematical and Physical Sciences, 201, 159. https://www.jstor.org/stable/98395

Terry, K. D., & Tucker, W. H. 1968, Science, 159, 421, doi: 10.1126/science.159.3813.421

Tetzlaff, N., Torres, G., Neuhäuser, R., & Hohle, M. M. 2013, Monthly Notices of the Royal Astronomical Society, 435, 879, doi: 10.1093/mnras/stt1358

Thomas, B. C. 2017, Astrobiology, 18, 481, doi: 10.1089/ast.2017.1730

Thomas, B. C., Atri, D., & Melott, A. L. 2020, arXiv:2009.14078 [astro-ph, physics:physics]. http://arxiv.org/abs/2009.14078

Thomas, B. C., Engler, E. E., Kachelrieß, M., et al. 2016, The Astrophysical Journal, 826, L3, doi: 10.3847/2041-8205/826/1/L3

Thomas, B. C., Neale, P. J., & Snyder, II, B. R. 2015, Astrobiology, 15, 207, doi: 10.1089/ast.2014.1224

Thomas, B. C., Melott, A. L., Jackman, C. H., et al. 2005, The Astrophysical Journal, 634, 509, doi: 10.1086/496914

Thompson, R. C. 1982, Radiation Research, 90, 1, doi: 10.2307/3575792

Tsujimoto, T., Yokoyama, T., & Bekki, K. 2017, The Astrophysical Journal, 835, L3, doi: 10.3847/2041-8213/835/1/L3

Vassh, N., Mumpower, M. R., McLaughlin, G. C., Sprouse, T. M., & Surman, R. 2020, The Astrophysical Journal, 896, 28, doi: 10.3847/1538-4357/ab91a9

Vassh, N., Vogt, R., Surman, R., et al. 2019, Journal of Physics G Nuclear Physics, 46, 065202, doi: 10.1088/1361-6471/ab0bea

Veeser, L. R., Arthur, E. D., & Young, P. G. 1977, Physical Review C, 16, 1792, doi: 10.1103/PhysRevC.16.1792

Vockenhuber, C., Casacuberta, N., Christl, M., & Synal, H.-A. 2015, Nuclear Instruments and Methods in Physics Research Section B: Beam Interactions with Materials and Atoms, 361, 445, doi: 10.1016/j.nimb.2015.01.061

Vockenhuber, C., Feldstein, C., Paul, M., et al. 2004, New Astronomy Reviews, 48, 161, doi: 10.1016/j.newar.2003.11.023

Wallis, M. K. 1987, Monthly Notices of the Royal Astronomical Society, 227, 331, doi: 10.1093/mnras/227.2.331

Wallner, A., Bichler, M., Buczak, K., et al. 2015a, Physical Review Letters, 114, 041101, doi: 10.1103/PhysRevLett.114.041101

Wallner, A., Faestermann, T., Feige, J., et al. 2015b, Nature Communications, 6, 5956, doi: 10.1038/ncomms6956

Wallner, A., Feige, J., Kinoshita, N., et al. 2016, Nature, 532, 69, doi: 10.1038/nature17196

Wallner, A., Feige, J., Fifield, L. K., et al. 2020, Proceedings of the National Academy of Sciences, doi: 10.1073/pnas.1916769117

Wallner, A., Froehlich, M. B., Hotchkis, M. a. C., et al. 2021, Science, 372, 742, doi: 10.1126/science.aax3972

Wallner, C., Faestermann, T., Gerstmann, U., et al. 2004, New Astronomy Reviews, 48, 145, doi: 10.1016/j.newar.2003.11.020

Wanajo, S. 2006, The Astrophysical Journal, 650, L79, doi: 10.1086/508568

—. 2013, The Astrophysical Journal, 770, L22, doi: 10.1088/2041-8205/770/2/L22

Wanajo, S., Janka, H.-T., & Müller, B. 2013, The Astrophysical Journal, 774, L6, doi: 10.1088/2041-8205/774/1/L6

Wanajo, S., Kajino, T., Mathews, G. J., & Otsuki, K. 2001, The Astrophysical Journal, 554, 578, doi: 10.1086/321339

Wanajo, S., Sekiguchi, Y., Nishimura, N., et al. 2014, The Astrophysical Journal, 789, L39, doi: 10.1088/2041-8205/789/2/L39

Wang, X., N3AS Collaboration, Fields, B. D., et al. 2020a, The Astrophysical Journal, 893, 92, doi: 10.3847/1538-4357/ab7ffd

Wang, X., N3AS Collaboration, Vassh, N., et al. 2020b, The Astrophysical Journal, 903, L3, doi: 10.3847/2041-8213/abbe18

Wehmeyer, B., Pignatari, M., & Thielemann, F. K. 2015, Monthly Notices of the Royal Astronomical Society, 452, 1970, doi: 10.1093/mnras/stv1352

Welsh, B. Y., & Shelton, R. L. 2009, Astrophysics and Space Science, 323, 1, doi: 10.1007/s10509-009-0053-3

Wiegert, P., & Tremaine, S. 1999, Icarus, 137, 84, doi: 10.1006/icar.1998.6040

Wilcken, K. M., Fifield, L. K., Barrows, T. T., Tims, S. G., & Gladkis, L. G. 2008, Nuclear Instruments and Methods in Physics Research Section B: Beam Interactions with Materials and Atoms, 266, 3614, doi: 10.1016/j.nimb.2008.06.009

Wilkin, F. P. 1996, The Astrophysical Journal Letters, 459, L31, doi: 10.1086/309939

Winkler, S., Ahmad, I., Golser, R., et al. 2004, New Astronomy Reviews, 48, 151, doi: 10.1016/j.newar.2003.11.021

Winteler, C., Käppeli, R., Perego, A., et al. 2012, The Astrophysical Journal, 750, L22, doi: 10.1088/2041-8205/750/1/L22

Woosley, S. E., Heger, A., & Weaver, T. A. 2002, Reviews of Modern Physics, 74, 1015, doi: 10.1103/RevModPhys.74.1015

Xiong, Z., Sieverding, A., Sen, M., & Qian, Y.-Z. 2020, The Astrophysical Journal, 900, 144, doi: 10.3847/1538-4357/abac5e

Yamazaki, Y., Kajino, T., Mathews, G. J., et al. 2021, arXiv e-prints, arXiv:2102.05891

Yan, Y., Bender, M. L., Brook, E. J., et al. 2019, Nature, 574, 663, doi: 10.1038/s41586-019-1692-3

Yeghikyan, A., & Fahr, H. 2004, Astronomy & Astrophysics, 415, 763, doi: 10.1051/0004-6361:20034609

Yeghikyan, A. G., & Fahr, H. J. 2003, Annales Geophysicae, 21, 1263, doi: 10.5194/angeo-21-1263-2003

Yin, X., He, M., Dong, K., et al. 2015, Nuclear Instruments and Methods in Physics Research Section B: Beam Interactions with Materials and Atoms, 361, 488, doi: 10.1016/j.nimb.2015.07.124

Yong, D., Kobayashi, C., Da Costa, G. S., et al. 2021, Nature, 595, 223, doi: 10.1038/s41586-021-03611-2

Zank, G. P. 1999, Space Science Reviews, 89, 413, doi: 10.1023/A:1005155601277

Zank, G. P., Pauls, H. L., Cairns, I. H., & Webb, G. M. 1996, Journal of Geophysical Research: Space Physics, 101, 457, doi: https://doi.org/10.1029/95JA02860

Zbinden, O., & Saha, P. 2019, Research Notes of the AAS, 3, 73, doi: 10.3847/2515-5172/ab2130

Zhu, Y., Wollaeger, R. T., Vassh, N., et al. 2018, The Astrophysical Journal, 863, L23, doi: 10.3847/2041-8213/aad5de

Zhu, Y. L., Lund, K. A., Barnes, J., et al. 2021, The Astrophysical Journal, 906, 94, doi: 10.3847/1538-4357/abc69e

Zinner, E. 1998, Annual Review of Earth and Planetary Sciences, 26, 147, doi: 10.1146/annurev.earth.26.1.147

Zucker, C., Goodman, A. A., Alves, J., et al. 2022, Nature, 1, doi: 10.1038/s41586-021-04286-5

Zwart, S. P., Pelupessy, I., Elteren, A. v., Wijnen, T. P. G., & Lugaro, M. 2018, Astronomy & Astrophysics, 616, A85, doi: 10.1051/0004-6361/201732060

Ćirković, M. M., & Vukotić, B. 2016, Acta Astronautica, 129, 438, doi: 10.1016/j.actaastro.2016.10.005